Dissertation

Defence held on June 29th 2023 in Besançon
to obtain the degrees of

DOCTEUR DE L'UNIVERSITÉ DU LUXEMBOURG EN SCIENCES DE L'INGÉNIEUR

and

DOCTEUR DE L'UNIVERSITÉ DE BOURGOGNE FRANCHE–COMTÉ EN MÉCANIQUE

by

Aflah ELOUNEG

born on August 10th 1992 in Guerrara (Algeria)

In vivo mechanical characterization of soft tissues: application to human skin and keloids

Dissertation defence committee:

Dr Stéphane Bordas, dissertation supervisor
Professor, Université du Luxembourg

Dr Emmanuelle Jacquet
Professor, Université de Franche-Comté

Dr Olivier Francis, Chairman
Professor, Université du Luxembourg

Dr Michel Destrade
Professor, University of Galway

Dr Georges Limbert, Vice Chairman
Professor, University of Southampton

Dr Johannes Weickenmeier
Assistant Professor, Stevens Institute of Technology

THESE DE DOCTORAT DE L'ÉTABLISSEMENT UNIVERSITE
BOURGOGNE FRANCHE-COMTE EN CO-TUTELLE AVEC
L'UNIVERSITE DU LUXEMBOURG PREPAREE A
L'UNIVERSITE DE FRANCHE COMTE

École doctorale n°37
Sciences Pour l'Ingénieur et Microtechniques

Doctorat de Mécanique

Par

Aflah ELOUNEG

Caractérisation mécanique *in vivo* des tissus mous : application à la peau humaine et la chéloïde

Thèse présentée et soutenue à Besançon, le 29 juin 2023

Composition du Jury :

Emmanuelle Jacquet	Professeure des universités, Université de Franche-Comté	Co-directrice de thèse
Stéphane Bordas	Professeur des universités, Université du Luxembourg	Co-directeur de thèse
Arnaud Lejeune	Ingénieur de recherche, Université de Franche-Comté	Co-directeur de thèse
Olivier Francis	Professeur des universités, Université du Luxembourg	Examinateur, président du jury
Georges Limbert	Professeur des universités, Université de Southampton	Rapporteur
Michel Destrade	Professeur des universités, Université de Galway	Rapporteur
Johannes Weickenmeier	Maître de conférences, Institut de Technologie Stevens	Examinateur

In vivo mechanical characterization of soft tissues: application to human skin and keloids

Aflah Elouneg

To my parents, Aïcha & Aoumeur,

my siblings, Asma, Amine,

and my life partner, Amel,

"The knowledge I have now is not the knowledge I had then."
– Stokely Carmichael

Acknowledgments

The thesis would not have been accomplished without the contribution of many people and organizations that I want to thank sincerely hereafter. First of all, I am grateful to my supervisors, Emmanuelle Jacquet, Jérôme Chambert, and Arnaud Lejeune, from Université de Franche-Comté, and Stéphane Bordas, from Université du Luxembourg.

Emmanuelle, I am immensely thankful for granting me the opportunity to join the soft tissue biomechanics team and work on such an exciting topic. Thanks for your trust, scientific guidance, and mental support. It has been an absolute pleasure to work under your leadership, both as a PhD student and as a colleague in teaching missions.

Jérôme, your astonishing expertise in continuum mechanics and extensive knowledge of the bibliography have been invaluable to me. You helped me a lot in understanding the hyperelastic theory and building mechanical models. Your relevant observations and constructive feedback on the results and methodology were precious for the work.

Arnaud, your contribution to this thesis has been immense, encompassing both the numerical aspects and the methodology. Whether it was your expertise in handling numerical simulations or your emphasis on scientific rigor, the utilization of open-source frameworks, and sharing data, I have learned invaluable lessons from you.

Stéphane, You provided me with the opportunity to conduct research in a foreign country and explore a new discipline. After collaborating on numerous papers, I must acknowledge that your scientific writing spirit has greatly influenced me, and I am grateful for the impact it has had on my writing style. I was happy to be part of the Legato team.

I express my gratitude to the members of my thesis defense jury members for agreeing to review my work. I would like to thank Georges Limbert and Michel Destrade to have accepted to be my dissertation examiners. Their works have inspired me greatly to progress in tackling the problem. The suggestion of Michel, whom I met in summer school, about using the Gent model to fit data was of massive help. It was a turning point in my thesis. Warm thanks go to Olivier Francis, the chairman, and Johannes Weickenmeier, an external examiner. It is a great honor for me to share my research with them.

Thank you Danas Sutula. I was able to understand your framework code thanks to your explanations. How you organized the functions and files taught me how to build a new framework from scratch. I

Contents

List of Figures

List of Tables

Acronyms

BC	Boundary Condition
DIC	Digital Image Correlation
FEM	Finite Element Method
FEMU	Finite Element Model Updating
FEɴɪCS	Finite Element Computational Software
FD	Force-Displacement
MARSAC	Multi-Axial Ring Suction for Anistotropy Characterization
MCMC	Markov Chain Monte Carlo
RF	Reaction Force
SEDF	Strain Energy Density Function
SoғTI	Soft Tissue Identification
ST	Soft Tissue
ZOI	Zone of Interest

Relevant Symbols

$\boldsymbol{u}$	Displacement field
λ	Stretch
$\boldsymbol{f}$	Reaction force
$\boldsymbol{t}$	Traction force
$\boldsymbol{\sigma}$	Cauchy stress tensor
$\boldsymbol{P}$	First Piola-Kirchhoff stress tensor
$\boldsymbol{S}$	Second Piola-Kirchhoff stress tensor
$\boldsymbol{F}$	Deformation gradient tensor
$\boldsymbol{x}$	Spatial Cartesian coordiantes
$\boldsymbol{X}$	Material Cartesian coordiantes
$\boldsymbol{I}$	Identity tensor
$\boldsymbol{C}$	Right Cauchy-Green deformation tensor
I_1, I_2, I_3	Invariants of $\boldsymbol{C}$
$\boldsymbol{n}$	normal vector in the deformed configuration
ψ	Strain energy density function
$\boldsymbol{m}$	Material parameters
μ, J_m	Gent model parameters
Ω	Mesh domain
Ω_{msr}	ZOI observation domain
Γ_{CS}	Force sensor boundary
$\mathcal{J}$	Objective function
Λ	Lagrange multiplier
$\boldsymbol{G}$	Gradient vector
$\boldsymbol{H}$	Hessian matrix
$\boldsymbol{C}_{\mathrm{e}}$	Linear orthotropic stiffness tensor
$\boldsymbol{\varepsilon}$	Strain tensor
p	Annular suction pressure
σ_r	radial stress
a, b	Semi-axes of ellipse-shaped deformation
ϕ	Langer's line orientation
E_1, E_2	Elastic moduli along and across Langer's line
ν_{12}, ν_{21}	Poisson's ratio along and across Langer's line
r	radial position
θ	angular position
r_{fit}	Model fitting circle
R_{cor}	Correlation coefficient
d_G	Digital image correlation grid step size
a_W	Digital image correlation subset window size
th	thickness

Introduction

Context

Skin biomechanics, a discipline that studies the mechanical aspects of cutaneous tissue, has become an interesting research area for interdisciplinary protagonists in the last decades. Scientists, clinicians, and engineers cooperated in various research works to understand human skin behavior under load and environmental conditions. The knowledge acquired from this challenging adventure would help prevent or treat dermatological disorders like wounds. For this purpose, the mechanical properties of the first defense line in the body are characterized by a combination of experimental, theoretical, and numerical methods. On some anatomical sites subjected to durable and substantial natural tensions, abnormal scars can emerge from cutaneous wounds that may cause heterogeneity in the mechanical properties of the medium. Hence, intrinsic mechanical stress would arise on the scar periphery, driving specific cells to emit biochemical signals that eventually boost scarring. Therefore, it is judicious to study their growth at the tissue scale from a mechanical point of view.

Keloid is one of the most problematic pathological scars, which may impose a significant clinical and social burden on the patient because of its unpleasant shape. Despite the enormous efforts put into play to elucidate the internal mechanism, keloids, considered benign tumors, are still misunderstood by the clinical community. Unlike a hypertrophic scar, a keloid doesn't fade with time. Several methods are proposed to reduce its appearance, but none solve the problem permanently. After eliminating the keloid, the scar tissue may grow back again, and sometimes it grows back larger than before.

Based on a patient-specific pipeline, the thesis aims to tackle the keloid's growth problem with a novel approach. Instead of using invasive techniques to delete the tumor, it would be appropriate to contain it at an early stage, by reducing the mechanical stress in the area, and prevent further propagation. To this end, *in vivo* experimental measurements are conducted on a subject and used as inputs to fit macro-scale simulation models. Optimal material parameters are identified through numerical methods and serve to quantify the mechanical stress in the medium enclosing the studied scar and map its privileged direction locally. Specifications of a retention medical solution could be asserted to conceive a restraint device adapted to the patient-specific keloid scar.

Advanced characterization studies contribute to scientific progress in perceiving the skin's response. In the actual context, it improves the reliability of the beforementioned framework and hence the efficiency of the medical solution. Accordingly, the thesis addresses in a parallel project a feature that was neglected in the first study: anisotropy in healthy skin modeling. The study involves building a second pipeline to identify the anisotropic material parameters from a multi-axial extension test and applying it to a clinical trial database to analyze the subject-to-subject variability.

Outlines

The thesis plan comprises six chapters covering two main research topics on top of a literature review written in the first chapter: the mechanical characterization of hyperelasticity in bi-material in

Chapters 2 to 4 and anisotropy in human skin in Chapters 5 et 6. Chapter 1 will describe the methods used in skin biomechanics literature according to the three main features of the subject, experiments, modeling, and parameter identification.

Chapter 2 will describe separately the components and methods of Finite-Elements-based open-source numerical framework, SoFTI[1], to identify the material parameters of a bi-material heterogeneous soft tissue, and their implementation using FEniCS libraries. It is an improvement of a program initialized by Sutula [1], a former post-doc researcher in *BiomecaT* team from the FEMTO-ST institute. The validation of the most crucial computational methods will be presented as well. Later in Chapter 3, the accuracy and precision of material parameter identification will be studied regarding a selection of uncertainty sources, particularly finite elements discretization errors, experimental data quantity and quality, topology, and the tri-dimensional aspect. *In silico* data were generated with additive synthetic noise to simulate the variability around a reference parameter set belonging to the Gent model, a hyperelastic constitutive law. Subsequently, Chapter 4 takes advantage of SoFTI to identify the parameters of a keloid scar and surrounding healthy skin starting from patient-specific experimental data. The latter captured with a uni-axial extensometer should be within the limits of parameter identification validity determined earlier. Afterward, the maximum mechanical stress in and around the tumor will be quantified, which could be interpreted as its growth's preferential directions. This process would predict the future keloid shape and propose a medical solution specification to prevent its propagation.

The second topic will address the anisotropic behavior of the skin through the two last chapters. Chapter 5 will introduce MARSAC pipeline[2] designed to estimate Langer's line and the stiffness along and across it. The methodology was constructed around displacement fields obtained with an annular suction device to provide a multi-axial extension of the skin surface and converted with the Digital Image Correlation. An application to a series of tests on one volunteer's forearm for validation and investigation of *intra*-subject variability will be addressed. Chapter 6 exploits the MARSAC method to analyze the subject-to-subject variability over a clinical trial that involved 30 volunteers. This part will report the experimental protocol's adaptation, data management, and treatment. It will present the relevant results of variability's significance in parameters regarding factors such as age and sex.

---

[1]`https://github.com/aflahelouneg/inverse_identification_soft_tissue`
[2]`https://github.com/aflahelouneg/MARSAC`

Scientific Contributions

Journal Articles

- **Anisotropic mechanical characterization of human skin by in vivo multi-axial ring suction test**,
  Aflah Elouneg, Jérôme Chambert, Arnaud Lejeune, Quentin Lucot, Emmanuelle Jacquet, Stéphane P. A. Bordas, *Journal of the Mechanical Behavior of Biomedical Materials*, March 2023, 105779,
  `https://doi.org/10.1016/j.jmbbm.2023.105779`

- **In vivo skin anisotropy dataset from annular suction test**,
  Aflah Elouneg, Audrey Bertin, Quentin Lucot, Vincent Tissot, Emmanuelle Jacquet, Jérôme Chambert, Arnaud Lejeune, *Data in Brief*, Volume 40, February 2022, 107835,
  `https://doi.org/10.1016/j.dib.2022.107835`

- **An open-source FEniCS-based framework for hyperelastic parameter estimation from noisy full-field data: Application to heterogeneous soft tissues**,
  Aflah Elouneg, Danas Sutula, Jérôme Chambert, Arnaud Lejeune, Stéphane P. A. Bordas, Emmanuelle Jacquet, *Computers & Structures*, Volume 255, 15 October 2021, 106620,
  `https://doi.org/10.1016/j.compstruc.2021.106620`

- **Biomechanical characterization of earlobe keloid by ring suction test**,
  Aflah Elouneg, Quentin Lucot, Elodie Veyrat-Durebex, Arnaud Lejeune, Jérôme Chambert, Thomas Lihoreau, Brice Chatelain, Gwenaël Rolin, Emmanuelle Jacquet, Volume 23, 2020 - Issue sup1: 45th Congress of the Société de Biomécanique,
  `https://doi.org/10.1080/10255842.2020.1812173`

- **An open source pipeline for design of experiments for hyperelastic models of the skin with applications to keloids**,
  Danas Sutula, Aflah Elouneg, Marco Sensale, Franz Chouly, Jérôme Chambert, Arnaud Lejeune, Davide Baroli, Paul Hauseux, Stéphane P. A. Bordas, Emmanuelle Jacquet, *Journal of the Mechanical Behavior of Biomedical Materials*, Volume 112, December 2020, 103999,
  `https://doi.org/10.1016/j.jmbbm.2020.103999`

Softwares

- **Multi-Axial Ring Suction for Anistortopy Characterization (MARSAC)**,
  Git repository: `https://github.com/aflahelouneg/MARSAC`, GPL-3.0 license

- **Soft Tissue Identification (SofTI)**,
  Git repository: `https://github.com/aflahelouneg/inverse_identification_soft_tissue`, MIT license

Open-Data

- *In vivo* **skin anisotropy dataset for a young man (28 years old) by annular suction**,
  Data repository: `http://dx.doi.org/doi:10.25666/DATAOSU-2021-08-25`, CC BY-NC-SA 4.0 license

Clinical Trial Data

- **Construction of a human skin mechanics database for mathematical modeling of uncertainties in cutaneous tissue**, Department of Dermatology, Centre Hospitalier Régional

Universitaire de Besançon. Identification number: 2020-A01863-36

Conference Presentations and Posters

- *In vivo* **mechanical characterization and tissue-scale modelling of keloid and surrounding healthy skin**,
  Aflah Elouneg, Audrey Bertin, Nicolas Marie, Quentin Lucot, Danas Sutula, Franz Chouly, Arnaud Lejeune, Thomas Lihoreau, Brice Chatelain, Gwenaël Rolin, Stéphane P. A. Bordas, Emmanuelle Jacquet, Jérôme Chambert,
  26th Congress of the European Society of Biomechanics, Milan, Italy, 2021

- **Inverse identification of bi-material soft tissue parameters**,
  Aflah Elouneg, Danas Sutula, Arnaud Lejeune, Jérôme Chambert, Franz Chouly, Stéphane P. A. Bordas, Emmanuelle Jacquet,
  14th World Congress on Computational Mechanics (WCCM), ECCOMAS Congress, Paris, France, 2020

- **Parameter identification problem in bimaterial human skin and sensitivity analysis: Uncertainties in biomechanics of skin**,
  Danas Sutula, Aflah Elouneg, Marco Sensale, Franz Chouly, Jérôme Chambert, Arnaud Lejeune, Davide Baroli, Paul Hauseux, Stéphane P. A. Bordas, Emmanelle Jacquet, Congrès Français de Mécanique, Aug 2019, Brest, France,
  `https://hal.archives-ouvertes.fr/hal-02376994`

- **Mechanical parameters identification of keloid and surrounding healthy skin using Digital Image Correlation measurements** *in vivo*,
  Aflah Elouneg, Danas Sutula, Marco Sensale, Franz Chouly, Jérôme Chambert, Arnaud Lejeune, Davide Baroli, Paul Hauseux, Stéphane Bordas, Emmanuelle Jacquet, Congrès Français de Mécanique, Aug 2019, Brest, France
  `https://hal.archives-ouvertes.fr/hal-02376993`

- **Caractérisation** *in vivo* **du comportement mécanique des tissus cutanés par essai de succion annulaire (CutiScan®)**,
  Aflah Elouneg, Quentin Lucot, Jérôme Chambert, Arnaud Lejeune, Emmanuelle Jacquet,
  1st Keloid mini-symposium, Besançon, France, 2019

- **Implementation and simulations of hyperelastic constitutive laws, in soft tissues: Application on human skin and arteries**,
  Maha Reda, Aflah Elouneg, Jérôme Chmabert, Arnaud Lejeune, Christophe Noël, Emmanuelle Jacquet,
  27ème Séminaire Franco-Polonais de Mécanique, Besançon, France, 2019

Seminars

- **Mechanical Properties of the Skin and Uncertainties in Biomechanics**,
  Doctoral Programme Computational Science, Esch-sur-Alzette, Luxembourg, 2022

- **Anisotropy characterization of human skin through a multi-axial ring suction test**,
  Legato team seminar, Uni Lu, Esch-sur-Alzette, Luxembourg, 2022

- **Inverse Identification of Heterogeneous Skin Parameters**,
  Conference simulation, Besançon, France, 2020

- **Identification of keloid and surrounding healthy skin material parameters using Digital Image Correlation measurements *In vivo*,**
  Legato team seminar, Uni Lu, Esch-sur-Alzette, Luxembourg, 2020

- **Propriétés mécaniques de la peau et incertitudes en biomécanique,**
  Séminaire interne FEMTO-ST, Besançon, France, 2019

Chapter 1

Literature review

1.1 Scar Formation

First of all, we describe the composition of keloid scars and the mechanical phenomenon behind their growth in this section. For that, we need to explore the structure of damaged human skin on a micro-scale, understand the mechanism of wound healing, and explain how and in which conditions a keloid takes shape.

1.1.1 Skin Structure

The skin is the body's largest organ, with a total area of 2 m^2 and weight of 3 kg. It is a barrier to the body against environmental damage [2], such as harmful microbes, ultraviolet radiation, and dehydration. Also, it helps regulate body temperature. Its complex structure consists of three main different cell layers, namely the epidermis, the dermis, and the hypodermis, as shown in Fig. 1.1. Its total thickness varies from 1 mm to 8 mm depending on the anatomical site, subject, sex, and age [3]
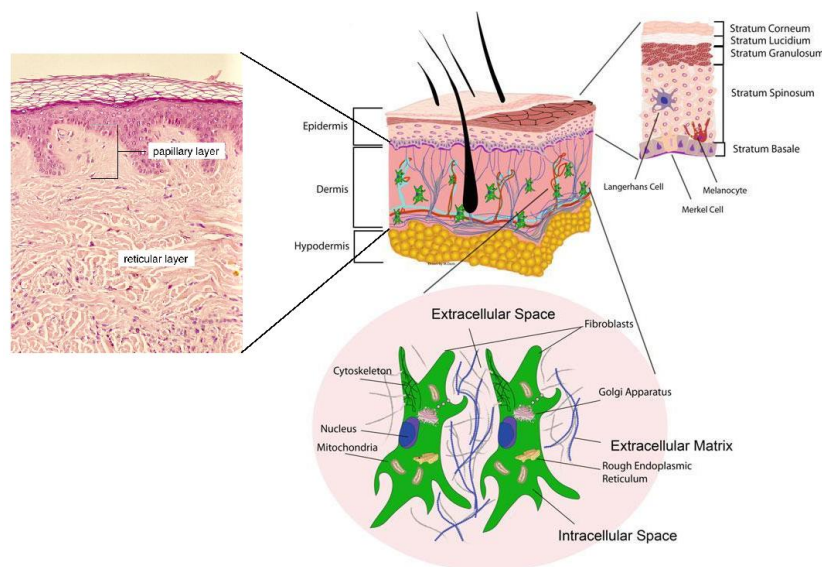
Figure 1.1: Compositions of the skin layers at micro-scale. Adapted from [4] and [5].

1.1.1.1 Epidermis

This superficial layer, with a thickness of approximately 75–150 μm [6], is stratified and composed of five highly cellular layers. In the *stratum basale*, we find the keratinocytes, which act as a source of proliferation, continuously replacing cells in the other superficial epidermal layers. Over

approximately 4 weeks, the cells lose their nuclei to become mature corneocytes that form the skin-air interface [7]. The *stratum spinosum* and *stratum granulosum* comprise cells releasing keratinocytes, which progress through distinct phases of differentiation into corneocytes [2]. Located between the *stratum granulosum* and *stratum corneum* layers, the transparent layer of *stratum lucidium* contains three to five layers of dead and flattened keratinocytes [8]. The epidermis includes other cells such as melanocytes (pigmentation), Langerhans's cells (immunity), and Merkel cells (pressure sensing) [9].

Stratum Corneum

A relatively important layer in the epidermis, from a mechanical point of view, the *stratum corneum* (SC) consists of one to three cell-thick layers of dead keratinocytes featuring a $10 - 30$ μm thickness [10]. It is the prime line of defense against external threats, such as infection and injury. In particular, the mechanical properties of the *stratum corneum* are fundamental in conditioning the transmission of loads and subsequent deformations of the other underlying skin layers. In addition, it offers the opportunity to observe the healing processes of wounds [11].

Dermis-Epidermis Junction

The dermis-epidermis junction of human skin is a complex network of interconnecting proteins which lend an intricate architecture to this zone of enormous mechanical stability [12]. The DEJ controls the transit of biomolecules between the dermis and epidermis according to their dimension and charge. It allows the passage of migrating and invading cells under normal conditions (melanocytes and Langerhans cells) or pathological (lymphocytes and tumor cells). Mechanically, this high surface area enhances the adhesion between the dermis and the epidermis and protects the dermis from physical trauma by diffusing external forces along the contact area [13].

1.1.1.2 Dermis

The intermediate layer, the dermis, $15 - 40$ times as thick as the epidermis [9], is mainly constituted of an extracellular matrix (ECM). ECM is a large network of proteins and other molecules that surround, support, and give structure to cells and tissues in the dermis. ECM includes a loose network of fine collagen, elastic fibers, and ground substance. The main ingredients of ground substance are hyaluronic acid and various proteoglycans. ECM itself is populated primarily by sparsely distributed fibroblasts, which synthesize consistently, among others, the structural components cells of the dermis, *i.e.*, collagen, elastic fibers, and the ground substance (Fig. 1.1). Fibroblasts play a critical role in wound healing [14]. We also find in the dermis mechanoreceptors that provide the sense of touch and thermoreceptors that provide the sense of heat. In addition, there are hair follicles, sweat glands, nerves, and blood vessels. The dermis can be divided into two layers: a superficial layer called the papillary dermis (PD) and a deeper layer called the reticular dermis (RD) (Fig. 1.1). The papillary and reticular layers are both made of connective tissue but differ in the type of tissue present [15].

Papillary dermis

It is made of areolar connective tissue, a loose connective tissue with a low number of scattered cells, including fibroblasts, macrophages, and an abundance of ECM. Blood vessels in PD are smaller, and some sensory receptors are sensitive to touch. PD contains dermal papillae, finger-like projections covered by the overlying epidermal ridges. These papillae are important in binding the epidermis. Dermal papillae are responsible for the pattern of fingerprints. If the overlying epidermis is destroyed, it regrows with the same pattern as before, based on the layout of the dermal papillae below.

Reticular dermis

It is thicker than PD and contains blood vessels, glands, hair follicles, lymphatics, nerves, and fat cells. RD has fewer fibroblasts and immune cells, more collagen, and less ground substance than PD. Collagen fibers are larger and often arranged in bundles, making the extracellular matrix of the

reticular layer much coarser when compared to the almost invisible distributed collagen fibers seen in the loose connective tissue of PD. RD has plentiful blood vessels and a rich nerve supply.

Collagen fibers

Collagen is responsible for the strength of the extracellular matrix and is primarily synthesized by fibroblasts. It is one of the body's vital natural resources and a component of skin tissue that can benefit all stages of wound healing [16]. As the main component of ECM in biological tissues, collagen is the most abundant protein in mammals [17], making up 25% to 35% of the whole-body protein content and approximately 70% of the dry weight of dry dermis [18]. The proportion of this component can vary considerably between the tissues of origin: skin, tendon, arteries, lungs, and heart valves. It consists of triplets of amino acid chains, known as α-chains, of elongated fibril known as a collagen helix (Fig. 1.2) [19]. Each chain is characterized by repeating the triplet (Gly-Pro-Hyp), where Gly stands for glycine, Pro for proline, and Hyp for hydroxyproline. The collagen bundles' diameter ranges from 1 to 100 μm [20].
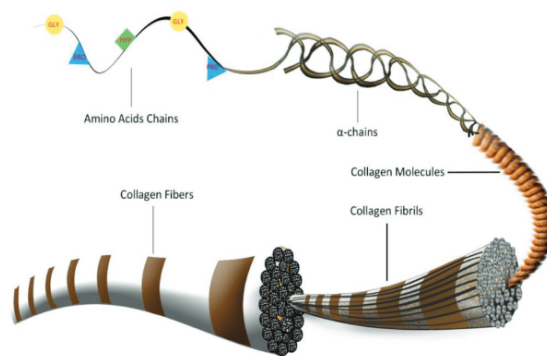
Figure 1.2: Sketch of the structure levels of collagen fiber [21].

Over 29 different collagen types are known, which can be divided (from a bio-engineering viewpoint) into fibril-forming and non-fibrillar collagens. In the skin we may find 13 types [21]. Fibrillar collagen Type-I and III (respectively 70-80% and 18-21% of total collagen content) are structurally the most significant contributors to the mechanics of soft tissues (biological tissues) acting as stiff fibrous units within tissues [22–24]. Compared with other tissues, such as tendons and cornea, the micro-architecture of collagen fibril bundles in human skin appears less well defined, which makes the physical interpretation of skin deformation challenging at the macro-scale.

Elastic fibers

The elastic fiber is comprised of an amorphous elastin core (which constitutes 90% of the fiber mass) surrounded by a protective microfibril sheath (Fig. 1.3) [25]. Similar to collagen fibers, thick horizontal bundles of elastic fibers dominate the deep reticular dermis of the skin. However, unlike collagen fibers, elastic fibers are responsible for the recoiling mechanism after stress or deformation has been applied (Elastin derives its name from this function) [26, 27]. Their diameter ranges from $0.2 - 1.5$ μm [20]. The mechanics of elastin networks is driven primarily by entropic elasticity [28], as they are far more rubber-like in conformation compared to collagen fibrils.

Although not collagen, this elastin resembles collagen protein closely, the main difference being that, unlike collagen, it contains only a little proline and much lysine. It is the major insoluble protein in elastic tissues, where it contributes to their elasticity and influences cell migration, proliferation, and elastin synthesis [29].

Ground substance
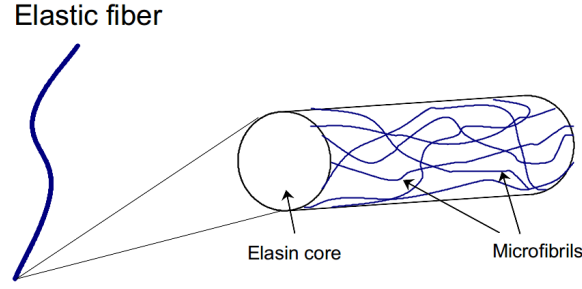
Figure 1.3: Components of an elastic fiber.

The ground substance is a gel-like amorphous phase constituted of all ECM components except collagen and elastic fibers [30]. It includes, but not limited to, proteoglycans, glycoproteins (e.g., fibronectin), and blood and lymph-derived fluids involved in is transporting substances crucial to cellular and metabolic activities. The ground substance has been shown to play a role mainly in the viscoelastic properties of the skin because of its high-water content (64%) and complex time-dependent interstitial fluid motion [31]. It has been shown in [32] that there was no effect on the mechanical response of skin because of its low stiffness, while some studies suggest that ground substance probably only plays a major role when soft tissue is subject to compression [31, 33].

1.1.1.3 Hypodermis

Also called "sub-cutaneous" tissue, the hypodermis is the deepest skin layer and is composed of loose connective tissue and adipocytes cells (lobules of fat) (Fig. 1.4) [34]. It also contains larger blood vessels and nerves than those found in the dermis. The number of adipocytes varies among different body sites, while their size varies according to the body's nutritional state. The subcutaneous fat can be measured using body fat calipers to estimate total body adiposity roughly. It acts as a shock absorber and provides some minor thermo-regulation via insulation. It is located between the dermis and the fascia, a thin but strong membrane of connective tissue encapsulating bones, muscles, and other organs underneath the skin. The hypodermis constitutes about 10% of the body mass [35], has a low stiffness modulus (a few kPa to 100 kPa), and is difficult to separate from the dermis. As a consequence, the mechanical properties of the hypodermis have barely been studied [36].
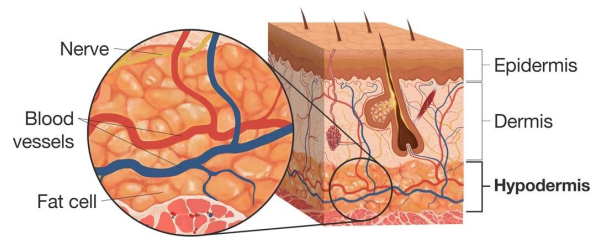
Figure 1.4: Subcutaneous micro-structure [37].

1.1.1.4 Skin Thickness

The thickness of the epidermis and dermis can be assessed with different Imaging techniques in agreement with the targeted penetration depth z_p and the suitable resolution Δ_{z_p} [38, 39]:

- Confocal Microscopy (CM): $z_p = 0.2$ mm, $\Delta_{z_p} = [0.5 - 1]$ µm.

- Optical Coherence Tomography (OCT): $z_p = 2$ mm, $\Delta_{z_p} = [4 - 10]$ µm.

- High-frequency Ultrasound (US): $z_p = 15$ mm, $\Delta_{z_p} = 30$ µm.

11

- Computed Tomography (CT): total body penetration, $\Delta_{z_p} = 100$ μm.

- Magnetic Resonance Imaging: total body penetration, $\Delta_{z_p} = 100$ μm.

A trade-off between penetration depth and resolution is unavoidable when examining skin depth. The CT, MRI, and US have high penetration depths but at the expense of reduced resolutions. Conversely, the CM has high resolution at a much lower z_p (Fig. 1.5). The OCT is the best candidate for dermal studies as it can image deeper tissues than confocal microscopy while maintaining resolution exceeding those of CT, MRI, and US.
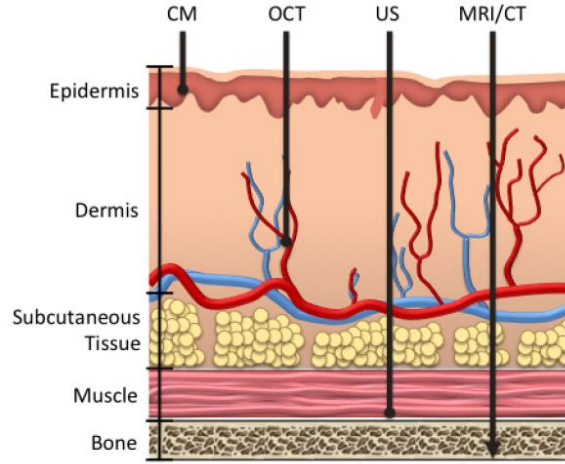
Figure 1.5: Penetration depth of Imaging techniques [40].

Human skin thickness was measured in a large number of studies during the last decades [18, 36, 41–47]. In Table 1.1, we report some of the measurement values of the total thickness, which includes the epidermis and dermis thicknesses. The analyses of collagen density proved that it is tightly related to skin thickness [48, 49]. In the aging process, the skin becomes thinner because of a functional deficit in the skin through structural and molecular degradation [50] and changes in the dermal collagen network configuration [51]. It was found that the skin thickness is lower in females *versus* males of the same age, which can be attributed to the hormonal imbalance linked with menopause (decrease of estrogen) [52].

Table 1.1: Skin thickness in the literature.

Anatomical site	Thickness [μm]	References
Forehead	1284 ± 223	[43, 44, 53]
Cheek	1375 ± 185	[43, 44]
Chest	1439 ± 201	[44]
Breast	1550 ± 250	[45]
Abdomen	1528 ± 208	[18, 43, 44]
Back	2196 ± 240	[18, 44]
Upper arm	1181 ± 162	[18, 44]
Forearm	1202 ± 335	[18, 36, 41–44, 46]
Hand	1121 ± 93	[44]
Palm	1350 ± 120	[44]
Thigh	1276 ± 127	[18, 44]
Leg	1089 ± 115	[44]
Foot	1164 ± 139	[44]

1.1.2   Wound Healing

When the skin is injured, our body sets into motion a series of automatic operations, often referred to as the "wound healing process," in order to recover injured tissues. Under uncontrolled circumstances, and because of a mechanical tensile field developing in the wound plane [54, 55], abnormal scars may be formed, such as chronic wounds, hypertrophic scars, and keloids [56–58].

1.1.2.1   Skin Repair

A normal wound healing process mechanism is divided into four overlapping phases: Hemostasis, Inflammation, Proliferation, and Remodeling (Fig. 1.6). Wound healing phases are not discrete. The proliferation phase begins even before the inflammation phase has been completed and continues even as remodeling has begun [59].
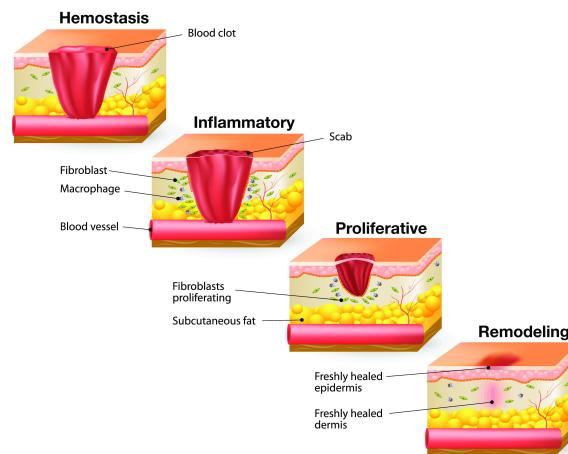
Figure 1.6: Wound healing phases. Adapted from [60].

Hemostasis
Hemostasis begins at the onset of injury, aiming to stop the bleeding. The body activates in this phase its emergency repair system, the blood clotting system, and forms a dam to interrupt blood loss. Such a dam protects the body against external aggressors, thus facilitating cell migration throughout the injured area. In forming the clot, platelets aggregate along the injured endothelium, where they degranulate, releasing a host of molecules involved in the coagulation cascade [61].

Inflammation
After hemostasis is achieved, immune cells infiltrate the wound site and mount an inflammatory response within hours after injury. Within 1–2 days, monocytes are activated to become macrophages to remove foreign matter, bacteria, non-functioning host cells, damaged matrix components, and other non-essential materials. These cells also secrete growth factors and proteins that attract immune system cells to the wound to facilitate tissue repair. This phase often lasts four to six days and is often associated with edema, erythema (reddening of the skin), heat, and pain. Once the wound is cleaned out, fibroblast, epithelial and endothelial cells migrate, and the proliferation phase begins [62].

Proliferation
The reconstitution of the dermis proceeds in a manner conducive to rapid tissue replacement and effective wound contraction. Fibroblasts are synthesized and deposit a new ECM filling the physical defect caused by the injury. This approach requires fibroblasts to reside in stratified planes/axes parallel to the epidermal surface. Consequently, collagen fibers are laid down in a similar configuration, resulting in a fabricated ECM that can be contracted to reduce wound volume. It has been asserted

in [54,55] that during the skin wound healing process, a mechanical tensile field develops in the wound plane as result of this contraction. Also, quantitative measurements by laser light scattering showed that the collagen fibers are oriented along the direction of the major contraction vector of the wound rather than randomly oriented [63]. Once fibroblasts migrate all the way through the healing space, the provisional ECM scaffold is gradually replaced by the newly formatted collagen fibers type-I and type III [64]. Despite attaining more significant amounts of collagen cross-linking over time, the maximum tensile strength of scar tissue (achieved during the third month) is no more than 70–80% of that of normal skin [65]. Relative to collagen, elastic fibers play a much smaller role during wound repair. They are secreted in smaller amounts and at a considerably slower rate [66].

Remodeling

The new tissue slowly gains strength and flexibility about two weeks after injury. During this time, excess collagen fibers are removed, and the remaining collagen fibers are reorganized, adding stability to the ECM and providing a more suitable micro-environment for cellular function. The tissue remodels and matures, and there is an overall increase in tensile strength [61, 62]. The Maturation phase varies greatly from a wound to wound, often lasting anywhere from 21 days to two years.

1.1.2.2   Scar Mechanobiology

An understanding of wound healing mechanics is critical for the design of medical devices that find application in preventing alterations. It is critical to understand how the ECM environment reacts to the mechanical stimuli and transmits the forces to its cellular components, which secrete various growth factors and cytokines [67].

Cellular Scale

Mechanical forces, including stretching [68], compression, shear, and hydrostatic and osmotic pressures, can be perceived by cellular mechano-receptors (including cytoskeleton) and/or nerve fiber receptors that produce the somatic sensation of mechanical force [68–70]. When mechanical forces deform the ECM, the cytoskeleton is altered, and mechano-receptors ion channels, such as Ca^{2+}, are activated. Cells convert mechanical stimuli into electrical signals through mechano-receptors, thereby accelerating cell proliferation through various mechano-transduction pathways (Fig. 1.7).
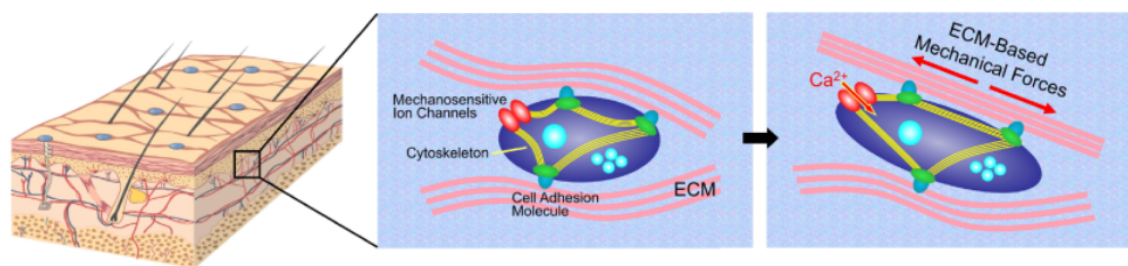
Figure 1.7: Effect of mechanical force on cellular mechano-receptors. Adapted from [67].

Tissular Scale

It has been demonstrated that the reduction of intra- or extracellular tensile forces decreases fibroblasts' conversion rates, resulting in the absence of contraction and the resultant wounds are likely to fail to remodel [71]. The manipulation of the scars in pigs and mice model by increasing the mechanical stress loads tends to produce aberrant scarring [72, 73]. Moreover, the wound is also influenced by extrinsic forces, including skin's natural tension.

Langer's lines

The influence of mechanical forces during the skin repair process has been widely examined since the existence of skin tension lines was reported by Langer in 1861 [74]. Historically, surgical incisions on the skin are made parallel to Langer's lines to produce the least tension, as incisions generally heal better with less scarring and fibrosis [75]. The density distribution of collagen fibers shows a preferential direction of lower extensibility correlated with Langer's lines [74, 76] in numerous studies [77–82]. It is known that incisions across Langer's lines are exposed to greater tension and form more scar tissue quantitatively. The incision should be performed then along Langer's lines [59, 83]. Relaxed Skin Tension Lines (RSTL), also called Borges' lines, follow furrows when the skin is relaxed and are produced by pinching the skin [84]. Generally, Langer's and Borges' lines run similar over many parts of the body but are different in mechanically complex areas such as the mouth corner and temple [59].

An appropriate intrinsic tension is necessary for incisional wound closure. External mechanical forces can also lead to scarring. Scar formation is determined by the balance between those forces [67]. However, strong extrinsic forces can accelerate cell proliferation and hyperproduction of collagen, resulting in abnormal scar formation.

1.1.2.3 Abnormal Scarring

Optimal healing consists of the total regeneration of new tissue with the same physical, biological, and aesthetic characteristics of healthy-skin. However, this is far from the case. There are four possible cases of healing: regeneration (exact replacement), regular repair (reestablished equilibrium), deficient healing (chronic ulcers), and excessive proliferation (fibrosis) [85]. The rate and quality of scar formation vary among individuals as it depends upon the size, depth, location of the scar and genetic disposition, hormones, skin color, *etc.*, factors that may cause alterations in the healing process.

Excessive Proliferation

Commonly seen in keloids and hypertrophic scars (HS), excessive healing occurs when collagen regeneration in the dermis exceeds the amount we find in a typical scar [86]. It is often preceded by an amplified inflammatory response with the resultant overproduction of growth factors [66]. We may name hereafter four cases [87]:

- **Raised dermal scars**: They are bulky, itchy, and sometimes painful. Raised dermal scars grow within the wound margins.

- **Keloids**: Clinical keloids are defined as dermal fibro-proliferative tumors rising beyond the boundaries of original wounds and rarely regressing over time. Unique to humans, they are characterized by excessive collagen deposition in the dermis secondary to traumatic or surgical injures.

- **Hypertrophic scars**: Raised fibrous scars, remaining within the original boundaries. They include dermal layer damage [88].

- **Scar contractures**: Appearing usually after burn injury in each part of the body that is subjected to contraction, like joints or skin. These scars commonly develop into hypertrophic scars.

Keloids *versus* Hypertrophic Scars

Keloid scars are sometimes tricky to identify and can be confused with hypertrophic scars (HS), with some clinical similarities. The main distinction between keloids and hypertrophic scars is that HS is enclosed by the wound's margins, whereas keloids extend beyond wound boundaries (Fig. 1.8b) [89, 90]. A keloid scar is a potential diagnosis if a raised scar is still emerging after 12 months. On the other hand, hypertrophic scars generally show some evidence of regression over this period. Compared to HS scars, fibroblast is upregulated in keloids, and thus collagen levels are 2–3 times

higher. Moreover, hypertrophic scars contain a higher subpopulation of myofibroblasts than keloids. Histologically, it is not rare to find keloid scars containing areas of HS, but some sites can host HS and not keloids [67]. Keloids display scar and adjacent skin redness; in contrast, redness on adjacent skin is not observed in HS [91]. It is difficult to distinguish between the HS and the keloids based on what the inner layer looks like, but hypertrophic scars have more cells that contract, and keloids have very thick bands of connective tissue in their inner layer [92]. To avoid confusion, the scar's keloidic state should be confirmed after 12 months [87].

(a) Keloid   **(b)** Hypertrophic scar
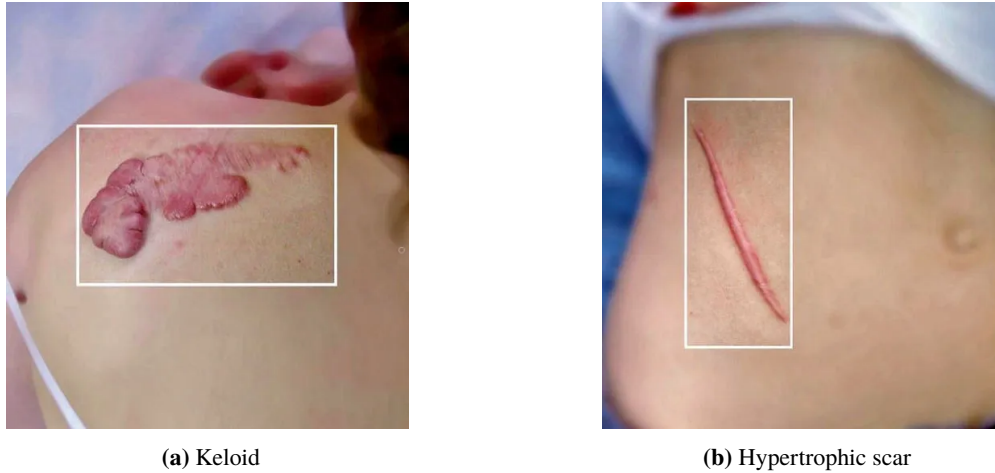
Figure 1.8: Comparison of keloid and hypertrophic scars with regards to the original wound margin [93].

1.1.3 Keloids

A focus on this type of proliferative scar must be of concern in order to establish a clear link between the applied mechanics and a clinical solution to prevent keloid appearance and growth. Keloid is a tumor that forms in the dermis and gradually spreads to the skin's surface, around the original wound. It often reappears after her excision and can be triggered by a pimple problem, burns, sternum infections, chickenpox, or any other injury that damages the skin [86, 94]. Keloid is benign and has no problematic symptoms but can affect psycho-social development and cause anxiety and loss of self-esteem because of its unpleasant shape. Also, a keloid scar can cause movement limitation due to flexibility loss. The very first recorded keloid in human history dates from the time of ancient Egypt, and it is described in Smith's papyrus [95]. The word "keloid," deriving from the Greek "Chele," (crab's claw) was first used by Alibert (1802) [96].

1.1.3.1 Formation

Normal and keloid scar formation processes are similar in the early stage. Nevertheless, the exact mechanism of wound healing in the case of keloids remains unknown [97]. It is related to many factors: anatomy, genetics, and mechanics. African, Hispanic, and Asian races seem more predisposed to develop them [86, 98]. In addition, keloid formation is related to hormonal changes (pregnant women and adolescents) and the immunological system.

On a cellular scale, keloid formation is associated with excessive collagen production during the proliferation phase [94, 99] and/or insufficient degradation of collagen and other ECM components [100]. Numerous theories have been suggested to explain this behavior involving abnormal production of factors, such as transform growth factors TGF-β, responsible for controlling the proliferation of cells, including collagen [101]. In addition, many studies suggest that keloids arise as a result of abnormal regulation of the inflammatory phase. Nevertheless, no conclusive evidence has been provided about

the development of this tumor to date.

On a tissular scale, keloids are more likely to develop and rise in more aggressive and recurrent manners on some sites where skin tension is significant, as shown in Figure 1.9 [102–104]. On those sites, the balance of intrinsic and extrinsic forces is not in favor of a well-closed wound. This hypothesis is also supported by the noticed tendency of keloids to adopt specific shapes. Additionally, Figure 1.9 demonstrates how abnormal scars are deep through skin layers, exceeding the dermis [105, 106].
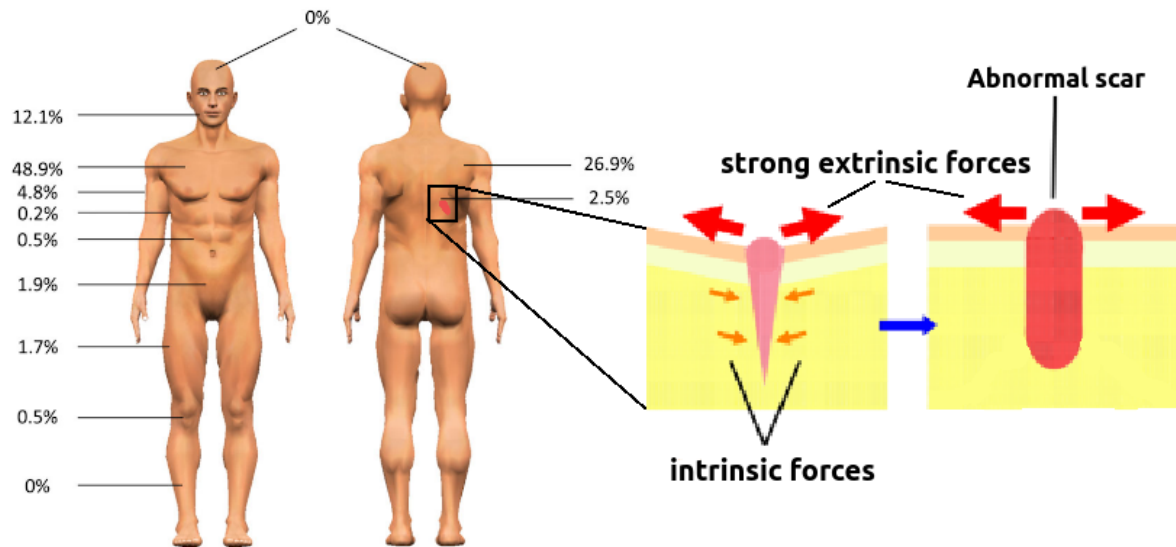
Figure 1.9: Site specificity of scars and relationship between mechanical forces and scarring. Modified from [67, 107].

Indeed, although keloids grow and spread abundantly in all directions, their horizontal growth (tangential to skin surface) results in characteristic shapes that depend on the zone where they appear. For example, keloids on the anterior chest grow in a "crab's claw"-like pattern, whereas shoulder keloids grow in a "butterfly" shape (Fig. 1.10) [67, 108]. The regions where keloids commonly occur seem to be related to natural tension forces, stretching the initial wound occurring in the keloid formation. However, earlobe keloids seem to be the exception to that, appearing in an area with almost no tension forces [96]. The excessive proliferation in the earlobe keloid may be due to pressure loads resulting from recurrent contact between ear and pillow.

(a) Anterior chest

(b) Shoulder

Figure 1.10: Keloid propagation directions [56].

These patterns appear to be related to the mechanical force distribution and the direction of the

skin tension fibers (Langer's lines) [109, 110]. Combined with the natural body movement, the stress developed within the tissue surrounding the keloid scar plays an important role in forming the irregular shapes observed in the keloid scar [111, 112]. In Figure 1.11, we may notice a similarity between Langer's lines, as pictured by Langer in 1861 [76], and the axes of the ellipsoid shape of the keloids in the anterior back.
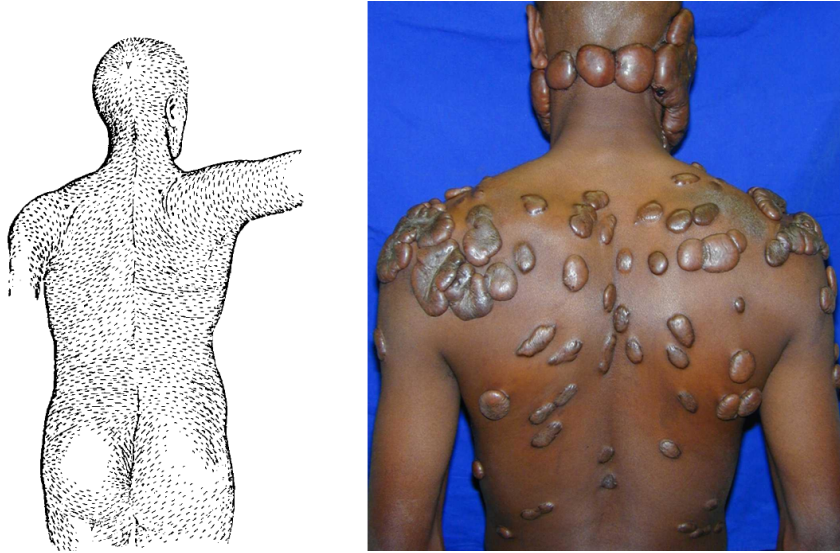
Figure 1.11: Site specificity of scars and mechanical forces effect on scarring. Modified from [67, 107].

1.1.3.2 Scar Treatment

Several invasive and non-invasive methods have been used to treat keloid scars. Among them are surgical excision, radiation laser therapy, corticosteroid, and intralesional steroid injections [113]. Besides biochemical solutions, the wound healing of the skin may be improved via the manipulation of the skin mechano-environment. Thus, some medical devices, such as paper tape, bandages, and silicone gel sheets (SGH), have been developed to cancel mechanical stress and high tension. A randomized-controlled trial (RCT) showed that SGH significantly reduces the incidence of hypertrophic scar and keloids [114]. Other RCT has shown that applying paper tape after a cesarean section on 70 subjects helped to prevent HS formation with significantly less scar volume [67, 115]. An innovative pressotherapy device consisting of silicon clips equipped with magnets was recently developed by the University of Franche-Comté (Besançon) and tested in the University Hospital of Besançon. After keloid surgery, it was applied to the earlobe to prevent keloid recurrence [116]. Controlling the forces in the extracellular fluid (ECF) can help prevent scars through various devices (*e.g.*, vacuum-assisted closure) by inducing hydrostatic pressure gradients and shear forces. The magnitude and balance of these force patterns must be further studied to develop sophisticated patient-specific devices for scar prevention.

1.1.3.3 Keloid Biomechanics

According to Davis's law (a corollary to Wolff's law applied to osseous tissue), soft tissues heal according to how they are mechanically stressed [117]. This theory may also be valid for the skin since soft tissues share a common component that is mechanically dominant, which is collagen. Various research works were conducted to analyze the relationship between stress field and keloid scar shape. When it comes to predicting the evolution of its form, utilizing numerical simulation would be necessary.

The simulation of an elliptical-shaped scar under tension indicates that the highest stress concentration occurs around the corners of the scar. The stress field forms a butterfly shape (Fig. 1.12) which can also be clearly seen in the real keloid scar (Fig. 1.10b). A more pronounced concentration in such an area represents an accumulation of more significant amounts of collagen.
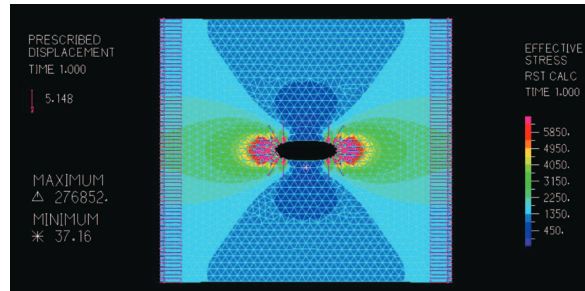
Figure 1.12: Stretching simulation of ellipsoid skin wound [111].

The prediction of the privileged directions of extension of a presternal keloid as a function of mechanical stress field was carried out by Chambert *et al.* [104]. A bi-dimensional bi-material finite elements model composed of an oblong keloid surrounded by healthy-skin was implemented to predict the progression of the scar. The mentioned study suggests that the extension of the keloid is related to the direction of maximum shear stress. Starting from an initial oval shape and through the analysis of the shear stress field, the evolution of the keloid form could be successfully forecasted (Fig. 1.13). The experimental and the numerical results of the preferential growth angle were in good agreement. The highest stress concentration was reported to be taking place on the oblong corners. However, as pointed out by the authors, the preferential directions of scar growth are sensitive to the ratio of initial natural stress in X- and Y-directions. This ratio may play a predominant role in keloid evolution and needs to be assessed accurately alongside the shear stress. The latter hypothesis was explored in the thesis.
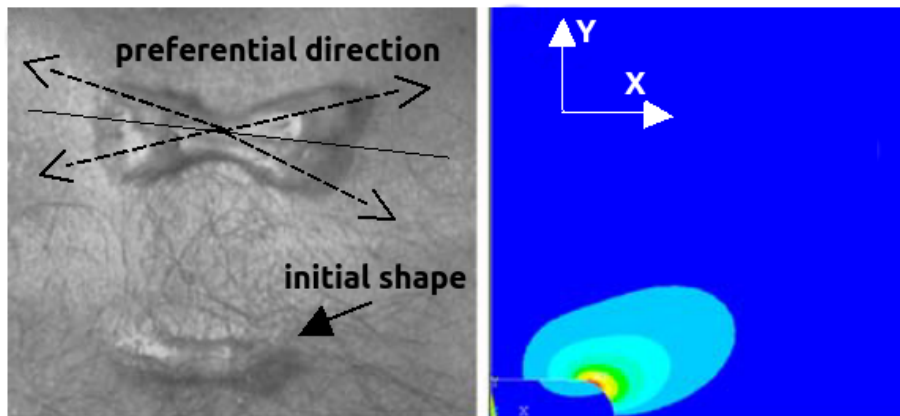
Figure 1.13: Simulated shear stress field of a 40-year-old man with two presternal keloids (oblong and butterfly shapes) reproduced from [108] and simulated by [104].

Quantifying the stress in the keloid and around it is a promising way to predict the privileged direction of scar growth. Since the topology of the studied zone matters, using numerical simulation becomes essential. Because of the high variability between subjects and the sensitivity of model outputs with respect to the inputs, biomechanical analysis of keloids to prevent their growth should lie on a "patient-specific" approach [118]. The model is built upon data gathered from the studied individual, *i.e.*, geometry and material parameters. The methodology followed to characterize the mechanical properties of the keloid, and the healthy-skin around it lies in essential steps ordered as follows, measurement (Sec. 1.2), modeling (Sec. 1.3), and parameter identification (Sec. 1.4) [119, 120].

1.2 Mechanical Characterization Experiments

The *in vivo* mechanical investigation of scars was conducted in a few studies [1, 106, 121–125]. The results show that the scars are stiffer than the injured skin because of the abundance of collagen. The latter is the stiffest biological component in the skin. Since scars and healthy-skin consist primarily of collagen fibers, which drive the mechanical response of the tissue, the mechanical characterization experiments on both materials can be performed similarly. There are no general standards for measuring human skin's elasticity. The choice of methods and materials depends on the targeted material parameters and site accessibility. But, an important step is always included in the protocol, which is Preconditioning. Preconditioning was first introduced by Fung in 1972 [126] and is an initial load applied at low strains so that the skin behavior becomes reproducible. Preconditioning aims to reduce measurement variability due to randomness of fiber orientation or the existing pre-stress. Experimental tests of skin materials can be categorized into two distinct methods, *ex vivo* and *in vivo*: the sample is excised from it before testing or tested non-invasively and directly on the living subject. For ethical reasons, *in vivo* testing is usually favored in humans, although *ex vivo* testing provides more rigorous results because of kinematics and geometry simplicity. Besides, as we are interested in preventing keloid growth, *in vivo* results are more realistic. In this section, we enumerate the *in vivo* experiments carried out on uninjured skin during the last decades.

1.2.1 Stretch Test

In tensile tests, the skin is stretched parallel to its plane by means of extensometers, equipped with two or more pads to be fixed on the surface of the tested material. This experiment quantifies the skin's stiffness and the elastic parameters along the stretched direction(s) through stress–strain curves. This method seems to be the most reliable as the deformations are in-plane, corresponding to the alignment of collagen fibers parallel to the dermis layer.

1.2.1.1 Uni-Axial Stretch

In this type of testing, the skin is stretched along one direction (by letting the two orthogonal directions free of load). Regarding the ease of designing an extensometry apparatus, and the facility of interpreting the outputs, the uni-axial test has been operated in countless studies on long and large sites, such as the forearm [78, 106, 127–143]. While two pads stuck to the surface are moved one from each other at a constant speed (Fig. 1.14), tissue deformation is measured in both longitudinal and transversal directions.
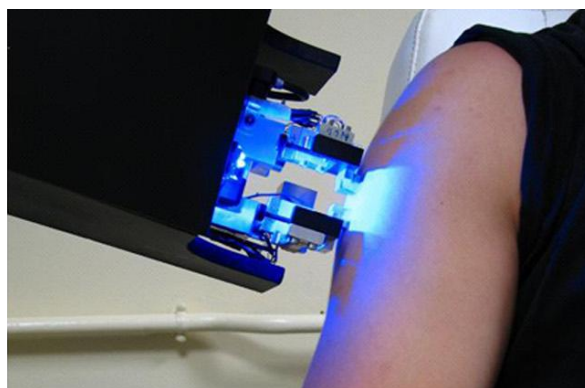
Figure 1.14: Quasi-static device applying uni-axial stretch to the upper arm skin between pads [141].

For a better assessment of transversal deformation, the displacement of the whole surface between pads is captured with Digital Image Correlation (DIC) technique [133, 142]. The reaction forces can be measured with stress gauges and load cells. Pad adhesion to the skin is of major concern and can

be secured with adhesive tape or slipless contact. Even if the uni-axial tension is uni-directional, it was used along many angles to characterize the anisotropy [130, 131, 140]. Furthermore, recording the measurement over time was employed to characterize the viscosity [134]. Such an experiment can be improved by adding external shields from both sides to isolate the tested area and minimize the effects of peripheral forces from the skin around [142, 144] (Fig. 1.15).
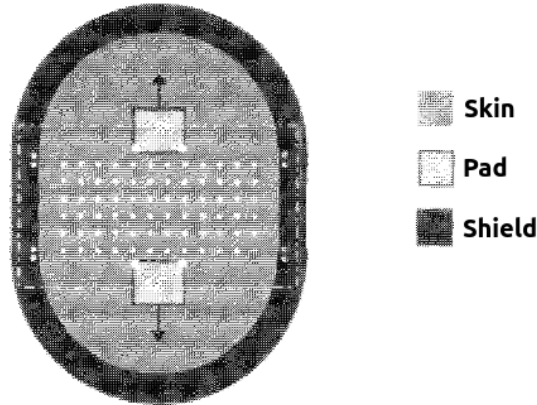
Figure 1.15: *In vivo* uni-axial stretch of skin isolated from the surrounding effects. Modified from [133].

1.2.1.2 Multi-Axial Stretch

The multi-axial tensile test was conducted *in vivo* on human skin in several studies to investigate the anisotropic behavior [18, 145, 146]. The latter is related to the distribution of the Langer's lines in the measured site. The experiment can be conceived in the form of multiple simple tensile tests in many directions arranged in circular configuration (Fig. 1.16).
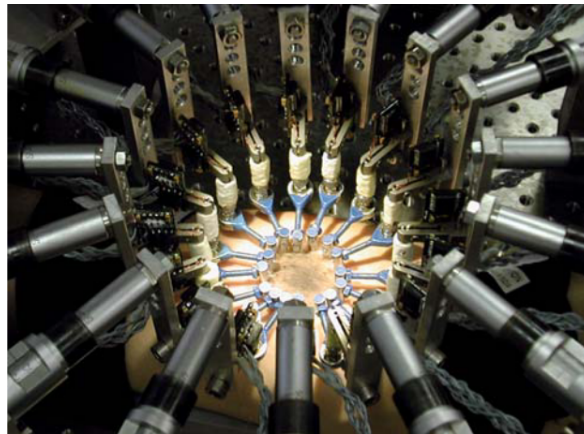
Figure 1.16: *In vivo* multi-axial testing on the subject's skin [146].

Besides the variation of skin stiffness in every direction, the multi-axial test leads to identifying the Langer's line on the tested site. The angle with the lowest strain corresponds to the privileged direction of collagen fibers. However, this technique has several drawbacks. Conducting multiple tests to obtain a load–extension curve in each direction is time-consuming. Conversely, reducing the number of angles with which the direction of the minimum extensibility can be defined will affect the accuracy [147]. Moreover, it cannot be applied to small regions. A novel technique was recently used to investigate the anisotropy of soft tissue in all directions simultaneously, continuously, and locally. By applying suction load p within an annular surface (to not be confused with the suction testing), the central zone is subjected to multi-axial stretch (Fig. 1.17). The preferential direction of collagen fibers is precisely quantified from the resulting full-field displacements. For that purpose, Laiacona

et al. [148] have developed a homemade device with inner and outer diameters, respectively, 30 mm and 49 mm. Such a large test area cannot fit on a small site on the body. A commercial device CutiScan CS 100® [149], utilized in [124, 150–154], has been introduced in the market by Courage + Khazaka electronic GmbH, with an inner diameter of 5 mm (respectively outer diameter of 14 mm), granting measurement of multi-axial stretch on small regions, such as the earlobe [124]. Although the device is reliable and promising [154], it has some limitations, as reported in [124]. Indeed, the angle of the minimum displacement (equivalent to Langer's line) is given in the associated software, but access to the data of the displacement full-field is not provided. One of my thesis contributions is developing a numerical method to exploit efficiently and entirely the output displacement field captured by the device.
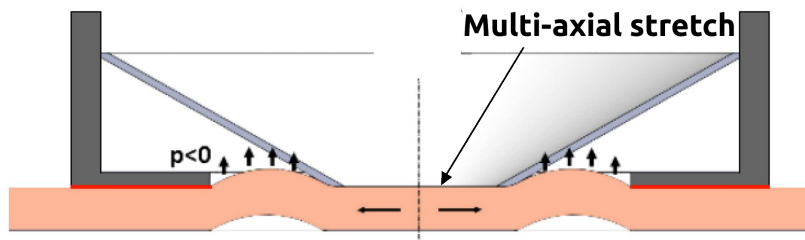
Figure 1.17: The multi-axial test performed with an annular ring suction probe. Adapted from [124].

1.2.2 Indentation Test

In this experiment, used for the first time in 1912 [155], a rigid indenter applies a controlled perpendicular displacement (depth) at a given site on the subject's skin, and the normal reaction force is recorded, or *vice versa* [147, 155–167]. From the impact shape data, the elasticity modulus can be determined *via* contact-based physical models. Indentation can also be carried out with contactless method, for example, by projecting air flow [168, 169]. One of the benefits of this technique is eliminating the sliding effect (occurring between the probe and the skin), which can induce measurement errors.
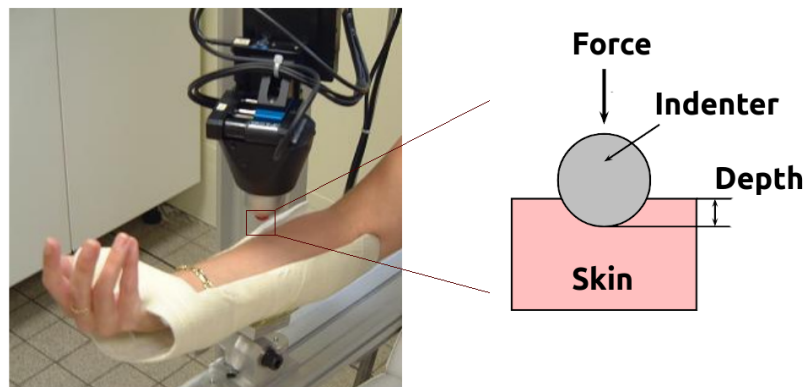
Figure 1.18: Spherical indentation device. Adapted from [170].

The usefulness of the indentation test consists in studying the skin layers' contribution to the mechanical response, as the load is normal to the surface. Hence, the test was combined with skin measurement techniques, ultrasound [171], and MRI [172]. The indentation technique helps also monitor changes in mechanical properties of a patient's skin with respect to aging [159]. It has been noticed that the skin softens with age and progressively loses elasticity, most likely due to microstructural changes in the dermis and hypodermis [165, 166].

If the indentation testing is simple to design, the interpretation of its results is, however, not clear. Many mechanical aspects are at stake: viscoelasticity, nonlinearity, and contact, which complicates obtaining consistent experimental results [173]. Because of its axisymmetrical nature, the models used to fit the data are mostly isotropic (or transverse isotropic in the case of multi-layer media). Thus, the anisotropy of the skin cannot be resolved directly with such a method. A way to overcome this limitation is to capture the elliptic contact edge during deformation and analyze its eccentricity [167].

1.2.3 Suction Test

One of the most used techniques to characterize the mechanical properties of the skin [41, 125, 162, 174–188], the suction test consists in applying a negative pressure inside a sealed axisymmetrical chamber mounted on the tested skin region, resulting in an out-plane deformation of a dome (Fig. 1.19). The dome height is measured with different methods, such as ultrasound [177, 181], OCT [180], camera when possible [185]. The height can be fixed when using a mechanical stopper in the form of a thin pipe, through which the suction is supplied until the inflated dome closes it [184]. Ultrasound methods add additional experimental constraints as the use of liquid interfacing the probe with the tissue is required (wet skin behaves differently compared to dry skin). The mechanical stopper method provides data for a unique point, which might increase experimental errors. Optical methods are usually preferred since there is no unnecessary contact [189].
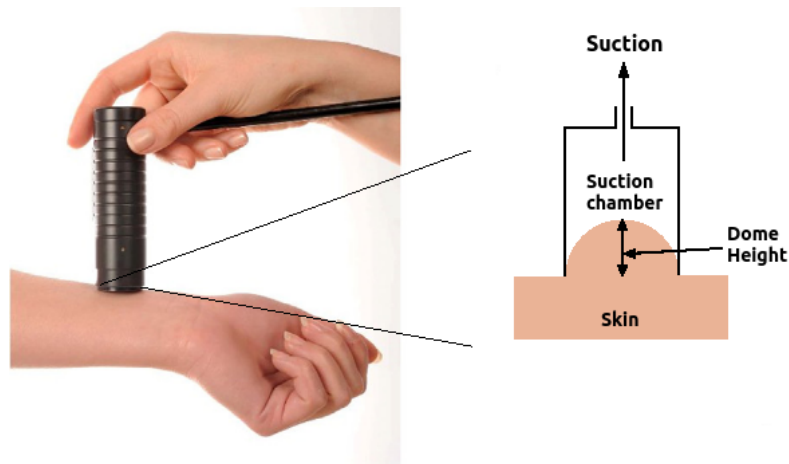
Figure 1.19: The suction testing working principle. Photograph of the Cutometer® [190].

The stress-strain curve is obtained from the relationship between the height of the bulged dome and the suction pressure. Most suction devices presented in the literature use a $2-8$ mm opening diameter with a pressure of up to 500 mbar [4], which makes it accessible to cornered and/or small areas, *i.e.*, the breast [183] and parotid [185]. Clinical studies have shown that suction tests provide reliable indicators for skin aging [174, 191, 192].

Suction testing has some limitations. Like the indentation test, the mechanical analysis is based on the simplifying assumption that skin is isotropic (or transverse isotropic). Indeed, given the circular opening of typical suction probes, it is not obvious to characterize the anisotropy of skin. We can cite the only study related to the context, where the anisotropy of the skin through the bulge test (similar to suction) was investigated *ex vivo* [193]. The authors pointed out that the need for pre-inflation to prevent a buckled reference state is a disadvantage of the bulge test. It has been reported for thin films that the error introduced by pre-inflation can be significant. Therefore, there is no confirmation about using suction testing to capture the anisotropic behavior. Another limitation of the suction test is the repeatability, as it depends on accurate probe handling, especially for hand-held devices. Alignment of probe and skin and control of contact pressure is key to ensure reproducible measurement data.

1.2.4 Torsion Test

It was designed to characterize the shear modulus in the material. In the torsion experiment, a shear load is imposed on the superficial skin layer as a result of the friction head (disk) rotation in contact with the skin's surface. The disk's rotation is in the form of torque or angular displacement. A tube shield can be associated with the friction head to isolate the tested site from the surrounding skin (Fig. 1.20) [194]. The measured torque-angular displacement curve (analogous to the stress-stain curve for the tensile test) can quantify the skin's viscoelastic response and compare the variations in skin elasticity regarding age, gender, and location [49, 128, 195, 196]. Although the torsion technique is quick to apply and not restrictive in terms of accessibility, it cannot be used to assess anisotropy because torsion tests are not directional.
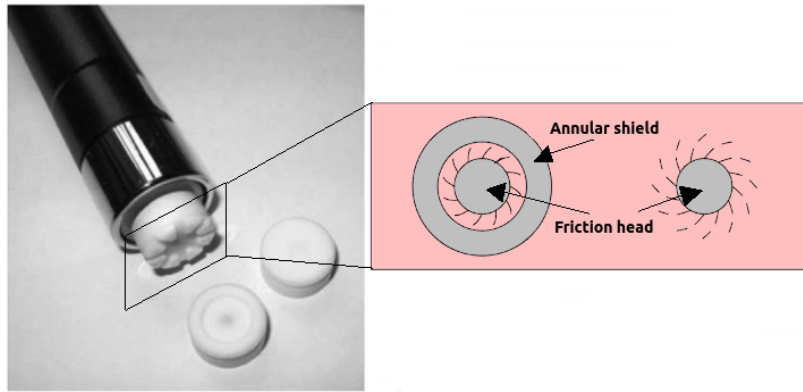
Figure 1.20: The torsion test device. Adapted from a photograph of the Frictiometer® FR 700 [190] and [141].

1.2.5 Elastography

Over the last two decades, different methods have been developed to perform elasticity imaging, where the soft tissue's elastic and viscoelastic properties are mapped [197, 198]. Every elasticity imaging method combines two common operations: force excitation (mechanical, radiation force, endogenous) and measurement (ultrasound, MRI, acoustic) [198]. As an example in Figure 1.21, a plane shear wave is generated in soft tissue by shaking a rigid plate with a vibrator. The wave propagates along the direction k. Simultaneously, connected to a scanner, a transducer array with 128 pins captures the propagated shear waves. Then, based on speckle images stored in memory, a correlation algorithm computes the displacement field u. Once the response has been observed, the stiffness can be quantified by measuring the wave velocity: the mechanical shear waves travel faster through stiffer than softer tissue [199]. The anisotropy can also be assessed with elastography [200, 201].
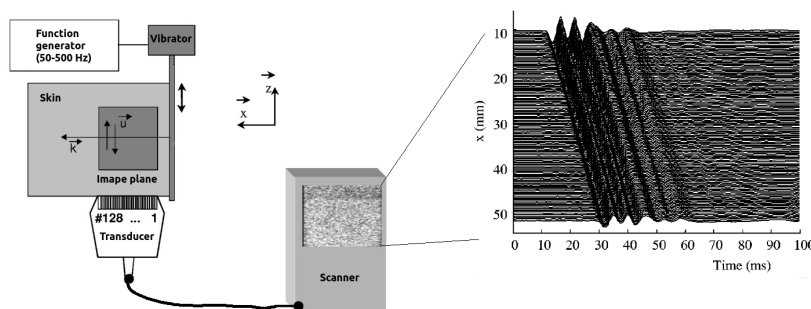
Figure 1.21: Experimental setup based on the elastography technique. Adapted from [197]

1.2.6   Supplementary Experiments

Less common skin characterization methods have been employed in some studies, for instance, ballistometry, and the vertical pull method (excluding the bulge test, which is not applicable for *in vivo* experiments). They are not widely used because of many limitations, including high measurement sensitivity and difficulty interpreting output data through a well-established model. However, they can help assess the mechanical properties when the classical approaches upward cannot be carried out. Other stiffness assessment techniques were used on the living skin, *i.e.*, optical approaches [202, 203] and friction [204].

1.2.6.1   Ballistometry

With a ballistometer [205], the material properties are measured by the successive rebounds of a light ball dropped from a height on the skin surface (Fig. 1.22) [206–210]. It measures the skin surface after a known mass has impacted it with a known force. The method was developed initially for testing homogenous, hard industrial materials but is today used to determine the mechanical properties of the skin. The magnitude of the first rebound represents skin stiffness, and the damping factor the viscosity [206]. The method is simple to conduct and does not require direct contact with the skin. Also, it strongly correlates with the aging effect (linear correlation [206]). On the other hand, the surrounding skin contributes dynamically to the mechanical response, complicating the identification of material parameters.

Rebound
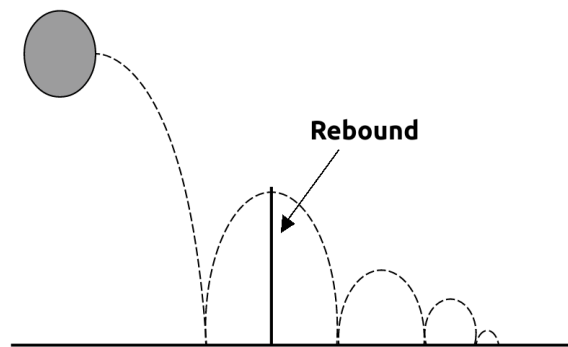
Figure 1.22: Ballistometry working principle [211].

1.2.6.2   Vertical Pull

This testing is based on a vertical pull of a disk stuck to the skin with double-sided adhesive tape. When using a pulley system, the reaction force is measured by skin deflection upwards (Fig. 1.23) [212–214]. It can be seen as an inverse process of indentation testing. To date, no model has been developed to mimic the material deformation under such load. Thus, the interpretation of the results is hard to fulfill. Nevertheless, the method can be utilized for qualitative comparison regarding many factors: age, gender, and location.

Summary

Various experiments *in vivo* to analyze and quantify skin stiffness, as well as the preferential direction of collagen fibers, were described in this section. Faced with the multitude of existing mechanical tests and analysis methods, we must select one approach compatible with our expectations. Due to the differences between solicitation natures, hypotheses, experimental conditions, and physical models, it seems understandable not to obtain similar results. As the main objective is characterizing the mechanical properties of the keloid, the selection focuses on the predominant mechanical cause of
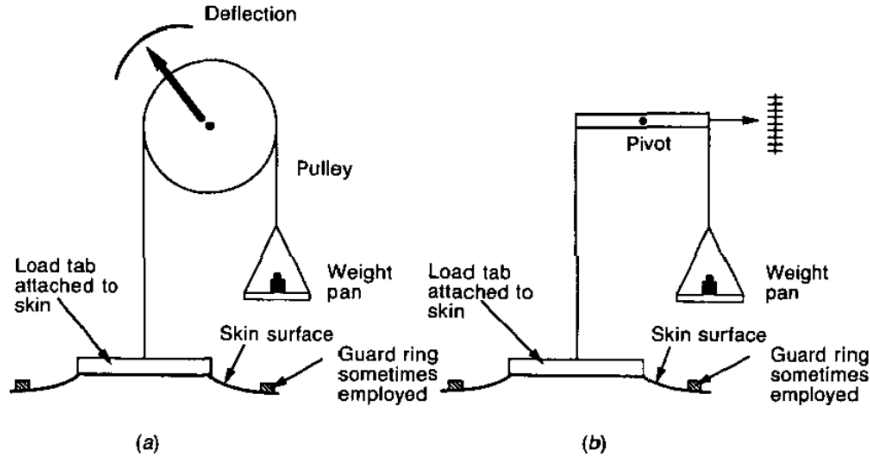
Figure 1.23: Vertical pull technique [214]. (a) Pulley system. (b) Pivoted support system.

the scar growth, which is natural skin tension. For more reliable results, the type of solicitation should follow the alignment of the stiffer component in the skin, collagen fibers [133]. Therefore, the keloid characterization would be based on in-plane loading. In this case, tensile tests. In the next section, the physical models developed in the literature to simulate the stress-stretch state of the skin are introduced.

1.3 Skin Modeling

In recent years, modeling the material behavior of the skin has been a primary concern for many researchers. Description of the material behavior of largest human organ is necessary for many clinical applications, including the prevention of scar growth. A way out of this is to quantify the dominant forces in the studied media and counter them. Under permanent natural tension and given a physical model predicting the mechanical response of the tissue, the stress field can be computed to determine those dominant forces and their privileged directions. A skin model consists of constitutive law describing the tissue's kinematics and constants, called material parameters. The latter are gathered from the mechanical characterization experiment introduced in 1.2. Hereafter, we present an overview of reliable methods and approaches that lead to simulating the deformation of soft tissues.

1.3.1 Hypotheses

George Box stated that all models are wrong, but some are useful [215]. In other words, although the models are incomplete and do not represent "reality," they simplify the problem by focusing on the significant aspects and neglecting less important factors. Simulating all the details is unimaginably costly and may lead to paradoxical results. Let us consider assumptions that reality is held up within certain limitations.

1.3.1.1 Limitations

A valid model is both as accurate and as simple as possible. No matter how good they can represent reality, skin models have some limitations. First of all, we need to introduce the two main modeling limits independently of the scientific field: simplicity and approximation. In the first case, unnecessary details are skipped for easy use without altering the physical characteristics under the loop (for example, ball-and-stick models in chemistry). While in the approximated models, we make several assumptions about those characteristics. Nevertheless, these two approaches help scientists build concise models in order to: (i) explain physical phenomena roughly but enough, (ii) fit the

experimental data, and (iii) predict what might happen in particular circumstances.

In the context of skin biomechanics, we would imagine simulating in the best scenario the motion of the skin exactly as it happens in real life, but it is very challenging. The state-of-art models allow us only to characterize the mechanical properties of the living tissue and predict its deformation for a given load value and *vice versa*. For example, estimating precisely how many wrinkles appear on a 60-year-old subject's forehead is impossible. Historically, phenomenological mechanical models have been built principally to fit experimental data without taking into account the micro-structural effect, such as cutaneous layer components. If the model fits remarkably the observable data, it is thus validated. Dozens of 'black-box' models have been established to mimic the skin according to a particular data set [216–218]. Skin biomechanics modeling could be limited by the following barriers:

- Geometric complexity: 3-dimensions, multi-layers, multi-phases, and multi-scale.

- Interdisciplinarity: dermatology, biology, mechanics, mathematics.

- Multi-physical aspects: nonlinearity, anisotropy, viscosity, incompressibility.

- Computational challenges: costs, convergence, stability.

- Inter- and intra-subject variability.

If we consider modeling the skin with all the above constraints, we will never fit any experimental curve. Conversely, by neglecting one or many aspects, we will come up with incorrect models by the end of the day, but some are useful. It is, after all, not appropriate to "go hunting" for the standard model that simulates any skin behavior. The biomechanical modeling is limited by how the problem is simplified, approximated, computed, and, more importantly, by the noised observable data, set as a referential mirror to develop the best digital twin. A reasonable way of thinking about the 'rightness' of modeling would be focusing on applying the identified model to predict future mechanical responses locally. Biomechanics modeling needs small steps to push its limits further and so the frontiers of our knowledge in this young field.

1.3.1.2 Mechanical Characteristics of Soft Tissues

Before describing a model for the skin, it is instructive to give some insight into its general mechanical characteristic. The skin shares the same mechanical characteristic as other soft tissues (ST), namely, arteries, tendons, and ligaments, where collagen is responsible for mechanical performance and strength and represents the common main structural component between those tissues. As we do not master the skin modeling, it would be wise to enlarge our criteria and try out models used on other ST.

Mechanically, ST are complex fiber-reinforced composite structures. Their mechanical behavior is strongly influenced by collagen and elastic fibers concentration and structural organization [219]. ST behave anisotropically because of their fiber arrangement, which tends to have preferred directions (two fiber families on arteries [220]). For the connective tissue parts of the skin, the three-dimensional network of fibers appears to have preferred directions parallel to the surface. However, some fiber orientations also have out-of-plane components to prevent out-of-plane shearing. In contrast to hard tissues (bone, tooth enamel), ST may undergo large tensile deformations with a nonlinear stress-strain curve that can be divided into 3 stages related to the stretch rate of collagen fibers (Fig. 1.24):

- **Phase 1: Toe region**. In the absence of load, collagen fibers gradually align with the tensile direction. The tissue behaves like a very soft isotropic linear rubber material, and the elastin fibrils ($5 - 10\%$ of the dry weight of the skin [219]) are mainly responsible for tissue elasticity [26]. The toe phase data are used to identify Young modulus parameters.

- **Phase 2: Heel region**. As the load increases, the aligned fibers along the tensile direction start uncrimping.

- **Phase 3: Linear region**. The stress-strain relation becomes linear again. Aligned and straightened fibers undergo stretching sliding past each other and ultimately failing, causing macroscopic damage and failure (up to $30 - 70\%$ of strain in the skin [219]).
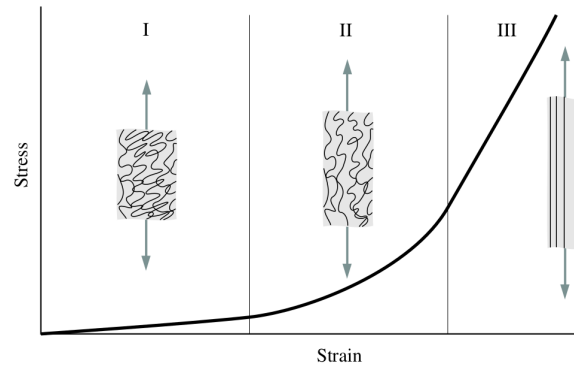
Figure 1.24: Evolution of stress-strain response of dermis combined with the aligning state of collagen fibers [219].

Also, some ST show viscoelastic behavior, which has been associated with the shear interaction of collagen with the ground substance, which provides viscous lubrication between collagen fibrils [221]. Many other factors can affect the stretch rates, such as topography, age, gender, temperature, osmotic pressure, and humidity. Nevertheless, in every mechanical characterization study of ST, the results should be interpreted with hypothetical arrangement of the main parts of the material, namely, collagen and elastin fibers. Table 1.2 attempts to present ranges of values of collagen/elastin contents (% dry weight) in some soft organs.

Table 1.2: Collagen and elastin fibers content in soft tissues. From [219]

Soft tissue	Collagen (% dry weight)	Elastin (% dry weight)
Tendon	75-85	< 3
Ligament	70-80	10-15
Aorta	25-35	40-50
Skin	60-80	5-10

1.3.1.3 Similarities Between Soft Tissues and Rubber-like Materials

The first ever referenced work drawing attention to the similarity between soft biological tissues and rubber-like materials backs to 1881 [222]. Roy showed that the animal arteries behave as caoutchouc materials in a mechanical and thermodynamic way, unlike metals. When a metal is stretched, it becomes colder, and the opposite occurs when it is compressed. Such a thermal behavior is not met in rubber-like materials or ST. From these observations, two classes of solids can be distinguished regarding their thermodynamic functioning [223]: 'entropic elasticity' (rubbers, ST) and 'energetic elasticity' (metals, glass, dry wood). Hereafter, some common characteristics of rubber-like material and soft biological tissues are listed, making them somehow equivalent from a mechanical point of view [223].

- **Micro-structure**: The three-dimensional networks of both rubbers and ST consist of macromolecules held together by van der Waals and covalent bonds (unlike metals, as inter-atomic

bonds hold their structures). Although they are composites, their homogenized response is only considered most of the time, at least for macroscopic problems (examples are skin, lung, and bone).

- **Anisotropy**: As in many ST, such as skin, ligaments, and arteries, the stiffening effect is based on the embedding of collagen fibers, which leads to the characteristic anisotropic mechanical behavior. Some are oriented along the privileged direction (Langer's lines in the skin). The reinforced polymer chains also align in a specific direction, which results in an anisotropic rubber [224].

- **Nonlinearity**: Many characterization studies carried out on ST have shown that their relative stress-stretch curves are highly nonlinear at large strains. The same observations occur on rubber-like materials. The nonlinearity is seemingly due to the increase of stiffening as the polymer chains align straight when the material is gradually stretched.

- **Viscosity**: Both materials can exhibit a dissipation effect because of the motion of the chains within the viscous ground substance matrix. In fact, ST behaving as viscoelastic materials (relaxation and/or creep) show shear interaction of collagen with proteoglycans found in the extracellular matrix [221].

1.3.2 Hyperelasticity

As mentioned earlier, the mechanical response of the skin, in the form of a stress-strain curve, is a J-shaped nonlinear curve when it undergoes large tensile deformation. It is still possible to use data only from the toe region, where the behavior is of type linear elastic, to estimate the elastic parameters, Young's modulus, and Poisson's ratio. However, with such a partial dataset, the uncertainty about the parameter identification's accuracy is high [1]. Therefore, using as much consistent data as possible, from up to the heel region, is preferred to identify accurate material parameters using a nonlinear model. This part describes the main steps to constructing nonlinear constitutive laws.

1.3.2.1 Geometry and Material Nonlinearity

When we mention the term "nonlinear," two natures of nonlinearity should be considered: geometric and material [225]. Material nonlinearity occurs when, for whatever reason, the stress-strain curve is nonlinear beyond the linear limit. If changes in stiffness come only from changes in shape, nonlinear behavior is defined as geometric. For example, a flat membrane deflects under pressure. Initially, the membrane resists the pressure load only with bending stiffness. After the pressure load has caused some curvature, the deformed membrane exhibits stiffness additional to the initial bending stiffness. Another shape of geometric nonlinearity is the load direction changing as the model deforms in cases of large deformations. Hyperelastic materials, such as rubbers and ST, may be considered both geometrically and materially nonlinear.

1.3.2.2 Kinematics

An alternative coordinate systems is employed to define stress-strain relations, namely, material and spatial descriptions associated with the names of Lagrange and Euler, respectively. The inertia effects are discarded in this section. The continuous deformable body is represented as an assemblage of an infinity of material particles whose position with respect to the Cartesian basis E_I has the coordinates X (Fig. 1.25) in the initial configuration. The current position of each particle at time t is represented by the coordinates x with respect to the Cartesian basis e_i. The two bases are taken to be coincident. And the motion of trajectory between initial and current position is described through a bijective function χ as

$$x = \chi(X, t) \tag{1.1}$$

Then, the displacement vector for each material particle is expressed as

$$u = x - X \tag{1.2}$$
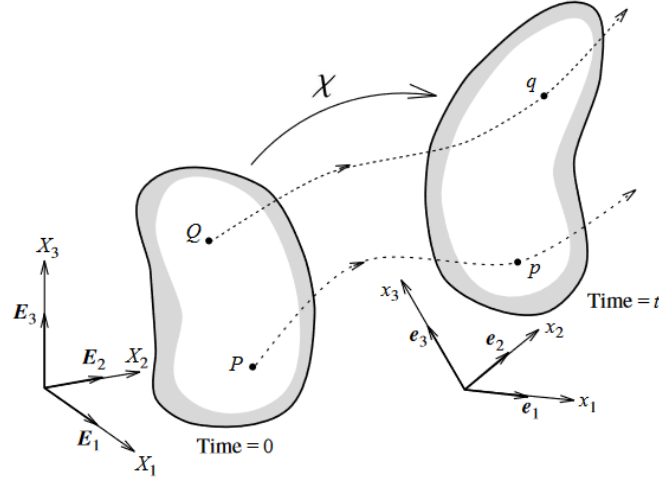
Figure 1.25: Motion of deformed body [226].

Deformation Gradient Tensor

The main key to linking physical quantities present in the bodies before and after deformation is the deformation gradient tensor F. For instance, the strain-energy density function (SEDF) during deformation should contain this entity. The deformation gradient tensor enables the relative spatial position of two neighboring particles P and Q. We consider the elementary vector $dX = X_Q - X_P$. After deformation, in current spatial positions, it becomes (Fig. 1.25)

$$dx = x_q - x_p = \chi(X_P + dX, t) - \chi(X_P, t) \tag{1.3}$$

Therefore, the *deformation gradient tensor* is defined as

$$F = \frac{\partial \chi}{\partial X} = \nabla \chi(X, t) \tag{1.4}$$

where $\nabla \chi$ is the gradient with respect to material configuration. Generally the elementary vector dx can be expressed in terms of dX as

$$dx = F dX \tag{1.5}$$

Another way to obtain F is by combining Equations 1.2 and 1.5

$$F = \frac{dx}{dX} = I + \frac{du}{dX} \tag{1.6}$$

with I an identity second-order tensor.

Strain Tensor

One standard way to measure the deformation is using the square of local change in distances. That leads to using a rotation-independent deformation tensor since a pure rotation should not induce any strains in a deformable body. Let us consider

30

$$dx \cdot dx = (FdX)^T (FdX)$$
$$= dX \cdot F^T FdX \tag{1.7}$$
$$= dX \cdot CdX$$

George Green introduced a deformation tensor known as the *right Cauchy–Green deformation tensor*. It can be defined as[1]

$$C = F^T F \tag{1.8}$$

F can be decomposed into a product of two tensors U and R, using polar decomposition

$$F = RU \tag{1.9}$$

The latter equation implies that the deformation of dX onto dx (Eq. 1.5) may be obtained separately in two steps: dX is stretched by a symmetric definite positive tensor U, i.e, $dx' = UdX$, followed by an orthogonal rotation R, i.e, $dx = Rdx'$. That explains why C is a rotation-independent tensor:

$$C = UR^T RU = U^2 \tag{1.10}$$

Volume Variation

In the material configuration, the elementary change of volume is expressed as the multiplication of edges width parallel to the Cartesian axes given by $dX_i = dX_i E_i$, hence

$$dV = dX_1 dX_2 dX_3 \tag{1.11}$$

By analogy, in the spatial configuration the volume change is a triple product of edges parallel to the Cartesian basis e_i [226] (where $\times$ denotes the vector product),

$$dv = dx_1 \cdot (dx_2 \times dx_3) \tag{1.12}$$

such as

$$dx_i = FdX_i = \frac{\partial \chi}{\partial X_i} dX_i; \quad i = 1, 2, 3 \tag{1.13}$$

then from the two last equations,

$$dv = \frac{\partial \chi}{\partial X_1} \cdot \left(\frac{\partial \chi}{\partial X_2} \times \frac{\partial \chi}{\partial X_3} \right) dX_1 dX_2 dX_3 \tag{1.14}$$

The above triple product is the determinant of F; thus, the volume variation in terms of the Jacobian is

$$dv = JdV; \quad J = \det(F) \tag{1.15}$$

For incompressible materials, $J = 1$, *i.e.*, the volume change is null. And, in terms of principal stretch, λ_i,

$$J = \lambda_1 \lambda_2 \lambda_3 \tag{1.16}$$

---

[1]The F in $F^T F$ is situated on the right.

Right Cauchy-Green tensor invariants

SEDF is often expressed as a function of invariants of the strain tensor. Hereafter we introduce the invariants of $\boldsymbol{C}$

$$
\begin{aligned}
I_1 &= \mathrm{tr}(\boldsymbol{C}) = \lambda_1^2 + \lambda_2^2 + \lambda_3^2 \\
I_2 &= \frac{1}{2}\left[(\mathrm{tr}\,\boldsymbol{C})^2 - \mathrm{tr}(\boldsymbol{C}^2)\right] = \lambda_1^2\lambda_2^2 + \lambda_2^2\lambda_3^2 + \lambda_3^2\lambda_1^2 \\
I_3 &= \det(\boldsymbol{C}) = \lambda_1^2\lambda_2^2\lambda_3^2
\end{aligned}
\tag{1.17}
$$

with λ_i are stretch ratios initially oriented along the eigenvector directions of stretch tensor and are not generally aligned with the coordinates system axis.

Objectivity

Objectivity is an alternative definition of frame indifference, where the position of an observer does not affect any quantities of interest. In our context, the rigid body motion should not alter the stress and strain quantities of the deformed subject. To express this concept in a kinematic framework, let us consider an elementary vector $d\boldsymbol{X}$ that deforms to $d\boldsymbol{x}$. The latter is rotated to $d\tilde{\boldsymbol{x}}$ without changing its magnitude *via* an orthogonal tensor $\boldsymbol{Q}$. The relationship between these vectors is

$$
d\tilde{\boldsymbol{x}} = \boldsymbol{Q}d\boldsymbol{x} = \boldsymbol{Q}\boldsymbol{F}d\boldsymbol{X}
\tag{1.18}
$$

We show hereby that the right Cauchy-Green strain tensor is nonobjective quantity, in other words, its relative rotated tensor $\boldsymbol{C}_r$ does not equal $\boldsymbol{Q}\boldsymbol{C}\boldsymbol{Q}^T$,

$$
\boldsymbol{C}_r = \boldsymbol{F}^T \boldsymbol{Q}^T \boldsymbol{Q} \boldsymbol{F} = \boldsymbol{F}^T \boldsymbol{F} = \boldsymbol{C}
\tag{1.19}
$$

However, it is unaffected by any rigid body motion [227].

1.3.2.3 Thermodynamic Theory

As SEDF will be used to simulate the mechanical response under loads, specific attention should be attributed to the thermodynamic concept of the energetic approach. The first thermodynamic law stipulates that the time rate change of the internal energy $\dot{E}(\mathcal{P},t)$, for any part $\mathcal{P} \subset \mathcal{D}$ of a deformable body $\mathcal{D}$, is compensated by the total heat flux $Q(\mathcal{P},t)$, and the total mechanical power $W(\mathcal{P},t)$ [228].

$$
\dot{E}(\mathcal{P},t) = Q(\mathcal{P},t) + W(\mathcal{P},t)
\tag{1.20}
$$

According to the second law, the change rate of entropy $\dot{S}(\mathcal{P},t)$ is composed of exchanges of entropy and production of entropy, which can be only positive (or null if the transformation occurs with no dissipation). Then the exchanges of entropy under the temperature Θ, in non-isotherm transformation, follow the relation:

$$
\dot{S}(\mathcal{P},t) \geq \frac{Q(\mathcal{P},t)}{\Theta}
\tag{1.21}
$$

By merging the two laws (1.20) and (1.21), we obtain

$$
\dot{E}(\mathcal{P},t) - \Theta\dot{S}(\mathcal{P},t) \leq W(\mathcal{P},t)
\tag{1.22}
$$

The mechanical power is obtained as follows

$$
W = \boldsymbol{\sigma} : \boldsymbol{L}
\tag{1.23}
$$

where $\boldsymbol{L}$ is the strain rate tensor and $\boldsymbol{\sigma}$ is the Cauchy stress tensor describing the rate of stretching and shearing, it is the symmetric part of the velocity gradient tensor [228]. Consequently,

$$\dot{E}(\mathcal{P},t) - \Theta\dot{S}(\mathcal{P},t) \le \boldsymbol{\sigma} : \boldsymbol{L} \tag{1.24}$$

The equation above shows that the work done by the stress induces either a decrease in the entropy or an increase in the internal energy. When $\boldsymbol{\sigma} : \boldsymbol{L}$ induces mostly a decrease in entropy ($\dot{E} \ll \|\Theta\dot{S}\|$), the elasticity of $\mathcal{P}$ is entropic. ST tissues are composed of cross-linked chains in the network sample. External stress changes the end-to-end equilibrium distance of a chain, and it adopts a less probable conformation [120, 229, 230]. Thus, its entropy decreases. The elasticity of soft tissues is said to be purely entropic.

1.3.2.4 Constitutive Law

Fundamental Relations
Once the strain tensors in adequation with kinematic criteria, *i.e.*, objectivity and rotation-independence to deformation, are defined, we employ them to build a hyperelastic constitutive law. The concerned strain energy density depends only on the deformation gradient $\boldsymbol{F}$. It may be written as:

$$\psi(\boldsymbol{X},t) = \psi(\boldsymbol{F}(\boldsymbol{X},t),\boldsymbol{X}) \tag{1.25}$$

The total strain energy is the internal work done by stresses during the elastic deformation of a given material. Without dissipation effects, the work is dependent only on the initial and the last configuration. It is said to be path-independent. As a consequence, the stored energy can be established as a function of first Piola-Kirchhoff stress tensor, $\boldsymbol{P}$, and the time derivative of the deformation gradient tensor, $\dot{\boldsymbol{F}}$, [227]:

$$\psi(\boldsymbol{F}(\boldsymbol{X}),\boldsymbol{X}) = \int_{t=0}^{t} \dot{\psi}\, dt; \quad \dot{\psi} = \boldsymbol{P}(\boldsymbol{F}(\boldsymbol{X}),\boldsymbol{X}) : \dot{\boldsymbol{F}} \tag{1.26}$$

We learned from section (1.3.2.2) that $\boldsymbol{C}$ is independent of the rotational part of $\boldsymbol{F} = \boldsymbol{R}\boldsymbol{U}$, as well as ψ which depends only on the stretching part of $\boldsymbol{F}$. Hence, we may write

$$\psi(\boldsymbol{F}) = \psi(\boldsymbol{U}) = \psi(\boldsymbol{C}) \tag{1.27}$$

Consider the time derivative of $\psi(\boldsymbol{F})$. Utilizing the chain rule differentiation, we obtain

$$\dot{\psi} = \frac{\partial\psi(\boldsymbol{F})}{\partial\boldsymbol{F}} : \dot{\boldsymbol{F}} \tag{1.28}$$

By comparing to Eq. (1.26), since $\boldsymbol{F}$ and $\dot{\boldsymbol{F}}$ can take on any value independent of the other, the first Piola-Kirchhoff stress is defined by

$$\boldsymbol{P} = \frac{\partial\psi(\boldsymbol{F})}{\partial\boldsymbol{F}} \tag{1.29}$$

Hereafter, we look for stress expressions for $\boldsymbol{F}$ and $\boldsymbol{C}$. By using the Property $\boldsymbol{P} : \dot{\boldsymbol{F}} = \mathrm{tr}(\boldsymbol{P}^T\dot{\boldsymbol{F}})$ and the chain rule on $\boldsymbol{C}$:

$$\dot{\psi} = \mathrm{tr}\left[\left(\frac{\partial\psi(\boldsymbol{F})}{\partial\boldsymbol{F}}\right)^T \dot{\boldsymbol{F}}\right] = \mathrm{tr}\left[\left(\frac{\partial\psi(\boldsymbol{C})}{\partial\boldsymbol{C}}\right)^T \dot{\boldsymbol{C}}\right] \tag{1.30}$$

As $\boldsymbol{C}$ is a symmetric second-order tensor, the scalar-valued energy gradient $\psi(\boldsymbol{C})$ is also symmetric. Therefore,

$$\dot{\psi} = \mathrm{tr}\left[\frac{\partial\psi(\boldsymbol{C})}{\partial\boldsymbol{C}}\dot{\boldsymbol{C}}\right] \tag{1.31}$$

To express the derivative of $\boldsymbol{C} = \boldsymbol{F}^T\boldsymbol{F}$ with respect to time t, we introduce the spatial velocity gradient $\boldsymbol{l}$, such that $\dot{\boldsymbol{F}} = \boldsymbol{l}\boldsymbol{F}$ (by using the property $\overline{\boldsymbol{F}^T} = \dot{\boldsymbol{F}}^T$):

$$\dot{C} = \overline{\dot{F}^T F} + F^T \dot{F} = \dot{F}^T F + F^T \dot{F}$$
$$= F^T l^T F + F^T l F = F^T (l^T + l) F \tag{1.32}$$

As demonstrated in [227],

$$\dot{\psi} = \text{tr} \left[\left(\frac{\partial \psi(F)}{\partial F} \right)^T \dot{F} \right] = 2\text{tr} \left[\frac{\partial \psi(C)}{\partial C} F^T \dot{F} \right] \tag{1.33}$$

The relationship between F and C derivatives in the context of hyperelastic deformation is:

$$\left(\frac{\partial \psi(F)}{\partial F} \right)^T = 2 \frac{\partial \psi(C)}{\partial C} F^T \tag{1.34}$$

which, when substituted in (1.29), reads:

$$P = 2F \left(\frac{\partial \psi(C)}{\partial C} \right)^T = 2F \frac{\partial \psi(C)}{\partial C} \tag{1.35}$$

The first Piola-Kirchhoff P stress tensor is non-symmetric. Therefore, we express two symmetrical stress tensors, Cauchy σ and the second Piola-Kirchhoff stress tensor S [226], as function of C:

$$\sigma = J^{-1} F P^T = 2J^{-1} F \frac{\partial \psi(C)}{\partial C} F^T \tag{1.36}$$

and

$$S = F^{-1} P = 2 \frac{\partial \psi(C)}{\partial C} \tag{1.37}$$

The second Piola-Kirchhoff stress tensor formulation could be used to construct a constitutive model based only on the invariants of the right Cauchy-Green deformation tensor C.

Anisotropic Hyperelasticity

The relationship between the energy density ψ and C must be independent of the material axes chosen and, consequently, ψ must only be a function of C tensor's invariants. Thus, with the assumption that the strain energy density can be decoupled into isotropic and anisotropic parts [219], one could write:

$$\psi = \psi_{\text{iso}}(C(X); I_1, I_2, I_3) + \psi_{\text{aniso}}(C(X); I_4, I_5, I_6, I_7) \tag{1.38}$$

The fiber orientations are formulated in the anisotropic parts through the additional term ψ_{aniso}. Anisotroy invariant equations are based on the concept of structural tensors [231–233]. The invariants are introduced below [234]:

$$I_4^{(k)} = N_{\text{f}}^{(k)} \cdot C N_{\text{f}}^{(k)}, \quad I_5^{(k)} = N_{\text{f}}^{(k)} \cdot C^2 N_{\text{f}}^{(k)} \tag{1.39}$$

The unit vector $N_{\text{f}}^{(k)}$ describes the initial orientation of the k-th fiber family (commonly 1 family for the skin). These invariants depend primarily on one direction each, but it is possible count for the interaction between different directions:

$$I_6^{(k,l)} = \left(N_{\text{f}}^{(k)} \cdot N_{\text{f}}^{(l)} \right) \left(N_{\text{f}}^{(k)} \cdot C N_{\text{f}}^{(l)} \right), \quad I_7^{(k,l)} = \left(N_{\text{f}}^{(k)} \cdot N_{\text{f}}^{(l)} \right)^2 \tag{1.40}$$

Other invariant forms were also proposed in the literature [235, 236]. By considering only the isotropic restriction, the second Piola–Kirchhoff stress tensor can be rewritten from Equation 1.29 as

$$S = 2\frac{\partial\psi}{\partial C} = 2\left(\frac{\partial\psi}{\partial I_1}\frac{\partial I_1}{\partial C} + \frac{\partial\psi}{\partial I_2}\frac{\partial I_2}{\partial C} + \frac{\partial\psi}{\partial I_3}\frac{\partial I_3}{\partial C}\right) \tag{1.41}$$

The derivative forms of the isotropic invariants concerning C are expressed as follows:

$$\frac{\partial I_1}{\partial C} = I; \quad \frac{\partial}{\partial C_{IJ}}\sum_{K=1}^{3}C_{KK} = \delta_{IJ} \tag{1.42}$$

$$\frac{\partial I_2}{\partial C} = I_1 I - C; \quad \frac{\partial I_2}{\partial C} = \frac{1}{2}\left(2\mathrm{tr}(C)I - \frac{\partial}{\partial C_{IJ}}\sum_{K=1}^{3}\sum_{L=1}^{3}C_{KL}C_{LK}\right) \tag{1.43}$$

The derivative of the third invariant is more conveniently evaluated using the expression for the linearization of the determinant. The partial derivative is related to the directional derivative by choosing an arbitrary increment tensor ΔC.

$$D_{I_3}[\Delta C] = \sum_{I,J=1}^{3}\frac{\partial I_3}{\partial C_{IJ}}\Delta C_{IJ} = \frac{\partial I_3}{\partial C} : \Delta C \tag{1.44}$$

On the other hand, the linearized determinant is rewritten as [226]:

$$D_{I_3}[\Delta C] = \det(C)C^{-1} : \Delta C \tag{1.45}$$

Thus from the two last Equations (1.44) and (1.45),

$$\frac{\partial I_3}{\partial C} = \det(C)C^{-1} = I_3 C^{-1} \tag{1.46}$$

which leads to develop the form of the second Piola-Kirchhoff stress tensor (1.41)

$$S = 2\frac{\partial\psi(C)}{\partial C} = 2\left[\left(\frac{\partial\psi}{\partial I_1} + I_1\frac{\partial\psi}{\partial I_2}\right)I - \frac{\partial\psi}{\partial I_2}C + I_3\frac{\partial\psi}{\partial I_3}C^{-1}\right] \tag{1.47}$$

The multiplication of $\partial\psi(C)/\partial C$ by C from both sides leads to the same result. We say that $\partial\psi(C)/\partial C$ is coaxial C (they have the same eigenvectors), which is essential for isotropy [227].

In the spatial description, we express the Cauchy stress tensor in the same way as S, via the formula $\sigma = J^{-1}FSF^T$. It would be more convenient to rewrite the result in terms of the left Cauchy-Green strain tensor $B = FF^T$, as $FIF^T = B$, $FCF^T = (FF^T)^2 = B^2$ and $FC^{-1}F^T = (FF^{-1})(F^{-T}F^T) = I$. we deduce then:

$$\sigma = 2J^{-1}\left[I_3\frac{\partial\psi}{\partial I_3}I + \left(\frac{\partial\psi}{\partial I_1} + I_1\frac{\partial\psi}{\partial I_2}\right)B - \frac{\partial\psi}{\partial I_2}B^2\right] \tag{1.48}$$

Strain Energy Density Functions

The hyperelastic models that define the material are characterized by their relative strain energy density function. These functions are to be found intuitively such that the derived stresses and strains represent well the mechanical response of the material under loads. Their constant parameters are identified based on optimizing the discrepancy between the model and the experimental data. The hyperelastic constitutive models can be classified into three main categories: phenomenological, structural, and hybrid models (structurally based phenomenological) [218]. The first one is purely mathematical that ignores the micro-structure properties, and describes the nonlinear evolution of stress as function of stretch. Although this approach allows to fit the experiments efficiently , it has a principal drawback: the built behavior law (constitutive model) does not often have a clear physical interpretation.

The usual strategy for building a phenomenological hyperelastic model is generally based on three steps: formulation, data-fitting, and validation [237, 238]. The choice of the model form is based on

two major points of view: assumptions and experimental facts. Among many hyperelastic constitutive models, we list below some famous ones (incompressible form) that have been used in soft tissue characterization studies [223, 234, 239–241]. They can be in the form of, or combines, power, polynomial, exponential, or logarithmic terms.

- Mooney-Rivlin [242, 243]:

$$\psi_{\mathrm{MR}} = C_1(I_1 - 3) + C_2(I_2 - 3) \tag{1.49}$$

where I_1 and I_2 are the first and the second invariant of $\boldsymbol{C}$. $C_1 \geq 0$ and $C_2 \geq 0$ are empiric material parameters and can be accurately determined with a uniaxial tensile test. For consistency with linear elasticity, the shear modulus is equal to $\mu_s = 2(C_1 + C_2)$. The Mooney–Rivlin model is a special case of the generalized Rivlin model [244], whose variants have been used for simulating the motion of tongue [245], facial skin [246], thigh [247], and spine (the ground substance of annulus bulk) [248]. As mentioned in [249], the Mooney-type models have difficulty describing this highly nonlinear behavior.

- Neo-Hookean [243]:

$$\psi_{\mathrm{NH}} = C_1(I_1 - 3) \tag{1.50}$$

It is the simplest model among all the incompressible materials. It can be obtained by setting $C_2 = 0$ in Mooney-Rivlin SEDF. Hence, the shear modulus is $\mu_s = 2C_1$. The Neo-Hookean (NH) model is based on the statistical thermodynamics of cross-linked polymer chains [250]. A comparison of experimental analyses shows that this model fails to fit highly nonlinear curves because of its linear dependence on I_1 [251]. At very low strains, Young's modulus approximates $E \approx 6C_1$. NH model were used for the spine [248], skin [164], calf [252], foot [253], breast [254], and keloid [1].

- Yeoh [255]:

$$\psi_{\mathrm{Y}} = C_1(I_1 - 3) + C_2(I_1 - 3)^2 + C_3(I_1 - 3)^3 \tag{1.51}$$

This polynomial SEDF was proposed to predict the shear modulus in carbon-black-filled rubber significantly dropping at low strains [255]. In contrasts with Mooney-Rivlin and Neo-Hookean models, which have a constant shear modulus, Yeoh material has shear modulus that varies with deformation. As pointed out in [251], the dependence on the I_2 invariant is not significant and the function may contain only I_1 and I_3. Therefore a negative value of C_2 is not necessarily incorrect. Similarly to the two previous model, the linear consistency condition implies that the initial shear modulus $\mu_s^{(0)} = 2C_1$. As for C_3, it is interpreted as half the initial bulk modulus. Yeoh model was employed to identify the material parameters of the tongue [256], spine (the ground substance of annulus bulk) [248], and liver [249].

- Gent [257]:

$$\psi_{\mathrm{G}} = -\frac{\mu}{2} J_m \ln\left(1 - \frac{I_1 - 3}{J_m}\right) \tag{1.52}$$

Based on the concept of limiting chain extensibility, the Gent model has been developed to characterize rubber-like materials better when subjected to large deformations. μ parameter has the same physical interpretation as in the NH strain energy function. At the same time, J_m is an additional parameter that controls the chain extensibility (see Section 1.3.2.5 for more details). In the form of a logarithmic function, the Gent model has a singularity when I_1 reaches the limit $J_m + 3$. Hence, for incompressible material, $J_m > I_1 - 3$. ψ_{G} was applied to several recent ST characterization and simulation studies, arteries [258–260], brain tissue [261–264], skin [264], pelvic organ [265], and keloid [266].

- Ogden [267]:

$$\psi_O = \sum_{p=1}^{N} \frac{\mu_p}{\alpha_p} \left(\lambda_1^{\alpha_p} + \lambda_2^{\alpha_p} + \lambda_3^{\alpha_p} - 3 \right) \tag{1.53}$$

The Ogden strain-energy function is expressed directly in the principal stretches λ_i, which are more intuitive measures of deformation than the invariants. μ_p and α_p are the material parameters for each order p. For the same tissue, μ_p calibrated with a uniaxial tensile experiment is not equal to the one from an equibiaxial test [251]. Despite its gaining popularity among users of finite element analysis and its ability to fit very well the classical experimental data of Treloar [268], the Ogden model offers no real advantage over the Rivlin form (Mooney-Rivlin and Neo-Hookean). Because one load mode (associated with two-terms Ogen function) is insufficient to characterize the rubber-like material [269]. Using a higher-order function will increase the number of parameters. Among many applications to ST, we may cite the cases of brain tissue [270], aortic [271], liver [272], and skin [136, 139].

We find in the literature other phenomenological SEDF used to model the deep soft tissues [249], for instance Fung [273], Veronda-Westmann [274], Demiray [275], *etc.*

Model Stability

The strain energy density cannot be chosen without restriction. Other criteria are to check over when validating a hyperelastic strain energy function. The ones related to stability are not mandatory but highly recommended. These criteria are:

- **Drucker criterion**. This criterion [276], is a strong condition stipulating that the incremental internal energy of a deformed material can only increase. Hill's stability criterion is a similar postulate for elastic-plastic materials [277]. As pointed out in [278] that unstable energy functions can cause inconsistency and divergence in the nonlinear numerical solution algorithms used in FEM simulation. The Drucker criterion may be written in the following form:

$$d\boldsymbol{\sigma} : d\boldsymbol{\epsilon} \geq 0 \tag{1.54}$$

One could express the inequality above with principal stresses and strains at any point in the solid:

$$\sum_{i=1} d\sigma_i d\epsilon_i \geq 0 \tag{1.55}$$

Principal Cauchy stresses and strains are related through the tangential stiffness matrix $\boldsymbol{D}$:

$$\begin{pmatrix} \sigma_1 \\ \sigma_2 \\ \sigma_3 \end{pmatrix} = \begin{pmatrix} D_{11} & D_{12} & D_{13} \\ D_{21} & D_{22} & D_{23} \\ D_{31} & D_{32} & D_{33} \end{pmatrix} \begin{pmatrix} \epsilon_1 \\ \epsilon_2 \\ \epsilon_3 \end{pmatrix} \tag{1.56}$$

In practice, the inequality (1.54) can be satisfied by justifying that $\mathrm{tr}(\boldsymbol{D}) \geq 0$ and $\det(\boldsymbol{D}) \geq 0$. D_{ij} depend on the load mode, and the strain energy function [279].

- **Ellipticity condition**. The strong ellipticity condition verifies nonlinear elasticity [280]. It was used for incompressible [281] and compressible [282] isotropic materials. In some cases, the model witnesses a loss of ellipticity [283], where the classical local continuum theory fails to describe the problem correctly; in this situation, the boundary value problem is ill-posed, and the elliptic equations become hyperbolic [284].

The generic condition to verify the strain energy in the absence of body forces can be written as [285, 286]:

$$\frac{1}{J}F_{p\alpha}F_{q\beta}\frac{\partial^2\psi}{\partial F_{i\alpha}\partial F_{j\beta}}v_{1p}v_{1q}v_{2i}v_{2j} > 0; \quad v_1 \neq 0 \text{ and } v_2 \neq 0 \tag{1.57}$$

with v_1 and v_2 are arbitrary non-zero vectors. This condition is always difficult to verify [234]. A simplified condition for plane-strain deformation of isotropic material is proposed in [287].

- **Poly-convexity**. The direct analysis of the ellipticity condition can be overcome by studying the polyconvexity in the sense of Ball [288] that implies ellipticity [289].

1.3.2.5 Gent Model

A Note About Model Selection

A question about the representativity and the validity of phenomenological models should be tackled and discussed. One of the aims of modeling is the identification of material parameters. A hyperelastic model is validated as soon as it helps to fit the gathered experimental data. However, in plenty of material characterization studies [251, 290–292], more than a model can fit the same data. Hence, a model selection procedure would be based on dictated criteria, such as Occam's razor [293]. Phenomenological models have been qualified as consistent with fundamental theory but forgo any attempt to explain the relationship between the nature of the parameters and the measured values [294]. On the other hand, the micro-structural models (overviewed in [218]) are more realistic and representative. Even though they fit the data accurately, they are overcharged with parameters, which may increase their uncertainty. Also, their formulation and implementation are very costly.

Furthermore, As it is widely known, the stretching limit is inevitably reached on human skin if the extension undergoes large deformations *in vivo*. Therefore, the chosen model should include the concept of stretching limit (Fig. 1.26). It has been shown previously that *Gent* model is an appropriate semi-empirical candidate model to be associated with extensibility limit, with the ability to predict non-linearities arising for small stretches ($\lambda_1 < 1.2$) [106]. In this section, we explain its components and relevance in skin application.
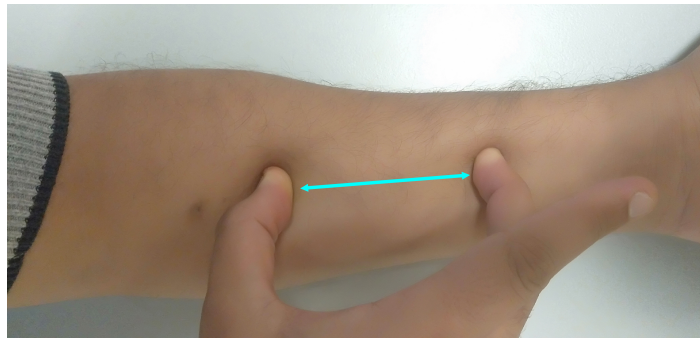
Figure 1.26: Limited stretch on the skin.

Semi-Empirical Behavior

Gent model, as introduced the first time in [257], is developed from both phenomenological and micromechanics concepts. It has been demonstrated that it has a near equivalence with Arruda-Boyce's model. These two constitutive laws are able to predict similarly complex three-dimensional deformation with only two material constants [295, 296]. Another conceptual link between micro-structural and phenomenological models has been discussed in [297, 298], where the authors showed that Gent behavior law is a very good approximation of a non-Gaussian full-network model involving the inverse Langevin function (see Section 1.3.2.5). Its phenomenological parameters μ and J_m can be formulated in terms of microscopic properties, providing a significant advance in establishing the

connection between statistical mechanics and continuum mechanics.

As thoroughly as necessary, let us propose a molecular interpretation of the Gent model inspired by the Arruda-Boyce eight-chain model [241] since their respective mechanical responses are close [295, 296]. Figure 1.27 demonstrates equivalent values of the initial shear modulus for Gent and 8-chain (Arruda-Boyce) materials but not for the Neo-Hookean. The physical description of the two formers was carried out by assuming the equivalence of their respective Cauchy stress expressions. By substituting (1.52) in (1.48):

$$\boldsymbol{\sigma}_G = -p\mathbf{I} + \mu \frac{J_m}{J_m - (I_1 - 3)} \boldsymbol{B} \tag{1.58}$$

The averaged macroscopic constitutive equation for the Cauchy stress tensor in Arruda-Boyce eight-chain model is [299]:

$$\boldsymbol{\sigma}_{AB} = -p\mathbf{I} + \mathcal{X}(I_1)\boldsymbol{B} \tag{1.59}$$

where p is the hydrostatic pressure in both equations above. Thus, the main idea is to prove that it is possible to provide a molecular interpretation to the semi-phenomenological constitutive parameters in (1.52), *i.e.*,

$$\mathcal{X}(I_1) \approx \mu \frac{J_m}{J_m - (I_1 - 3)} \tag{1.60}$$

We discuss first the theoretical molecular concept of the 8-chain model, as introduced by Beatty [299].
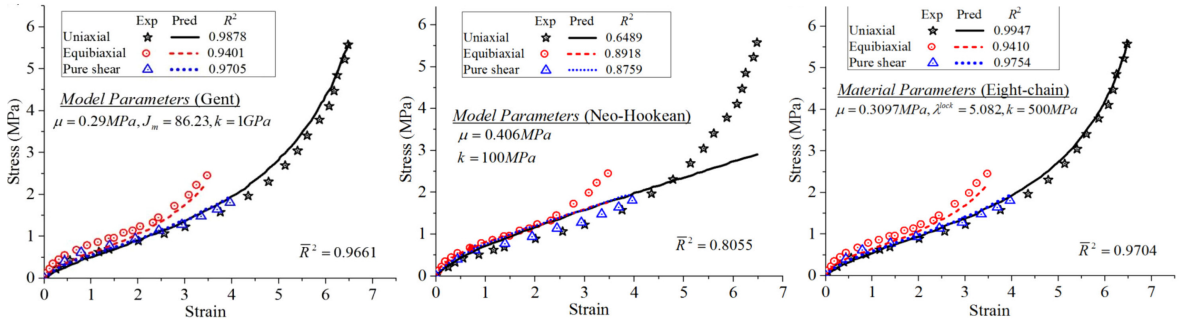
Figure 1.27: Comparison of the stress-strain curves for Gent, Neo-Hookean, and 8-chain models [251].

Eight-Chain Model

Many rubber elasticity models use as a measure of the deformation the change in length of the end-to-end distance $\boldsymbol{r}$ between molecular cross-links (Fig. 1.28). It is assumed that the macroscopic stretch is related to chain stretch via a non-Gaussian probability distribution function $P(\boldsymbol{r})$. In the reference configuration, the chain-end points occupy the most probable position over a uniform non-Gaussian network [300–302]. Among many flexible-chain networks developed to characterize the mechanical response of isotropic rubber-like materials, we can define the most successful Arruda-Boyce 8-chain network [303] in Figure 1.28. Mathematically, it is simpler than others and fits well with different mechanical experiments [299].

When the chain is fully extended, its length is equivalent to the total length of N_c rigid links, as $r_L \equiv N_c l$. Its average length in the undeformed configuration is given by [301, 302]: $\bar{r} = \sqrt{N_c}l$. Consequently, the maximum chain stretch is defined by

$$\lambda_c \equiv \frac{r_c}{\bar{r}} \tag{1.61}$$
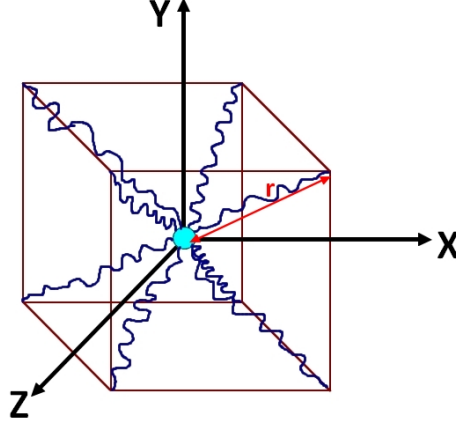
Figure 1.28: 8-chain cubic structure

Furthermore, the current relative chain stretch is introduced as

$$\lambda_r = \frac{r_c}{r_L} = \frac{\lambda_c \bar{r}}{\sqrt{N_c}\bar{r}} = \frac{\lambda_c}{\sqrt{N_c}} \tag{1.62}$$

The current relative stretch varies from $\lambda_r = 1/\sqrt{N_c}$ and 1 (in the undeformed state $\lambda_c = 1$). If the chain is completely rigid ($N_c \to \infty$), the relative stretch is null. One could introduce n_c as the chain density per unit volume, then the total strain energy for a homogeneous network is then [299]:

$$\psi(\lambda_r) = n_c \psi_c(\lambda_r) \tag{1.63}$$

Where the deformation work of a randomly-oriented chain ψ_c is determined by the second law of thermodynamics: $\psi_c = -\Theta S_c$. Kuhn and Grün have derived the configuration entropy S as a non-Gaussian approximate expression for $P(r)$ [300].

$$S = k \left[c - N_c \left(\beta_c \lambda_r + \ln \left(\frac{\beta_c}{\sinh \beta_c} \right) \right) \right] \tag{1.64}$$

k denotes the universal Boltzmann constant, and the constant c is chosen so that the energy vanishes in the absence of deformations, while $\beta_c = \mathcal{L}(\lambda_r)$ is the inverse of the Langevin function. Or, more precisely,

$$\lambda_r = \mathcal{L}(\beta_c) = \coth \beta_c - \frac{1}{\beta_c} \tag{1.65}$$

which can be approximated by $\beta_c \approx 3\lambda_r$ in some special cases, as explained in [299]. On using (1.64) in (1.63), the strain energy of the deformed chain is equal to

$$\psi_c = N_c k\Theta \left(\beta_c \lambda_r + \ln \left(\frac{\beta_c}{\sinh \beta_c} \right) \right) - kc\Theta \tag{1.66}$$

The next step will be constructing the current relative stretch according to the cubic structure of the Arruda-Boyce eight-chain model. Once considering $X = Y = Z$ in the rectangular Cartesian frame in Fig. 1.28, the length of the undeformed chain has the average value $\bar{r} = X\sqrt{3}$. Its direction vector is $\boldsymbol{a}_c = (1, 1, 1)/\sqrt{3}$. If we suppose that the frame containing the network is oriented along the local principal axes, the stretch of the eight chains, whose $\boldsymbol{a}_c$ is the initial orientation, is expressed in terms of the right Cauchy-Green tensor as

$$\lambda_c^2 = \boldsymbol{a}_c \cdot \boldsymbol{C} \boldsymbol{a}_c = \sum_{i=1}^{3} m_i^2 \lambda_i^2 \tag{1.67}$$

40

For every chain direction vector parallel to the cube diagonals $m = (a_c/\sqrt{3}, b_c/\sqrt{3}, c_c/\sqrt{3})$ with a_c, b_c, and c_c taking the values of -1 and 1, the results remain the same ($\lambda_c^2 = \lambda_1^2 + \lambda_2^2 + \lambda_3^2 = I_1/3$). As a function of the first invariant of C, the stretch of a single chain takes the form

$$\lambda_c = \sqrt{\frac{I_1}{3}} \tag{1.68}$$

and by using the Equation (1.62),

$$\lambda_r = \sqrt{\frac{I_1}{3N_c}} \tag{1.69}$$

The Arruda-Boyce 8-chain strain energy density as introduced in (1.63), and by combining the latter with (1.66) and (1.62), is defined by

$$\psi_{AB}(\lambda_r) = n_c k \Theta \sqrt{N_c} \left(\beta_c \sqrt{\frac{I_1}{3}} + \ln\left(\frac{\beta_c}{\sinh\beta_c}\right) \right) - n_c k c \Theta \tag{1.70}$$

Physical Interpretation

We recall that the main aim of this micro-structural study is to determine the molecular entities of $X(I_1)$ in Eq. (1.59). It is obtained by deriving the strain energy density (1.70) with respect to the first invariant, as mentioned in (1.48).

$$X(I_1) = 2 n_c k \Theta \sqrt{N_c} \beta_c \frac{1}{2\sqrt{3I_1}} = \frac{n_c k \Theta \beta_c}{3\lambda_r} \tag{1.71}$$

In many theoretical and experimental studies conducted across the years on entropic rubbers, it has been shown that the shear modulus in the undeformed state $\mu_s^{(0)}$ is linear with the temperature Θ [241, 300, 301, 304]

$$\mu_s^{(0)} \equiv nk\Theta \tag{1.72}$$

Therefore,

$$X(I_1) \equiv \frac{\mu_s^{(0)} \beta_c}{3\lambda_r} \tag{1.73}$$

On comparing the latter with Eq. (1.60), one obtains the expressions that describe the molecular structure of Gent parameters. It is trivial that the constant μ is equivalent to

$$\mu \equiv \mu_s^{(0)} = nk\Theta \tag{1.74}$$

Then, a physical description of J_m is valid if and only if it is equivalent to

$$J_{mG} \equiv \frac{\beta_c(I_1 - 3)}{\beta_c - 3\lambda_r} = \frac{3\beta_c(N_c\lambda_r^2 - 1)}{\beta_c - 3\lambda_r} \tag{1.75}$$

However, the inverse Langevin function introduced earlier, $\beta_c = \mathcal{L}^{-1}(\lambda_r)$, cannot be determined analytically and directly. A way to overcome this issue is to define J_m differently and find the expression of β_c. To do, we know that at large strains, the ultimate extensibility of the network is activated when all the flexible links are aligned $\lambda_r = 1$ so that the distance end-to-end on a single chain is the sum of its rigid links $I_1 = 3N_c$. On the Gent model, the maximum extensibility is reached when $J_m = I_1 - 3$ (1.58), which leads to

$$J_m = 3(N_c - 1) \tag{1.76}$$

41

In this situation, (1.58) becomes

$$\sigma_{\text{Gent}} = -p\mathbf{I} + \mu \frac{N_c - 1}{N_c(1 - \lambda_r^2)}\boldsymbol{B} \tag{1.77}$$

Finding a proper expression for β_c based on (1.60) would be secured through the approximation of (1.73). Nevertheless, the use of polynomial expressions to approximate β_c is somewhat misleading because of the existence of singularity $\lambda_r \to 1$. For this reason, the comparison carried out in [295] between the Arruda-Boyce eight-chain model and the Gent model is not complete. To approximate the inverse Langevin function, it is necessary then to use rational functions, such as Padè approximants [305]. The reader is referred to [241, 298, 306, 307] for more details.

The take-home message in the present section is to show that is possible to give an *a posteriori* 'molecular' interpretation of the Gent model which is exactly equivalent of the one proposed for the Arruda–Boyce model. In other words, Gent model is a suitable simplification of the 8-chain network model.

1.4 Parameter Identification

Characterizing the mechanical behavior of structures and materials includes assessing their representative models' parameters. It is possible to deduce them by comparing models and experiments directly. Since the subject is vast, this section focuses on the techniques, commonly known as *inverse problems*, developed and used to identify soft tissue material parameters included in the constitutive laws.

1.4.1 Inverse Problem Strategies

This inverse problem can be summarized into a forward problem (or direct problem), and an inverse problem [308]. A direct problem is always well-posed and determines an expected output result, $\boldsymbol{d}$, from sufficiently given input data, such as material parameters, geometry, and boundary conditions (Fig 1.29). The inverse problem is, however, concerned with the determination of an unknown input from some incomplete output results. In our case, the unknown inputs are material parameters, and the outputs are measurements.

The forward problem can be either analytical or numerical. Numerical forward problems are widely employed since the physical modeling requires some complexity to simulate better reality. They can be computed with different techniques, such as Finite Elements Method (FEM). The latter is the most used in computational mechanics, which takes into account both physics and topology. Both analytical and FEM-based numerical models were used in my thesis depending on the feasibility.

The inverse problems know two main difficulties: ill-posedness and nonlinearity. In the first case, the experimental data are not diversified enough to determine all the parameters accurately. While in the second case, the error optimization is performed with sophisticated algorithms that may lead to non-unique solutions. It is then recommended to add constraints that reduce the solutions space to have a unique solution regardless of the initial guess (set arbitrarily). We can enumerate several inverse problems strategies used to characterize solid materials as follows [309, 310].

1.4.1.1 Equilibrium Gap

This approach has been developed for elastic heterogeneity cases and aims to identify the contrasts of mechanical properties that obey internal equilibrium from a given displacement. The basic assumption is that the displacement data are available on a measurement grid, which can be obtained either by finite element analyses or digital image correlation. A linear system has to be solved (Eq. 1.78), where the
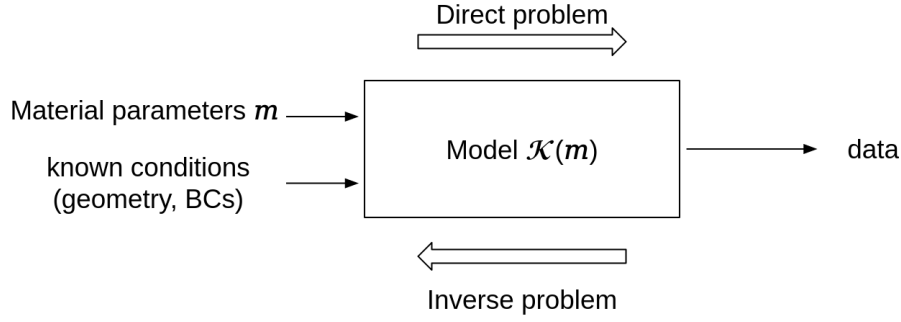
Figure 1.29: Inverse problem's general scheme. BCs stand for boundari conditions.

unknowns are the contrasts among the element-wise constant Young's moduli $\boldsymbol{c}^T = \{C_1, C_2, ..., C_{N_e}\}$ (N_e denoting the number of elements), and the displacements measured at the nodes are known. The two quantities are linked by an operator $[\boldsymbol{M}]$ retrieved from jump conditions between two elements, applied to the equilibrium equation $\mathbf{div}\boldsymbol{\sigma} = \mathbf{0}$.

$$[\boldsymbol{M}]\{\boldsymbol{c}\} = \{\boldsymbol{d}\} \tag{1.78}$$

The system above is usually solved by minimizing the following norm [311]:

$$\mathcal{N} = \|[\boldsymbol{M}]\{\boldsymbol{c}\} - \{\boldsymbol{d}\}\|^2 \tag{1.79}$$

1.4.1.2 Virtual Fields

The method leads to explicit identification formula of material parameters. It requires full-field measurements of the strain $\boldsymbol{\epsilon}$ in the domain Ω (alternatively through differentiation of a measured displacement field) [312]. This approach is based on the virtual work principle applied with well-chosen virtual fields and can be written in the absence of body force as

$$-\int_\Omega \boldsymbol{\sigma} : \boldsymbol{\epsilon}^\star \, d\Omega + \int_{\partial\Omega} \boldsymbol{t} \cdot \boldsymbol{u}^\star \, ds = \int_\Omega \rho\boldsymbol{\gamma} \cdot \boldsymbol{u}^\star \, d\Omega \tag{1.80}$$

with $\boldsymbol{\gamma}$, the acceleration vector, ρ, the mass per unit volume, and $\boldsymbol{t}$, the distribution of the applied traction on the boundary surface $\partial\Omega$. '$\star$' stands for a kinematically admissible virtual field. The idea of the virtual fields method is to replace the Cauchy stress tensor using the constitutive equation $\boldsymbol{\sigma} = \mathbb{C} : \boldsymbol{\epsilon}$. In the case of quasi-static linear bi-dimensional isotropic elasticity, and within the hypothesis of small deformations, this problem is rewritten as

$$\int_\Omega C_{11}\left(\epsilon_{11}\epsilon_{11}^\star + \epsilon_{22}\epsilon_{22}^\star + \frac{1}{2}\epsilon_{12}\epsilon_{12}^\star\right) d\Omega + \int_\Omega C_{12}\left(\epsilon_{11}\epsilon_{22}^\star + \epsilon_{11}\epsilon_{22}^\star + \frac{1}{2}\epsilon_{12}\epsilon_{12}^\star\right) d\Omega = \int_{\partial\Omega} \boldsymbol{t} \cdot \boldsymbol{u}^\star \, ds \tag{1.81}$$

As the material is considered homogeneous, material parameters C_{ij} can be taken out of the integrals, and the latter are approximated by discrete sums. It results in a linear equation in the C'_{ij}s, which are to be identified. For assessing the Poisson's ratio, one could write $\nu = C_{12}/C_{11}$ [313]. The VFM was applied to many solid mechanics studies, including soft tissue's [314–316].

1.4.1.3 Constitutive Equation Gap

For a set of admissible stress fields $\mathcal{S}$, the constitutive equation gap method minimize the distance between admissible stress $\boldsymbol{\tau}$ and another stress field computed through a constitutive model from a given experimental displacement field $\hat{\boldsymbol{u}}$. For the linear case, the quantity to minimize is

$$\mathcal{E}(\hat{\boldsymbol{u}}, \boldsymbol{\tau}, \mathbb{C}) = \frac{1}{2} \int_{\Omega} (\boldsymbol{\tau} - \mathbb{C} : \boldsymbol{\epsilon}(\hat{\boldsymbol{u}})) : \mathbb{C}^{-1} : (\boldsymbol{\tau} - \mathbb{C} : \boldsymbol{\epsilon}(\hat{\boldsymbol{u}})) \, \mathrm{d}\Omega \tag{1.82}$$

The measurement $\hat{\boldsymbol{u}}$ is interpolated over the domain using finite element shape functions. Then the elastic parameters (components of $\tilde{\mathbb{C}}$) are identified through the equation

$$\tilde{\mathbb{C}} = \arg \min_{\tilde{\mathbb{C}} \in \mathbb{C}_s} \mathcal{E}_C(\tilde{\mathbb{C}}) \quad ; \quad \mathcal{E}_C(\tilde{\mathbb{C}}) = \min_{\boldsymbol{\tau} \in \mathcal{S}} \mathcal{E}(\hat{\boldsymbol{u}}, \boldsymbol{\tau}, \tilde{\mathbb{C}}) \tag{1.83}$$

with $\mathbb{C}_s$ the space of the admissible elastic tensor, corresponding to symmetric and positive definite fourth-order tensors. In particular, the procedure is seen to involve two partial minimization, with respect to $(\hat{\boldsymbol{u}}, \boldsymbol{\tau})$, followed by a partial minimization with respect to $\tilde{\mathbb{C}}$. With this approach, at most, three parameters of heterogeneous materials can be locally determined [309].

1.4.1.4 Finite Element Model Updating

The goal of the Finite Element Model Updating (FEMU) approach is to identify the material parameters gathered in the vector $\boldsymbol{m}$ by updating the forward problem based on FEM formulation iteratively until reaching the minimum of the discrepancy $\mathcal{J}(\boldsymbol{m})$ between either known and predicted data, displacement and/or force, (Fig. 1.30):

$$\mathcal{J}(\boldsymbol{m}) = \sum_{i=1}^{N_d} \|d_{\text{exp}}^{(i)} - d_{\text{model}}(\boldsymbol{m})^{(i)}\| \tag{1.84}$$

where d_{exp} and d_{model} are observation and model data, respectively. They are summed over N_d data points.
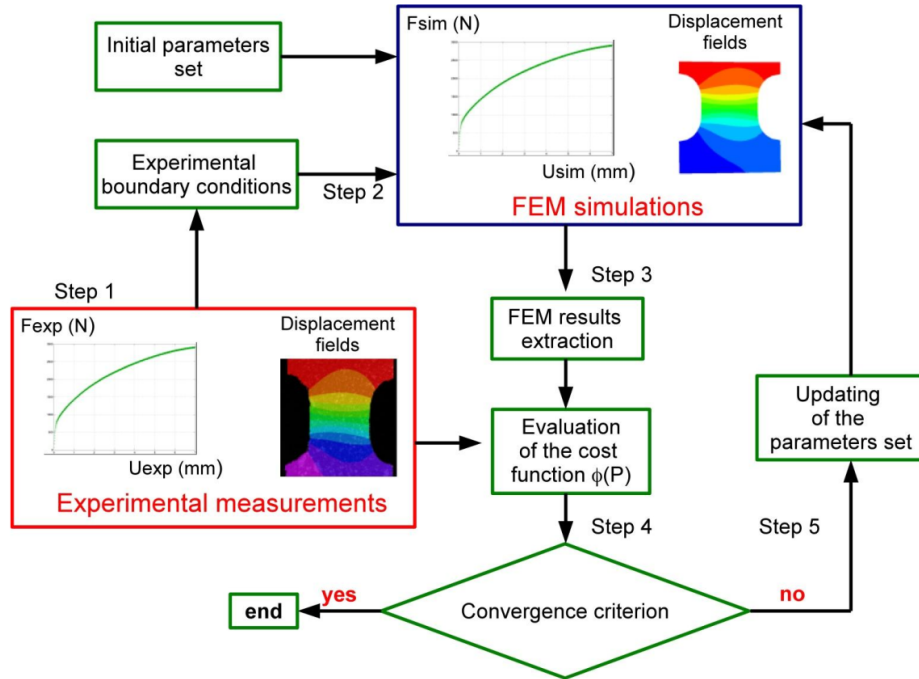
Figure 1.30: Flow-chart of the Finite Element Method Updating identification procedure.

This type of inverse problems may combine full-field measurements and the finite element method (FEM), ans it was often used [309, 312, 317, 318]. The earliest implementation of FEMU was possibly

performed in 1971 by Kavanagh and Clough [319], where they tackled the problem of identifying mechanical properties in elastic solids. To acquire full-field measurements, different optical techniques, including digital image correlation (DIC) are commonly used [312, 320]. The procedure has been integrated into FEMU frameworks in many mechanical characterization studies: in linear elasticity [321–324], in elasto-plasticity [325–329], in viscoelasticity [330, 331], and hyperelasticity [332–334]. A practical example of its application to human skin is presented in Section 1.4.4.2.

Unlike the three inverse problems introduced earlier, the FEMU allows characterizing many mechanical aspects: nonlinearity, anisotropy, viscoelasticity, and pre-stress. Indeed, because of its intuitive conception, the modeler needs to implement separately and simply a FE model and an optimizer solver. The former is relatively easy to carry out thanks to many commercial and free open-source frameworks. The latter, on the other hand, requires a suitable error minimization algorithm, given the constraints, for instance, computation cost, measurement data consistency, and uncertainty, ... Consequently, an overview of the optimization algorithms used in characterizing the soft tissues is presented hereafter. They can be broadly classified into two categories: deterministic methods and stochastic methods [335].

1.4.2 Deterministic Optimization

This branch of numerical optimization focuses on finding exact solutions to an optimization problem within some predefined tolerance. The term "deterministic optimization" typically refers to rigorous methods that converge to the global optimum in finite time. However, in ill-posed problems, the solution space is not fully convex, which makes optimization algorithms converge toward the local and not the global optimum. A remarkable advantage of the deterministic approach is that the convergence to a solution requires a lower number of evaluations of the cost function $\mathcal{J}$ and their respective derivatives compared to the use of stochastic optimization algorithms. We address the two main aspects of deterministic optimization, namely: unconstrained and constrained optimization [336, 337].

1.4.2.1 Unconstrained Optimization

An unconstrained optimization problem can be written in terms of the minimization of an objective function for N_m model parameters

$$\text{minimize } \mathcal{J}(\boldsymbol{m}), \quad \boldsymbol{m} \in \mathbb{R}^{N_m} \tag{1.85}$$

An UPM algorithm starts from an initial guess $\boldsymbol{m}^{(0)}$ and generates a sequence of points $\boldsymbol{m}^{(n)}$ in the solution space converging to the solution $\hat{\boldsymbol{m}}$ in the direction $\boldsymbol{s}$ with a step δm. At iteration n, it reads

$$\boldsymbol{m}^{(n+1)} = \boldsymbol{m}^{(n)} + \delta m^{(n)} \boldsymbol{s}^{(n)}, \tag{1.86}$$

An optimal set $\hat{\boldsymbol{m}}$ must satisfy the following conditions

$$\begin{cases} \boldsymbol{s}^T \boldsymbol{G}(\hat{\boldsymbol{m}}) = 0 \ \ \forall \boldsymbol{s} \in \mathbb{R}^{N_m} \\ \boldsymbol{s}^T \boldsymbol{H}(\hat{\boldsymbol{m}}) \boldsymbol{s} \geq \ \ \forall \boldsymbol{s} \in \mathbb{R}^{N_m} \end{cases} \Rightarrow \begin{cases} \boldsymbol{G}(\hat{\boldsymbol{m}}) = \boldsymbol{0} \\ \boldsymbol{H}(\hat{\boldsymbol{m}}) \text{ is positive semi} - \text{definite} \end{cases} \tag{1.87}$$

with $\boldsymbol{G}$ and $\boldsymbol{H}$, respectively, the gradient and the Hessian of the objective function with respect to the model parameters. We assume that the objective function is sufficiently smooth, at least for the second order, class C^2 (or class C^1 if we need to compute gradients only). For numerical reasons and formulation limitations, $\boldsymbol{G}$ and/or $\boldsymbol{H}$ can be approximated using Finite Difference Equation. UPM algorithms are usually based on approximating the objective function using a Taylor series expansion up to the second order. Some famous strategies exist for that: *Line Search* [338], *Trust Region*, and *Downhill Simplex* [339].

Line Search Approach

The line search approach finds a descent direction along which the objective function $\mathcal{J}$ will be minimized and then computes a step size that determines how far $\boldsymbol{m}$ should move along that direction. The principal steps of this strategy are:

- determine a descent direction $\boldsymbol{s}$.

- find $\delta m^{(n)}$ by minimizing Eq. (1.85).

- set the new parameter from the Eq. (1.86)

Trust Region Approach

Instead of finding an optimal solution for the cost function, in this approach, we define a neighborhood area $\mathcal{B}$ around the current optimal solution as a trust region in each iteration. Unlike the Line Search algorithm, it selects the direction $\boldsymbol{s}$ and step size δm simultaneously. First, $\mathcal{J}(\boldsymbol{m})$ is approximated by a quadratic function $q^{(n)}(\boldsymbol{\delta}_{\mathrm{m}})$ obtained by truncating the Taylor series applied to $\mathcal{J}(\boldsymbol{m}^{(n)} + \boldsymbol{\delta}_{\mathrm{m}})$ (involving the approximation of the gradient and the Hessian of $\mathcal{J}$). The neighborhood as a function of the radius h is expressed by

$$\mathcal{B}^{(n)} = \{\boldsymbol{m}, \text{ such that } \|\boldsymbol{m} - \boldsymbol{m}^{(n)}\| \leq h^{(n)}\} \tag{1.88}$$

We seek the solution $\boldsymbol{\delta}_{\mathrm{m}}^{(n)}$ of

$$\min_{\boldsymbol{\delta}_{\mathrm{m}}} q^{(n)}(\boldsymbol{\delta}_{\mathrm{m}})$$
$$\text{subject to } \|\boldsymbol{\delta}_{\mathrm{m}}\| \leq h^{(n)} \tag{1.89}$$

$\boldsymbol{m}^{(n+1)} = \boldsymbol{m}^{(n)} + \boldsymbol{\delta}_{\mathrm{m}}^{(n)}$ is then chosen.

Downhill Simplex Approach

This method, proposed by John Nelder and Roger Mead [340], known as the Nelder-Mead algorithm, uses the concept of a simplex, a special polytope of $n + 1$ vertices in n dimensions. Let us take a 2D space as an example, where triangles are used to find an objective function's local minimum or maximum in a direct search. For each iteration n, the objective function is evaluated on 3 test points $\boldsymbol{m}_1^n, \boldsymbol{m}_2^n, \boldsymbol{m}_3^n$, and then extrapolated beyond the triangle. The simplest approach is to replace the worst parameter $\boldsymbol{m}_p$ set (with the highest cost) with another set $\boldsymbol{m}_q$ reflected through the centroid of the remaining 2 points. If $\mathcal{J}(\boldsymbol{m}_q) > \mathcal{J}(\boldsymbol{m}_p)$, the triangle is contracted along this line. Conversely, the triangle shrinks across a valley.

Unlike modern optimization methods, the Nelder–Mead heuristic can converge to a non-stationary point unless the parameter space is entirely convex. Furthermore, the overall number of iterations to the proposed optimum may be high. Regardless of the computational cost of the FEMU process, the simplex approach can be a good candidate to optimize the errors as the derivation is not applied. In the literature, the simplex method was used to identify the parameters of human skin through the FEMU model in [136, 164, 185].

1.4.2.2 Gradient-based Optimization Methods

In this part, we describe the schemes of some famous least squares methods for nonlinear optimization based on the gradient of the objective function. Those methods can compute the descent direction in the Line Search approach. They have been used successfully in hyperelastic material characterization with FEMU approach [141, 146, 163, 319, 332, 333]. Their main advantage is the fast rate of convergence. In practice, they need to be modified for robustness and computational efficiency. However, the derivatives of $\mathcal{J}$ must be provided for continuous space.

Newton's Method

It is the most classic nonlinear programming algorithm. In Newton's method (or Newton-Raphson), a quadratic model of the objective function is obtained from second-order-truncated Taylor series expansion, as following

$$\mathcal{J}(\boldsymbol{m}^{(n)} + \boldsymbol{\delta}_{\mathrm{m}}) \approx q^{(n)}(\boldsymbol{\delta}_{\mathrm{m}}) = \mathcal{J}^{(n)} + \boldsymbol{\delta}_{\mathrm{m}}^{T} \boldsymbol{G}^{(n)} + \frac{1}{2} \boldsymbol{\delta}_{\mathrm{m}}^{T} \boldsymbol{H}^{(n)} \boldsymbol{\delta}_{\mathrm{m}} \tag{1.90}$$

The method requires $\boldsymbol{G}$ and $\boldsymbol{H}$ to be computed analytically. Consequently, the change in parameters vector $\boldsymbol{\delta}_{\mathrm{m}}$ is obtained by resolving the system $\boldsymbol{H}^{(n)} \boldsymbol{\delta}_{\mathrm{m}} = -\boldsymbol{G}^{(n)}$ and added to the previous $\boldsymbol{m}^{(n)}$ to get $\boldsymbol{m}^{(n+1)}$. We point out that Newton's method may fail to converge when $\boldsymbol{H}$ is not positive definite. There are many ways to modify the Hessian matrix and combine it with other methods, such as the steepest descent method [335].

Quasi-Newton Method

They are alternatives to Newton's method when the Hessian derivative cannot be available or are too expensive to compute at every iteration. The main idea is to approximate $\boldsymbol{H}$ by finite differences in the gradient vector. To have a symmetrical matrix, $\boldsymbol{H}$ is replaced by $\frac{1}{2}\left(\tilde{\boldsymbol{H}} + \tilde{\boldsymbol{H}}^{T}\right)$, such that its i-th column is made of terms like

$$\tilde{\boldsymbol{H}}_{i}^{(n)} = \frac{\boldsymbol{G}\left(\boldsymbol{m}^{(n)} + \tilde{\boldsymbol{\delta}}_{\mathrm{m}i}\right) - \boldsymbol{G}\left(\boldsymbol{m}^{(n)}\right)}{\Delta H_{i}} \tag{1.91}$$

Yet, this is not enough to ensure a positive definite Hessian approximation. A way around that is to approximate directly the inverse of the Hessian matrix at every iteration in such a way so that a symmetric positive definite matrix is always secured. The most popular update formulas are Broyden–Fletcher–Goldfarb–Shanno (BFGS), Davidon–Fletcher–Powell (DFP), and Broyden's method [341].

Levenberg–Marquardt Method

Also known as the Damped Least-Squares method, The Levenberg–Marquardt method is an improvement of Newton's method, which means that in many cases, it finds a solution even if it starts very far off the final minimum. It is used in many software applications for solving curve-fitting problems. However, like other iterative optimization algorithms, the algorithm finds only a local minimum, which is not necessarily the global minimum. The update in parameters $\boldsymbol{\delta}_{\mathrm{m}}$ is computed by solving a system (similar to Eq. 1.90)

$$\left(\boldsymbol{H}^{(n)} + \lambda_{\mathrm{LM}} \boldsymbol{I}\right) \boldsymbol{\delta}_{\mathrm{m}}^{(n)} = -\boldsymbol{G}^{(n)} \quad \lambda_{\mathrm{LM}} \geq 0 \tag{1.92}$$

where the damping multiplier λ_{LM} is chosen so that $\left(\boldsymbol{H}^{(n)} + \lambda_{\mathrm{LM}} \boldsymbol{I}\right)$ is positive definite. There are many strategies to set the damper on the basis of theoretical arguments, such as *delayed gratification*. It consists of increasing the parameter by a small amount for each uphill step (increasing $\mathcal{J}$) and decreasing it by a large amount for each downhill step (decreasing $\mathcal{J}$). The idea behind this strategy is to avoid moving downhill too fast at the beginning of optimization, restricting the steps available in future iterations and therefore slowing down convergence [342].

1.4.2.3 Constrained optimization

In this type of optimization, constraints $\mathcal{J}_c$ that are required to be satisfied are added to the statement Eq. (1.85):

$$\begin{aligned}
\text{minimize} \quad & \mathcal{J}(\boldsymbol{m}) \quad && \boldsymbol{m} \in \mathbb{R}^{N_m} \\
\text{subject to} \quad & \mathcal{J}_{ci}(\boldsymbol{m}) = c_i \quad && i \in E, \quad c \in \mathbb{R} \\
& \mathcal{J}_{cj}(\boldsymbol{m}) \leq d_j \quad && j \in I, \quad d \in \mathbb{R}
\end{aligned} \tag{1.93}$$

E and I are sets of equality and inequality constraints. Many constrained optimization algorithms can be adapted to the unconstrained case, often *via* a penalty method. However, search steps taken by the unconstrained method may be unsuccessful for the constrained problem, leading to a lack of convergence [343]. For elementary problems, the *substitution method* can be carried out but not for such complex problems case, as in FEMU models. In this method, one would solve the constraint equation for one of the variables and substitute the latter in the cost function to be minimized. We introduce in this section two common methods of constrained optimization: *penalty* and *Lagrange multiplier* methods.

Penalty Method

In the penalty method, the constrained optimization problem (Eq. 1.93) is replaced by a series of unconstrained problems whose solutions ideally converge to the solution of the original constrained problem. The new formulation includes new additive terms, called penalty function $\mathcal{I}$, multiplied by the penalty coefficient k_p [344]. The problem is formulated as

$$\text{minimize} \quad \mathcal{J}(\boldsymbol{m}) + k_p \sum_{j \in I} \mathcal{I}(\mathcal{J}_{cj}(\boldsymbol{m})) \tag{1.94}$$

with the measure of violation of the constraints

$$\mathcal{I}(\mathcal{J}_{cj}(\boldsymbol{m})) = \max(d_j, \mathcal{J}_{cj}(\boldsymbol{m}))^2 \tag{1.95}$$

The violation measure is non-zero when the constraints are violated and is zero in the cases where constraints are not violated. Because of the non-differentiability of the penalty functions, the objective function can be approximated by a continuous function if the user prefers using gradient-based optimization techniques. Conversely, direct search, such as Simplex, can be incorporated into the minimizer. As for k_p, it is set to be larger for each iteration. Therefore, the constraint violations are severely penalized, thereby forcing the minimizer of the penalty function closer to the feasible region for the constrained problem.

Lagrange Multiplier Method

If the constrained problem has only equality constraints, the method of Lagrange multipliers, where we introduce a new variable Λ called a Lagrange multiplier, can be used to convert it into an unconstrained problem.

Suppose the constrained problem has only equality constraints. In that case, the method of Lagrange multipliers, where we introduce a new variable, Lagrange multiplier Λ, can be used to convert it into an unconstrained problem.

$$\text{minimize } \mathcal{L}(\boldsymbol{m}, \Lambda) = \mathcal{J} + \sum_{i \in E} \Lambda_i \mathcal{J}_{ci}(\boldsymbol{m}) \tag{1.96}$$

whose number of variables is the original number of variables plus the original number of equality constraints. The Lagrange multiplier theorem states that at any local optimum of the function evaluated under the equality constraints, the gradient of $\mathcal{L}$ (to find the stationary points) can be expressed as a linear combination of the gradients of the constraints, with the Lagrange multipliers acting as coefficients [345]. Thus, all partial derivatives should be null, including the partial derivative with respect to Λ. To summarize

$$\nabla_{m_1, \dots, m_{N_p}, \Lambda} \mathcal{L}(m_1, \dots, m_{N_p}, \Lambda) = \boldsymbol{0}, \quad m_i(i = 1, \dots, N_p) \in \boldsymbol{m} \tag{1.97}$$

This unconstrained system can be solved using gradient-based optimization algorithms, such as Newton or Levenberg-Marquardt methods. A more direct method can be applied to deal with both equality and inequality constraints, named Sequential Quadratic Programming (SQL). It consists of solving iteratively subproblems in which the objective function is approximated to a quadratic function, and

the constraints functions are linearized. Practically, at every iteration n, the Lagrangian function is approximated by Taylor series expansion. For one equality constraint, it writes

$$\boldsymbol{\nabla}\mathcal{L}\left(\boldsymbol{m}^{(n)} + \boldsymbol{\delta}_{\mathrm{m}}, \Lambda^{(n)} + \delta_{\Lambda}\right) \approx \boldsymbol{\nabla}\mathcal{L}\left(\boldsymbol{m}^{(n)}, \Lambda^{(n)}\right) + \boldsymbol{\nabla}^2\mathcal{L}\left(\boldsymbol{m}^{(n)}, \Lambda^{(n)}\right)\begin{pmatrix}\boldsymbol{\delta}_{\mathrm{m}} \\ \delta_{\Lambda}\end{pmatrix} \quad (1.98)$$

As a result, the change in parameters $\boldsymbol{\delta}_{\mathrm{m}}$ and δ_{Λ} are calculated by solving the following stationary problem

$$\left(\boldsymbol{\nabla}^2\mathcal{L}\left(\boldsymbol{m}^{(n)}, \Lambda^{(n)}\right)\right)\begin{pmatrix}\boldsymbol{\delta}_{\mathrm{m}} \\ \delta_{\Lambda}\end{pmatrix} = -\boldsymbol{\nabla}\mathcal{L}\left(\boldsymbol{m}^{(n)}, \Lambda^{(n)}\right) \quad (1.99)$$

1.4.3 Stochastic Optimization

Stochastic optimization (SO) includes randomness in the search procedure. The randomness may appear in variables, objective functions, and constraints if possible. Some stochastic optimization methods use random iterates to solve stochastic problems [346]. Compared to deterministic optimization methods:

- Their mathematical formulation is less complicated than deterministic optimization. For example, the calculation of the derivatives is not needed.

- They allow global optimization to be performed as the randomness of the sampling can attain better sets beyond local minima.

- In some methods, such as Bayesian inference, the uncertainty is estimated as well.

- They are easy to implement in the case of multi-objective optimization.

Conversely:

- They contain randomness in the search procedure, thus no exact identification.

- They have a much slower convergence towards the optimum solution.

- Their computation costs are enormous.

1.4.3.1 Evolutionary Algorithms

SO algorithms could be classified into different families, to cite the most popular: Evolutionary Algorithms (EA). EA methods aim at emulating the evolution of species through successive generations of better-performing individuals by natural selection according to Darwin's theory [347]. It is the most important category of stochastic optimization together with the genetic algorithm. The main steps of the EA approach are [335]:

- Initialization: the initial population $\boldsymbol{m}^{(0)}$ is created and evaluated.

- Mutation and cross-over: a mutant individual $\tilde{m}_i^{(n)}$ is created randomly for each individual in the actual population $\boldsymbol{m}^{(n)}$ and combined with, creating a parent-child link, namely, the trial individual.

- Evaluation: the fitness of the trial individual is assessed.

- Selection: the best between the trial individual and its parent is selected to survive to the next generation $\boldsymbol{m}^{(n+1)}$.

Steps 2 to 4 are repeated until reaching convergence. Different techniques for mutation, evaluation, and selection are possible. For instance, genetic algorithm (GA), evolutionary programming (EP), evolution strategy (ES), *etc.*

1.4.3.2   Bayesian Inference

Bayesian approaches are particular stochastic methods that rely on prior expert knowledge to build the inverse problem by constraining the search space for material parameters. Once incorporated into the inverse solver, it has two major roles: parameter estimation and model selection. Parameter estimation of a given model's parameters is often carried out using standard sampling methods e.g. Markov Chain Monte Carlo (MCMC) [348]. Model selection, on the other hand, deals with the evidence for each candidate mathematical model to approximate a particular observed dataset.

In practice, the Bayesian inference provides the posterior probability density with the information of the prior density (primary knowledge about material parameter) and error in model and/or measurement. In other words, the framework allows estimating the parameter values and their uncertainties simultaneously. Even so, FE-based inverse solvers with MCMC sampling has a high computational cost, requiring the full computation of the forward solver at least 10^4 times. This method has been recently employed in mechanics to assess the material parameter in more than one study [292,349–356].

1.4.4   Application to Skin Identification

After briefly introducing the concept of the most used optimization process, we describe their application to some mechanical characterization studies to identify the material parameters of human skin from *in vivo*, *in vitro*, *in situ*, and *ex vivo* experiments.

1.4.4.1   Non-structural Approach

Identifying the parameters of skin samples have been classically performed directly from the stress-strain curve, alternatively stress-stretch curve, to solve complex mechanical models. The use of the force-displacement curve is reliable since theoretical cross-section assumptions are unnecessary. This approach is simple and does not require sophisticated tool, as geometry of samples is not considered. The use of stress-strain data can be fruitful and accurate when the characterization experiment is carried out on isolated samples, *i.e.*, *in vitro* and *ex vivo*. Because of the nature of the load, the stress-strain data from *in vivo* in-plane tensile tests can also be exploitable to identify the parameters directly. However, in cases where the structure of the experiment was involved in the mechanical response, the material parameters were estimated according to simplified models (over different assumptions). This may explain the high variability in stiffness parameter, Young's modulus, $E = [1 \text{ kPa}, 57 \text{ MPa}]$, calibrated in dozens of studies [30, 357, 358].

Tangent Method
Regarding the evolution of the stress-strain curve of the skin in (Fig. 1.24), the tangent of the curve at the toe region can be interpreted as the initial stiffness of the skin with a weak contribution of the collagen, whereas the tangent at the linear region represents mainly the stiffness of the collagen fibers. The two coefficients are, respectively, minimal and maximal values of E, denoted by $E_{\min}$ and $E_{\max}$. In this case, the material is modeled as bi-linear elastic, and the stress-strain relation obeys Hooke's law with Young's modulus of $E_{\min}$. When the strain passes the heel region, the material responds to the strain linearly with the new Young's modulus of $E_{\max}$ [162]. A summary of bi-linear model parameters is presented in Table 1.3.

Model Fitting
Several theoretical models have been developed and coupled with experiments to characterize rubber-like materials (including skin). The built models would simulate one or many aspects at once, such as nonlinearity, anisotropy, and viscoelasticity, but not the shape of the studied material. The parameters

Table 1.3: Identified parameters of bi-linear equivalent model.

Anatomical site	Experiment	$E_{\min}$ MPa	$E_{\max}$ MPa	Reference
Abdomen	*in vitro* uni-axial	0.1	18.8	[359]
Arm	*in vivo* uni-axial	$0.047 - 0.048$	$0.258 - 0.608$	[106]
Back	*in vitro* uni-axial	0.54	112.47	[81]
Back	*in vitro* bulge	0.73	13.86	[193]
Breast	*in vivo* uni-axial	$1.02 - 1.41$	N/A	[129]
Calf	*in vivo* uni-axial	0.3	20	[131]
Forearm	*in vivo* suction	$0.102 - 0.218$	N/A*	[176]
Forearm	*in vivo* suction	$0.041 - 0.131$	$0.187 - 0.365$	[162]
Forearm	*in vivo* uni-axial	$0.121 - 0.493$	N/A	[135]
Forehead	*in vivo* suction	$0.121 - 0.431$	N/A*	[176]

*In linear curve, the stiffness remains constant during the load, $E_{\min} = E_{\max}$.

are identified through inverse problem methods, where optimization systems are solved analytically or numerically. To cite an example; a mathematical model linking material properties of skin layers to measurement data of indentation test has been developed based on the Hertz contact theory [360]:

$$F_I = \frac{4E_r r_I^3}{R_{\mathrm{si}}} \tag{1.100}$$

F_I is the load applied to provide the resulting indentation, R_{si} is the radius of the spherical indenter, and r_I is the contact radius of the indenter on the material being tested. The reduced elastic parameter is expressed as function of Young's modulus E, Poisson's ratio v and indenter's Young's modulus E_I

$$E_r = \left(\frac{1 - v^2}{E} + \frac{1 - v^2}{E_I} \right)^{-1} \tag{1.101}$$

This method can evaluate the elastic loading response but does not cover the conditions in which skin exhibits strongly nonlinear mechanical behavior. For this, the Ogden model was utilized (1.53). The parameters of both Hertz and Ogden models were computed through data fitting by a nonlinear regression method in MATLAB®(Sec. 1.4.2.2). Figure 1.31 shows data fitting results of experimental data with the two models for different indenter size, whose identified parameters can be retrieved from [360]. The indentation displacement is equal to $r_I^2/R_{\mathrm{si}} \left[1 - 2/3 \left(r_{I0}/r_I \right)^{3/2} \right]$, with r_{I0} the contact radius at zero load. In Table 1.4, a non-exhaustive list of skin models is presented with their different relative identified parameters. By confronting Young's modulus in different experiments and models, one may notice that its variation is huge, from 1 kPa to 1 MPa. In fact, many assumptions and hypotheses formulated in these studies may lead to apparent elastic moduli but not the real ones. It is still not a deadlock for researchers since the method can be used to compare stiffness between many subjects in the same experimental conditions.

1.4.4.2 FEMU Approach

Stretching a T-shaped sample would have a different mechanical response than an I-shaped sample. When considering the tested material's geometry, the analytical models are not precise in simulating the real behavior. Therefore, using numerical simulation methods is a must in this case. The most used one in characterizing a soft tissue material is Finite Element Model Updating method.
The major advantage of this approach is the identification of every possible mechanical parameter in regions that are difficult to access; or in unstable medium where the uncertainty is high, especially for materials undergoing large deformations. Moreover, it is widely used in topology optimization. In
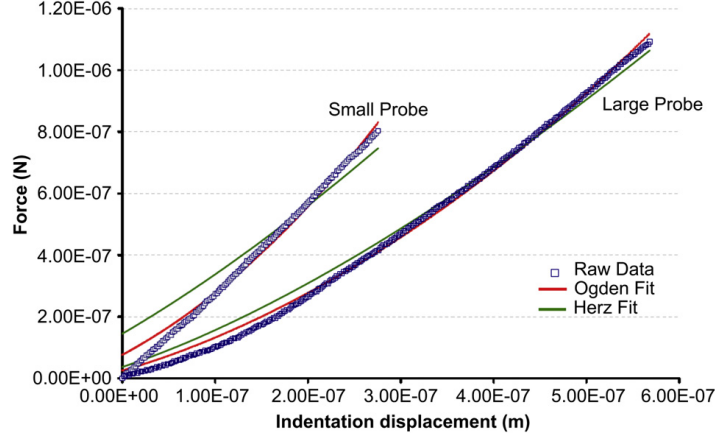
Figure 1.31: Fitting of indentation test data with Ogden and Hertz model [360].

Table 1.4: Identified parameters of non-structural skin models from *in vivo* experiments.

Experiment	Model	Identified parameters	Ref.
- Torsion - Forearm	$E = \frac{2T_T(1+\nu)}{4th_sR_d^2\theta_T}$ T_T: torsion th_s: skin thickness R_d: radius of disk θ_T: rotation angle	$E = 0.026 - 0.107$ MPa $E_{\text{collagen}} = 100 \times E$	[195]
- Torsion - Forearm	$E = \frac{T_T}{0.8\pi R_{d1}R_{d2}th_sUE}$ R_{d1}: inner torsion ring radius R_{d2}: outer torsion ring radius UE: immediate extensibility	$E = 0.42 - 0.85$	[196]
- Torsion - Forearm	$E = \frac{T_T}{0.8\pi R_{d1}R_{d2}th_sUE}$	$E = 1.1 - 1.32$ MPa	[49]
- Suction - Forearm	$P_S = \frac{4u_3th_s}{u_3^2+r_0^2}\left(\frac{E}{1-\nu}A(u_3) + \sigma_0\right)$ $A(u_3) = \left(\frac{u_3^2+r_0^2}{2r_0u_3}\right)\arcsin\left(\frac{2r_0u_3}{u_3^2+r_0^2}\right) - 1$ P_S: suction pressure r_0: suction area radius σ_0: initial stress u_3: out-plane displacement	$E = 0.04 - 0.22$ MPa	[177]
- Torsion - Uni-axial - Forearm	$G = \frac{T_T}{4\pi th_s\theta_T}\left(\frac{1}{R_{d_1}^2} - \frac{1}{R_{d_2}^2}\right)$ G: Shear modulus (torsion) E_1: along Langer's line (uni-axial) E_2: across Langer's line (uni-axial)	$E_1 = 1.1$ MPa $E_2 = 0.34$ MPa $G = 0.021$ MPa	[128]
- Indentation - Leg	$E = \frac{1-\nu^2}{2r_I\kappa_I}\frac{F_I}{u_3}$ $\kappa_I(\nu, r_I/th_s)$: scaling factor	$E = 10.4 - 89.4$ kPa	[171]
- Indentation - Forearm	Neo-Hookean (1.50) $E = 2\mu_0(1+\nu)$	$\mu_0 = 1.598$ kPa $E = 4.794$ kPa	[167]
- Multi-axial - Abdomen	Hookean orthotropic [361] $\nu_{12}/E_1 = \nu_{21}/E_2$ ν_{12}: along Langer's line ν_{21}: across Langer's line	$E_1 = 5.702$ Nm/g $E_2 = 3.421$ Nm/g $\nu_{12} = 0.498$ $\nu_{21} = 0.299$ $G = 0.95$ Nm/g	[18]

contrast, the process is limited by computation performance, cost, and environmental issues [362].

Regarding human skin, the FEMU was applied in many studies during the last decades. Despite the need for geometry modeling, the use of FEMU was motivated by the fact that hyperelastic models are the most precise in mimicking the skin deformation, which are hard to solve analytically. A summary of some FEMU-based parameter identification studies is exposed in Table 1.5.

In the next chapter, we will present a FEMU-based framework implemented in an open-source code to identify the parameters of a bi-material soft tissue subjected to the uni-axial tensile test. It has been developed by a colleague, Danas Sutula, then corrected and validated by myself. Through this numerical tool, we aim to assess the parameters of a keloid scar and healthy-skin from a specific dataset.

Table 1.5: Overview of FEMU-based inverse method results in the literature.

Experiment	Constitutive law	Optimization method	Identified values	Ref.
- Multi-axial - Forearm	Tong and Fung [363] $\psi_{TF} = \frac{1}{2}(\alpha_{TF1}\varepsilon_{11}^2 + \alpha_{TF2}\varepsilon_{22}^2)$ $\quad + \frac{C_{TF}}{2}\exp(a_{TF1}\varepsilon_{11}^2 + a_{TF2}\varepsilon_{22}^2)$ ε_{11}: strain along Lange's line ε_{22}: strain across Lange's line	Nonlinear Least Square	$\alpha_{TF1} = 58.45$* $\alpha_{TF2} = 74.38$* $C_{TF} = 5.8\ 10^{-6}$* $a_{TF1} = 54.60$ $a_{TF2} = 150.49$	[146]
- Uni-axial - Forearm	Lanir's model [364] $\boldsymbol{\sigma} = J^{-1}\int_0^\pi\left(R(\theta)K_c(\lambda-1)\boldsymbol{F}\frac{\partial\lambda}{\partial\boldsymbol{E}}\boldsymbol{F}\right)d\theta - p\boldsymbol{I}$ $R(\theta) = 1/\pi + C_L(\cos^4(\theta-\phi) - 0.375)$ K_c: collagen stiffness C_L: anisotropy parameter ϕ: Langer's orientation	Constrained maximum-likelihood [365]	$K_c = 46$ MPa $C_L = 0.58$ $\phi = 18.85°$	[133]
- Uni-axial - Forearm	Hookean orthotropic	Levenberg-Marquardt	$E_1 = 146$ kPa $E_2 = 40$ kPa $G = 14$ kPa $\nu_{12} = 0.226$ $\phi = 37.57°$	[141]
- Suction - Forearm	Extended Mooney $\psi_{EM} = C_1(I_1 - 3) + C_2(I_1 - 3)(I_2 - 3)$ $E = 6C_1$	Sequential quadratic programming	$C_1 = 9.4$ kPa $C_2 = 82.0$ kPa $E = 56.4$ kPa	[178]
- Indentation - Forearm	Hookean isotropic	Extended Kalman Filters [366]	$E = 5.67$ kPa $\nu = 0.48$	[367]
- Indentation - Forearm	Jamus-Green-Simpson [368]	Newton	$C_{10} = 5.4$ kPa $C_{01} = 5.7$ kPa $C_{11} = 18.6$ kPa $C_{20} = 11.7$ kPa $C_{30} = 19.6$ kPa	[163]
- Indentation - Forarm	Neo-Hookean (1.50) $E = 4\mu(1 + \nu)$	Nelder-Mead simplex (NMS) [340]	$E = 0.43$ MPa	[164]
- Uni-axial - Forearm	Ogden one-term (1.53)	NMS coupled with stochastic method	$\mu_p = 10$ Pa $\alpha_p = 26$	[136]
- Uni-axial - Upper arm	Ogden one-term	Trust-region	$\mu_p = 9.6$ kPa $\alpha_p = 35.94$	[139]
- Suction - Face	Rubin and Bodner [369] (15 parameters) $\psi_{RB} = \frac{\mu_0}{2q}(e^{qg})$ $g = g(m_2, \Gamma_1, \Gamma_2, r_2)$	NMS	$\mu_0 = 86$ kPa $q = 39.74$ $m_2 = 0.027$ $\Gamma_1 = 1.34$ Hz $\Gamma_2 = 67.3$ $r_2 = 6.91$	[185]

* Unity not mentioned

Chapter 2

Bi-material Mechanical Characterization: Inverse Problem

As described in the Outlines section, Chapters 2, 3, and 4 belong to a project that addresses the mechanical characterization of a heterogeneous material undergoing large deformations. In view of the motivations of the *BiomecaT* team from FEMTO-ST, this material consists of a partial plane surface of human skin with a keloid tumor. The project's final objective is to provide a patient-specific scientific-based numerical pipeline to help the surgeon predict the privileged direction of keloid growth to prevent it. The inputs are in the form of experimental data acquired from the *in vivo* uni-axial tensile test and the 3D shape of the tumor. On the other side, the outputs are tension and shear stress fields. The latter will assist the surgeon in calibrating his medical solution to the patient's skin behavior. This chapter concisely describes the components and operations of this methodology and the hypotheses formulated given physical conditions and circumstances. Based on FEMU, the numerical methodology has been implemented in FEniCS and was used to identify the material parameters of the two media, the keloid, and the surrounding healthy-skin, by fitting the experimental data. It was baptized SofTI (Soft Tissue Identification) and is available for free for the community: `https://github.com/aflahelouneg/inverse_identification_soft_tissue` Besides, the validation of the forward problem, *via* a commercial software, and the inverse solver, using perfectly known synthetical data, will be reported in this chapter.

2.1 Methodology

The way the framework is designed can be used to characterize any soft tissue material under the condition that the experiment is performed identically to the presented study. One could imagine the whole keloid characterization process patient-to-clinical-solution occurs with the following main steps (Fig. 2.1). In the beginning, the 3D shape acquired for living keloid, a Computer-Aided Design (CAD) modeling is carried out to represent the tumor numerically, which is transformed into a 2D mesh for simulations. Afterward, a uni-axial stretch experiment takes place on a plane patient's skin surface. The resulting data are eventually filtered and converted into compatible data. By inserting the latter in SofTI, the optimal parameter set for keloid and healthy-sin is identified and then employed to simulate the stress field, given the natural tension in the skin. Consequently, the surgeon will have clues about the specifications of a customized medical device to confine keloid growth or prevent it. Every step in the introduced methodology is thoroughly described and supported with a real keloidic case presented in the study of Chambert *et al.* [106].

2.1.1 Geometrical Model

Prior to my thesis project, Marco Sansale, a former Master student in ISIFC (Institut supérieur d'ingénieurs de Franche-Comté), had worked on the FEM modeling of the keloid during his R&D
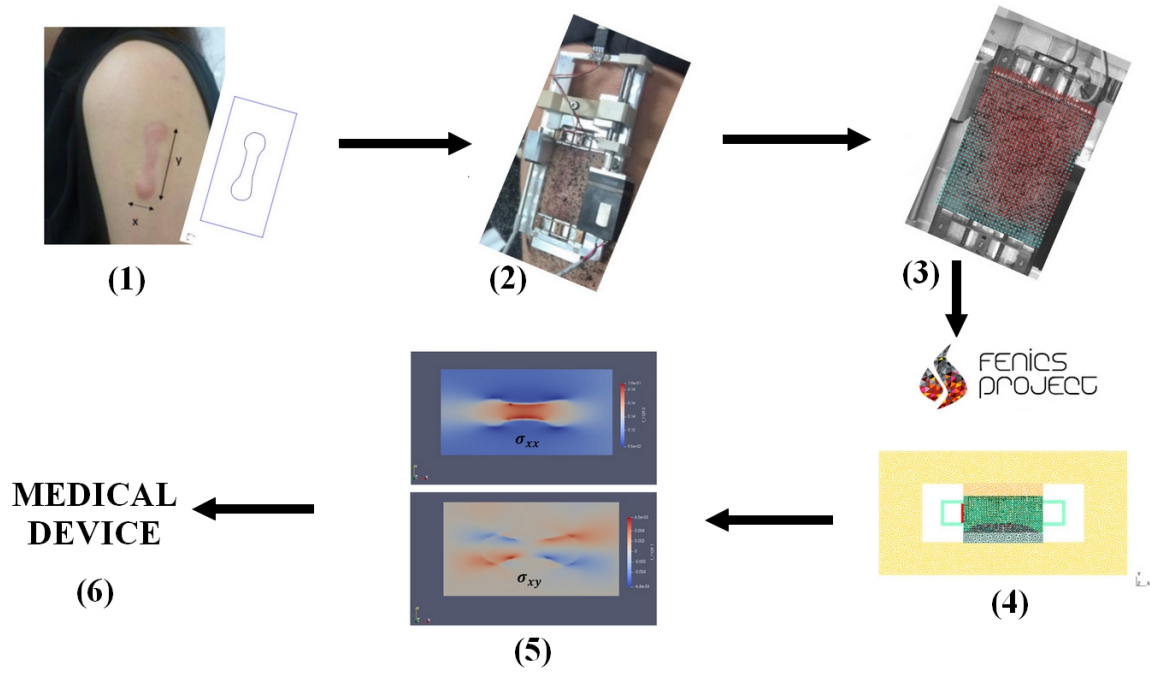
Figure 2.1: Patient-to-clinical-solution numerical pipeline [370]. (1): Keloid geometry model. (2) Uni-axial tensile test. (3) Data treatment. (4) FEMU-based material parameters identification. (5) Stress fields. (6) Clinical solution to prevent keloid growth.

project. One of his significant contributions is providing a 3D points cloud of a patient's keloid using silicone.

2.1.1.1 3D Shape Acquisition

Figure 2.2 exhibits a print of butterfly-shaped keloid carved into a silicone-made mold. An optical 3D surface measurement, with a resolution of 14μ m, and designed by Bruker alicona [371], was applied to the mold to generate the inverse medium's 3D shape: the negative values corresponding to cavities depth are converted into positive values that represent the height of keloid's profile, with respect to the skin surface.

Figure 2.2: Keloid shape obtained by silicone-based molding. Retrieved from Sensale's report.

The 3D surface acquisition is based on the Focus Variation technique. Its operating principle combines an optical system's small depth of focus with vertical scanning to provide topographical information from the focus variation. As the distance between the sample in movement and the camera objective is varied, images are continuously captured. An algorithm is used to compute the position of each grid point uniformly mapped by analyzing the focus.

Focus Variation requires optics with very little depth of field and is adapted for surface metrology. In other words, it measures the waviness and roughness of samples. Regardless of the tool's high price, using it to measure deeper prints (inversely, more cambered tumors) is less reliable. Also, the captured boundary points are not aligned, which is the case in the real sample. I would suggest scanning the keloid's shape directly on the patient for better performance. Plenty of reliable, free, and user-friendly 3D scanning apps developed for a smartphone can secure it, such as *Spin Me Round*.

2.1.1.2 2D Model Generation

For ease, the full 3D shape is reduced to a 2D geometrical model (the integration of the full 3D model will be investigated in Section 3.4). For that, an STL (Standard Tessellation Language) file, containing the out-plane coordinates of a uniformly-mapped grid, is read by the free open-source Blender [372] (Fig. 2.3a). The shape imported as a CAD model (alternatively mesh) is oriented manually and set to the origin because the raw shape boundaries are not aligned. In order to extract the 2D form, a cross-section plane is generated and oriented perpendicular to the skin surface. As a result, the CAD model is split into two materials: keloid and healthy-skin (Fig. 2.3b). Therefore, the boundary between the two materials is defined such that the internal surface represents the keloid and the external, the surrounding healthy-skin.
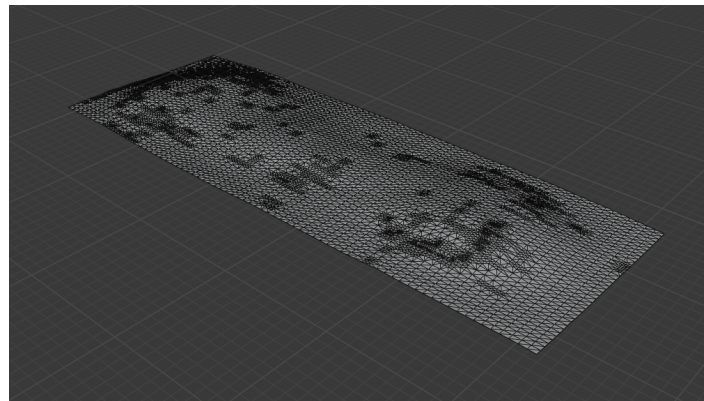
(a) Raw 3D shape
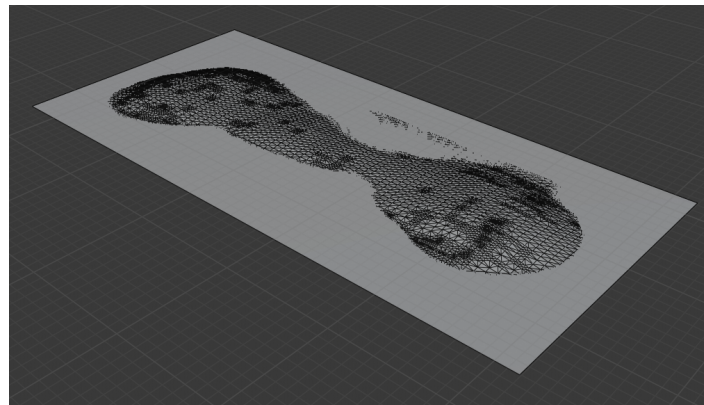
(b) Extracted 2D shape

Figure 2.3: 2D model extraction from 3D keloid shape.

At this level, the interface boundary is considered to be well-established. Nevertheless, in reality, keloid shape detection is imprecise. Considering this element while characterizing the material, the interface keloid/healthy-skin is implicitly represented using a level-set method [373]. An optimal regularization parameter can determine the location and approximate shape of material subdomains in the presence of topological uncertainties [374]. Having said that, using the full 3D information remains the most reliable way to represent the problem, but at the cost of computation. It is eventually beyond the CPU (Central Processing Unit) limits.

2.1.2 Experimental Data

As discussed in Section 1.4, the ill-posedness in inverse problems can be tackled by diversifying reference data types. Combining at least two independent sources of information helps reduce the uncertainty of the identified parameters since the latter may strongly correlate with each data type. In our situation, and given the material within our reach, we collected the data of force displacement (FD) and displacement full-field, denoted, respectively, $\boldsymbol{u}_{\mathrm{msr}}$ and $\boldsymbol{f}_{\mathrm{msr}}$. Moreover, following the structural-based approach in identifying the material parameters, the FEM model in the forward problem should include the experiment design. Hence, the link between the apparatus and the data will be emphasized. Before that, we need to introduce the device used to stretch the specimen *in vivo* and capture the deformation.

2.1.2.1 Uni-Axial Extensometry

A home-made ultra-light extensometer for stretching soft tissues *in vivo*, presented in Figure 2.4, has been developed by Jacquet *et al.* [142] (the technical details are listed in Table 2.1). It was conceived so that only the pads are in contact with the tested area with a large visible zone that permits simultaneous image recording. The motion of the moving pad with respect to the fixed pad results in a uni-directional stretch, and it is provided by an electric motor *via* a screw-nut mechanism. A linear variable displacement transducer (LVDT) controls the moving pad displacement. Even though the pad position is measured with a sensor, it is assumed to be exact. Each square pad is surrounded by a "U-shaped" (moved together) to protect the measuring zone from peripheral forces. The force sensor consists of beams made in bronze-beryllium equipped with strain gauges (Fig. 2.4b), whose deformation is converted into a reaction force measurement. It should be noticed that the initial distance between pads, namely, L_{IP0}, is not fixed. The user needs to measure it before any stretch operation. Because stability is crucial, L_{IP0} is assessed after setting the pads on non-draggable zones. This maneuver is key for a reproducible experiment.

Table 2.1: Technical sheet of the tensile device.

Weight	36 g
Square pad side: S_P	8 mm
U-shaped pad length: L_P	24 mm
U-shaped pad width: W_P	17 mm
Extensometer length: L_E	100 mm
Extensometer length: W_E	40 mm
Force accuracy	5 mN
Observable area limits	45×24 mm^2

2.1.2.2 Displacement Field

Unlike FD curves obtained directly from the device, the displacement fields are measured synchronously with a vision system. Thus, the recorded video is split into frames treated with the Digital Image Correlation technique (DIC). In the outputs, 2D uniform grids, with displacement vector,
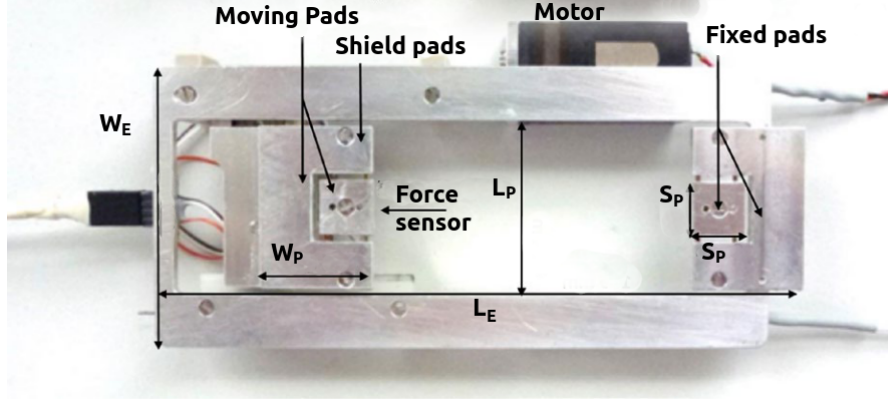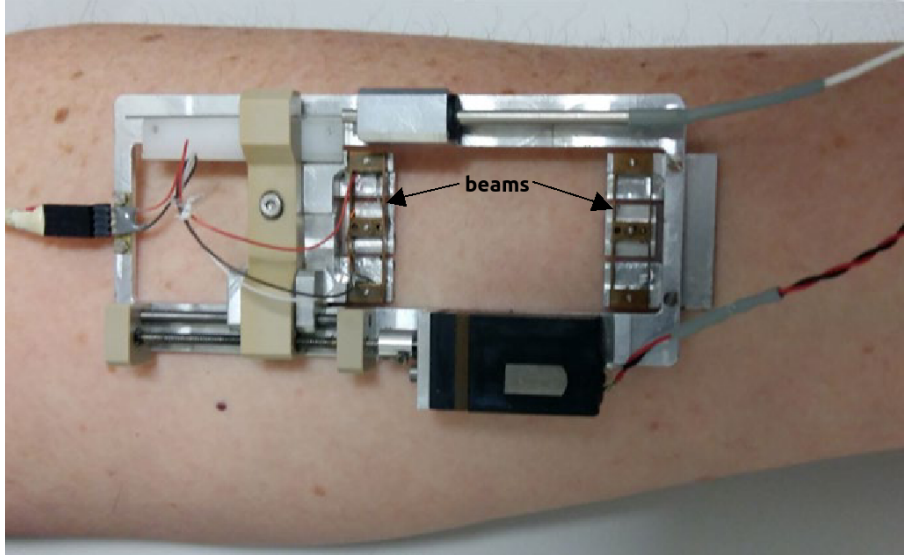
Figure 2.4: A ultra-light extensometer for uni-axial tensile testing. Modified from [142]. (a) The apparent front side is stuck on the skin surface. (b) Tensile test on the forearm.

$u_i = \{u_{1i}, u_{2i}\}$ expressed on each node i in a Cartesian referential, are retrieved. The DIC tool implemented in the framework is based on the optical flow method, where the relative displacement of an object between two successive frames is estimated. A graphic free open-source Python library, `OpenCV` [375] (Computer Vision), has been chosen for that. In Figure 2.5, a characteristic parameter a_W of the correlation process is annotated. It represents the side of a square correlation window centered on every grid node G_p. A second parameter, d_G, representing the step size between grid points, is also considered in displacement measurement. The two parameters are to be calibrated from an optimization error procedure.

The concept of optical flow was introduced by the American psychologist James J. Gibson in the 1940s to describe the visual stimulus provided to animals moving through the world [376]. The method is based on two essential assumptions:

- The pixel intensities of an object do not change between consecutive frames.

- Neighboring pixels have similar motion.

Let us consider a pixel $p(x, y)$ moving between two successive frames by $\Delta x, \Delta y$. As its intensity does not change, the brightness constancy constrain is given as follows
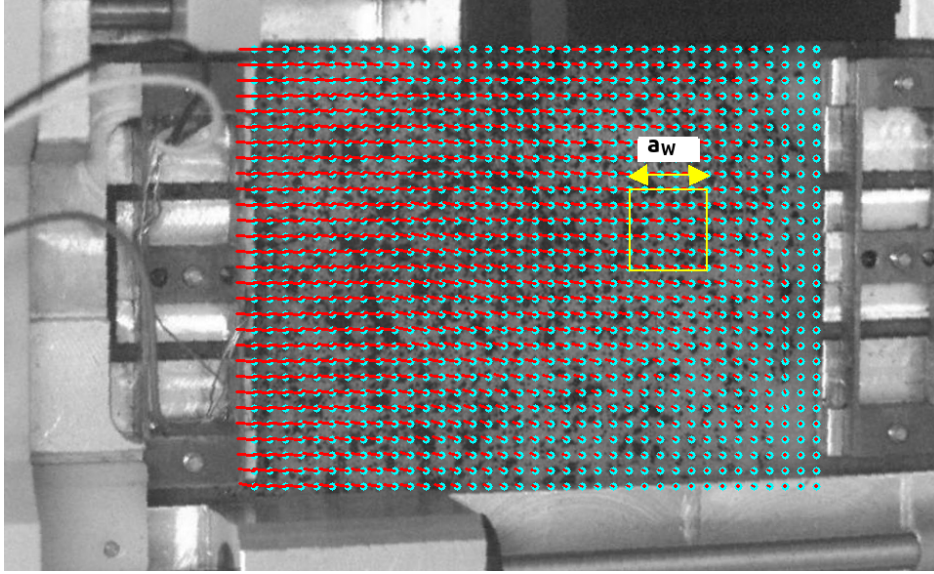
Figure 2.5: DIC application to video frames of the uni-axial tensile.

$$I(x, y, t) = I(x + \Delta x, y + \Delta y, t + \Delta t) \tag{2.1}$$

t and Δt are pseudo-time and its variation. Suppose small displacement theory, the equation above in terms of the Taylor series is given by

$$I(x + \Delta x, y + \Delta y, t + \Delta t) = I(x, y, t) + \frac{\partial I}{\partial x}\Delta x + \frac{\partial I}{\partial y}\Delta y + \frac{\partial I}{\partial t}\Delta t \tag{2.2}$$

Therefore, replacing (2.2) in (2.1) results in:

$$\frac{\partial I}{\partial x}\frac{\Delta x}{\Delta t} + \frac{\partial I}{\partial y}\frac{\Delta y}{\Delta t} + \frac{\partial I}{\partial t} = 0 \tag{2.3}$$

By considering the velocities V_x and V_y, as temporal derivatives of Δ_x and Δ_y, respectively, and the brightness derivatives I_x, I_y, I_t, the optical flow equation is obtained,

$$I_x V_x + I_y V_y + I_t = 0 \tag{2.4}$$

With two unknown variables, this single equation cannot be solved directly. The latter is known as the aperture problem of the optical flow algorithms. Several methods based on partial derivatives of the image signal are provided to solve this problem: Lucas-Kanade method [377], Horn–Schunck method [378], and many others [379]. The former is included in `OpenCV`, and is widely used to track motions [377]. The Lucas-Kanade method assumes that the displacement is approximately constant within a neighborhood of $G_\mathrm{p}(x, y)$. The optical flow equation can be assumed to hold for all $q_i(x, y)$ pixels within a window centered at G_p:

$$I_x(q_1)V_x + I_y(q_1)V_y = -I_t(q_1)$$
$$I_x(q_2)V_x + I_y(q_2)V_y = -I_t(q_2)$$
$$\vdots$$
$$I_x(q_n)V_x + I_y(q_n)V_y = -I_t(q_n)$$

The resulting linear system (in the form of $Av = b$) is usually over-determined as it has more equations than unknowns. The Lucas–Kanade method obtains a trade-off solution by the least squares method by solving system $v = (A^T A)^{-1}A^T b$:

$$\begin{bmatrix} V_x \\ V_y \end{bmatrix} = \begin{bmatrix} \sum_i I_x(q_i)^2 & \sum_i I_x(q_i)I_y(q_i) \\ \sum_i I_y(q_i)I_x(q_i) & \sum_i I_y(q_i)^2 \end{bmatrix}^{-1} \begin{bmatrix} -\sum_i I_x(q_i)I_t(q_i) \\ -\sum_i I_y(q_i)I_t(q_i) \end{bmatrix} \qquad (2.5)$$

2.1.3   Forward Problem

A FEM model has been built to simulate the experiment accordingly to the accessible information (measurements and commands) (Fig. 1.29). From the inputs: (i) material parameters, and (ii) boundary conditions, it provides the outputs: (i) displacement fields, and (ii) reaction forces.

2.1.3.1   Assumptions

With this, we state the assumptions followed to build a solvable problem as representative as possible. Besides considering the quasi-static state (by neglecting the viscoelasticity contribution for low stretch rate), several aspects are discussed.

Bi-Material Behavior

Heterogeneous ST with abnormal shapes, *e.g.*, keloids, ulcers, or brain tumors, may be modeled as materials with two domains of different mechanical responses. However, common components with high mechanical contribution are well present in both parts, making the latter similar. In the keloid/healthy-skin case, both structures are dominated by collagen fibers, but with differences in bundle diameter and orientation, [380]. Since the orientation of collagen fibers in keloids is random [381], the respective behavior law could be considered isotropic. It was stated in [380] that thicker collagen bundles are present in keloidal scars. That may explain why they are stiffer than healthy skin, as noticed in [106]. Therefore, the anisotropy effect in the healthy skin on the mechanical response of keloid could be neglected.

As a consequence, same isotropic constitutive law, but with different parameters, is assigned to the materials in the framework. Implementing different constitutive laws is always possible, but it was not investigated in the thesis. As introduced in Section 1.3.2.5, Gent model compatible with the limiting chain extensibility, occuring when stretching the skin *in vivo*, is a promising candidate to include non-linearities arising for small stretches, in accordance with the observations in [106]. Thus, the material parameters of the bi-material are: μ_k and J_{mk} for keloid, and μ_{hs} and J_{mhs} for the healthy-skin.

Plane Strain Condition

Counting for the 3D aspect in a novel FEMU methodology would lead to failures. Therefore, in the first step, the direct problem was reduced to a 2D FEM model. The choice of plane strain conditions was held for the following reason. The skin structure implies that the inner layer of skin is attached to muscles and subcutaneous tissues. In the case of in-plane stretch, the out-plane deformations, ϵ_{13}, ϵ_{23}, and ϵ_{33} are not significant compared to the total thickness. In the framework, the deformation gradient tensor is implemented as

$$F_{PS} = \begin{pmatrix} F_{11} & F_{12} & 0 \\ F_{21} & F_{22} & 0 \\ 0 & 0 & F_{33} \end{pmatrix} \qquad (2.6)$$

such that F_{33} is the out-plane component, and is expressed as $F_{33} = th_f/th_i$, where th_i and th_f denote, the thickness in the undeformed and deformed configurations, respectively [382]. One should notice that for plane strain condition, $F_{33} = 1$.

Reaction Force Equivalence

In a 2D FEM reduced model, the reaction force (RF) is derived from nodal displacement. It is intuitively equivalent to the integral of the normal stress σ_{xx} over Γ_{CS}, the cross-section of soft tissue tangent to the square pad side (Fig. 2.6). Using a full 3D model that includes the sensor structure is possible but has two limitations. Firstly, the sensor's geometry is so complex that only extreme fine mesh is used, which makes the computations very challenging regarding the performance limits of the computers. Secondly, to identify the parameters using gradient-based methods (with few iterations), the derivation of the force (deriving from the displacement field) with respect to the material parameters is calculated in all areas, including the sensor. The convergence of the optimization algorithm in this case may not be guaranteed. To overcome the latter limitation, the use of Simplex method (Sec. 1.4.2.1) is a suitable choice.
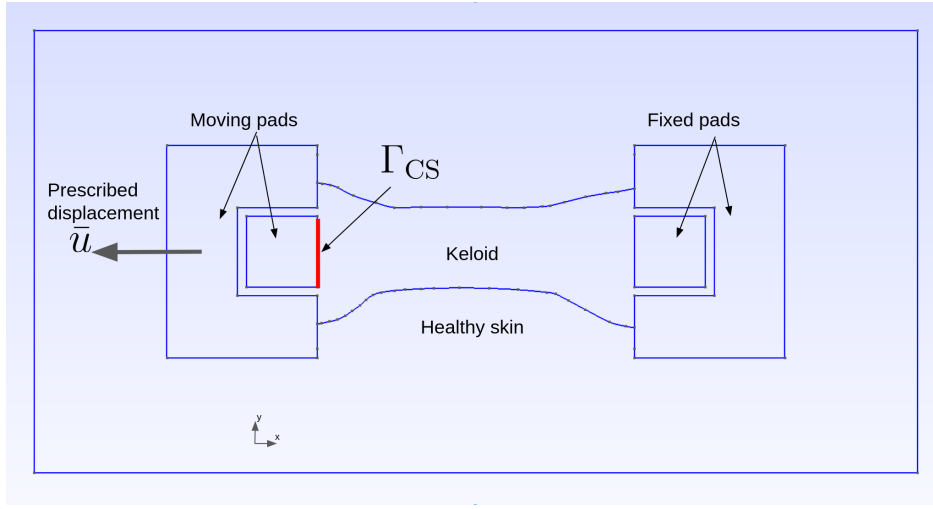
Figure 2.6: 2D equivalent model of the uni-axial extensometry.

2.1.3.2 Nonlinear FE-Model

The features of the forward nonlinear FEM solver are described in this section as follows: domain, boundary conditions (BC), and weak formulation. Later, we will expose their code excepts implemented via FEniCS libraries.

Domains

There are two types of a domain on which the functions are expressed and discretized, surface and edges. As for surfaces, they represent the volume occupied by the two materials in 2D. Hence, the global domain is divided into two sub-domains $\Omega = \{\Omega_k \cup \Omega_{hs}\}$, where k and hs denote keloid and healthy-skin, respectively. As illustrated in Figure 2.7, the blue dashed lines separate the healthy-skin domain into measurable and non-measurable sub-domains: Ω_{hs}^{msr} and Ω_{hs}^{unmsr}. Measurable areas will be used to fit the experimental displacement fields. Since the apparent keloid's surface between the pads is entirely measured, we introduce the measurable bi-material domain $\Omega^{msr} = \{\Omega_k \cup \Omega_{hs}^{msr}\}$. As for the edges, they represent in Figure 2.7 the boundaries of the moving pad Γ_{MP} (red frame) and the fixed pad Γ_{FP} (black frame). The outside boundaries are free of any displacement constraint. The white surfaces correspond to the rigid pads, they are not meshed because the deformations are null (thus null elastic energy).

Boundary Conditions

For each pseudo-time t_k, discretized in set of observation times $\{t_k\}_{k=0,1,...,N_E}$, the imposed boundary conditions on the pads are all of Dirichlet type: $\boldsymbol{u}(\Gamma_{MP}, t_k) = \bar{\boldsymbol{u}}(t_k)$ on the moving pad's edges
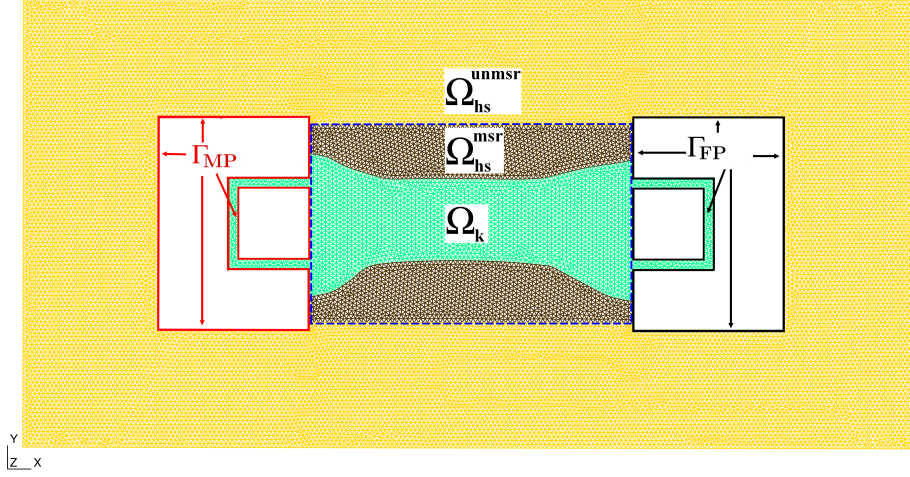
Figure 2.7: FE-model domains of the forward problem. The mesh contains 44 k cells and was performed with `Gmsh` [383]. Modified from [266].

and $\boldsymbol{u}(\Gamma_{\text{FP}}, t_k) = \boldsymbol{0}$ on the fixed pad's edges. Considering the quasi-static hypothesis, the forward problem is solved at each load step indicated by t_{k*} associated with every DIC frame and its relative displacement command. Although the measured displacement fields and $\bar{\boldsymbol{u}}(t_k)$ are independent, they are synchronized with each other through the assessment of the pad displacement with the DIC process.

Weak Formulation

Given the BC and the deformation configuration at t_k, the total elastic energy is expressed, in the absence of body and surface forces, as

$$\Pi(\boldsymbol{u}(t_k), t_k) = \int_{\Omega_{\text{k}}} \psi_{\text{k}}(\boldsymbol{u}, t_k)\, d\Omega + \int_{\Omega_{\text{hs}}^{\text{msr}} \cup \Omega_{\text{hs}}^{\text{unmsr}}} \psi_{\text{hs}}(\boldsymbol{u}, t_k)\, d\Omega \tag{2.7}$$

where ψ_{k}, respectively ψ_{hs}, is the strain energy density function related to keloid, respectively healthy-skin. It is a modified Gent function developed for nearly-incompressible materials (Eq. 2.8) [384]. Like other hyperelastic incompressible materials, the purely incompressible version of Gent's model (Eq. 1.52) cannot be implemented with basic elements in FE solvers. Because of the volumetric locking, which is the over-stiffening of elements when the material is incompressible (Poisson's ratio ν nearing 0.5), the solver fails to converge. The incompressibility of hyperelastic materials was successfully incorporated in FEniCS-based solver by involving the mixed displacement–pressure elements [385, 386]. During my thesis, incompressibility had been implemented for Gent's model, but it turned out that the inverse solver failed to identify the material parameters.

$$\psi_{\text{G}}^{\text{NI}} = -\frac{\mu}{2} \left(J_m \ln\left(1 - \frac{I_1 - 3}{J_m}\right) + 2\ln(J) \right) \tag{2.8}$$

At the equilibrium, the total potential energy is minimized for each t_k [225, 387]. Let us denote $\mathcal{U}(\Omega)$ the admissible displacement fields space that verifies the BC on Γ_{MP} and Γ_{FP}, and $\mathcal{V}(\Omega)$ the space of admissible variations $\boldsymbol{v}$ such that $\boldsymbol{v} = \boldsymbol{0}$ on $\Gamma_{\text{MP}} \cup \Gamma_{\text{FP}}$. Hence, for all admissible variations $\boldsymbol{v} \in \mathcal{V}(\Omega)$, the forward problem consists in finding the displacement field $\boldsymbol{u} \in \mathcal{U}(\Omega)$ solution of

$$L(\boldsymbol{u}; \boldsymbol{v}) = \boldsymbol{0} \quad \forall \boldsymbol{v} \in \mathcal{V} \tag{2.9}$$

whose weak formulation for the quasi-static equilibrium is the directional derivative of Π with respect to change in $\boldsymbol{u}$ in the direction of $\boldsymbol{v}$. It is given by

$$L(\boldsymbol{u}; \boldsymbol{v}) \approx \left. \frac{d\Pi(\boldsymbol{u} + \epsilon\boldsymbol{v})}{d\epsilon} \right|_{\epsilon \to 0} \tag{2.10}$$

Depending on the SEDF $\psi(\boldsymbol{u})$, $L(\boldsymbol{u}; \boldsymbol{v})$ can be nonlinear in $\boldsymbol{u}$. In such a case, the problem is solved using Newton's method, which has many benefits, like rapid convergence. However, it is essentially a local method. Its performance is satisfactory when the initial displacement vector is set near a solution.

The system above must be derived but not necessarily by hand. In FEniCS, we may find the module `dolfin` that automates the derivation. This automation of nonlinear solvers is key to modern computational tools. Despite that, it makes programming more accessible and eliminates potential errors due to hand-derived algorithms. Later in Section 2.2, we will show how the forward solver has been implemented in FEniCS and what are the accessible changes for users, for instance, modifying the SEDF and its parameter $\boldsymbol{m}$.

Model data

As outputs of the forward problem, we need two data types similar to the experiment outputs for fitting, displacement field, and reaction force. By solving the system in Eq. 2.9, a set of predicted nodal displacement is gathered at every time step t_k denoted by $\boldsymbol{u}_{\text{FE}}(t_k)$. While, for the predicted RF, it is computed in post-processing from $\boldsymbol{u}_{\text{FE}}$ by integrating the traction $\boldsymbol{t}$, resulting from the first Piola-Kirchhoff stress (Eq. 1.29), over the surface Γ_{CS} (Fig. 2.6)

$$\boldsymbol{f}_{\text{FE}}\left(\boldsymbol{u}_{\text{FE}}(t_k, \boldsymbol{m}), t_k\right) = \int_{\Gamma_{\text{CS}}} \frac{\partial \psi\left(\boldsymbol{u}_{\text{FE}}(t_k, \boldsymbol{m})\right)}{\partial \boldsymbol{F}\left(\boldsymbol{u}_{\text{FE}}(t_k, \boldsymbol{m})\right)} \boldsymbol{N} \, d\Gamma \tag{2.11}$$

In the undeformed configuration, $\boldsymbol{N}$ is the unit normal vector to the boundary surface Γ_{CS}. An alternative way to compute the traction vector is to use the Cauchy stress tensor and the unit normal vector $\boldsymbol{n}$ in the deformed configuration (Eq. 2.12) [227]. In the latter case, $\boldsymbol{n}$ must be determined from the deformed mesh with the boundary surface Γ_{d}

$$\int \boldsymbol{\sigma}\left(\boldsymbol{u}_{\text{FE}}\right) \boldsymbol{n} \, d\Gamma_{\text{d}} = \int \boldsymbol{P}\left(\boldsymbol{u}_{\text{FE}}\right) \boldsymbol{N} \, d\Gamma \tag{2.12}$$

2.1.4 Inverse Identification

After defining the structure and the functions of the direct problem, from BCs and material parameters $\boldsymbol{m}$ to $\boldsymbol{u}_{\text{FE}}$ and $\boldsymbol{f}_{\text{FE}}$, we present the methodology that leads to identify the material parameters in the reverse direction, from experimental data, $\boldsymbol{u}_{\text{msr}}$ and $\boldsymbol{f}_{\text{msr}}$, to $\boldsymbol{m}$.

2.1.4.1 Objective Functions

One would express the optimal Gent material parameters vector for keloid and healthy skin as $\hat{\boldsymbol{m}} = \{\mu_{\text{k}}, J_{m\text{k}}, \mu_{\text{hs}}, J_{m\text{hs}}\}$. The identification of $\hat{\boldsymbol{m}}$ is based on minimizing an objective function (or cost function) that expresses the discrepancy between the experimental and model data (Eq. 1.84). In our case, the optimizer minimizes the discrepancies of the displacement, through $\mathcal{J}_u$ subject to the constraint of null discrepancies of the RF, *i.e.*, $\mathcal{J}_f$, accordingly to the Lagrange multiplier approach (Eq. 1.96). With an additional parameter to be identified, the Lagrange multiplier $\hat{\Lambda}$, such that $\hat{\boldsymbol{m}}_L = \hat{\boldsymbol{m}} \cup \{\hat{\Lambda}\}$, the unconstrained optimization is defined as [337]

$$\hat{\boldsymbol{m}}_L = \underset{\boldsymbol{m}, \Lambda \in \mathbb{R}^{N\boldsymbol{m}+1}}{\text{argmin}} \ \mathcal{J}_{\text{L}}(\boldsymbol{m}, \Lambda) = \underset{\boldsymbol{m}, \Lambda \in \mathbb{R}^{N\boldsymbol{m}+1}}{\text{argmin}} \ \mathcal{J}_u(\boldsymbol{m}) + \Lambda \mathcal{J}_f(\boldsymbol{m}) \tag{2.13}$$

We hereafter explicit separately the discrepancies in displacements, respectively RF, with the two following expressions

$$\mathcal{J}_u(\boldsymbol{m}) = \frac{1}{2\alpha_u^2 N_E} \sum_{k=1}^{N_E} \|\boldsymbol{u}_{\text{FE}}(\boldsymbol{m}, t_k) - \boldsymbol{u}_{\text{msr}}(t_k)\|_{\Omega^{\text{msr}}}^2 \tag{2.14}$$

$$\mathcal{J}_f(\boldsymbol{m}) = \frac{1}{\beta_f N_E} \sum_{k=1}^{N_E} \left(f_{X\,\text{FE}}(\boldsymbol{u}_{\text{FE}}(\boldsymbol{m}, t_k)) - f_{X\,\text{msr}}(t_k) \right) \tag{2.15}$$

where $\|.\|_{\Omega^{\text{msr}}}$ is a convenient norm defined as $\|\boldsymbol{q}\|_{\Omega^{\text{msr}}}^2 = \int_{\Omega^{\text{msr}}} \boldsymbol{q} \cdot \boldsymbol{q} \, d\Omega$. The predicted RF $f_{X\,\text{FE}}$, respectively the measured $f_{X\,\text{msr}}$, is the X-component of $\boldsymbol{f}_{\text{FE}}$, respectively $\boldsymbol{f}_{\text{msr}}$, in the material coordinates oriented along the direction of the uni-axial extension. α_u and β_f are weighting coefficients used to scale the misfit of displacement to force over time. They are computed through

$$\alpha_u = \max_{k=0,1,\ldots,N_E} \|\boldsymbol{u}_{\text{msr}}(t_k)\|_{\Omega^{\text{msr}}} \tag{2.16}$$

and,

$$\beta_f = \max_{k=0,1,\ldots,N_E} |f_{X\,\text{msr}}(t_k)| \tag{2.17}$$

In the constraint Equation 2.15, we notice that the discrepancy of RFs is not quadratic. Indeed, since the quadratic constraint concerning $\boldsymbol{m}$ cannot be derived automatically due to some FENICSlimits, we opted for a non-quadratic term. Hence, to overcome this barrier, a quadratic version of $\mathcal{J}_f$ must be hand-derived and implemented in the solver from scratch [1]. This objective function is not a Lagrange multiplier method and takes the form

$$
\begin{aligned}
\mathcal{J}_q(\boldsymbol{m}) = {} & \frac{1}{2\alpha_u^2 N_E} \sum_{k=1}^{N_E} \|\boldsymbol{u}_{\text{FE}}(\boldsymbol{m}, t_k) - \boldsymbol{u}_{\text{msr}}(t_k)\|_{\Omega^{\text{msr}}}^2 \\
& + \frac{1}{2\beta_f^2 N_E} \sum_{k=1}^{N_E} \left(f_{X\,\text{FE}}(\boldsymbol{u}_{\text{FE}}(\boldsymbol{m}, t_k)) - f_{X\,\text{msr}}(t_k) \right)^2
\end{aligned}
\tag{2.18}
$$

In an independent study, a comparison of the four different objective functions, Eq. 2.13, Eq. 2.14, Eq. 2.15, and Eq. 2.18, was conducted to test their ability to identify the model parameters. Shortly said, the aim was to answer the question: what type of data do we need to assess all the coefficients accurately?

2.1.4.2 Optimization Algorithm

The flow chart in Figure 2.8 summarize the optimization process for parameter identification. It was designed for gradient-based methods (Sec. 1.4.2.2), where a change in $\boldsymbol{m}$ is sought at every iteration, until reaching the convergence criterion. We detail in this part the step of the optimization algorithm along these lines:

- **Step 1**: Set an initial guess of model parameters composed of an initial material parameters set $\boldsymbol{m}^{(0)}$, and initial Lagrange multiplier $\Lambda^{(0)}$). This operation is the most tricky part for a modeler. The initial set should be close to the local optimum in gradient-based optimizers. It can be based on an informative guess (prior knowledge about the correlation of material parameters with the force-displacement curve).

- **Step 2**: Solve the forward FEM for over all the N_E observation times $\{t_k\}_{k=0,1,\ldots,N_E}$ with the input parameters $\boldsymbol{m}^{(0)}$ and $\Lambda^{(0)}$. Retrieve the nodal displacement sets $\{\boldsymbol{u}_{\text{FE}}(t_k)\}_{k=0,1,\ldots,N_E}^{(n)}$.

- **Step 3**: Compute the RFs using the elastic energy function from the nodal solutions and gather them in vector $\{\boldsymbol{f}_{\text{FE}}(t_k)\}^{(n)}$.

- **Step 4**: Build the total objective function $\mathcal{J}_L(\boldsymbol{m}, \Lambda)^{(0)}$ and its derivatives, the Gradient vector $\boldsymbol{G}(\boldsymbol{m}, \Lambda)^{(0)}$, and eventually the Hessian matrix $\boldsymbol{H}(\boldsymbol{m}, \Lambda)^{(0)}$. For that purpose, the discrepancy of experimental and model data ($\mathcal{J}_{Lk}$) and its derivatives ($\boldsymbol{G}_k$, $\boldsymbol{H}_k$) are computed at every time step t_k and then summed directly. As the sets of data between observation times are independent, the following property was considered: $\sum_{k=0}^{N_E} \nabla \mathcal{J}_{Lk} = \nabla \sum_{k=0}^{N_E} \mathcal{J}_{Lk}$.

- **Step 5**: Calculate the parameter steps $\boldsymbol{\delta m}^{(n)}$ and $\delta\Lambda^{(n)}$ using one of the line search algorithms. Newton and Levenberg-Marquardt were implemented and tested in SoFTI.

- **Step 6** (for $n = 0$, jump to step 7): Compare $\boldsymbol{\delta m}^{(n)}$ with $\boldsymbol{\delta m}^{(n-1)}$. If $|\delta m_p| < \epsilon_{op}, \forall \delta m_p \in \boldsymbol{\delta m}^{(n)}$, the convergence is reached, thus $\hat{\boldsymbol{m}}_L = \hat{\boldsymbol{m}}^{(n)} \cup \Lambda^{(n)}$. Otherwise, go to step 7. The coefficient Λ can be excluded from the test operation since it may not converge while the material parameters do.

- **Step 7**: Update the model parameter set as Eq. 1.86, $\boldsymbol{m}_L^{(n+1)} = \boldsymbol{m}_L^{(n)} + \boldsymbol{\delta m}_L^{(n)}$ (the subscript L means that Λ is included in the model parameters vector). Then, repeat the pattern from step 2.
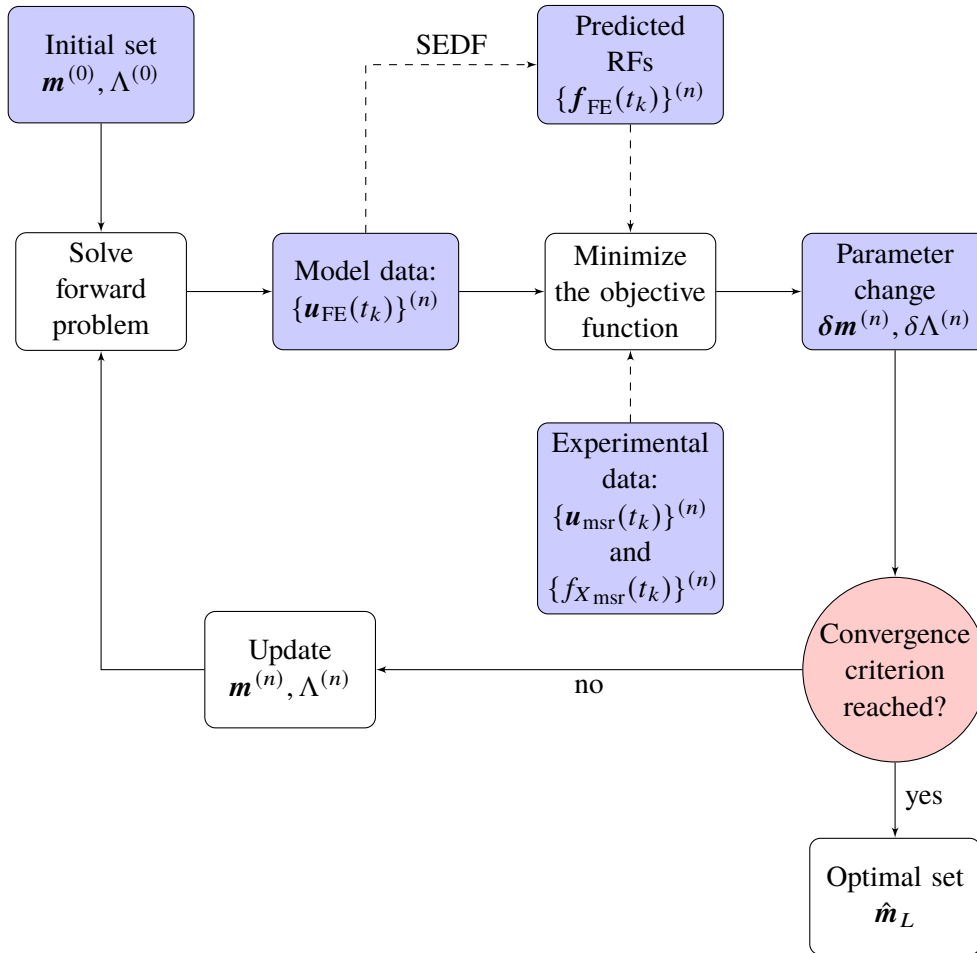
Figure 2.8: The inverse identification process scheme in SoFTI.

Some light must be shed on the reliability of the pipeline. One must be sure that the forward and optimization solvers are correctly implemented. Therefore, a validation study was carried out in Section 2.2.2.2. Additionally, Chapter 3 explores the uncertainty and limits of model identifiability regarding some controlled factors, specifically, discretization error, element degree, measurement noise, and data quantity.

2.1.5 Stress Field Computation

Assuming the validity of SoFTI's output, for instance the optimal material parameter set $\hat{\boldsymbol{m}}$, they are used to simulate the bi-material deformation as result of permanent stress. In the context of keloid/healthy-skin biomechanics, the permanent stress represent the natural skin tensions. Consequently, a FEM solver was established to compute the distribution of stress in keloid and around it for a patient-specific.

2.1.5.1 FEM Solver

The geometric model of the introduced problem is composed of only keloidic scar and peripheral healthy-skin, without pads (Fig. 2.9). In this model, the skin tensions are represented by Neumann BCs with traction vectors $\boldsymbol{t}_1$ and $\boldsymbol{t}_2$. With neglected body forces, the total elastic energy reads:

$$\Pi_{\mathrm{s}}(\boldsymbol{u}(t_l), t_l) = \int_{\Omega_{\mathrm{k}}} \psi_{\mathrm{k}}(\boldsymbol{u}, t_l)\, d\Omega + \int_{\Omega_{\mathrm{hs}}^{\mathrm{msr}} \cup \Omega_{\mathrm{hs}}^{\mathrm{unmsr}}} \psi_{\mathrm{hs}}(\boldsymbol{u}, t_l)\, d\Omega + \int_{\Gamma_R} \boldsymbol{t}_1(t_l) \cdot \boldsymbol{u}(t_l)\, d\Gamma + \int_{\Gamma_T} \boldsymbol{t}_2(t_l) \cdot \boldsymbol{u}(t_l)\, d\Gamma$$

$$(2.19)$$

t_l is the pseudo-time associated to the increments of the progressive imposed traction. They are discretized such that the solver converges successfully till the last load increment, which corresponds to the imposed natural tension values taken from the literature. The pseudo-time step decreases (inversely, the number of increments increases) for a highly nonlinear force-displacement curve.
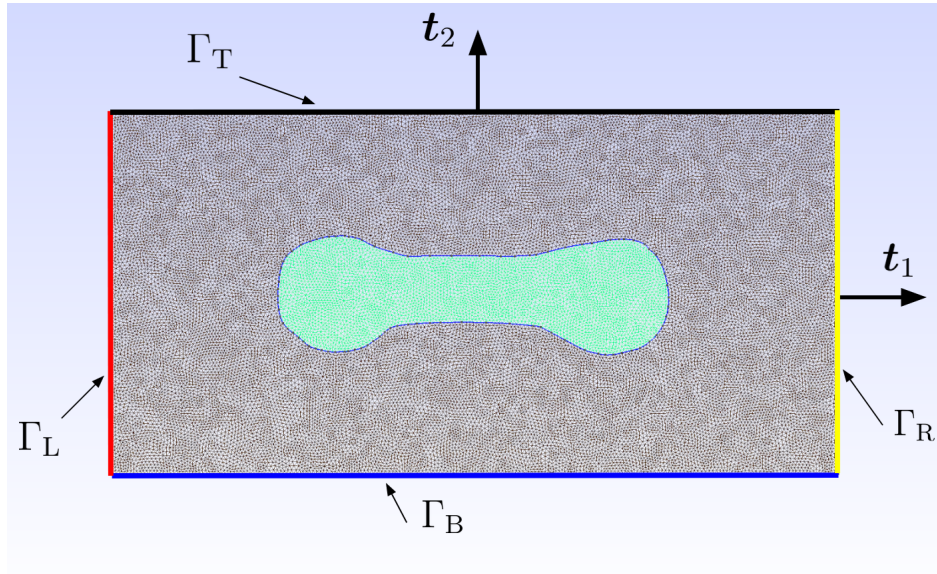
Figure 2.9: FE-model domain and boundary conditions for simulating keloid/healthy-skin natural tension. The mesh was performed with `Gmsh` and contains 53 k cells.

The Dirichlet-type BCs were put in place to create the symmetrical conditions in the studied domain bi-axially stretched (Fig. 2.9). Along the bottom boundary Γ_{B}, the vertical component of the displacement is set to be null in all configurations, i.e., $\boldsymbol{u}(t_l) = (u_1, 0)$ for all vertices in Γ_{B}. By analogy, $\boldsymbol{u}(t_l) = (0, u_2)$ for all vertices in Γ_{L}. Then, the nodal displacement is obtained by solving at each increment t_l a similar weak formulation to Equation 2.9:

$$\left. \frac{d\Pi_{\mathrm{s}}(\boldsymbol{u} + \epsilon \boldsymbol{v})}{d\epsilon} \right|_{\epsilon \to 0} \approx 0 \qquad (2.20)$$

2.1.5.2 Post-Treatment

At the output of SofTI framework, the surgeon obtains stress fields of the final deformed configuration to analyze the mechanical forces in the bi-material at a tissular scale. Let us focus on the keloid case. One would map the Cauchy stress on the whole domain for three components: tensional stress σ_{11} and σ_{22}, and shear stress σ_{12}.

Considering $\bar{\boldsymbol{u}}_{\mathrm{FE}}$ as the displacement solution in the final configuration, the Cauchy stress at a given material position $\boldsymbol{X}$ is calculated from Equations 1.29 and 1.36 as follows

$$\boldsymbol{\sigma}(\boldsymbol{X}) = J^{-1}\boldsymbol{F}(\bar{\boldsymbol{u}}_{\mathrm{FE}}(\boldsymbol{X}))\left(\frac{\partial\psi\left(\bar{\boldsymbol{u}}_{\mathrm{FE}}(\boldsymbol{X})\right)}{\partial\boldsymbol{F}\left(\bar{\boldsymbol{u}}_{\mathrm{FE}}(\boldsymbol{X})\right)}\right)^{T} \tag{2.21}$$

Stress fields are obtained by projecting the stress expressions onto the mesh elements space through the gradient of the interpolation functions. Thus, gradient discontinuity may be present between neighboring elements. In FEniCS, the application of projection can turn discontinuous gradient fields into continuous ones [387]. It consists in solving a variational problem to get the nodal solution of the stress (as an approximation) and then interpolating the latter to get the stress values between the nodes [388].

The essential parts of the methodology, developed to identify a bi-material parameters with the FEMU method, have been formulated in the current section. We will see in the next one how they have been implemented in FEniCS.

2.2 SofTI Framework

This section covers the main features of SofTI implemented in FEniCS with a focus on the forward and optimization solvers. We will also emphasize the advantages of using FEniCS in constructing FEMU-based frameworks, with some code excerpts as examples. We will also present the verification procedures that were carried out based on reliable commercial software.

2.2.1 Overview

SofTI is composed of 4 fundamental files coded in `Python` linked to each together as illustrated in Figure 2.10 and detailed in Section 2.2.1.2. They were named: `main.py`, `invsolve.py`, `mesh.py`, and `projection.py`. Optional files were embedded to simplify the parameter modification in the solvers and/or filter measurement data.

2.2.1.1 FEniCS Project

FEniCS is a user-friendly tool set out in 2003 and based on a collection of free libraries for automated solution of partial differential equations [387]. Among its components, we may define two main libraries, namely, `DOLFIN` [389] and `UFL` [390], that are commonly used for FEMU method [391].

DOLFIN
It is a library that works as the main user interface of FEniCS. It was organized as an environment that handles the communications between various FEniCS core parts (such as `UFL`) and external software (such as `NumPy`), including data structures and algorithms for computational meshes and finite element assembly. `DOLFIN` provides a range of linear algebra objects: vectors, dense and sparse matrices, direct and iterative linear solvers, and eigenvalues solvers. Another central part of `DOLFIN` is its mesh class that supplies data structures for computational meshes (connectivity, refinement, cell marking). `DOLFIN` provides two near-identical interfaces: a traditional C++ library and as a Python library. The latter was used to build the SofTI.
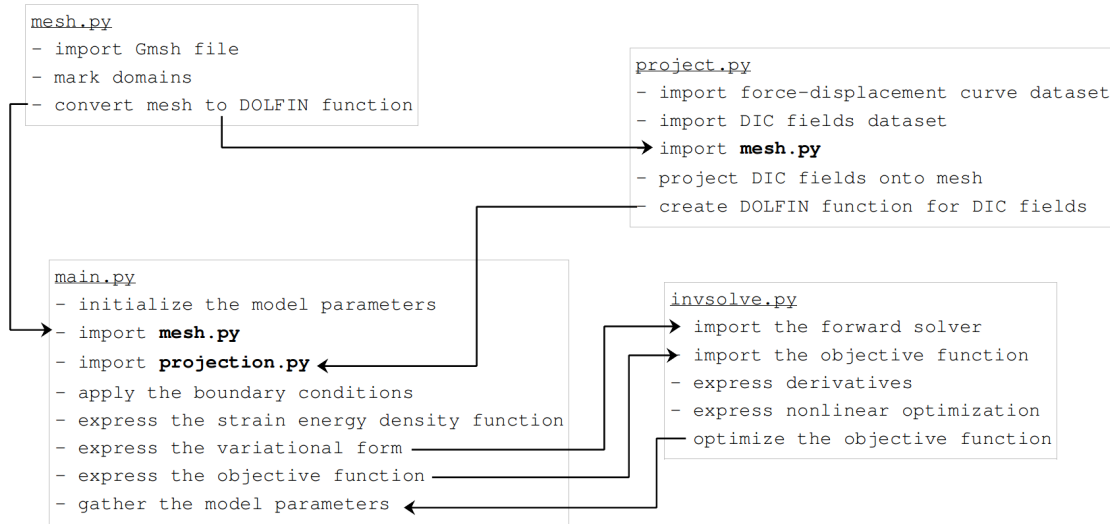
Figure 2.10: Overview of SoFTI's main functions.

UFL

The Unified Form Language library depends on `DOLFIN` and consists of a set of operators and expressions that can be used to express variational forms and functionals. Precisely, the language defines a flexible user interface for defining FE spaces and expressions in quasi-mathematical notation. It is possible then to derive the forward and the optimization model using the automatic differentiation features in `UFL`, but with some limitations. The link DOLFIN-UFL can be described with the following example. A variational form expressed in the `UFL` is passed to the form compiler to generate a code, which can then be used by `DOLFIN` to assemble linear systems.

2.2.1.2 Functions

In this part, we expose and explain the most important content inside the codes of SoFTI's blocks: the mesh, the measurement data, the forward solver, and the optimizer. The section is introduced as documentation for the reader to understand the framework's functioning effortlessly. Since the latter is an open-source program, it can be adapted freely to other applications, hence the need to popularize the tool.

Mesh

One of the positive characteristics of FEniCS is its compatibility with some external programs, among them `Gmsh`. The latter is an open-source 3D widely used to generate mesh from computer-aided design models. It allows marking the mesh subdomains and boundaries to facilitate their identification by `DOLFIN`. An output mesh from `Gmsh` is divided into 3 files: the mesh, the subdomain markers, and the boundary markers. As shown in Algorithm 2.1, they are imported and called in `MeshFunction` to convert the mesh into a `DOLFIN` function. The bi-material domains are formulated differently for the forward and optimization problems. In fact, we recall that in the case of keloid/healthy-skin bi-material, the surrounding skin is composed of 2 subdomains, Ω_{hs}^{msr} and Ω_{hs}^{unmsr} (Fig. 2.7). Both subdomains are considered in the forward solver because they form together one material. However, for the optimization problem, only Ω_{hs}^{msr} is considered side by side with Ω_{k}^{msr}, since there was no measurement on Ω_{hs}^{unmsr} to be fitted with the model.

```python
1   import dolfin
2
3   mesh_domain = dolfin.Mesh(mesh_file)
4   markers_domain = dolfin.MeshFunction('size_t', mesh, domain_markers_file)
5   markers_boundary = dolfin.MeshFunction('size_t', mesh, boundary_markers_file)
6
7   id_markers_domain = {'unmarked': 0, 'keloid_measure': 10, 'healthy_measure':
      20, 'healthy': 30,}
8   id_markers_boundary = {'unmarked': 0, 'pad_moving': 1, 'pad_fixed': 2, '
      force_measure': 3,}
9
10  dx_material = [
11      dolfin.Measure('dx', domain=mesh_domain, subdomain_data=markers_domain,
12          subdomain_id=(id_markers_domain['keloid_measure'])),
13      dolfin.Measure('dx', domain=mesh_domain, subdomain_data=markers_domain,
14          subdomain_id=(id_markers_domain['healthy'],
15          id_markers_domain['healthy_measure']))]
16  ds_sensor_pad = dolfin.Measure('ds', domain=mesh_domain, subdomain_data=
17      markers_boundary, subdomain_id=(id_markers_boundary['force_measure']))
18
```

Algorithm 2.1: Importing and marking the mesh.

Forward problem

Once the mesh function is 'standardized' according to DOLFIN's syntax, it is imported in the main.py file, where the forward problem is implemented. For easiness, the forward problem was not built in a separate file. It is represented by three major blocks, *i.e.*, behavior law, boundary conditions, and the variational formulation.

main.py starts with importing DOLFIN library (UFL is implicitly imported with) and the mesh functions, as well as the subdomains and boundaries, and their respective indices (Algorithm 2.2).

```python
1   import dolfin
2
3   from mesh import (
4     dx_material, ds_sensor_pad,
5     mesh_domain, markers_domain, id_markers_boundary
6     id_markers_domain, id_markers_boundary)
7
8   V = dolfin.VectorFunctionSpace(mesh_domain, 'Lagrange', element_degree)
9   disp_pad_moving = dolfin.Expression(('ux','uy'), ux=U_D, uy=0.0)
10  disp_pad_fixed = dolfin.Expression(('ux','uy'), ux=0.0, uy=0.0)
11
12  bcs = [
13    dolfin.DirichletBC(V, disp_pad_moving, markers_boundary,
14      id_markers_boundary['pad_moving']),
15    dolfin.DirichletBC(V, disp_pad_fixed, markers_boundary,
16      id_markers_boundary['pad_fixed']),
17    dolfin.DirichletBC(V, disp_pad_moving, markers_boundary,
18      id_markers_boundary['force_measure'])]
19
```

Algorithm 2.2: Assigning the boundary conditions to the forward problem.

In a multidimensional model, we use vector function space to define the fields based on the imported mesh. For quadratic elements, we set element_degree= 2. Afterward, we formulate the boundary conditions as UFL expression. The benefit of using an expression instead of assigning static values lies in modifying constants anywhere in the code. In other words, when the constant U_D, standing for Dirichlet-type boundary condition and equivalent to $\bar{\boldsymbol{u}}(t_k)$, is updated for value in t_k by a simple command, the whole forward problem is updated instantaneously. In classical approaches, where

the FEM solver is implemented from scratch, updating the boundary conditions is only possible after implementing manually the global linear system $[\widetilde{K}]\{u\} = \{f\}$, with $\widetilde{K}$ the assembled stiffness matrix.

The next block contains commands to introduce the behavior law as the strain energy density function. In Algorithm 2.3, we see the content of the function SEDF with the Gent model from Equation 2.8 as an example. The inputs are: displacement field's UFL expression, u, and a dictionary of the material parameters (mu = material_parameters['mu']). The use of the dictionary is recommended to assign the parameters to each material. If it is initialized outside the subroutine, it is not duplicated but conserved inside. The same function SEDF will be called for every material. In this case, the values of material parameters will be updated through UFL expression for each element depending on its nature: keloid or healthy skin.

```
1   def SEDF(u, material_parameters):
2
3     I = dolfin.Identity(3)
4     F = dolfin.variable(I + grad_reduc(u))  #F: deformation gradient tensor
5     C = F.T*F  # Right Cauchy-Green tensor
6     J = dolfin.det(F) # Jacobian
7     I1 = dolfin.tr(C) # Stretch first invariant
8
9     mu = material_parameters['mu']  # Gent's parameter 1
10    jm = material_parameters['jm']  # Gent's parameter 2
11
12    # Gent model (nearly incompressible)
13    psi = -0.5*mu*(jm*ln(1 - (I1 - 3)/jm) + 2*dolfin.ln(J))
14
15    return psi
16
```

Algorithm 2.3: Implementing the behavior law.

As for the variational form, it is constructed in the following order (Algorithm 2.4). The field u is retrieved from the vector function space, then inserted in the SEDF along side the parameters to generate the partial elastic energy function for each subdomain. The latter is in form of integrand (SEDF(u, param_k)*subdomain_k) to be assembled on each element. The integration is performed with Gaussian points. After that, similarily to Equation (2.9), the variational L and its derivative dL are defined and used to build the forward solver.

```
1   u = dolfin.Function(V)
2   subdomain_k = dx_material[0] # k stands of keloid
3   subdomain_hs = dx_material[1] # hs stands of healthy-skin
4
5   # total elastic energy
6   Pi = SEDF(u, param_k)*subdomain_k + SEDF(u, param_hs)*subdomain_hs
7
8   L = dolfin.derivative(Pi, u)
9   dL = derivative(L, u)
10
11  forward_problem = dolfin.NonlinearVariationalProblem(L, u, bcs, dL)
12  forward_solver =  dolfin.NonlinearVariationalSolver(forward_problem)
13
```

Algorithm 2.4: Setting the nonlinear variational equation.

Finally, given a list of imposed displacement values $\bar{u}(t_k)$ on the moving pad, U_D, the equilibrium problem for each pseudo-time t_k is solved with these lines (Algorithm 2.5). We must point out that the converged nodal solution u_{FE} for the iteration t_k is used as the initial set to seek solution for the iteration $t_k + 1$. Otherwise, the solver may not converge. The results are b, a boolean that equals 1 when a solution is found, and n, the number of iterations to achieve it.

```
1  for tk, *_ in enumerate(U_D):
2    disp_pad_moving.ux = U_D[t_k] # set Dirichlet BC at pseudo-time t_k
3    n, b = forward_solver.solve()
4
```

Algorithm 2.5: Solving the forward nonlinear problem.

Projection

We recall that two type of data are fitted with the model *via* the optimization problem, force-displacement curve and displacement fields (obtained by DIC technique). From a computational point of view, the implementation of force-displacement vector is so basic. While projecting the DIC fields uniformly mapped on a domain randomly meshed may not be obvious to conduct. Consequently, the treatment process of DIC field was established in an external block `projection.py`. The Algorithm 2.6 emphasizes the main steps to produce `DOLFIN` objects from DIC data.

The general concept behind generating displacement `DOLFIN` function is interpolating the DIC data on new points corresponding to mesh nodes. The coordinates of `x_MESH` are collected from the degrees of freedom of the function space `V` that shares the same features with the mesh. An internal class names `SimpleMeshlessInterpolation2d` is called to perform the interpolation based on a meshless method. At the end of the process, an initialized `DOLFIN` field (`u_MESH = dolfin.Function(V)`) hosts the displacement on its respective nodes, `u_MESH.vector()[:] = u_proj.vector().get_local()`.

```
1   import dolfin
2
3   def project_on_functions(x_DIC, u_DIC, V, meshless_degree=1):
4
5     x_MESH = V.tabulate_dof_coordinates()
6     u_MESH = dolfin.Function(V)
7
8     meshless = SimpleMeshlessInterpolation2d(x_DIC)
9     meshless.set_reference_values(u_DIC)
10    meshless.set_interpolation_points(x_MESH)
11    u_proj = meshless.interpolate(degree=meshless_degree)
12
13    u_MESH.vector()[:] = u_proj.vector().get_local()
14
15    return u_MESH
16
```

Algorithm 2.6: Creating `DOLFIN` objects from DIC fields.

SimpleMeshlessInterpolation2d was implemented to regroup the operations related to 2D interpolation such as `set_reference_values`, `set_interpolation_points`, and `interpolate`. By setting `meshless_degree= 1`, the displacement is linearly interpolated between the reference points by taking into account the influence of the neighbor points. For meshless methods, the connection between the mesh nodes (edges) is not required, but the interaction of each node with all its neighbors is considered.

Optimization problem

The file `invsolve.py` contains a bunch of subroutines and classes to conduct the model fitting. A pseudo-code was written to summarize the principal elements put into action to identify the material parameters by optimizing the discrepancy between the model and experimental data. It was segmented into three parts: objective function, nonlinear solver, and identification algorithm.

In Algorithm 2.7, we recognize the shapes of the misfit for displacement (Eq. 2.14) and reaction force (Eq. 2.15). Their non-integrated UFL expressions can be easily derived automatically and symbolically, thereby leading to automatic sensitivity analyses [390]. Having said that, FEɴɪCSis unable to derive a quadratic constraint, $(f_{X\,\mathrm{FE}} - f_{X\,\mathrm{msr}})^2$, with respect to material parameters. This barrier has been overcome by manually implementing the quadratic force mismatch function, and their respective derivatives by D. Sutula [1] (a detailed code is available in Appendices of [266]).

```
import dolfin

def cost (u_msr, t_msr, u_FEM, mesh_domain, dx_measure, ds_measure,
          alpha, beta): # for one pseuo-time

    J_u = 0.5*1/alpha**2*(u_FEM - u_msr)**2 * dx_measure

    N = dolfin.FacetNormal(mesh_domain)
    t_FEM = dolfin.dot(PK1, N)  # PK1: Piola-Kirchhoff tensor
    J_f = 1/beta*(t_FEM[0] - t_msr[0])*ds_measure # t_i: traction vectors

    return J_u + J_f
```

Algorithm 2.7: Building the objective function.

We explain why the automatic derivation of the quadratic constraint is beyond FEɴɪCS' ability. If one assumes that $f_{X\,\mathrm{FE}}$, respectively $f_{X\,\mathrm{msr}}$, are the resulted from integrating the X-component of the traction vector $t_{X\,\mathrm{FE}}$, respectively $t_{X\,\mathrm{msr}}$, over Γ_{CS}, than the quadratic constraint reads

$$(f_{X\,\mathrm{FE}} - f_{X\,\mathrm{msr}})^2 = \left(\int_{\Gamma_{\mathrm{CS}}} t_{X\,\mathrm{FE}} - t_{X\,\mathrm{msr}}\, d\Gamma \right)^2 \tag{2.22}$$

Unfortunately, `DOLFIN` was not designed to derivate a square of an integral regarding the parameters and variables without integrating. Still, there is a way to implement the quadratic constraint by squaring the discrepancy of traction instead of force through the following equation.

$$\int_{\Gamma_{\mathrm{CS}}} (t_{X\,\mathrm{FE}} - t_{X\,\mathrm{msr}})^2\ d\Gamma \tag{2.23}$$

However, in this situation, the discrepancy is basically never null, because the distribution of $t_{X\,\mathrm{FE}}$ over Γ_{CS} is not constant, unlike $t_{X\,\mathrm{msr}}$.

Later, the objective function is called in another subroutine to calculate their first and second derivatives (Algorithm 2.8), which can be utilized for other UFL forms. The sensitivity analysis for parameter optimization involves the derivatives $\frac{\partial \mathcal{J}}{\partial \boldsymbol{u}_{\mathrm{FE}}}$, $\frac{\partial \mathcal{J}}{\partial \boldsymbol{m}}$, $\frac{\partial^2 \mathcal{J}}{\partial \boldsymbol{u}_{\mathrm{FE}}^2}$, $\frac{\partial^2 \mathcal{J}}{\partial \boldsymbol{u}_{\mathrm{FE}} \partial \boldsymbol{m}}$, and $\frac{\partial^2 \mathcal{J}}{\partial \boldsymbol{m}^2}$.

Two different methods were implemented for computing $\boldsymbol{G}$ and $\boldsymbol{H}$: direct and adjoint. The first requires as many solves as their model parameters for each pseudo-time and iteration. On the other hand, the adjoint method requires one solution for any number of model parameters, but to the detriment of the physical memory in the computer [390].

```
1    def partial_derivatives(J, u, material_parameters):
2
3      # alias m: material_parameters
4      dJdu    = dolfin.derivative(J, u)
5      d2Jdu2  = dolfin.derivative(dJdu, u)
6      dJdm    = tuple(dolfin.diff(J, m_i) for m_i in material_parameters)
7      d2Jdudm = tuple(dolfin.diff(dJdu, m_i) for m_i in material_parameters)
8      d2Jdm2  = tuple(tuple(dolfin.diff(dJdm_i, m_j)
9        for m_j in material_parameters[i:])
10       for i, dJdm_i in enumerate(dJdm))
11       # upper triangular part (symeterical Hessian matrix)
12
13     return dJdu, dJdm, d2Jdu2, d2Jdudm, d2Jdm2
14
```

Algorithm 2.8: Evaluating objective function derivatives.

For simplicity, we explain how the Gradient vector is numerically evaluated hereafter. Its elements in the direct method are evaluated for each parameter m_i as

$$\frac{d\mathcal{J}(t_k)}{dm_i} = \frac{\partial \mathcal{J}(t_k)}{\partial m_i} + \left(\frac{\partial \mathcal{J}}{\partial \boldsymbol{u}_{\text{FE}}}\right)^T \frac{d\boldsymbol{u}_{\text{FE}}(t_k)}{dm_i} \quad (2.24)$$

where $\frac{\partial \mathcal{J}(t_k)}{\partial m_i}$ and $\frac{\partial \mathcal{J}}{\partial \boldsymbol{u}_{\text{FE}}}$ are assembled on each element. Assembling in FENICS means returning the corresponding value-tensor for a given form. To compute $\frac{d\boldsymbol{u}_{\text{FE}}(t_k)}{dm_i}$, a linear system (tangent system) calling for the global stiffness matrix needs to be solved:

$$\widetilde{\boldsymbol{K}}(t_k)\frac{d\boldsymbol{u}_{\text{FE}}(t_k)}{dm_i} = \frac{df_{X\,\text{FE}}(t_k)}{dm_i} - \frac{d\widetilde{\boldsymbol{K}}(t_k)}{dm_i}\boldsymbol{u}_{\text{FE}}(t_k) \quad (2.25)$$

Once the sensitivities in the form of total derivatives are gathered, they are summed over t_k for all observation times, accordingly to the property $\sum_{k=0}^{N_E} \nabla \mathcal{J}_{\mathrm{L}k} = \nabla \sum_{k=0}^{N_E} \mathcal{J}_{\mathrm{L}k}$ applied to Equations 2.14 and 2.15. Eventually, the Gradient and Hessian matrices are combined depending on the chosen algorithm, for instance, Newton in Algorithm 2.9, to identify the optimal material parameter set (as described in Sec. 2.1.4.2).

```
1    import scipy.linalg as linalg
2
3    num_iterations = 0; convergence = False
4    rtol = 1e-6 # relative toleranece
5
6    while not convergence:
7      DJDm = 0; D2JDm2 = 0;
8      for tk in observation_times:
9      DJDm += dJdm_method_direct(J, u, m, tk)
10     D2JDm2 += d2Jdm2_method_direct(J, u, m, tk)
11
12     # Compute model parameter change using the Newton method
13     dm = linalg.solve(D2JDm2, -DJDm)
14     m += dm
15
16     if np.all(np.abs(dm[:-1]) < np.abs(m[:-1])*rtol):
17     convergence = True
18
19   m_optimal = m
20
```

Algorithm 2.9: Identifying the optimal parameter set.

Through a series of code excerpts, we demonstrated the usefulness of working with FENICS to build a complete FEMU inverse problem for material parameters identification. Thereby, the user can quickly adapt the framework to his requirements. Although FENICS is getting attention from the

computational sciences community, it is not as widely used as commercial software. It may be due to the lack of detailed documentation of physical complex problems. Researchers may get interested if the complete code is shared with every published research with a FEniCS application. Last but not least, a new version of FEniCS, named `FEniCSx`, was recently developed. It has many major improvements over the legacy library, including support for a wide range of cell types and elements, memory parallelization, as well as complex number support. With its main library `DOLFINx`, SoFTI can be improved for efficient use.

2.2.2 Validation

Verifying the correctness of numerical tools is essential in order to provide reliable simulations. Despite the fact that `DOLFIN` modules and functions are continuously checked and publicly reviewed by the modelers, thanks to their open-source nature, their combined application to physical problems cannot be considered valid. Therefore, a validation study of the forward and optimization solvers was conducted in my thesis.

2.2.2.1 Forward Solver

The validation process in the direct problem case consists of comparing the simulation results issued from SoFTI to reference data. Regarding our computational materials, a commercial FE simulator, COMSOL Multiphysics®, was employed to construct a similar forward problem with some simplifications that will be enlighted in this section.

Approximation

Because of the file format incompatibility between FEniCS and COMSOL, comparing the simulation results using the same mesh with the same vertices and edges is not doable. Besides, importing the abnormal material outline (keloid, for instance) into COMSOL software is complicated. Hence, the mesh that represents the uni-axial experiment on the keloid/healthy-skin model (Fig. 2.7) was subjected to two approximations: (i) shaping the keloid as symmetrical polygon form, (ii) simulating the forward problem on two different meshes but almost the same number of elements.

Reference Model

On COMSOL Multiphysics®5.2, a mesh domain with 11k elements was generated automatically by setting the most extreme fine element standards (Fig. 2.11). A compressible version of Gent model (Eq. 2.26), the only form implemented in COMSOL [1], was assigned to each of keloid and healthy-skin materials but with different parameters. In addition to the reference material parameters $m_{\mathrm{ref}}^{\mathrm{bimaterial}}$ set arbitrarily as $\mu_{\mathrm{k}} = 0.05$ MPa, $J_{m\mathrm{k}} = 0.2$, $\mu_{\mathrm{hs}} = 0.016$ MPa, and $J_{m\mathrm{hs}} = 0.4$, the compressibility parameters were fixed with higher value so that the behavior became nearly-incompressible, *i.e.*, $\kappa_{\mathrm{k}} = \kappa_{\mathrm{hs}} = 1000$ MPa.

$$\psi_{\mathrm{G}}^{\mathrm{C}} = -\frac{\mu}{2} J_m \left(\ln \left(1 - \frac{J^{-2/3} I_1 - 3}{J_m} \right) - \frac{\kappa}{2} (J - 1)^2 \right) \tag{2.26}$$

The reference model also verifies the plane strain conditions, with a unit uniform thickness of 1 mm. The reaction force results from integrating the Piola-Kirchhoff X_{11}-component over the keloid cross-section, tangent to the pad edge (as introduced in Eq. 2.11). As for the boundary conditions, $u(\Gamma_{\mathrm{MP}}, t_k)$, 50 equidistant values imposed displacement increments were established, from 0 to -4 mm. Using

---

[1]One should report that, in COMSOL Multiphysics®5.2, the elastic energy equation of the Gent Model shown in `Material Settings` differs from the one implemented in the `Equation View` tab. The latter holds the real implemented formula for the solver.
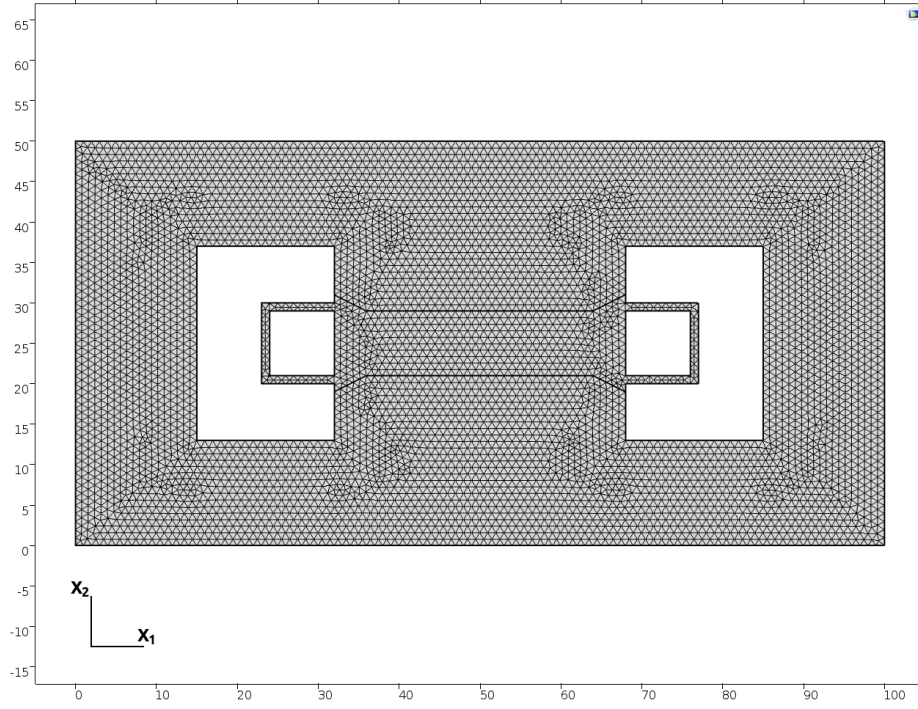
Figure 2.11: 11k-element mesh domain generated with COMSOL Multiphysics®.

the nonlinear solver of COMSOL, we obtain and then export 50 nodal displacement fields and a force-displacement curve. The output data are to be introduced in the forward problem of SoFTI for local comparison.

Comparison

On the other side, in SoFTI, the changes to be performed are no more than two lines. Indeed, after creating a similar mesh in `Gmsh`, the user needs to extend the material parameters for an additional compressibility coefficient and update the elastic energy function in Algorithm 2.3. To quantify the discrepancy between FEniCS and COMSOL simulation results, we use the following indicator for nodal displacements and reaction forces:

$$\varepsilon_u^{(i)} = |\boldsymbol{u}_{\text{COMSOL}}(\boldsymbol{X}_i) - \boldsymbol{u}_{\text{FEniCS}}(\boldsymbol{X}_i)| \tag{2.27}$$

$$\varepsilon_f = \frac{\|\bar{\boldsymbol{f}}_{X\,\text{COMSOL}} - \bar{\boldsymbol{f}}_{X\,\text{FEniCS}}\|_2}{\|\bar{\boldsymbol{f}}_{X\,\text{COMSOL}}\|_2} \tag{2.28}$$

$\varepsilon_u^{(i)}$ and ε_f are the absolute local bi-directional discard of nodal displacement (on a node $\boldsymbol{X}_i$) and the relative global discard of force-displacement curves. The comparison results are summarized in Figures 2.12 and 2.13. Starting with the reaction forces. The superposition of the curves calculated by COMSOL and FEniCSshows that their respective solvers provide similar results with $\varepsilon_f = 0.8$ %. The same observation can be made for the displacement but not over all the domain. In fact, ε_u is significant around the pads corners, which can be linked to the quality of mesh on those areas. For large deformation, the elements might undergo distortion. This hypothesis will be addressed in Section (3.1.1). Nevertheless, the edge effect had been considered in delimiting the measurement zone (Fig. 2.7).

For scaling reasons, the comparison of the solvers' outputs seems not conclusive on 2.12. A nodal displacement comparison was made on cutlines to overcome the issue. Horizontal and vertical cutlines, crossing all the domain in the center, was chosen for that purpose. For the horizontal cutline,

(a) Discard on ε_{u1}

(b) Discard on ε_{u2}
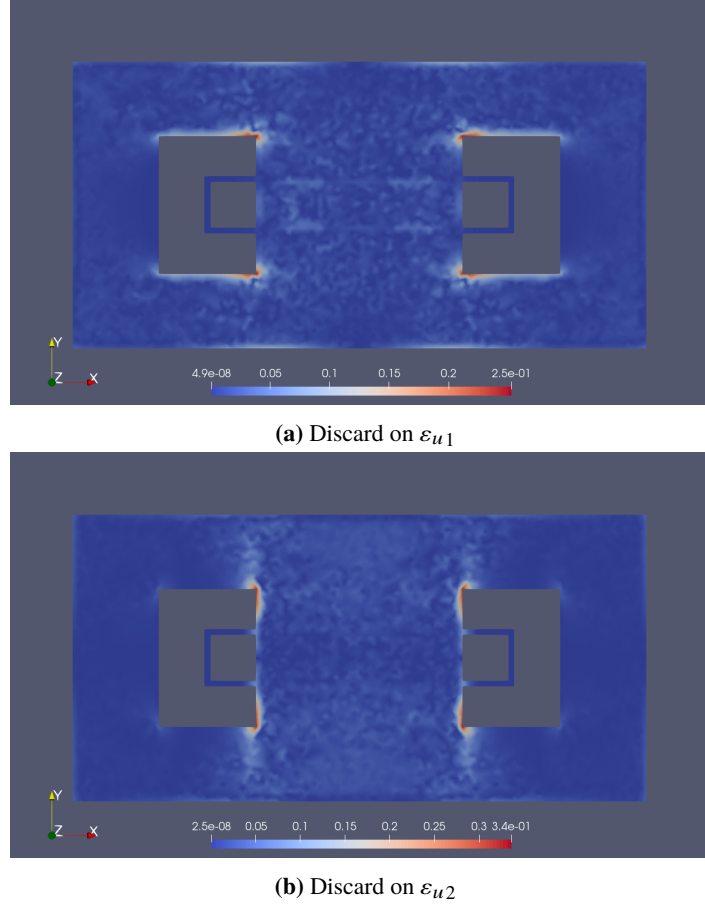
Figure 2.12: Comparison of nodal displacement between COMSOL Multiphysics®and FEɴɪCS. The fields correspond to the latest imposed displacement $t_k = 50$, with $\bar{u}_1 = -4mm$.

set on the coordinate $X_2 = 25$ (Fig. 2.11)), the comparison is plotted in Figure 2.14. The latter shows a good match of u_1 (X_1-component of $\boldsymbol{u}$) with a relative error of 0.4 %, which was calculated inspired from Equation 2.28. As for u_2 (X_2-component of $\boldsymbol{u}$), the simulation results from the two solvers fit averagely, but the COMSOL solver shows fluctuations due to numerical reasons.

Figure 2.15 exhibits a good fit between the solvers by comparing the simulation results on the vertical cutline, set on the coordinate $X_1 = 50$ (Fig. 2.11). The relatives errors for u_1 and u_2 are 0.3 % and 1.3 %, respectively. Fluctuations in u_2 was also noticed for the COMSOL solver. Furthermore, we learn from the previous figures that one component of displacement is uniform along the symmetrical lines, *e.g.*, the u_1 in Figure 2.15 is about -2 mm on all points of the vertical cutline.
One time the forward problem in SoғTI has been validated using a commercial framework as a reference; it will be updated following an optimization scheme to identify the material parameters given a hyperelastic model.

2.2.2.2 Optimization Solver

We present in this part the validation of the optimization problem characterized by a successful identification of the reference material parameters $\boldsymbol{m}_{\text{ref}}^{\text{bimaterial}}$. From the latter, a set of data was synthesized to play the role of measurement data in the form of DIC fields and force-displacement curve. The inverse solver in its entirety will then solve the forward problem for a bunch of parameter sets selected by the optimizer. If the optimizer converges toward $\boldsymbol{m}_{\text{ref}}^{\text{bimaterial}}$, two conclusions can be made. The SoғTI code is correctly implemented and the optimization scheme is well established.
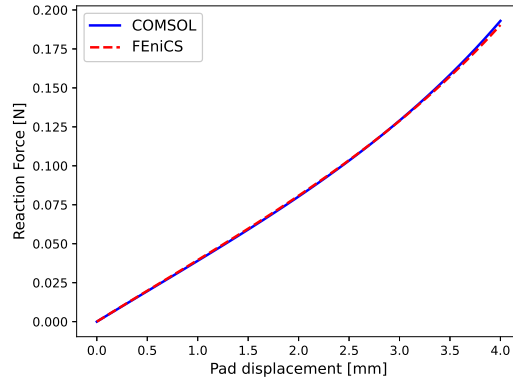
Figure 2.13: Comparison of reaction forces between COMSOL Multiphysics®and FEɴıCS.

(a) u_1

(b) u_2
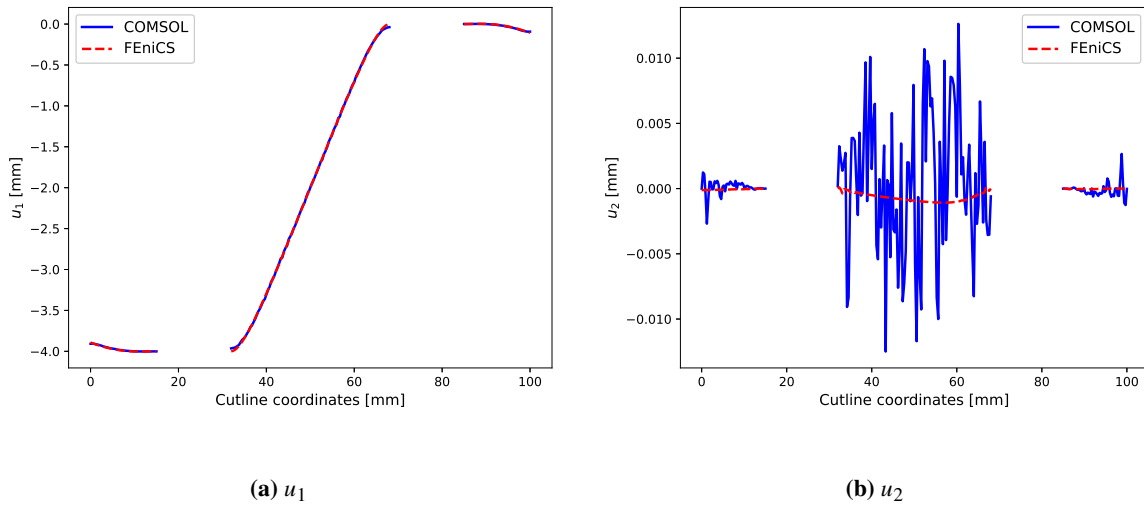
Figure 2.14: Comparison of displacement on the horizontal cutline The gap in the curves represent the non-meshed pads.

Synthetic Data

An adaptive mesh with 1300 cells was generated such that the computations are enough fast and accurate at the same time (Fig. 2.16). It was obtained by manually adding vertices on the high uncertainty areas, for instance, the pads' corners for more details, the reader is referred to Section 3.1.3. As we aim to validate an identification process, we do not consider factors that may complicate the line search procedure and hence a failure. Keeping in mind that the validation mesh should be simple, its elements were set linear. Same as in the forward problem validation, the synthetic displacement fields and reaction forces were fabricated for 50 pseudo-times so the imposed displacement sweeps from 0 to -4 mm, for the parameter set $m_{\mathrm{ref}}^{\mathrm{bimaterial}}$. A second case, where the material is monolithic and represents the healthy-skin, was explored as well, with 2 reference parameters $m_{\mathrm{ref}}^{\mathrm{monolithic}} = \{\mu_{\mathrm{hs}} = 0.016\,\mathrm{MPa}, J_{m\mathrm{hs}} = 0.4\}$. Technically, we assign the same parameter set for both subdomains Ω_{k} and Ω_{hs}.

Parameter Identification

All the four objective functions, Equations 2.13, 2.14, 2.15, and Eq. 2.18, were tested side by side in two separate studies: monolithic and bi-material. In this approach, we validate the parameter identification ability of the optimizer and investigate its various cost functions simultaneously. The initial sets were chosen not far from the targets $m_{\mathrm{ref}}^{\mathrm{bimaterial}}$ and $m_{\mathrm{ref}}^{\mathrm{monolithic}}$ as we are interested by the feasibility in the first position (As for the robustness, it will be addressed in Section 3). Consequently, the

(a) u_1 **(b)** u_2
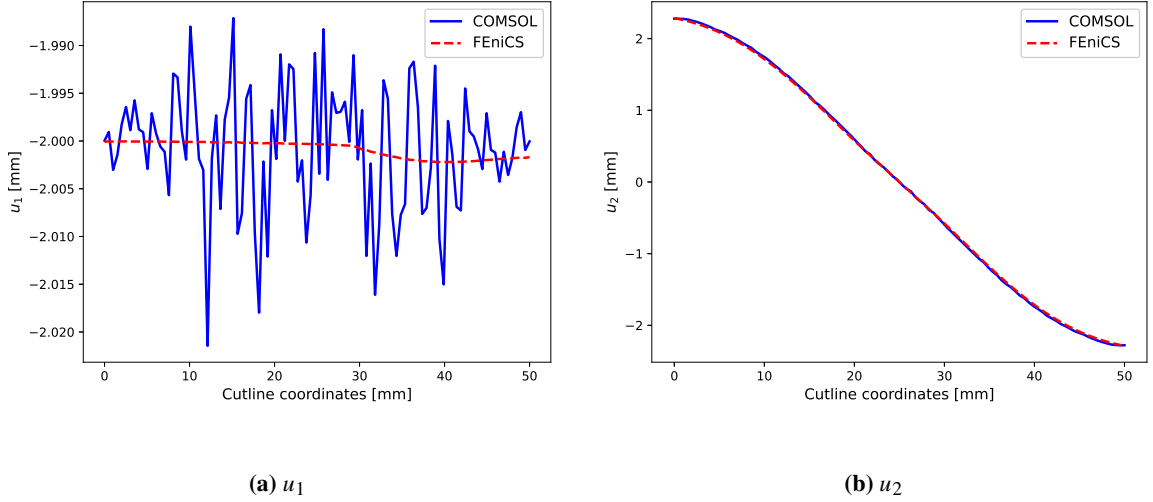
Figure 2.15: Comparison of displacement on the horizontal cutline The gap in the curves represent the non-meshed pads.
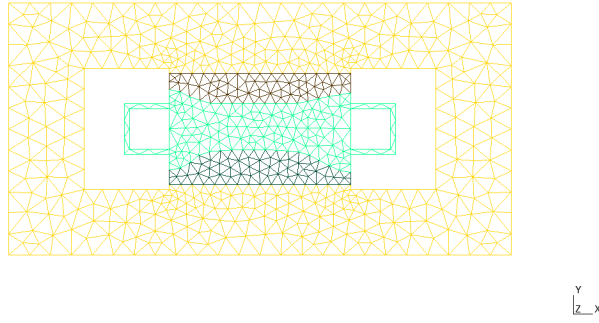
Figure 2.16: Adaptive mesh with 1300 elements for validating the optimization solver. Published in [266].

identification path is from $\boldsymbol{m}_L^{(0)} = \{\mu_\mathrm{k} = 0.01 \text{ MPa}, J_{m\mathrm{k}} = 0.01, \mu_\mathrm{hs} = 0.01 \text{ MPa}, J_{m\mathrm{hs}} = 0.01, \Lambda^{(0)}\}$ toward $\boldsymbol{m}_\mathrm{ref}^\mathrm{bimaterial}$, and from $\boldsymbol{m}_L^{(0)} = \{\mu_\mathrm{hs} = 0.01 \text{ MPa}, J_{m\mathrm{hs}} = 0.01, \Lambda^{(0)}\}$ toward $\boldsymbol{m}_\mathrm{ref}^\mathrm{monolithic}$.

As illustrated in Figure 2.17, only the objective function $\mathcal{J}_u + \Lambda \mathcal{J}_f$ let converging to the target within 120 s, while the three others fail to. In come cases, like for $\mathcal{J}_u$, the search was interrupted because of a divergence of the forward solver. To complete the set, the evolution of the Lagrange multiplier Λ is plotted in Figure 2.18, which shows a clear decrease toward 0 without convergence. The later result witnesses the necessity of excluding Λ from the parameter change vector $\boldsymbol{\delta m}$ as its has a sharp tangent at the convergence of the optimizer, at the iteration 12.

With a focus on Λ's variation, we may define two main phases before and after the iteration 8. In the first phase, Λ seems to stagnate while the material parameters $\boldsymbol{m}$ evolve in the direction of the reference. While in the second, it drops drastically as the tangents of all of the 4 other parameters decrease progressively closer to the target. To define the role of the Lagrange multiplier on the optimized cost, we need to draw the variation of the objective function with its separate parts for each iteration (Fig. 2.19) and oppose it to Figure 2.18. At first glance, the mismatch on the displacement appears to be dominating the total cots, as if the force mismatch has no impact on the error optimization. The reason behind that is the initial value $\Lambda^{(0)}$ fixed as 10^{-4} (so low in order to guarantee the convergence), making the force part neglected *versus* the displacement. However, we can notice in Figure 2.19 that

(a) μ_k

(b) J_{mk}

(c) μ_{hs}

(d) J_{mhs}
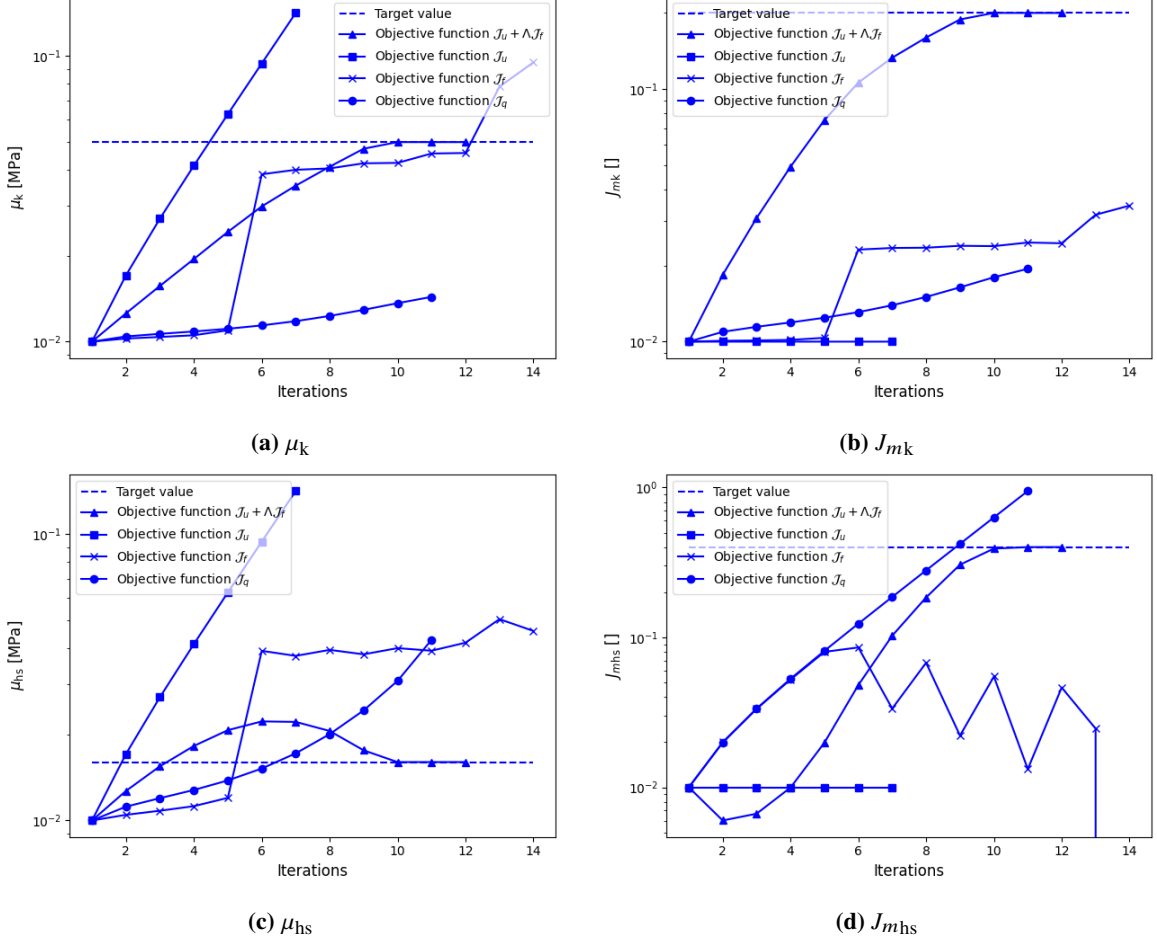
Figure 2.17: Bi-material parameters evolution for different objective functions in the validation process.

all costs are driven the same way since they are connected through Λ.

In an attempt to understand better the influence of the Lagrange multiplier on the total mismatch, a similar dummy identification was conducted for a higher value of the initial Lagrange multiplier: $\Lambda^{(0)} = 1$, but with a compatible $\boldsymbol{m}^{(0)}$ set, as $\mu_k^{(0)} = 0.005$ MPa, $J_{mk}^{(0)} = 0.05$, $\mu_{hs}^{(0)} = 0.005$ MPa, and $\mu_{hs}^{(0)} = 0.05$. Thereby, the variations of the costs were gathered in Figure 2.20. We see at the beginning the total mismatch is dominated by the force part, then it shifts to the displacement mismatch, as the Lagrange multiplier decreases continuously until the convergence. Even though the impact of the constraint, force mismatch, is not visible, one may affirm that it is essential for identifying the parameters of a heterogeneous material. To support this statement, we refer back to Figure 2.17 that demonstrates the incapability of the optimizer to find $\boldsymbol{m}_{\text{ref}}^{\text{bimaterial}}$ if the minimization deals with the displacement only through the objective function designed for that purpose. The same can be stated for the force. Herefore, combining displacement and force is necessary to identify the full set of parameters, but not in a random way. Indeed, the objective function that combines the latter (Eq. 2.18) failed also for the same initial guess. It worked correctly for another initial set closer to the target, which makes it less robust than the one based on the Lagrange multiplier. Nevertheless, identifying all the parameters of keloid/healthy-skin media with $\mathcal{J}_q$ remains possible. For that, the two parameters of healthy-skin are first assessed in a contra-lateral test, then fixed in a second process to identify the two remaining keloid parameters as applied by Sutula *et al.* [1].

By reducing the problem to a homogeneous media, the objective function $\mathcal{J}_q$ succeeded in identifying the 2 parameters of the monolithic material, unlike $\mathcal{J}_u$ and $\mathcal{J}_f$ separately. The parameters series
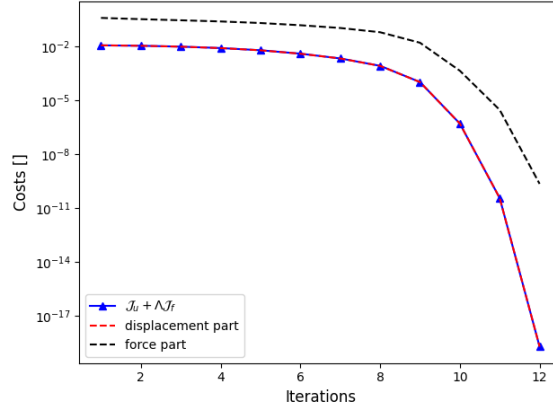
Figure 2.18: Lagrange multiplier variation for the objective function Eq. 2.13.
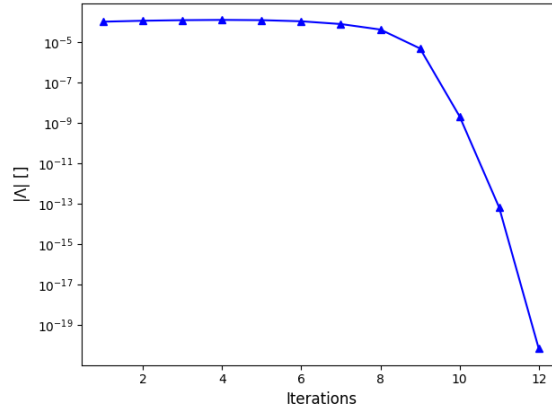
Figure 2.19: The variation of the objective function Eq. 2.13 and its separate parts.

during the optimization are reported in Fig. 2.21. In this simplified case, considering force mismatch as a constraint in $\mathcal{J}_u + \Lambda \mathcal{J}_f$ improves the convergence compared to the $\mathcal{J}_q$ form, where the duration of computations was respectively 41 and 1085 seconds. The delay is related to the number of iterations and the integration time for obtaining the manually implemented sensitivities (Gradient and Hessian).

Furthermore, the non-success of parameter identification with $\mathcal{J}_u$ and $\mathcal{J}_f$ may be due to the correlation between the material parameters and the data type. The synthetic displacement fields introduced in $\mathcal{J}_u$ as measurement, or reaction forces in $\mathcal{J}_f$, need to be diversified enough to identify μ_{hs} or J_{mhs}. Thus, displacement and forces measurement data had to be used all together in the optimization solver.

Conclusions

The present chapter addressed the principal structure of SoFTI with describing its two main parts, the forward and the optimization solvers. After introducing the theoretical continuum mechanics and justifying the assumptions, a series of codes implemented in FEniCS were explained in simplified excerpts. They were rewritten so that the modeler would easily understand the link between the functions. After that, a validation process of the direct FEM solver (based on comparison with commercial software) and the optimizer (based on synthetic data) was discussed, accompanied by a study of some objective functions. The latter numerical research showed that identifying the Gent

81

(a)

(b)
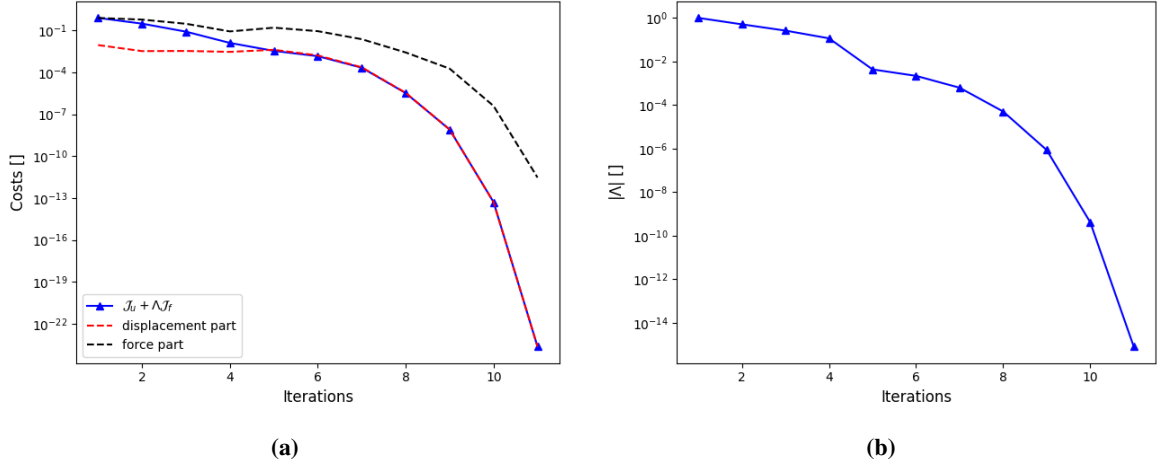
Figure 2.20: The variation of the objective function Eq. 2.13 and its separate parts for $\Lambda^{(0)} = 1$.

(a) μ_{hs}

(b) $J_{m\mathrm{hs}}$
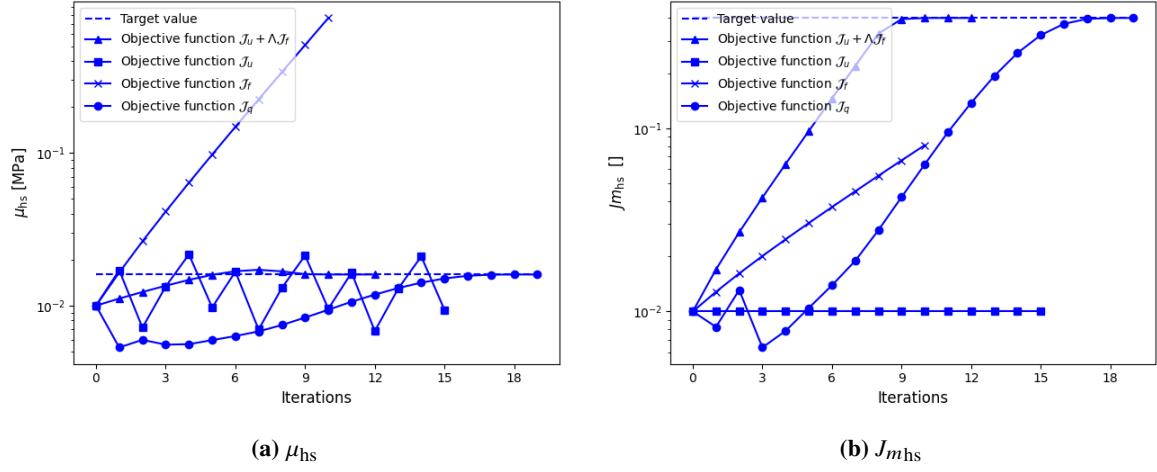
Figure 2.21: Monolithic material parameters evolution for different objective functions.

model parameters of a bi-material soft tissue undergoing uni-axial stretch can be performed only with constrained optimization with the Lagrange multiplier method. In the next chapter, we will study different aspects of uncertainty associated with parameter identification. The investigation aimed to evaluate the reliability of parameter estimation carried out in SoFTI before applying it to a real case.

Chapter 3

Bi-material Mechanical Characterization: Uncertainty Analysis

Numerical modeling has been recently developed and used in many research works to provide non-invasively immeasurable data inside the soft tissue, such as stress fields. The use of experimental techniques alongside computations aims to give evident knowledge to a deeper understanding of human skin functions leading to optimizing the treatment of wound healing disorders. There are several challenges for computational medicine to make reliable predictions. Providing accurate experimental data reflecting the biomechanical behavior of the studied site on a particular scale (tissue or cellular scale) is of major concern. These experimental data are commonly used as input data of numerical models to quantify output responses through physical and/or biological laws expressed by constitutive mathematical equations. Also, these data can be used to validate the modeling outcomes. However, uncertainties in the experimental data exist from several factors, such as inter-subject and intra-subject variability and differences in techniques and protocol parameters. Uncertainties related to computations may also exist, where numerical processes impact the exactness of model data.

The present chapter focuses on a selection of uncertainty studies on the identified model parameters regarding the methods and materials followed in pipeline. In fact, we will explore the mechanical response of the system (constituted of a bi-material soft tissue material and a uni-axial extension device) by varying parameters that control the discretization error, experimental data quantity and quality, topology, and the tri-dimensional aspect. The uncertainty can be quantified by evaluating the accuracy and/or precision. Accuracy is how close a given set of interest quantities are to their true value, while precision is how close the quantities are to each other. In our case, the true value, namely, the target, is known *a priori* and set arbitrarily. The sets of mechanical responses used to assess the discard are generated synthetically.

3.1 Discretization

In computational mechanics, a function of a continuous variable is represented in the computer by a finite number of evaluations, for example, on a mesh or lattice. The domain where the model equations are formulated is said to be "discretized." The solutions of the equation in this situation are numerically approximated, thus different from the exact solution. The discrepancy between the numerical and the exact solution is called discretization error (DE). For a consistent discretization of the model equations, the DE is expected to become smaller as the number of elements increases. However, the results are strongly affected by the density of the mesh and distribution of the nodal points (or vertices).

A mesh element has many features, including size and interpolation degree. The latter factors will be our variable in the uncertainty quantification of the inverse identification. In practice, this section forwards the accuracy of the identified parameters with respect to the change in mesh, intending to

find a compromise between uncertainty and computation cost.

3.1.1 Mesh study

A set of meshes were mapped on Gmsh to analyze the identification uncertainty [383]. By varying the average distance between vertices, from scale 0.05 to 2, Gmsh applies the Delaunay triangulation algorithm to generate the cells. As a result, 6 uniformly-distributed meshes, with the number of cells $N_{\text{elem}} \in \{540, 830, 1300, 1900, 3000, 4000, 6000, 9000, 12000, 22000, 44000\}$ will be tested in the uncertainty analysis.

3.1.1.1 Mesh Convergence

The mesh size scale was limited to 0.05 in accordance with the computer's extreme performance. Hence, we set the reference mesh assumed to provide sufficient accuracy with $44k$ quadratic triangular elements, equivalent to $2\,10^5$ degrees of freedom (Fig. 3.1).
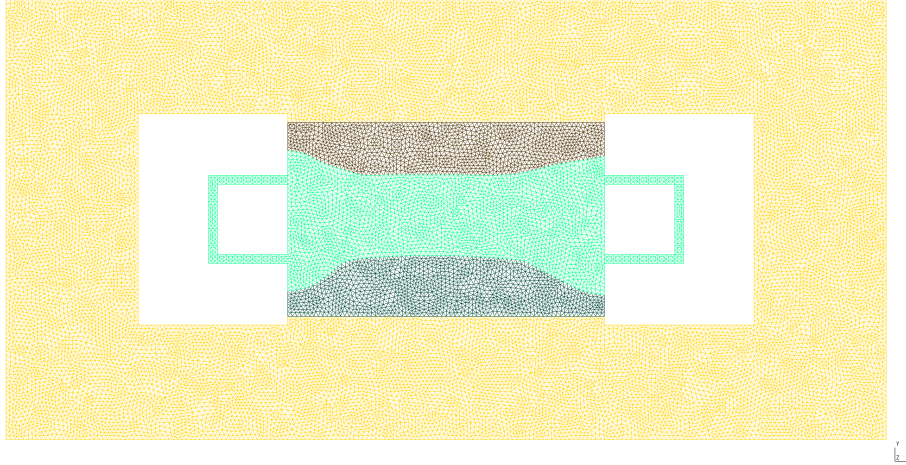
Figure 3.1: Reference mesh employed for convergence study and uncertainty analysis. Published in [266]. As the regions outside keloid and within the observation domain are separated, they have been displayed in different colors by Gmsh.

By analogy with data generation in Section 2.2.2.2, the reference solution was obtained by solving the forward problem with the same material parameters $m_{\text{ref}}^{\text{bimaterial}}$, and for the same boundary conditions. Therefore, we denote u_{ref}, respectively $f_{X\,\text{ref}}$, the reference nodal solutions (displacement), respectively the integrated force over the pad sensor, obtained from Equations 2.10 and 2.11. The nodal solutions and the integrated force on the other coarser meshes are denoted by u_{mesh} and $f_{X\,\text{mesh}}$. Thus, the relative errors, $\varepsilon_{\text{mesh}}^{u}$ and $\varepsilon_{\text{mesh}}^{F}$, are computed as:

$$
\begin{aligned}
\varepsilon_{\text{mesh}}^{u} &= \frac{\|u_{\text{mesh}} - u_{\text{ref}}\|_2}{\|u_{\text{ref}}\|_2} \\
\varepsilon_{\text{mesh}}^{fx} &= \frac{(f_{X\,\text{mesh}} - f_{X\,\text{ref}})^2}{f_{X\,\text{ref}}^2}
\end{aligned}
\tag{3.1}
$$

In Figure 3.2, we plot the evolution of the error norms expressed in Equation 3.1 and computed for each mesh density, and for triangular with linear and quadratic interpolation. Two different media were considered: bi-material (Fig. 3.2a) and mono-material (Fig. 3.2b). For the mono-material

case, the parameter set $\boldsymbol{m}_{\text{ref}}^{\text{monolithic}}$ was utilized. As result, we observe a monotonic decrease of $\varepsilon_{\text{mesh}}^{u}$ for both configurations. As the curves decrease with similar shape, one could conclude that the discrepancy is not due to the mechanical properties. $\varepsilon_{\text{mesh}}^{u}$-curves in Figure 3.2 also show a significant gap between linear and quadratic interpolation impacts. Hence, using linear elements to identify the parameters cannot be accurate, which will be inspected later. Moreover, $\varepsilon_{\text{mesh}}^{fx}$-curves does not exhibit a proper decrease for high mesh density, where the maximum value of $\varepsilon_{\text{mesh}}^{F}$ does not exceed 2.10^{-4}, for quadratic mesh. This non-monotonicity may be due to the derivation process, as the forces are obtained from the displacement gradient in post-treatment. The derivation could lead to additional numerical errors due to round-off, truncation, or interpolation errors [392]. Same as for $\varepsilon_{\text{mesh}}^{u}$, the discrepancy in reaction force is highly impacted by the interpolation degree. Also, in case of linear elements, the force is sensitive to the change in mechanical properties. Nevertheless, the analysis of discretization error revealed a successful mesh convergence for the quadratic elements.

(a) Bimaterial

(b) Monomaterial
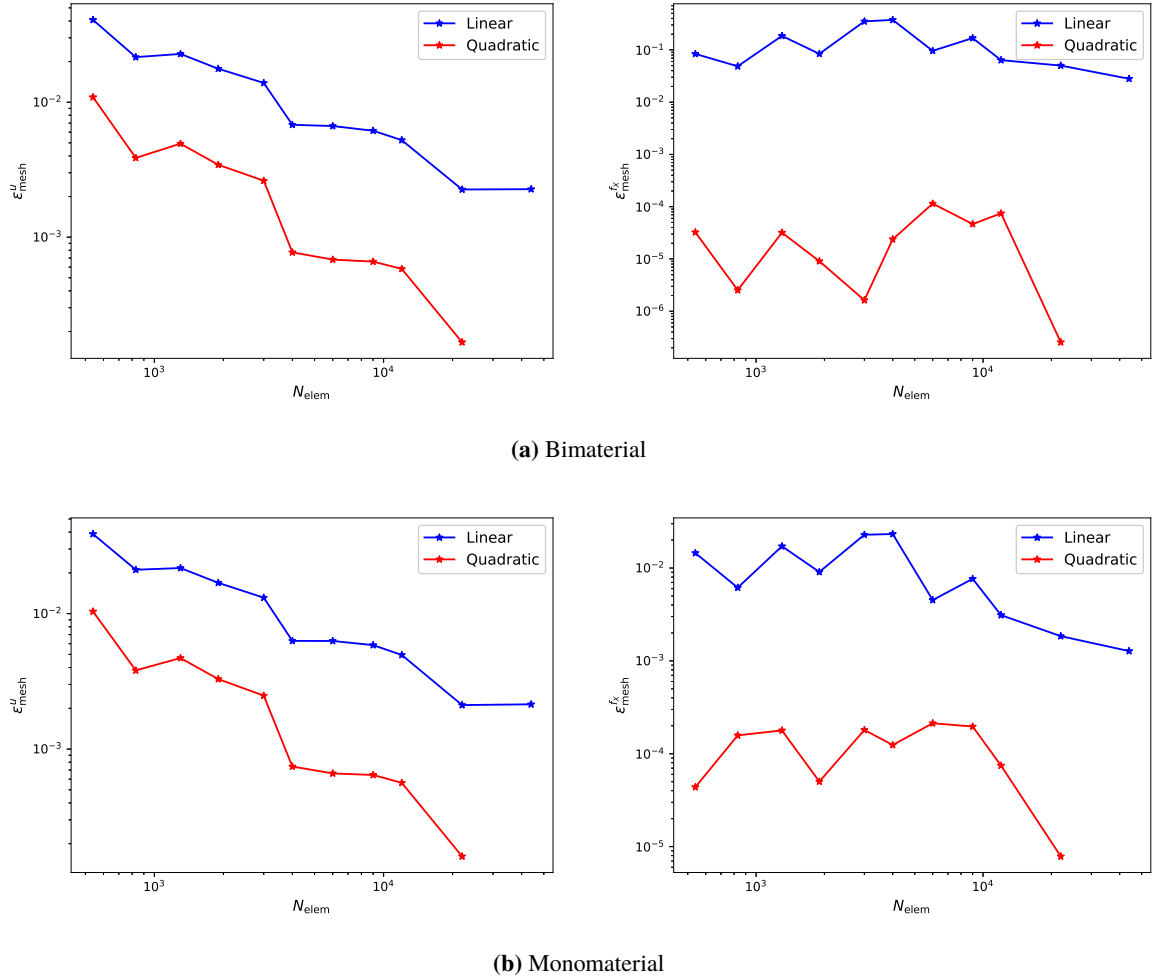
Figure 3.2: Discretization error study of the forward solver in terms of element degree and element size. The numerical values for each case are reported in Tables 3.1 and 3.2. All figure have been published in [266]

3.1.1.2 Computation Cost

The calculation duration, namely, the computation cost, is a major criterion in element density and interpolation choice. The computation in the forward solver should be fast enough to conduct many times in the iterative optimization process. As shown in Figure 3.3a, using the reference mesh of 44k elements is too costly, with around 1000 seconds to accomplish the 50 steps. When it comes to identifying $\boldsymbol{m}_{\text{ref}}^{\text{bimaterial}}$, as in Figure 2.17, the optimization process would be realized in 6 hours on a

Table 3.1: Values of mesh convergence analysis results illustrated in Figure 3.2, for coarse sizes. DOFs stands for Degrees of Freedom.

N_{elem}	540	830	1300	1900	3000	4000
Number of DOFs (linear)	650	970	1500	2100	3300	4300
Number of DOFs (quadratic)	2400	3600	5500	7800	12500	16400
$\varepsilon_{\mathrm{mesh}}^{\mathrm{u}}$ for $\boldsymbol{m}_{\mathrm{ref}}^{\mathrm{bimaterial}}$ (linear)	0.0407	0.0216	0.0228	0.0177	0.0139	0.0068
$\varepsilon_{\mathrm{mesh}}^{\mathrm{u}}$ for $\boldsymbol{m}_{\mathrm{ref}}^{\mathrm{bimaterial}}$ (quadratic)	0.0109	0.0039	0.0049	0.0034	0.0026	0.0008
$\varepsilon_{\mathrm{mesh}}^{\mathrm{u}}$ for $\boldsymbol{m}_{\mathrm{ref}}^{\mathrm{monolithic}}$ (linear)	0.0387	0.0211	0.0217	0.0169	0.0131	0.0063
$\varepsilon_{\mathrm{mesh}}^{\mathrm{u}}$ for $\boldsymbol{m}_{\mathrm{ref}}^{\mathrm{monolithic}}$ (quadratic)	0.0104	0.0038	0.0047	0.0033	0.0025	0.0007
$\varepsilon_{\mathrm{mesh}}^{fx}$ for $\boldsymbol{m}_{\mathrm{ref}}^{\mathrm{bimaterial}}$ (linear)	0.0838	0.0486	0.1853	0.0841	0.3517	0.3749
$\varepsilon_{\mathrm{mesh}}^{fx}$ for $\boldsymbol{m}_{\mathrm{ref}}^{\mathrm{bimaterial}}$ (quadratic)	$3.2\,10^{-5}$	$2.5\,10^{-6}$	$3.2\,10^{-5}$	$9.1\,10^{-6}$	$1.6\,10^{-6}$	$2.4\,10^{-5}$
$\varepsilon_{\mathrm{mesh}}^{fx}$ for $\boldsymbol{m}_{\mathrm{ref}}^{\mathrm{monolithic}}$ (linear)	0.0145	0.0061	0.0172	0.0091	0.0228	0.0232
$\varepsilon_{\mathrm{mesh}}^{fx}$ for $\boldsymbol{m}_{\mathrm{ref}}^{\mathrm{monolithic}}$ (quadratic)	$4.4\,10^{-5}$	$1.6\,10^{-4}$	$1.8\,10^{-4}$	5.0210^{-5}	$1.8\,10^{-4}$	$1.2\,10^{-4}$

Table 3.2: Values of mesh convergence analysis results illustrated in Figure 3.2, for fine sizes. DOFs stands for Degrees of Freedom.

N_{elem}	6000	9000	12000	22000	44000
Number of DOFs (linear)	5600	7900	11900	21000	46500
Number of DOFs (quadratic)	21500	30600	46500	82300	184000
$\varepsilon_{\mathrm{mesh}}^{\mathrm{u}}$ for $\boldsymbol{m}_{\mathrm{ref}}^{\mathrm{bimaterial}}$ (linear)	0.0067	0.0061	0.0052	0.0023	0.0023
$\varepsilon_{\mathrm{mesh}}^{\mathrm{u}}$ for $\boldsymbol{m}_{\mathrm{ref}}^{\mathrm{bimaterial}}$ (quadratic)	0.0007	0.0007	0.0006	0.0002	0
$\varepsilon_{\mathrm{mesh}}^{\mathrm{u}}$ for $\boldsymbol{m}_{\mathrm{ref}}^{\mathrm{monolithic}}$ (linear)	0.0063	0.0059	0.005	0.0021	0.0021
$\varepsilon_{\mathrm{mesh}}^{\mathrm{u}}$ for $\boldsymbol{m}_{\mathrm{ref}}^{\mathrm{monolithic}}$ (quadratic)	0.0007	0.0006	0.0006	0.0002	0
$\varepsilon_{\mathrm{mesh}}^{fx}$ for $\boldsymbol{m}_{\mathrm{ref}}^{\mathrm{bimaterial}}$ (linear)	0.0959	0.1684	0.0637	0.0501	0.028
$\varepsilon_{\mathrm{mesh}}^{fx}$ for $\boldsymbol{m}_{\mathrm{ref}}^{\mathrm{bimaterial}}$ (quadratic)	$1.1\,10^{-4}$	$4.7\,10^{-5}$	$7.5\,10^{-5}$	$2.6\,10^{-7}$	0
$\varepsilon_{\mathrm{mesh}}^{fx}$ for $\boldsymbol{m}_{\mathrm{ref}}^{\mathrm{monolithic}}$ (linear)	0.0045	0.0077	0.0031	0.0018	0.0013
$\varepsilon_{\mathrm{mesh}}^{fx}$ for $\boldsymbol{m}_{\mathrm{ref}}^{\mathrm{monolithic}}$ (quadratic)	$2.1\,10^{-4}$	$2\,10^{-4}$	$7.5\,10^{-5}$	$7.9\,10^{-6}$	0

desktop computer (Intel(R) Core(TM) i7-8700 CPU, 3.2 GHz, 8 GB RAM) providing that the initial guess lead convergence. The modeler needs to test many initial sets, which makes the whole operation last for days.

Figure 3.3b shows that the total number of iterations is not fully monotonic. The non-linear FEM convergence correlates with the number of elements only for the fine meshes, $N_{\text{elem}} > 6000$ elements. For $N_{\text{elem}} < 4000$, the non-linear FEM solver struggles somehow to find a stationary solution. Later, a focused study will be presented to explain this abnormality at low element density levels based on mesh quality. By dividing the values in Figure 3.3a by their respective in 3.3b, one would notice a strong correlation between the mesh density and the cost per one forward solver iteration in logarithmic (Fig. 3.3c) and linear (3.3d) scales, meaning that cost is mainly due to matrix inversion in the system $[\widetilde{K}]\{u\} = \{f\}$.

(a) Computation time

(b) Number of iterations

(c) Computation time
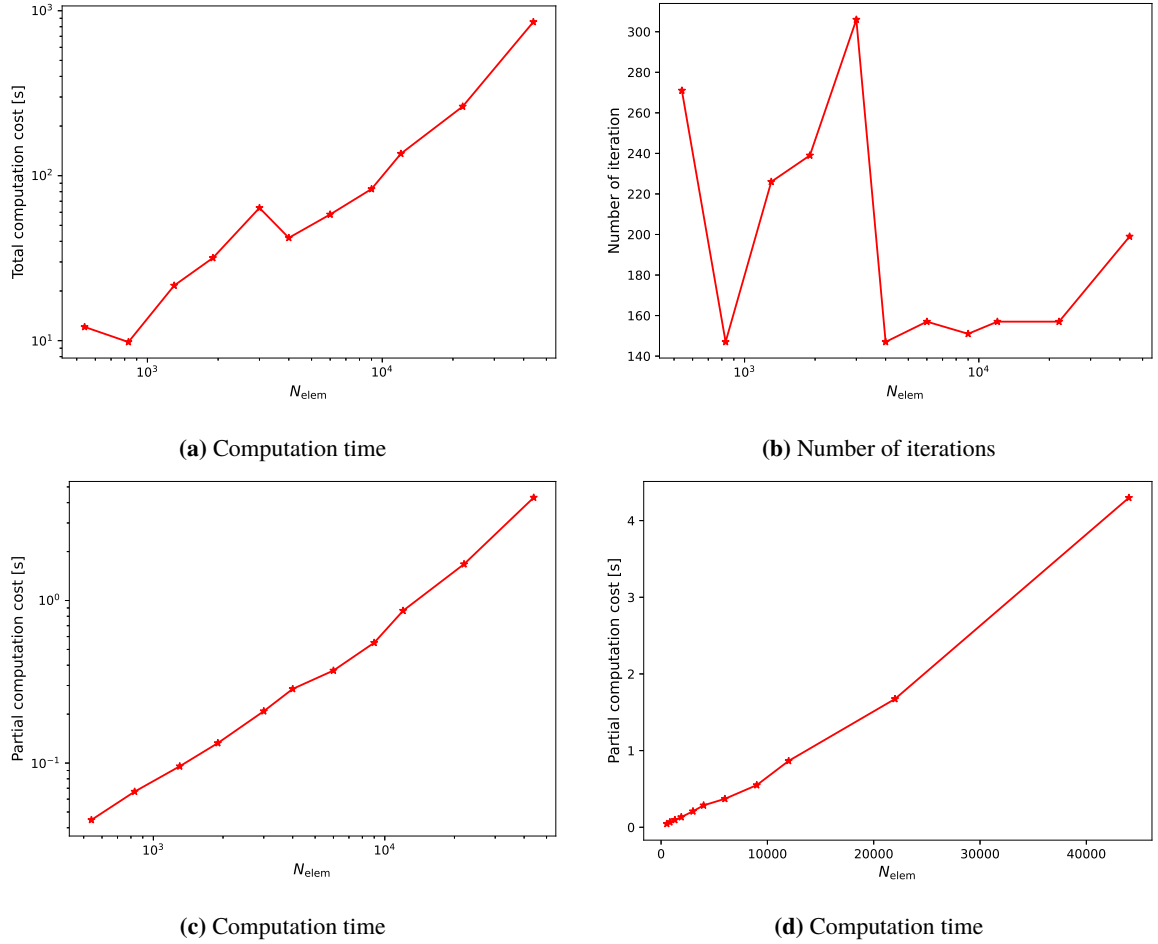
(d) Computation time

Figure 3.3: Computational costs of forward nonlinear simulation. The different meshes contain quadratic elements. (a) Total costs over the 50 load steps. (b) Number of iterations over the 50 load steps. (c) & (d) Cost per each iteration for logarithmic and linear scales, respectively. (a) and (b) have been published in [266]

In an attempt to explain why some coarse meshes require a few iterations to converge compared to finer ones (Fig. 3.3b), the number of iterations required from the linear solver (used for $\widetilde{K}$ matrix inversion) to converge was computed for each load step, for meshes with $N_{\text{elem}} < 4000$. The use of linear elements leads to a fast convergence within 3 sub iteration whatever the mesh density (Fig. 3.4a). However, with the quadratic elements, the linear solver struggles to converge for $N_{\text{elem}} = 3000$, but not for a coarser mesh, such as $N_{\text{elem}} = 830$, as noticed in Figure 3.4b. For $t_k \geq 30$, the number of iterations in the linear solver increases exponentially for $N_{\text{elem}} = 540$ and $N_{\text{elem}} = 3000$, which could be caused by a critical deformation of some cells, unlike $N_{\text{elem}} = 830$.

(a) Linear

(b) Quadratic
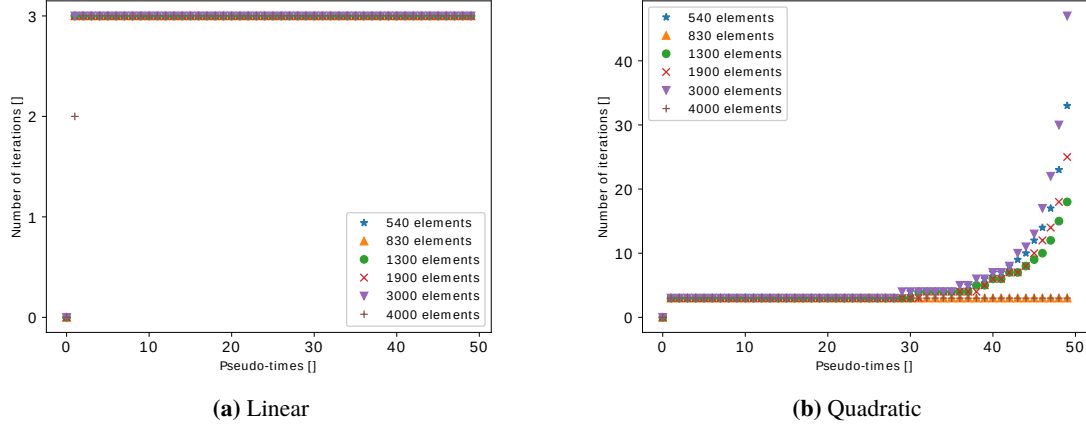
Figure 3.4: Linear solver iterations for each load step.

In Figure 3.5, values of the aspect ratio of all cells were mapped. For triangular elements, the aspect ratio quality criterion reveals the degree of conformity of an element to the regular triangle, where all edges have the same length. Its formula is given by [393]

$$q_a = \frac{l_{\max}(l_0 + l_1 + l_2)}{4\sqrt{3}A_{\text{elem}}} \tag{3.2}$$

where l_i ($i = 1, 2, 3$) is the edge length and A_{elem} the area. A direct comparison between meshes with 830 and 3000 elements revealed that q_a is no higher than 3.5, which is an acceptable ratio. Also, the distortion value of all elements is around 1. On that account, the convergence difficulty reported in Figure 3.4b might not be linked to the element shape in the deformed state, as confirmed by linear interpolation in Figure 3.4a. If quadratic elements had difficulty converging, unlike linear ones in the same mesh (3000 elements), one would assume that adding intermediate vertices would delay finding the stationary solution as the linear system becomes bigger. By referring to Figure 3.3b, we presume that the mesh generation for $N_{\text{elem}} < 4000$ has a hazardous impact on the nonlinear forward solver convergence. Using finer mesh would ensure that the solver converges within a few iterations.

3.1.2 Parameter Identification

Earlier in Section 2.2.2.2, I addressed the validation of the optimization solver through the identification of the target $\boldsymbol{m}_{\text{ref}}^{\text{bimaterial}}$ with an optimized mesh (described in Sec. 3.1.3). The identification process was applied to different meshes with linear then quadratic elements. For every identified parameter set $\hat{\boldsymbol{m}}$, the identification accuracy with respect to the target was assessed *via* the following relative discrepancy

$$\varepsilon_{\text{opt}_i} = \frac{|\hat{m}_i - m_i|}{|m_i|} \quad ; \quad \hat{m}_i \in \hat{\boldsymbol{m}} \text{ and } m_i \in \boldsymbol{m}_{\text{ref}}^{\text{bimaterial}} \tag{3.3}$$

3.1.2.1 Linear Mesh

Starting from an initial set relatively far from the target, $\boldsymbol{m}^{(0)} = \{\mu_{\text{k}} = 0.01 \text{ MPa}, J_{m\text{k}} = 0.01, \mu_{\text{hs}} = 0.01 \text{ MPa}, J_{m\text{hs}} = 0.01\}$ and $\Lambda^{(0)} = 10^{-4}$, the optimization solvers reduce iteratively the data discrepancy issued from a quadratic mesh with $N_{\text{elem}} = 44$ k elements, set as the reference, and linear meshes with less density. Table 3.3 summarizes the identified parameter values of each mesh with linear elements.
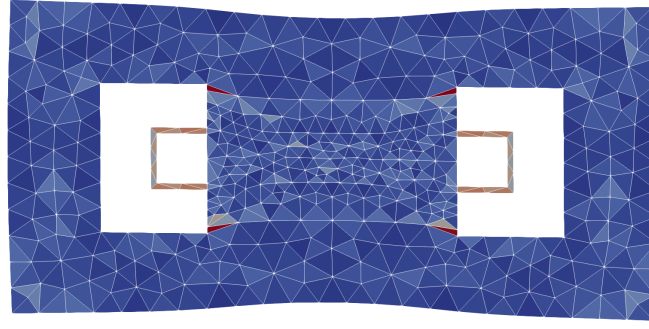
(a) $N_{\text{elem}} = 830$
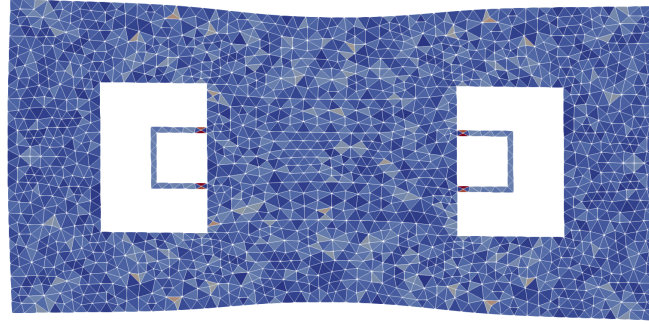
(b) $N_{\text{elem}} = 3000$

Figure 3.5: Mesh quality map in the deformed state based on the aspect ratio. The mapping was performed on `Paraview` using the `Mesh Quality` filter for the load step $t_k = 50$, such that $\bar{\boldsymbol{u}}(t_k) = \{-4, 0\}^T$ mm.

The results show a considerable gap between $\hat{\boldsymbol{m}}$ and $\boldsymbol{m}_{\text{ref}}^{\text{bimaterial}}$, which is caused by both discretization and interpolation factors. By focusing on the reference mesh, where only the interpolation differs, one would notice that the discard is significant for μ_{k} and μ_{hs}, but not for $J_{m\text{k}}$ and $J_{m\text{hs}}$. Supposing that the parameter μ is strongly correlated with the force-displacement curve, the important values of ε_{opt} can be explained by the link force/interpolation: as the force is obtained from the derivation of $\boldsymbol{u}$ (the derivation reduces the polynomial degree by one), using linear interpolation would results in a discard of the force-displacement curve with respect to a quadratic interpolation, and thus a discard in the estimated parameters with respect to $\boldsymbol{m}_{\text{ref}}^{\text{bimaterial}}$.

To conclude, the use of linear element demonstrated an incapacity to identify accurately the reference material parameters even when using data on highly refined mesh (44k elements). This inaccuracy can be associated with the large relative error observed for linear elements in Figure 3.2, where $\varepsilon_{\text{mesh}}^{fx} > 10^{-2}$ for the bi-material case. On the other hand, the results showed that the initial guess in the inverse solver can be relatively far from the reference in case of the linear interpolation, i.e., up to $\frac{|\hat{m}_i|}{|m_i|} \approx 40$ for $\hat{m}_i \in \hat{\boldsymbol{m}}$ and $m_i \in \boldsymbol{m}_{\text{ref}}^{\text{bimaterial}}$.

Table 3.3: Material parameters identification from reference data projected on linear meshes.

N_{elem}	Converged parameter set $\hat{\boldsymbol{m}}$	ε_{opt}
540	$\mu_{\text{k}} = 40.37$ kPa	0.1926
	$J_{m\text{k}} = 0.1949$	0.0255
	$\mu_{\text{hs}} = 7.5$ kPa	0.5313
	$J_{m\text{hs}} = 0.491$	0.2275
1300	$\mu_{\text{k}} = 36.358$ kPa	0.2729
	$J_{m\text{k}} = 0.1931$	0.0345
	$\mu_{\text{hs}} = 10.237$ kPa	0.3602
	$J_{m\text{hs}} = 0.4549$	0.1373
6000	$\mu_{\text{k}} = 38.825$ kPa	0.2235
	$J_{m\text{k}} = 0.2008$	0.0040
	$\mu_{\text{hs}} = 12.265$ kPa	0.2334
	$J_{m\text{hs}} = 0.4166$	0.0415
12000	$\mu_{\text{k}} = 41.432$ kPa	0.1714
	$J_{m\text{k}} = 0.2006$	0.003
	$\mu_{\text{hs}} = 12.906$ kPa	0.1934
	$J_{m\text{hs}} = 0.4138$	0.0345
22000	$\mu_{\text{k}} = 42.51$ kPa	0.1498
	$J_{m\text{k}} = 0.2019$	0.0095
	$\mu_{\text{hs}} = 13.19$ kPa	0.1756
	$J_{m\text{hs}} = 0.4042$	0.0105
44000	$\mu_{\text{k}} = 44.04$ kPa	0.1192
	$J_{m\text{k}} = 0.2002$	0.0010
	$\mu_{\text{hs}} = 13.91$ kPa	0.1306
	$J_{m\text{hs}} = 0.406$	0.0150

3.1.2.2 Quadratic Mesh

In the case of quadratic interpolation, setting the same initial guess as in Section 3.1.2.1, far from the target, requires costly computations and, most of the time, results in a divergence. Hence, the identified values with linear meshes were set as the initial guess for the quadratic meshes. For example, $J_{m\text{hs}}^{(0)} = 0.01 \rightarrow J_{m\text{hs}}^{\text{linear}} = 0.406 \rightarrow J_{m\text{hs}}^{\text{quadratic}} = J_{m\text{hs}}^{\text{reference}} = 0.4$. The complete list of the converged parameter sets $\hat{\boldsymbol{m}}$ for each quadratic mesh is reported in Table 3.4.

The values of $\hat{\boldsymbol{m}}$ and ε_{opt} confirm that using coarse meshes would cause uncertainties in parameter identification; 8% of error occurred in the identification of $J_{m\text{hs}}$ when using a 540-elements mesh. Starting from finer mesh, $N_{\text{elem}} \leq 6000$, the errors drops to 1%, unlike in Table 3.3 with errors around 23% for $N_{\text{elem}} = 6000$. The last comparison affirms that when choosing between discretization and interpolation to improve the identification accuracy, the priority is to use elements with higher interpolation degrees. Besides, if one assumes that the quadratic elements represent better the captured DIC fields, using successively linear, then a quadratic mesh would be an efficient technique to converge to the most accurate parameter set.

3.1.3 Adaptive mesh

Based on criteria qualitatively assessed, affordable computation cost and low discretization error, an "optimal" coarse mesh was designed and tested to investigate the possibility to identify the material parameters accurately with less dense mesh.

Table 3.4: Material parameters identification from reference data projected on quadratic meshes.

N_{elem}	Converged parameter set $\hat{\boldsymbol{m}}$	ε_{opt}
540	$\mu_{\text{k}} = 49.88$ kPa	0.0024
	$J_{m\text{k}} = 0.1923$	0.0385
	$\mu_{\text{hs}} = 16.031$ kPa	0.0019
	$J_{m\text{hs}} = 0.4325$	0.0813
1300	$\mu_{\text{k}} = 50.344$ kPa	0.0069
	$J_{m\text{k}} = 0.1971$	0.0145
	$\mu_{\text{hs}} = 16.115$ kPa	0.0072
	$J_{m\text{hs}} = 0.4133$	0.0333
6000	$\mu_{\text{k}} = 50.52$ kPa	0.0104
	$J_{m\text{k}} = 0.2001$	0.0005
	$\mu_{\text{hs}} = 16.166$ kPa	0.0104
	$J_{m\text{hs}} = 0.4013$	0.0033
12000	$\mu_{\text{k}} = 50.431$ kPa	0.0086
	$J_{m\text{k}} = 0.1999$	0.0005
	$\mu_{\text{hs}} = 16.059$ kPa	0.0037
	$J_{m\text{hs}} = 0.4015$	0.0038
22000	$\mu_{\text{k}} = 50.038$ kPa	0.0008
	$J_{m\text{k}} = 0.2002$	0.001
	$\mu_{\text{hs}} = 16.022$ kPa	0.0014
	$J_{m\text{hs}} = 0.3998$	0.0005
44000 (reference)	$\mu_{\text{k}} = 50.0$ kPa	0.0
	$J_{m\text{k}} = 0.2$	0.0
	$\mu_{\text{hs}} = 16.0$ kPa	0.0
	$J_{m\text{hs}} = 0.4$	0.0

3.1.3.1 Mesh Building

Based on a 540-quadratic-element mesh, additional vertices should be added manually on zones with high discretization error inside the ZOI since the latter is an effective observable zone subjected to the optimization problem. To be able to identify these zones, the difference in nodal solutions between the 540-elements and the reference mesh is first mapped in Figure 3.6. Many vertices were added arbitrarily to the uniform mesh (Fig. 3.7a) in the zone marked by the green ellipses to obtain a moderately fine mesh comprised of 1300 elements. To avoid confusion with another mesh studied earlier comprising 1300 elements uniformly distributed, we name the recent one "optimized mesh" (Fig. 3.7b).

3.1.3.2 Application

In comparison with Figure 3.6, a drop of a factor of 10 was observed in ZOI on Figure 3.8. Thus, the manually-refined adaptive mesh can be a suitable candidate for low-cost yet accurate simulations.

Note that it would be preferable to use a quantitative error indicator. Estimators are used *a posteriori* to evaluate the discretization error. This information is then used to adaptively refine elements where the error is high [394]. During his internship in the Biomechanics team – Department Applied Mechanics/FEMTO-ST – Nicolas Marie worked on creating an adaptive mesh based on the dual-weighted-residual (DWR) method developed for linear elasticity [395]. The DWR method allows for localizing the error contributions to the simulation, compared to an exact solution, on each element. As a result, as shown in Figure 3.9, refinement was applied automatically on the pad corners, and keloid/healthy-skin interface according to a given quantity of interest, for instance, $tr(\boldsymbol{\sigma})$. At first glance, the refinement was in accordance with the error pattern in Figure 3.8. The DWR-based
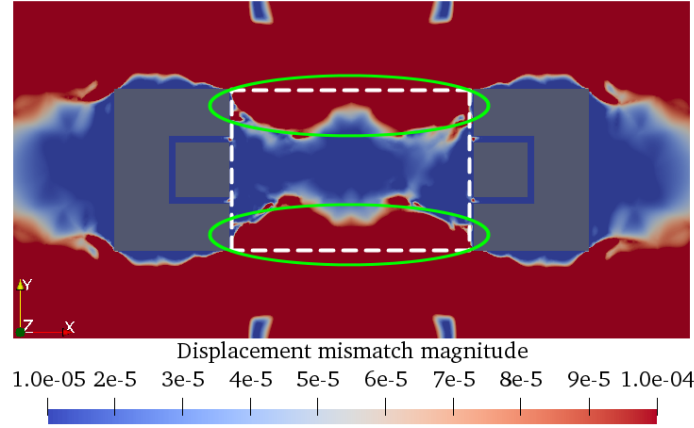
Figure 3.6: The distribution of nodal solutions difference between the 540-elements and reference mesh. Published in [266]

adaptive mesh contained a massive number of elements, $N_{\text{elem}} = 11$ k, which is relatively costly. By changing the targeted precision, the latter could have less number of elements. Its application to our case revealed to be a suitable tool for adaptive mesh refinement in future works.

The optimized mesh was tested in the parameter identification process and compared alongside the meshes introduced in Section 3.1.1. Table 3.5 regroups the identified values $\hat{\boldsymbol{m}}$ and their respective error regarding the target for two interpolation degrees. For quadratic mesh, the maximum value of $\varepsilon_{\text{opt}_i}$ is 1.33 %, which makes it a valid candidate to replace the reference mesh with 44 k elements.

Table 3.5: Material parameters identification from reference data projected on the optimized mesh (1300 elements).

Interpolation	Converged parameter set $\hat{\boldsymbol{m}}$	ε_{opt}
Linear	$\mu_{\text{k}} = 44.101$ kPa	0.1180
	$J_{m\text{k}} = 0.1988$	0.006
	$\mu_{\text{hs}} = 13.28$ kPa	0.17
	$J_{m\text{hs}} = 0.431$	0.0775
Quadratic	$\mu_{\text{k}} = 50.219$ kPa	0.0044
	$J_{m\text{k}} = 0.1994$	0.003
	$\mu_{\text{hs}} = 16.157$ kPa	0.0098
	$J_{m\text{hs}} = 0.4053$	0.0133

In order to emphasize the usefulness of using an adaptive mesh to reduce computation cost without reducing the accuracy in parameter identification, the values of Tables 3.3, 3.4, and 3.5 are combined and plotted in Figure 3.10. A direct comparison of $\hat{\boldsymbol{m}}$'s accuracy between meshes revealed that using adaptive mesh is equivalent to using uniform meshes for $N_{\text{elem}} \leq 6000$ but with fewer costs, which confirms that the adaptive mesh can be very helpful in FEMU processes that run the forward solver hundreds of times, such as Markov chain Monte Carlo scheme.

3.2   Experimental Data

The uncertainty about the identified model parameters studied in the previous part was related only to the discretization error. Another well-known error source that may govern the identification uncertainty is data accuracy. The data acquired from the experiments are commonly accompanied by noise. It can be evaluated by experimenting at least three times. Within our context, the experimental input data are in the form of force-displacement curves and DIC fields. This section aims to study the

(a) 540 elements

(b) Optimized mesh
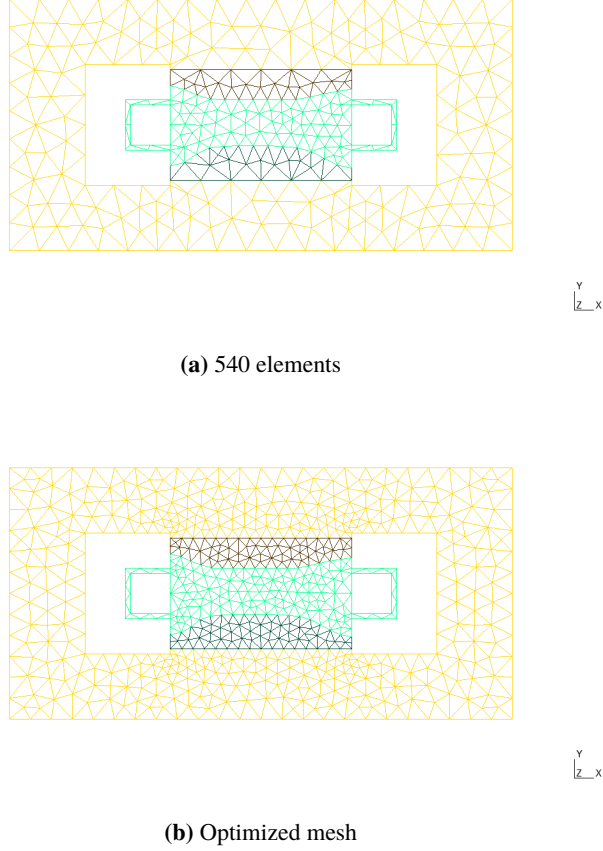
Figure 3.7: Coarsest operational meshes. Published in [266]

influence of their variation on the identified parameters and then set a threshold for every data type that permits control of the identification precision.

3.2.1 Data Uncertainty

In biomechanics, the acquisition of specific-patient data is uncertain because of several factors, among them the *intra*-subject variability, the sensor's stability, and the environmental conditions. The present study focuses on the most crucial factor: the apparatus' precision. Instead of assessing every apparatus component's precision, the whole system's global precision is to be evaluated directly on the experiment outputs. Since the force-displacement and DIC field data are collected independently, their respective uncertainties are uncorrelated and are characterized by their probability distributions.

3.2.1.1 Data Synthesizing

Due to a lack of experimental data (to evaluate their precision), dummy data were generated from the forward FEM solver using the reference mesh with quadratic element and the reference material parameters $\boldsymbol{m}_{\text{ref}}^{\text{bimaterial}}$. Then, for each observation time t_k, Additive White Gaussian Noises (AWGN) were processed on nodal solutions (to synthesize noisy DIC fields) over the ZOI, Ω^{msr}, and on the reaction force (to synthesize noisy force-displacement sets) [397]. The AWGN is a noise model used to mimic the effect of many natural random processes and adds a discrepancy to a point. This discrepancy is governed by zero-mean Gaussian distribution with standard deviation representing the data precision, as such

Displacement mismatch magnitude

1.0e-05 2e-5 3e-5 4e-5 5e-5 6e-5 7e-5 8e-5 9e-5 1.0e-04
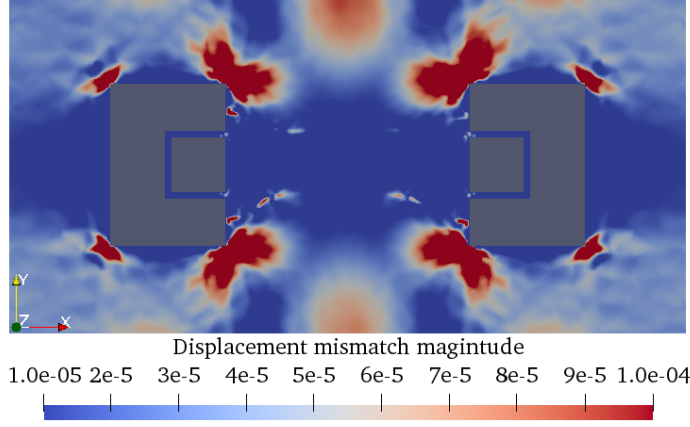
Figure 3.8: The distribution of nodal solutions difference between the optimized and reference mesh. Published in [266]
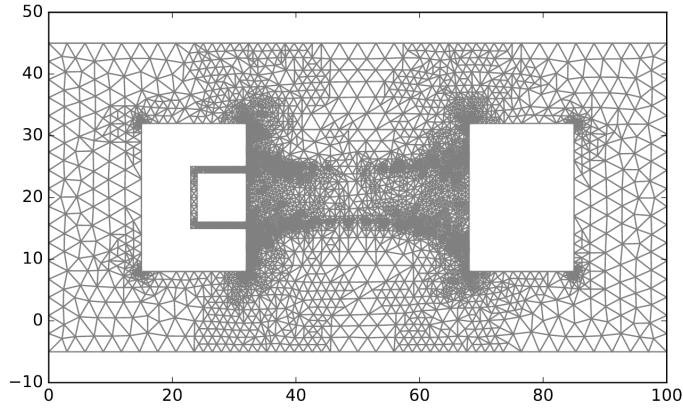
Figure 3.9: Adaptive mesh build upon the dual-weighted-residual method. The figure was reported from Nicola Marie's master thesis [396].

$$\boldsymbol{u}_{\mathrm{msr}}(\boldsymbol{X}_i, t_k) = \mathbf{u}(\boldsymbol{X}_i, t_k) + \Delta_u(\boldsymbol{X}_i, t_k); \quad \forall \boldsymbol{X}_i \in \Omega^{\mathrm{msr}}; \quad k = 0, 1, \ldots, N_E \tag{3.4}$$

and,

$$f_{X\,\mathrm{msr}}(t_k) = f_X(t_k) + \Delta_f(t_k); \quad k = 0, 1, \ldots, N_E \tag{3.5}$$

with Δ_u and Δ_f additive noises for the DIC field and reaction force, respectively. They are generated randomly from the normal distribution:

$$\Delta_u(\boldsymbol{X}_i, t_k) \sim S_{\mathrm{DIC}} \times \mathcal{N}(0, \boldsymbol{I}_2) \tag{3.6}$$

$\mathcal{N}(0, \boldsymbol{I}_2)$ denotes the 2-dimensional normal distribution, accordingly to the bi-dimensional domain Ω^{msr}. The reaction force precision is drawn as following

$$\Delta_f(t_k) \sim S_{\mathrm{force}} \times \mathcal{N}(0, 1) \tag{3.7}$$

S_{DIC} and S_{force} represent the measurement uncertainty in DIC fields and forces and then will be swept for different noise levels to study the identification precision. As an example, Figure 3.11 illustrates the "fuzzified" displacement and reaction force data with $S_{\mathrm{DIC}} = 200$ μm and $S_{\mathrm{force}} = 10$ mN. To quantify the global error resulted from the addition of the random noises to the reference data overall the observation times $N_E = 50$, two numerical indicators were used.
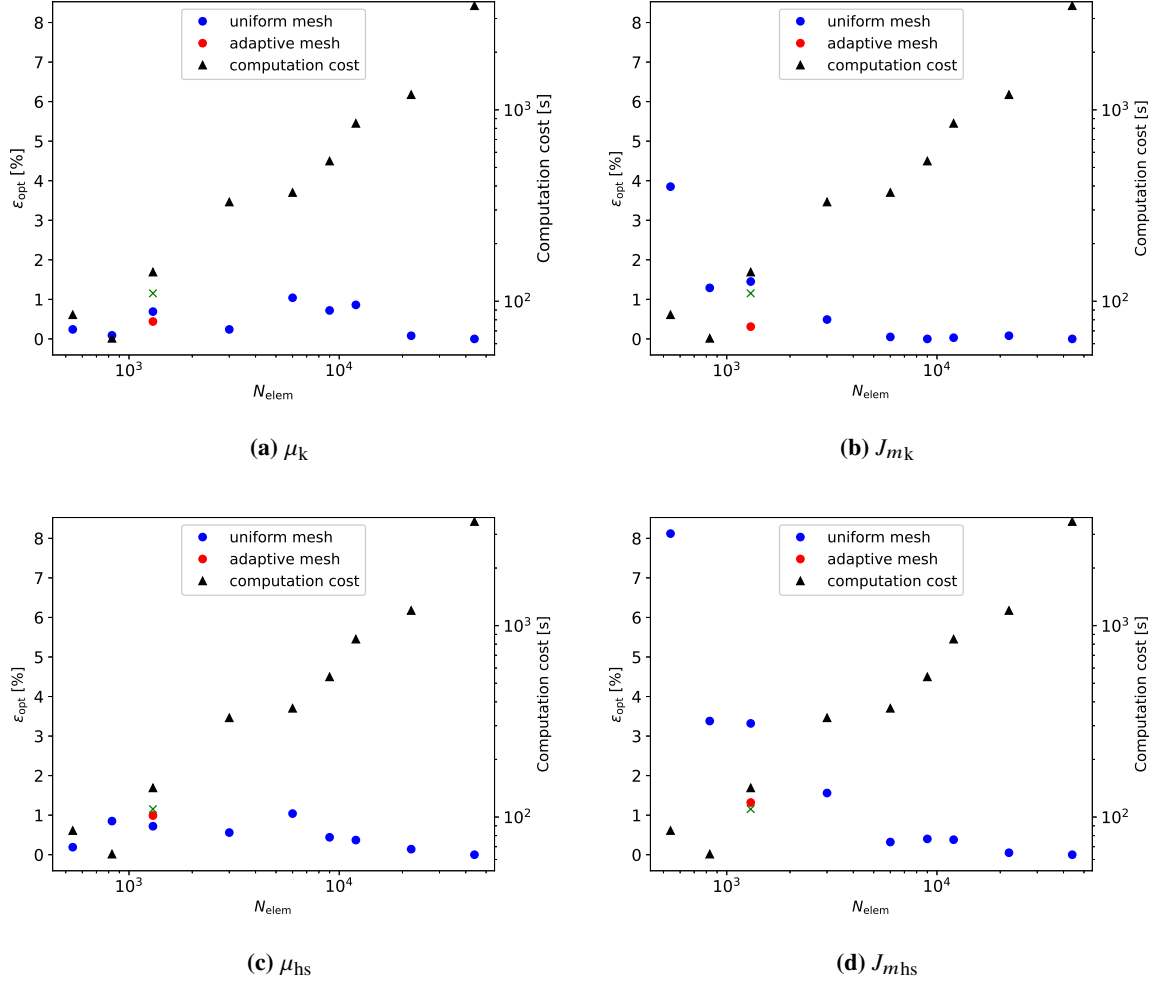
Figure 3.10: Comparison of parameter identification accuracy and computation cost for all meshes. The green cross represents the computation cost for the adaptive mesh.

$$\varepsilon_{\text{DIC}} = \frac{\sqrt{\sum_{k=1}^{N_E} \left\| \boldsymbol{u}_{\text{ref}}(t_k) - \boldsymbol{u}_{\text{msr}}(t_k) \right\|_{\Omega^{\text{msr}}}^2}}{\sqrt{\sum_{k=1}^{N_E} \left\| \boldsymbol{u}_{\text{ref}}(t_k) \right\|_{\Omega^{\text{msr}}}^2}} \tag{3.8}$$

$$\varepsilon_{\text{force}} = \frac{\sqrt{\sum_{k=1}^{N_E} \left(f_{X\text{msr}}(t_k) - f_{X\text{ref}}(t_k) \right)^2}}{\sqrt{\sum_{k=1}^{N_E} \left(f_{X\text{ref}}(t_k) \right)^2}} \tag{3.9}$$

3.2.1.2 Parameter Identification

All the 50 DIC frames were synchronized with the incremental prescribed displacement $\bar{\boldsymbol{u}}(t_k)$ (from undeformed configuration to 4 mm traction). Standard deviations for both dummy displacement field and reaction force were varied separately, with $S_{\text{DIC}} = \{0; 40; 120; 200\}$ µm and $S_{\text{force}} = \{0; 2; 6; 10\}$ mN. Therefore, the optimization solver used 16 noised synthetic data sets as experimental data. In the meantime, the zero-noise cases were considered to dissociate the effects of the two error sources on parameter identification. In opposition with the study in Section 3.1.2, the initial guess was set close to the target: $\boldsymbol{m}_L^{(0)} = \{\mu_k = 49 \text{ kPa}; J_{mk} = 0.19; \mu_{\text{hs}} = 15 \text{ kPa}; J_{m\text{hs}} = 0.39\}$. As the study only concerns measurement noise's effect on parameter identification precision, it would be reasonable to reduce the number of iterations toward convergence. Setting a further $\boldsymbol{m}_L^{(0)}$ in case
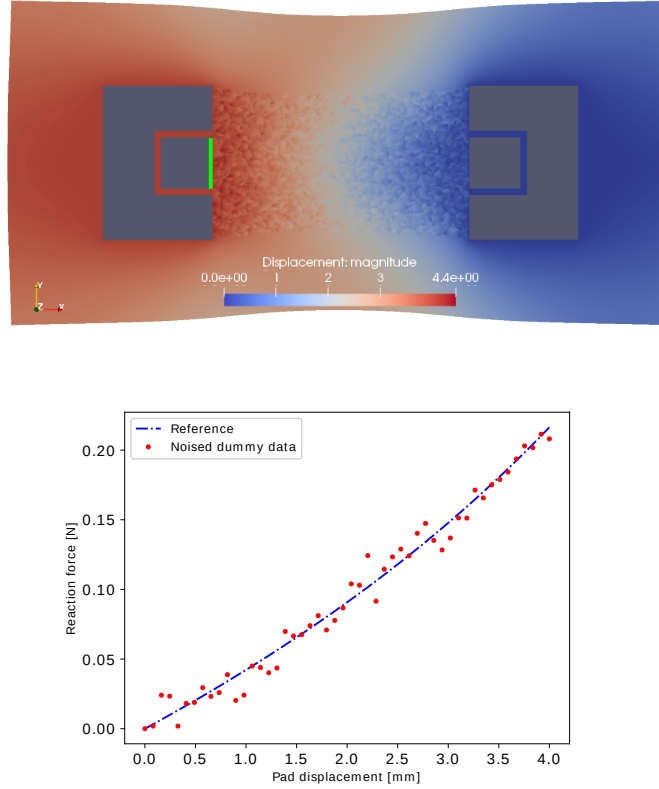
Figure 3.11: Application of the Additive White Gaussian process to DIC field and force-displacement curve. Published in [266]

of high data noise would result in convergence to an undesirable local minimum.

Two cases were investigated when studying the measurement noise's effect on the inverse solutions without then with considering discretization errors. In the former, the same mesh used to generate the data was used to identify the parameters. Hence, the discrepancies on each parameter ε_{opt} would inform how precise the identification was. While in the latter, the adaptive mesh was used to study the effect of discretization error combined with measurement noise. Figure 3.12 shows the discrepancies of the identified parameters from the first case for all noise level sets. As the noise distribution is based on randomness, the noised dummy data samples were drawn three times. The maximum value of discrepancies was retained and plotted in the form of 2D color maps (Fig. 3.12d). All the values are reported in Table A.1 (Appendix A). Similarly, the discrepancies of the identified parameters with data from the adaptive mesh are summarized in Figure 3.13 and detailed in Table A.2.

When the data were projected on the reference mesh, the maximum value of ε_{opt} did not exceed 2.5 % for noise indicators reaching up $\varepsilon_{\text{DIC}} = 8$ % and $\varepsilon_{\text{force}} = 12$ %. Once adding noise on forces only ($S_{\text{DIC}} = 0\ \mu\text{m}$), we notice that the identification of $J_{m\text{k}}$ and $J_{m\text{hs}}$ are perfectly precise. On the other hand, μ_{k} and μ_{hs} are equivalently sensitive to perturbations on the reaction force, meaning that those parameters are tightly related to material stiffness. Inversely, by focusing only on perturbed displacement ($S_{\text{force}} = 0$ mN), we notice that all parameters discrepancies, most important, $J_{m\text{k}}$ and $J_{m\text{hs}}$, increase for higher noise level on DIC. Finally, the combination of both DIC and forces measurement noise does not lead to higher mismatches as expected, and the maximum parameter discrepancy is below 2.5%. Combining data with nature would lead to mutual compensation in errors, and the identification tends to be accurate for measurement uncertainty lower than $S_{\text{DIC}} = 200\ \mu\text{m}$ and $S_{\text{force}} = 10$ mN.

In the adaptive mesh case, the relative discrepancies increase higher because of discretization errors.

(a) 1st draw

(b) 2nd draw

(c) 3rd draw

(d) Maximum
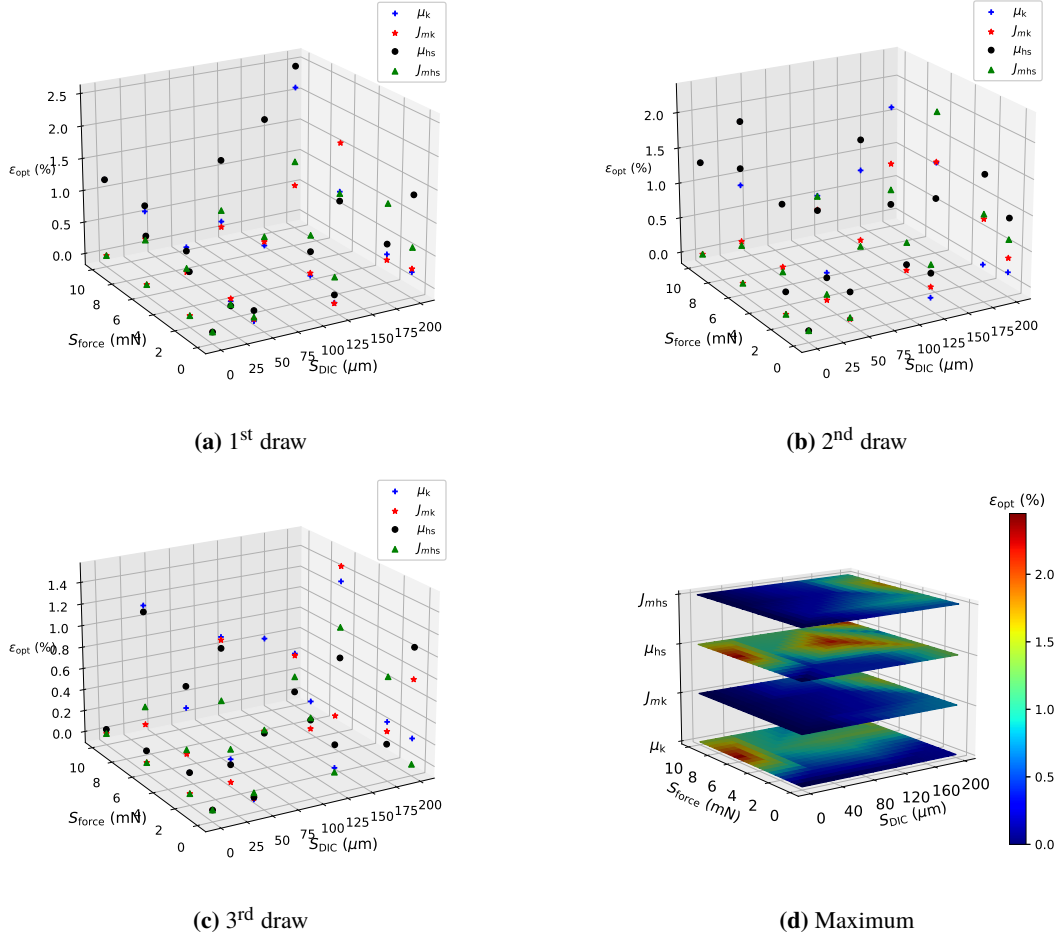
Figure 3.12: Parameter identification precision study performed on noised dummy data with different noise level sets using reference mesh. (d) has been published in [266]

Figure 3.13 shows that for all noise levels, ε_{opt} of keloid parameters, μ_{k} and $J_{m\text{k}}$, are likely very low (<1 %), except for some critical cases where it reaches 4 % (Table A.2). The other parameters, μ_{hs} and $J_{m\text{hs}}$, are more sensitive to the combination measurement noise and discretization error, with a maximum discrepancy approximating 7.5 %. The errors are high on the healthy-skin material because of the lack of vertices in the coarser adaptive mesh outside the keloid scar domain. In the healthy-skin domain, the nodal solutions are sensitive to material parameter change, which could be noticed in Sutula *et al.*'s work [1]. Also, Table A.2 shows clearly that the J_m parameter for both materials is not affected by a change of uncertainty in force as their values remain constant for a fixed S_{DIC} and variable S_{force}. Thus, efforts on reducing the DIC uncertainty are much recommended to enhance accuracy in identifying $J_{m\text{k}}$ and $J_{m\text{hs}}$. To conclude, although ε_{opt} is higher in the adaptive than the reference mesh, ε_{opt} is still lower than 5 % for all parameters and for all noise levels providing that the measurement uncertainties do not reach $S_{\text{DIC}}^{\text{adm}} = 120$ μm and $S_{\text{force}}^{\text{adm}} = 8$ mN. The latter will be used to check the validity of the acquired measurement data in a *in vivo* test.

3.2.2 Data Quantity

In this part, we study the effect of the amount of data on identification uncertainty. Consequently, we expect to answer the question, "how many DIC frames and load steps are needed to ensure stable values of $\hat{\boldsymbol{m}}$." We describe how the noised synthetical data were obtained and split according to equidistant observation times. Then, we report the parameter identification results for different datasets and discuss them.
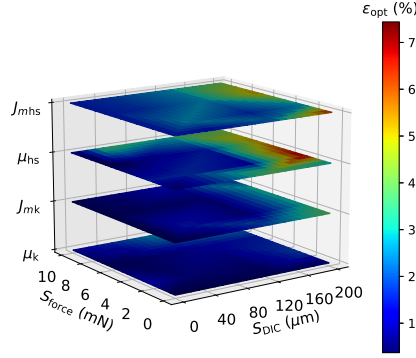
Figure 3.13: Parameter identification precision study performed on noised dummy data with different noise level sets using reference mesh. Published in [266]

3.2.2.1 Data Synthesizing

From the full set of the $N_E = 50$ perturbed dummy data, subsets with N_S observation times were selected and distributed uniformly over the whole time range. Two scenarios were explored: weakly and highly nonlinear force-displacement curves (Figures A.1 and A.2). The targeted material parameters $\boldsymbol{m}_{\text{ref}}$, the number of elements in N_E, and noises S_{force} and S_{DIC} were partially set differently for both cases. The noises were added to nodal displacements and derived forces computed with the reference mesh. As a reminder, the reference mesh contains 44 k quadratic elements.

For the weakly nonlinear case, the following was set, $\boldsymbol{m}_{\text{ref}}^{\text{w}} = \boldsymbol{m}_{\text{ref}}^{\text{bimaterial}}$, $S_{\text{force}} = 20$ mN, $S_{\text{DIC}} = 200$ μm, and $N_S \in \{5; 10; 20; 50; 100\}$. While for the highly nonlinear, it was set that $\boldsymbol{m}_{\text{ref}}^{\text{h}} = \{\mu_{\text{k}} = 10$ kPa; $J_{m\text{k}} = 0.017; \mu_{\text{hs}} = 8$ kPa; $J_{m\text{hs}} = 0.17\}$, $S_{\text{force}} = 20$ mN, $S_{\text{DIC}} = 200$ μm, and $N_S \in \{20; 25; 40; 100; 200\}$. In that situation, more points were added to cover the twisted part efficiently in the highly nonlinear curve. In additions, to simulate highly nonlinear reaction force, a zero-displacement condition in the Y-direction was applied to the top and bottom external boundaries (Fig. 2.6). To quantify global noises over the pseudo-times subsets, the same indicators ε_{DIC} and $\varepsilon_{\text{force}}$ were used by replacing N_E, the total number of time steps, with N_S, the number of the partial time sub-steps in Equations 3.8 and 3.9.

3.2.2.2 Parameter Identification

As the noise distribution is based on randomness, the dummy noises were drawn three times, and only the maximum discrepancies are maintained in Figure 3.14. All the other values are reported in Table A.3. At first glance, the error bars show that discrepancies in the identified parameters decrease with increasing DIC frames and load steps. For a low amount of data, $N_S \leq 50$, the identification is imprecise; hence if the method is applied to real data, the uncertainty about the identified parameters is high.

Moreover, in both cases, $J_{m\text{k}}$ and $J_{m\text{hs}}$ are more likely insensitive to data quantity. By referring to the explanation provided earlier, which stipulates that $J_{m\text{k}}$ and $J_{m\text{hs}}$ are correlated exclusively with the displacement fields, unlike μ_{k} and μ_{hs} (which are strongly correlated with the reaction force), one might conclude that the inverse solver needs few DIC frames to identify $J_{m\text{k}}$ and $J_{m\text{hs}}$. Securing precision and accuracy in identifying the parameters is conditioned by a rich force-displacement dataset. Therefore, based on the obtained results, a trade-off between the number of equidistant observation pseudo-times and computation cost should be carried on. Choosing N_S around 100 would necessitate reasonable cost and lead to enough precise estimation.

(a) Weakly nonlinear

(b) Highly nonlinear
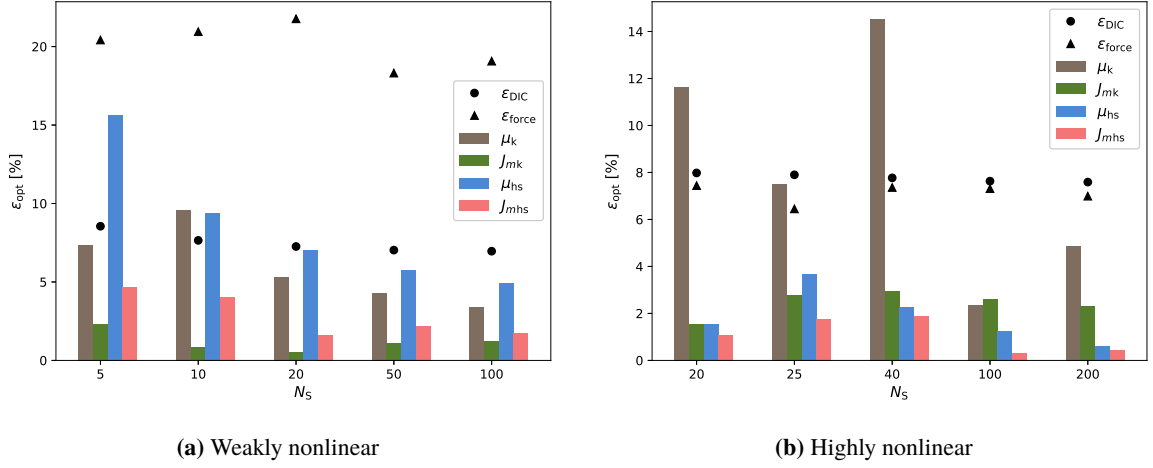
Figure 3.14: Study of data quantity on parameter identification precision. Published in [266]

3.3 Boundary Conditions

Another aspect that plays a role in characterization uncertainty is topology. To develop the method described in Chapter 2, the external boundary widths (Fig. 2.6) were set arbitrarily according to a previous study [1]. Even so, in Section 3.2.2.1, it was reported that modifying some boundary conditions could severely change the mechanical response, in occurrence weakly to highly nonlinear behavior. Thus, a study about the influence of the domain dimensions on the accuracy of the identified parameters was conducted and is reported in the current section.

3.3.1 Material and Methods

The final objective of this study is to determine the domain length and width, respectively, L_Ω and W_Ω (Fig. 3.15), such that the borders' effect on the simulated reaction force is null. We proceed by evaluating a relative discrepancy ε_{LW} between two different boundary condition configurations for a set of combinations of the topological parameters. In one of them, labeled "constrained boundaries", the displacement in Y-direction was set null along the top and bottom boundaries. In the other configuration, labeled "free boundaries", the same boundaries remained free on any constraint. The expression of ε_{LW} is given by

$$\varepsilon_{\text{LW}} = \frac{\sqrt{\sum_{k=1}^{N_E} \left(f_{X\,\text{free}}(t_k) - f_{X\,\text{constrained}}(t_k) \right)^2}}{\sqrt{\sum_{k=1}^{N_E} \left(f_{X\,\text{constrained}} \right)^2}} \tag{3.10}$$

It represents the relative mismatch between two force-displacement curves obtained for different configurations.

10 equidistant values for $L_\Omega \in [150, 300]$ mm and $W_\Omega \in [100, 300]$ mm were assigned to the geometry generator in `Gmsh` for every set of geometrical parameters. The value 300 mm as a maximum of W_Ω corresponds to the arm's circumference. Afterward, the geometrical models were meshed uniformly so that the number of elements neared the computation limits (Fig. 3.16). The average element was checked to be small enough to result in discretization error (based on the study in Section 3.1). The material parameters were set to simulate the highly nonlinear response, as the boundary conditions strongly impact the latter, thereby $\boldsymbol{m}_{\text{ref}}^{\text{h}} = \{\mu_{\text{k}} = 10 \text{ kPa}; J_{m\text{k}} = 0.017; \mu_{\text{hs}} = 8 \text{ kPa}; J_{m\text{hs}} = 0.17\}$.
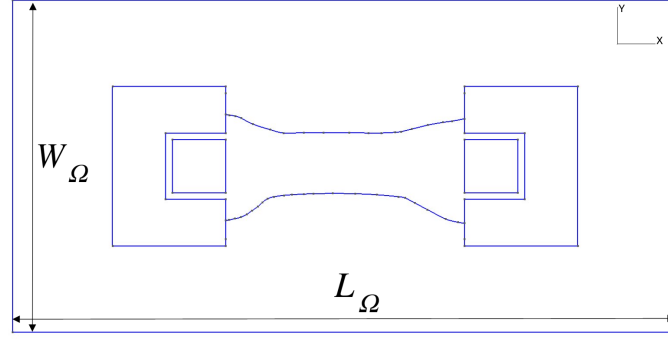
Figure 3.15: Topology parameters of the uni-axial extensometery's equivalent model.
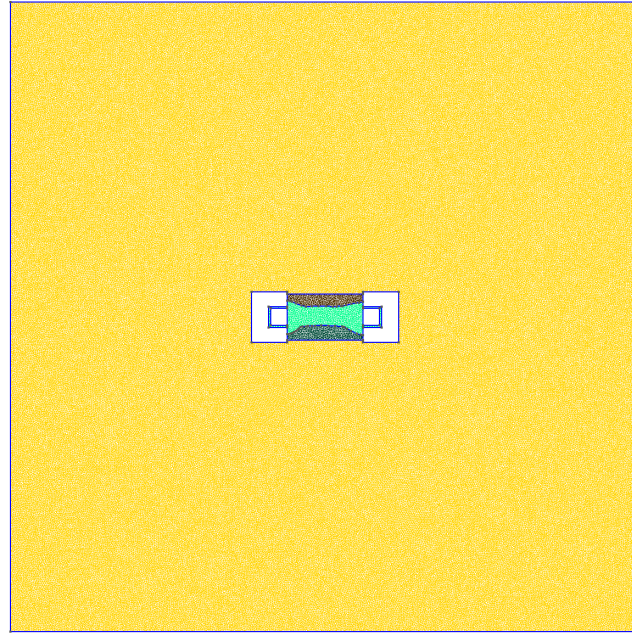
Figure 3.16: Extended mesh domain with $L_\Omega = 300$ mm and $W_\Omega = 300$.

3.3.2 Topology Uncertainty Analysis

Studying the boundary condition effects on the identified parameter uncertainty would not necessitate solving the inverse problem for each set of L_Ω and W_Ω. Because the uncertainty source is not related to experimental data, but to the geometrical model instead, the analysis targets the forward solver. By sweeping the geometrical parameters, the reaction force value was calculated and plotted for the "fixed" and "constrained" cases (Fig. 3.17a). Their values of ε_{LW} were calculated and summed up in Figure 3.17b, where the minimum mismatch is 2.8 % for $L_\Omega = 200$ mm and $W_\Omega = 300$ mm.

The shape in Figure 3.17b indicates that extending the domain in the X-direction (increasing the length L_Ω) does not affect the reaction force, which validates the usefulness of U-pads to isolate the observable zone from external changes. In Figure 3.15, we remark that ZOI might not be protected from the deformations of top and bottom boundaries. Therefore, the domain width must be too large (W_Ω close to 300 mm) to neglect the boundary effects, as seen in the latter figure. With an error less than 5 %, and for the sake of less expensive computations, we can determine the model boundaries to $W_\Omega = 300$ mm and $L_\Omega = 150$ mm.
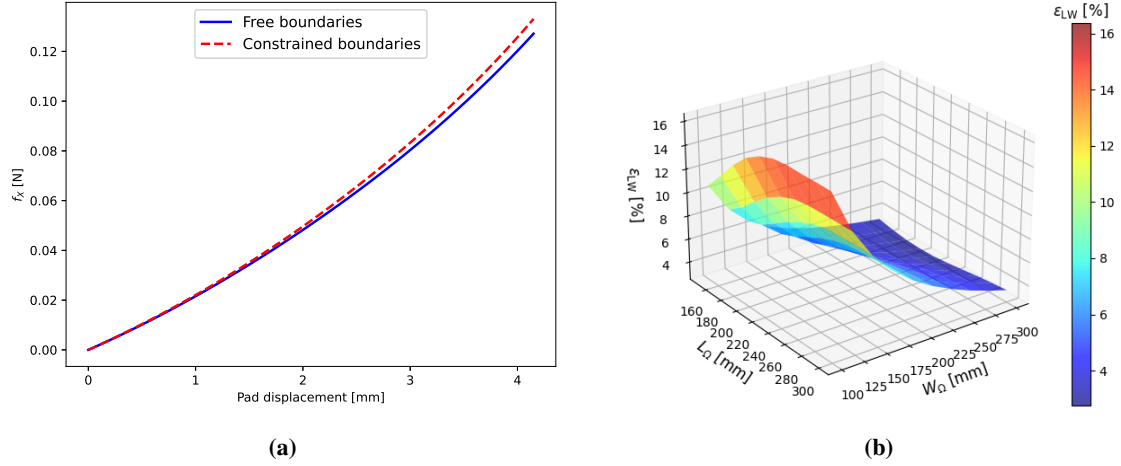
Figure 3.17: Study of boundary condition effects for different values of L_Ω and W_Ω.

The model becomes less representative with such a great width because the studied site is not flat. At the same time, eliminating the boundary effects is mandatory to ensure they do not impact the parameter identification. Given our situation, expanding the domain is the only solution to secure it. Regarding the representativity issue, one could point out that the similitude between the model and the experiment lies in the independence of measured force with the edges and not the dimensions. An alternative way to force the geometric similitude and reduce the edge effect would be imposing adaptive boundary conditions without altering the response.

3.4   3D modeling

The use of a 2D model was privileged for its simplicity and its reasonable computational costs, even though its results showed some complexity. In this part, we use a full 3D model to clearly understand how it can be replaced by the 2D equivalent model, which can be considered as an uncertainty source. We start by describing how the body was modeled based on the molded shape of keloid by means of free, open-source software. Then, we will introduce the implementation of the 3D FE forward problem and its validation. Afterward, we will study the equivalence of 2D and 3D models.

3.4.1   FE Forward Problem

Compared to the forward problem detailed earlier in Section 2.1.3, the 3D forward problem includes the same features (code structure, behavior law assigning, nonlinear algorithm) except for the geometry, boundary conditions, and element type. Hence, this part will address the CAD modeling, FEɴɪCS Implementation, and the forward solver validation.

3.4.1.1   Geometry Construction

As explained in Section 2.1.1.1, the keloid's shape was acquired with an optical 3D surface measurement and converted into a 3D points cloud. The latter was used to realize a CAD model on `Blender` [372], as illustrated earlier in Figure 2.3a. `Blender` allows through many filters smoothing the surfaces locally. Using Non-Uniform Rational Basis Splines could be possible, but the real keloid curvature was approximated, thus less accurate. The output surface mesh, in STL format (Standard Tessellation Language), is imported in a second free framework: `FreeCAD` [398]. The mesh is converted into a solid part, extracted, and then embedded onto a half-thin-cylinder, representing the skin epidermis and dermis in the arm, with a diameter of 47 mm (average measure on 30 volunteers). Because of the curvature effect, the downside half-thin-cylinder does not impact the upside domain.

This assumption will be addressed in Section 3.4.2.2. As a result, `FreeCAD` produces the CAD model in BREP format (Boundary REPresentation), where its volume limits define the 3D shape. Afterward, the BREP file is opened in `Gmsh` to generate tetrahedral elements within the volume boundaries, as illustrated in Figure 3.18. The keloid in red was modeled with its full varying thickness and the surrounding skin with a thickness 1.5 mm, accordingly to Chambert *et al.*'s measurement [106]. The keloid goes completely through the skin until reaching the inner wall.
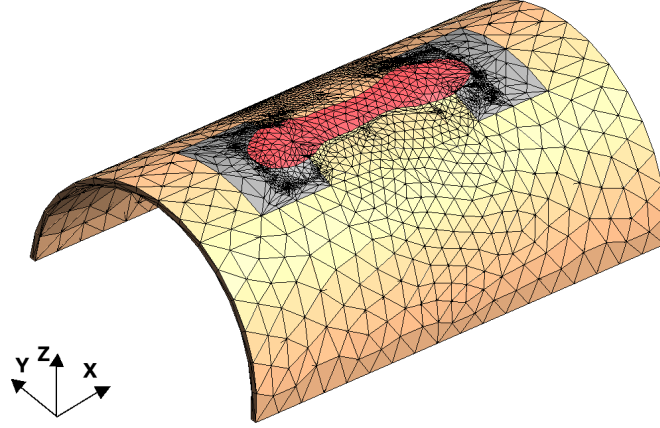
Figure 3.18: Representation of the bi-material 3D mesh composed of keloid and healthy skin.

3.4.1.2 Validation and Convergence

In the same way as the 2D equivalent model, the forward problem in 3D was implemented in FENICS, but with some adaptations. For the boundary conditions, in contrast with 2D configuration (Fig. 2.6), the top surface domains where the pads were stuck were empty. After all, meshing a rigid body would produce the same results, but it was mandatory for the 3D. All the vertices within the grey surfaces in Figure 3.18, even the ones from the keloid, were subject to the prescribed displacement in both fixed and moving pads. In addition, the displacement of the inner surface of the half-thin-cylinder, corresponding to the dermis bottom boundary, was set null along Z-direction. Thereby, the skin should slide following the stretch movement.

The validation of the forward solver was conducted based on COMSOL Multiphysics® software. The parameter set $\boldsymbol{m}_{\text{ref}}^{\text{bimaterial}}$ and the Gent model in its incompressible form were used for that. Knowing that the 3D geometry illustrated in 3.18 cannot be reproduced on COMSOL (for file incompatibility issues), I used a simplified flat 3D domain resulting from pulling out the 2D model (Fig. 2.11) with a distance of 1 mm. The objective of the validation is to verify that FENICS codes were correctly typed and that the functions are consistent with continuum mechanics, which means that the choice of the geometry can be arbitrary. The validation consisted in comparing the nodal solutions at the last observation pseudo-time, $u_1(t_k = N_E)$, $u_2(t_k = N_E)$, and $u_3(t_k = N_E)$ (along axes X, Y, and Z, respectively), from COMSOL and FENICS along two cutlines similar to the ones in Figures 2.14 and 2.15. The meshes had almost the same number of quadratic elements: 15 k for the COMSOL model and 16 k for the FENICS model. For the first cutline oriented horizontally on the center of the domain, the comparison of displacement data in Figure 3.19 showed a fitting with relative errors of 0.2 % and 3.5 % for u_1 and u_3, respectively. As for u_2, the mismatch in Figure 3.19b is due to the discretization since the displacement was supposed to be constant and null in that situation. On the other hand, the fitting in Figure 3.20, along the vertical cutline, also sketched on the center, showed an accuracy of 1.87 % and 3.4 % for u_2 and u_3, respectively. In the latter, a refined mesh of 65 k elements was employed after the 16000-element-mesh produced less accurate fitting. The high mismatches

in Figure 3.20a are again caused by the discretization, and the displacement u_1 was assumed to be uniform around -2.075 mm.
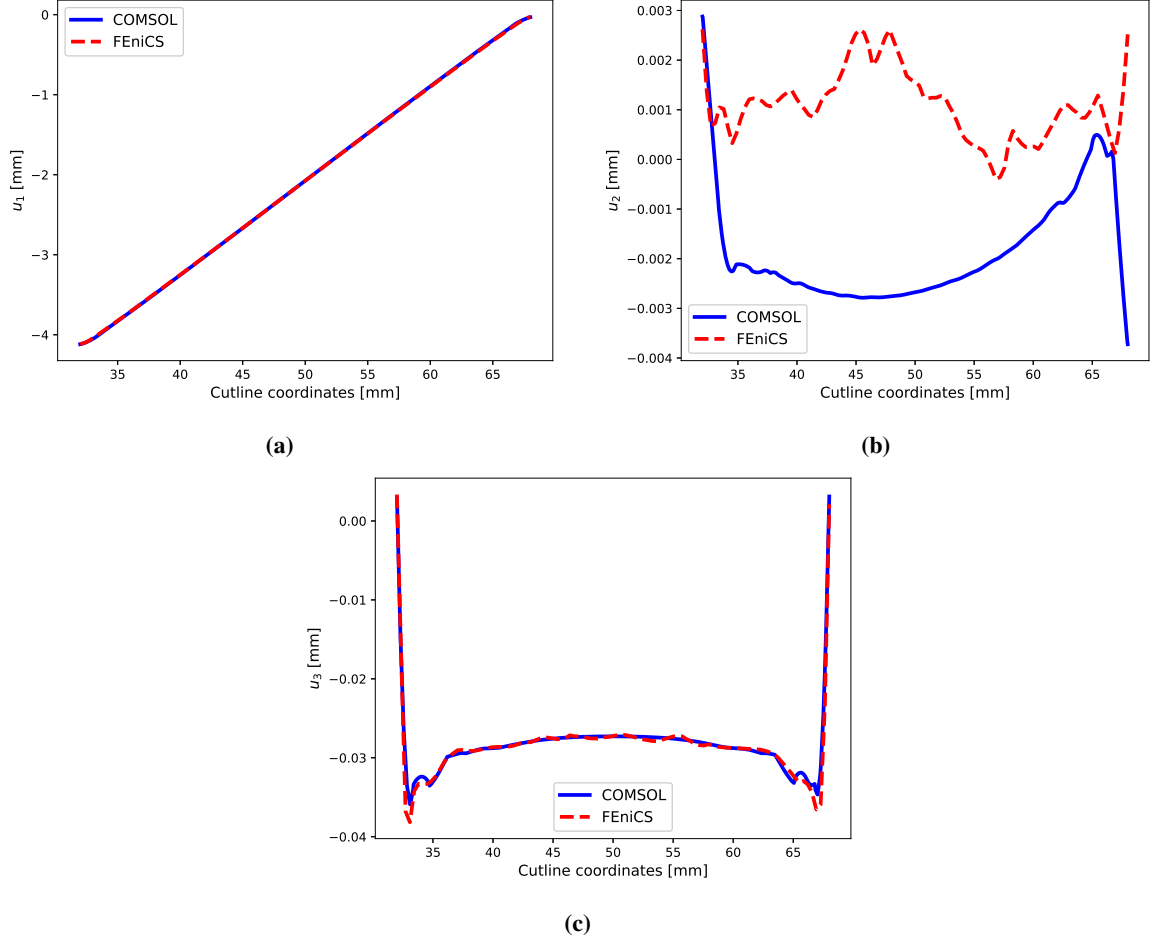
Figure 3.19: Comparison of displacement on the horizontal cutline between 3D models.

The latter results confirmed that the forward solver coded in FEniCS was operational and gives identical results once referred to an *a priori* validated commercial code. However, the comparison in Figure 3.20c would have us believe that the domain was efficiently meshed in COMSOL, as opposed to FEniCS. One had to refine the mesh from 16 k elements to 65 k elements to result in solutions close to the ones computed in COMSOL with 15 k elements. Following that, a mesh convergence study was carried out on the FEniCS-based forward solver.

A series of meshes issued from the half-thin-cylinder described in Section 3.4.1.1 were used for simulation to study the mesh density convergence. Every mesh was generated automatically on `Gmsh` but not uniformly. In 3D bodies, the mesh builder automatically refines the curved areas, unlike in 2D shapes. Besides, an adaptive mesh with 61 k elements was constructed based on the DWR method, where linear elasticity was applied instead of nonlinear. Regarding the interpolation degrees, the analysis revealed convergence starting from the quadratic order after comparing reaction force between linear, quadratic, and cubic meshes. Figure 3.21a illustrates the convergence of the quantity $\sum_{t_k}^{N_E} |f_X(t_k)|$ over the mesh series, which occurred for the 172 k mesh. To conduct such highly costly computations, I had to use a processor with 10 cores in the server, far beyond a simple desktop computer's performance. For $N_E = 100$, the computation cost was around 3000 s, which represents the duration of one iteration in identifying the material parameters. Hence, the total cost would be more than 10 hours, providing that the first tested initial guess leads to correct convergence. Figures
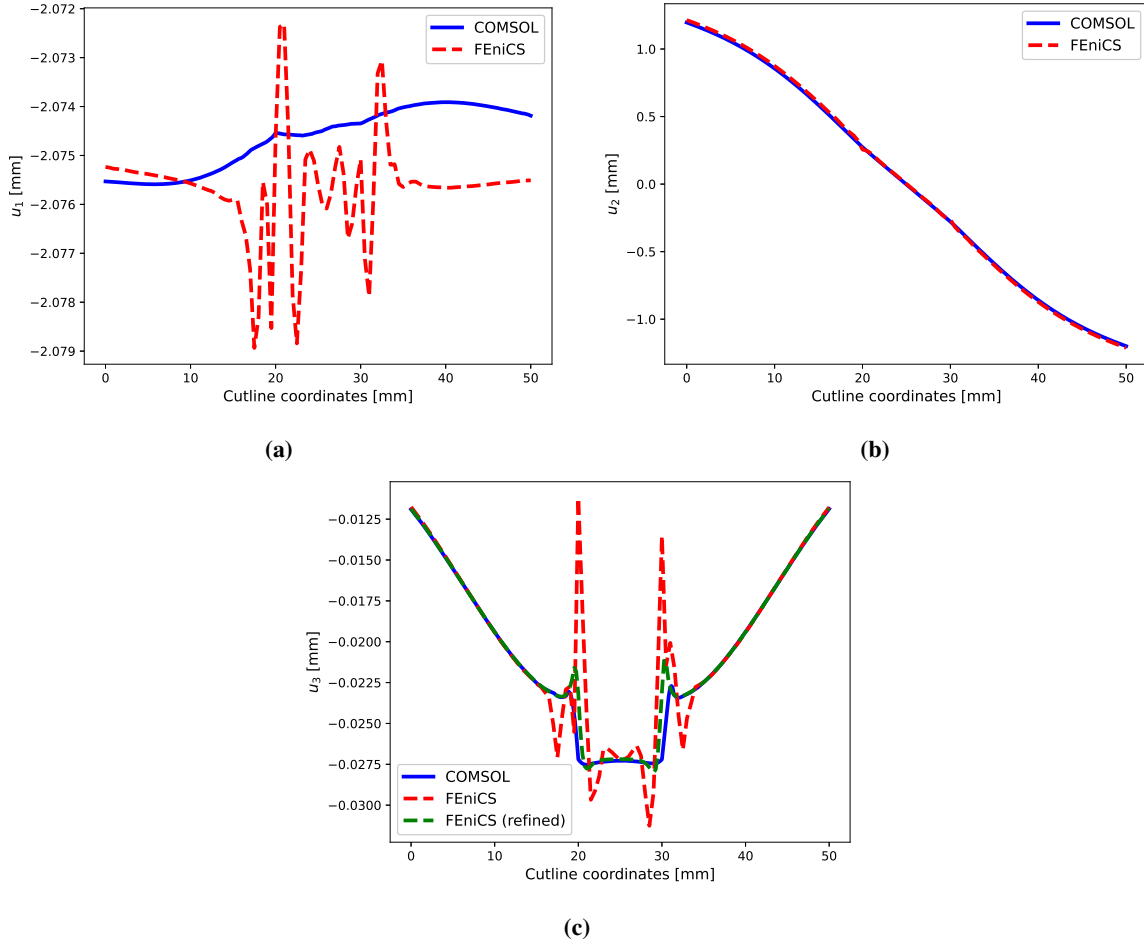
Figure 3.20: Comparison of displacement on the vertical cutline between 3D models.

3.21a and 3.21b indicate that using an adaptive mesh with 3 times less number of elements produces the same results but faster, around 500 s instead of 3000 s. In this case, utilizing the optimization solver is affordable.

3.4.2 Multi-Dimensional Uncertainty Analysis

The FE forward problem was solved for giving different configurations and parameters to study the change in reaction force, derived from nodal displacements.

3.4.2.1 Epidermis-Dermis Thickness

Several simulations were performed for the total healthy skin thickness th_{ed}, as an addition of the epidermis and dermis thicknesses. The curves exposed in Figure 3.22a revealed that the force retrieved on the measurement pad is strongly correlated with domain thickness. Accordingly, when using an equivalent 2D model, the total thickness should be considered in the constitutive equations. Otherwise, the material parameters will be misidentified. Figure 3.22 exhibits a linear correlation between force (taken at the last observation time $t_k = N_E$) and th_{ed}, which suggests that the integrated stress over the pad's surface is always constant (Eq. 2.11), and that the change in f_X is due only to the thickness variation.

Consequently, the equivalence between the 2D and 3D models can be justified by including the bi-material thickness in the elastic energy term. It is then proposed to extend Equation 2.7 to

104

(a)

(b)
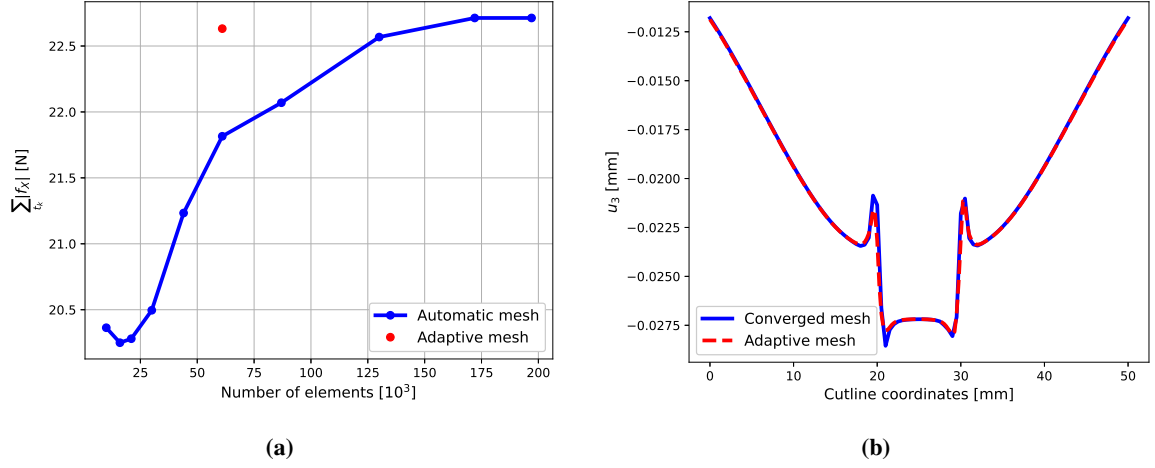
Figure 3.21: Convergence study of the FEniCS-based 3D forward problem. (b) The comparison focused on the u_3 mismatch along the vertical cutline since it showed weaker fitting in Figure 3.20c.

(a)

(b)
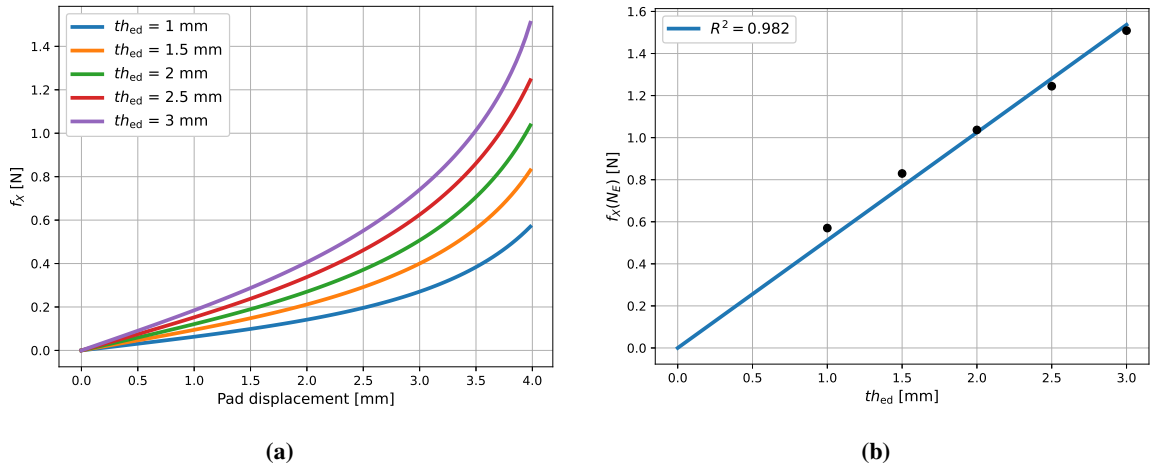
Figure 3.22: Analysis of thickness change on the reaction force.

$$\Pi(\boldsymbol{u}(t_k), t_k) = \int_{\Omega_k} \psi_k(\boldsymbol{u}, t_k) th_k \, d\Omega + \int_{\Omega_{hs}^{msr} \cup \Omega_{hs}^{unmsr}} \psi_{hs}(\boldsymbol{u}, t_k) th_{hs} \, d\Omega \tag{3.11}$$

with th_k and th_{hs} standing for, respectively, keloid and healthy-skin average thicknesses.

3.4.2.2 Curvature

The boundary effect on the mechanical response in the 2D equivalent model was addressed in Section 3.3, where an optimal rectangular domain with length $L_\Omega = 150$ mm and width $W_\Omega = 300$ mm. In this part, we explore whether this domain, in its flat shape, can produce the same behavior as a curved layer. Thus, the 2D model was swept perpendicularly with 1.5 mm to add thickness, resulting in a 3D flat bi-material. The latter was compared to two curved 3D models: a full thin-cylinder and its half, as displayed in Figure 3.23.

The first conclusion about the results is that modeling half of the thin cylinder is sufficient to simulate the deformation of a bi-material on the arm site. Second, using a flat model would bring some relative errors with 27 %; hence the uncertainty about the characterization increases. One could add a corrective coefficient in the model to recapture the discrepancy. However, without additional investigation, we cannot conclude that this correction is always 27 %. Given the constraints faced in
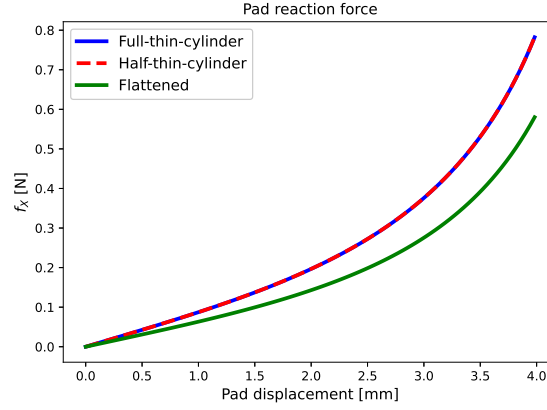
Figure 3.23: Analysis of curvature effect on the reaction force.

modeling, particularly the boundary effects and the curvature, reducing the domain to a surface where the curvature is negligible would be preferable. If one sets the maximum uncertainty to 5 % (based on Figure 3.17b), a $L_\Omega = 150$ mm and $W_\Omega = 150$ mm width will be a good compromise.

Conclusions

In this chapter, the focus was on analyzing the uncertainties related to parameter identification using different approaches and considering various sources of errors. These sources included mesh discretization, measurement data, boundary conditions, and tri-dimensional aspect. The uncertainty quantification was performed differently for each source, depending on the nature of the variables and data. For mesh discretization and measurement data, the discrepancy between identified parameters and a reference set was computed, respectively, for varying mesh density and measurement noise. Synthetic data was generated and sometimes significantly perturbed to simulate experimental data. For the analysis of boundary conditions, the uncertainty was represented by the discrepancy in the finite element model outputs between an arbitrary topology and a topology with very large sizes, with the latter having negligible effects on the reaction force. Regarding the tri-dimensional aspect, the uncertainty was qualitatively analyzed by assessing the reaction force on a 3D model with different characteristics such as curvature and thickness.

The investigation into the impact of mesh discretization on parameter identification accuracy and precision involved generating synthetic data from a reference mesh with a known set of parameters, which were then projected onto a series of coarser meshes. Material parameters were identified on each of these meshes using an optimization problem, and the mismatch between the identified parameters and the reference set was assessed. The study yielded two principal results. Firstly, it was found that linear elements provided convergence from a relatively distant initial guess, but were not accurate in identifying parameters from data originally produced by a quadratic mesh. Therefore, it is recommended to combine linear and quadratic meshes for improved performance. Secondly, constructing an adaptive mesh proved to be a time- and cost-effective approach for identifying parameters without sacrificing accuracy.

For the analysis of measurement noises effect on the inverse identification quality, dummy noises were added to the synthetic data, displacement fields and force-displacement curves, for several levels, combinedly or separately. The study then examines the influence of variation in the data on identified parameters and sets a threshold for every data type to control identification accuracy: $S_{\mathrm{DIC}}^{\mathrm{adm}} = 120$ µm and $S_{\mathrm{force}}^{\mathrm{adm}} = 8$ mN. The results demonstrated that each material parameter is closely linked to a certain data type, for instance μ_{k} and μ_{hs} with reaction force, and $J_{m\mathrm{k}}$ and $J_{m\mathrm{hs}}$ with displacement field. Last

but not least, a minimum of 100 DIC frames and their relative forces data are recommended to reduce uncertainty in parameter identification.

To account for the potential impact of boundary conditions on mechanical response, an uncertainty analysis was conducted to establish domain limits that minimize computational costs while ensuring minimal effect on output. The study determined that the optimal domain length and width are $L_{\Omega} = 150$ mm and $W_{\Omega} = 300$ mm. It is important to note, however, that extending the mesh domain may limit its applicability for modeling non-flat human skin sites such as the shoulder or jaw.

While incorporating the tri-dimensional aspect would enhance the realism of the identification process, it comes at the cost of increased computation time. Therefore, a study was conducted to evaluate the impact of multi-dimension uncertainty on identification accuracy, with the aim of improving accuracy in a 2D equivalent model. The findings demonstrate that considering skin thickness is crucial, and that curvature has a notable influence on the forward solution. Ultimately, the study suggests that a 3D model would be advantageous for achieving accurate parameter identification.

Chapter 4

Bi-material Mechanical Characterization: Application to a Patient-Specific Case

After introducing the inverse problem method to characterize the bi-material soft tissue and its relative numerical features in Section 2, the uncertainties about the identified parameters were addressed through quantitative and qualitative studies in Section 3. The uncertainty analysis helped define the validation limits of the methods and suggest further improvements. The next step is applying the SoFTI method to a patient-specific dataset acquired from the uni-axial extension test on a keloid scar situated on the upper arm. Consequently, the material parameters will be assessed, and the preferential directions of keloid growth will be identified.

This Chapter is divided into three main parts. The experiment performed on the patient and the resulting dataset is first described. The measurement errors will be quantified and checked if they are within the acceptable uncertainty based on the earlier works. Afterward, the material parameter identification will be reported for some different cases. Finally, the stress field is computed using the optimal parameter set to investigate the mechanical interaction between the keloid and the surrounding skin. This will lead us to conjecture about the future keloid shape. Once done, a medical solution specification to prevent keloid growth could be established.

4.1 Experiment

This part covers the procedures and results related to data acquisition from the uni-axial test applied to a domain consisting of a keloid scar and healthy skin. It covers as well measurement data processing and its errors. Because of the lack of real data, the application of the method laid on an existing dataset prior to the thesis from only one patient, which was mostly retrieved from Chambert *et al.*'s study [106].

4.1.1 *In vivo* Test

A series of measurements was held on a 22-year-old Caucasian female in an average temperature of $20 - 22\,°C$ and relative humidity of $40 - 60\,\%$ with a rest time of 20 minutes between each two load cycles. Under the Helsinki Declaration [399], a set of ethical principles regarding human experimentation, the devices used were non-invasive and painless to the patient. The patient gave consent to the experiment, and its keloid diagnosis was confirmed by a surgeon. No treatment was administered before the measurement.

4.1.1.1 Uni-Axial Extension Apparatus

Employing an ultra-light extensometer device, introduced in Section 2.1.2.1, a uni-axial extension test was carried out on a butterfly-shaped keloid scar. The latter was situated on the dorsal side of the left upper arm (Fig. 4.1a). To improve the accuracy of the DIC process, from videos captured during the stretch, a random speckle pattern with black ink was sprayed onto the keloid/healthy-skin domain (Fig. 4.1a). Later, the extensometer was stuck to the studied site with a surgical adhesive used in dermatological surgery. Only the pads were in contact with the specimen, especially on keloid lobes (Fig. 4.1c). The rest of the device is suspended. The apparatus also included a stabilized camera Canon PowerShot ® SX510 HS, to record the deformations within the observation zone (Fig. 4.1d). The distance between pads measured before the deformation was equal to $L_{\text{pads}_0} = 32$ mm.

| (a) | (b) | (c) | (d) |
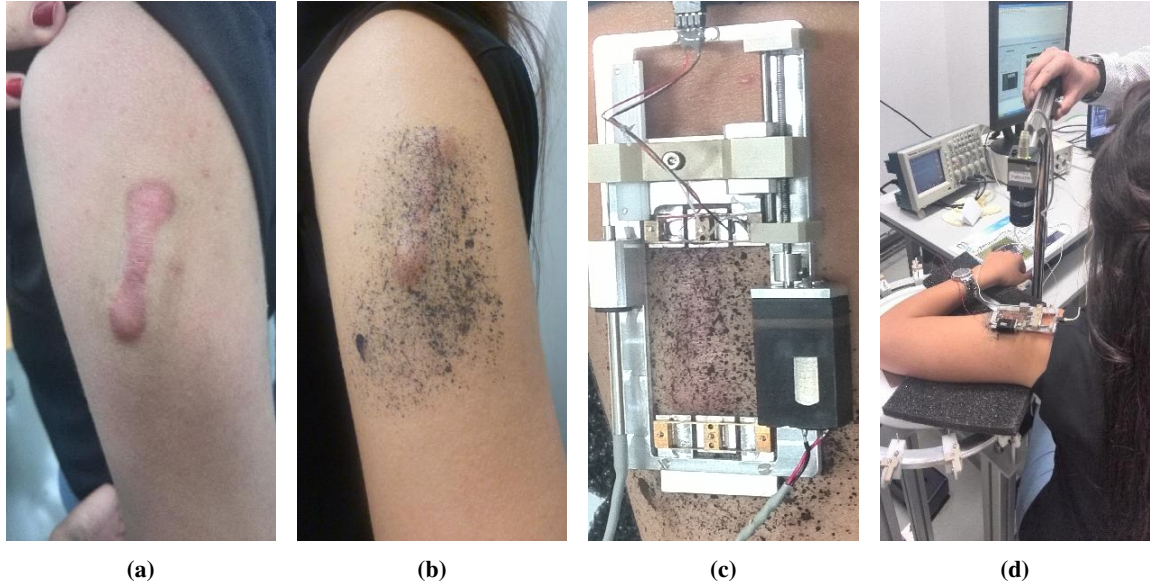
Figure 4.1: Uni-Axial extensometry performed on a 22-years-old Caucasian female subject with keloid. (a) Butterfly-shaped keloid scar positioned on the left upper arm. (b) Application of speckle pattern on the observable zone. (c) Ultra-light extensometer fixation to keloid/healthy-skin site. (d) Overview of the apparatus.

4.1.1.2 Thickness Measurement

The thickness of the surrounding skin th_{hs}, considered as the total thickness of epidermis and dermis layers, and the thickness of keloid scar th_{k}, as an addition of the emerged part and the surrounding skin, were assessed with high frequency ultrasound technique (detailed in [106]). Successive signal lines resulting from longitudinal scanning of the surface were used to reconstruct cross section images of the media. As results, $th_{\text{hs}} = 1.34 \pm 0.05$ mm and $th_{\text{k}} = 2.93 \pm 1.26$ mm. As the keloid has an irregular shape, the measurement of its height was expected to witness large standard deviation.

Figure 4.2 presents an ultrasound visualization of the studied soft tissues in their depth. Images retrieved from the healthy-skin case show a well-discernible interface between the epidermis-dermis layer and the hypodermis (dark zone). On the other side, the dermis and the hypodermis interface was hardly identified in keloid images by Chambert *et al*. [106]. According to their analysis, it may be due to the irregularity of fine vessels distributed inside the whole skin coat. They reported that the generally darker aspect of the image could express a liquid infiltration, a kind of edema due to inflammation.

(a) Healthy-skin zone

(b) Keloid zone
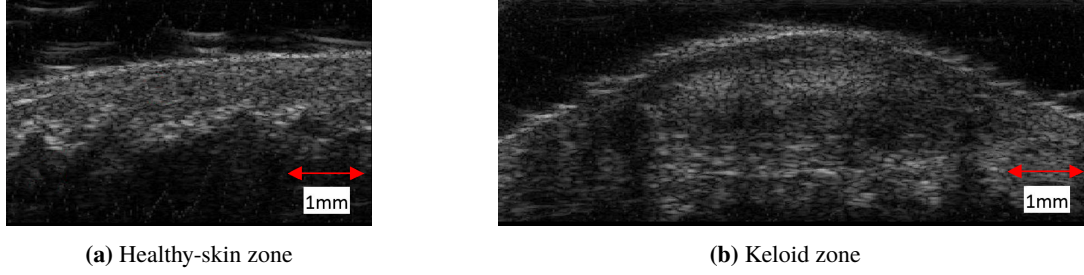
Figure 4.2: Ultrasound observation of deep layers of the studied area. Modifier from [106]

4.1.2 Data Treatment

The whole *in vivo* experiment consisted of 3 linear loading-unloading cycles at a controlled speed of 0.6 mm/s. The outputs, reaction forces, and displacement fields were simultaneously and continuously recorded. The primary results in [106] showed that the first cycle behaves differently compared to the second and the third, which are similar. This behavior has been linked to the preconditioning effect. Therefore, the second cycle (in its loading phase) was taken as reference data for parameter identification. Its two datasets, forces and DIC fields were separately treated and then synchronized.

4.1.2.1 Force-Displacement Curve

Around 400 points of reaction forces were collected from the pad sensor along the pad displacement. Although the latter was measured, it can be set as known values since the precision is less than 4 µm, which is negligible compared to displacement magnitude order. Figure 4.3a displays the evolution of the force-displacement curve with raw measurements. Noise related to the vibration of the electric motor (Fig. 2.4a) can be noticed between 0 and 3 mm. A way to check the measurement uncertainty resulting from that noise, as reported in the device specifications (5 mN in Tab. 2.1), is to calculate the standard deviation of the difference between the raw points and their average curve. The average was computed based on the moving average technique by adding up all the data points during a specific period and dividing the sum by the number of time periods. In our case, the moving average was conducted three times, with 9, 5, and 3 points per period, respectively. Thereby, the uncertainty on reaction force was S_{force} = 7.6 mN, which is beyond the accuracy reported in Table 2.1 but within the threshold set in the uncertainty analysis, $S_{\text{force}}^{\text{adm}}$ = 8 N (Sec. 3.2.1.2).

Figure 4.3b summarizes the offset procedure utility. It has been observed on the force and displacement sensors non-null values for a null strain. The offset involves shifting the curve such that the first point meets the null-displacement and null-force. Without this manipulation, additional errors would necessarily be when matching the model response. In any hyperelastic model, for null deformation (null strain energy), the displacement is imperatively null. It should not be confused with the pre-stress effect, which exists actually but is not measurable with the extensometer. Unlike Flynn *et al.*' study [139], the shift is not due to pre-stress effect. Our curves from the first, second and third cycles start from the same non-null point. The moving average was used only to identify the first point by smoothing the curve. However, the raw measurement subjected to the offset will be utilized for the identification process.

4.1.2.2 Digital Image Correlation

The video recorded during the second loading was split into 98 frames, whose first was set as the initial configuration. The displacement fields were obtained by computing the cumulative relative displacement between two successive frames through the DIC technique. The algorithm based on
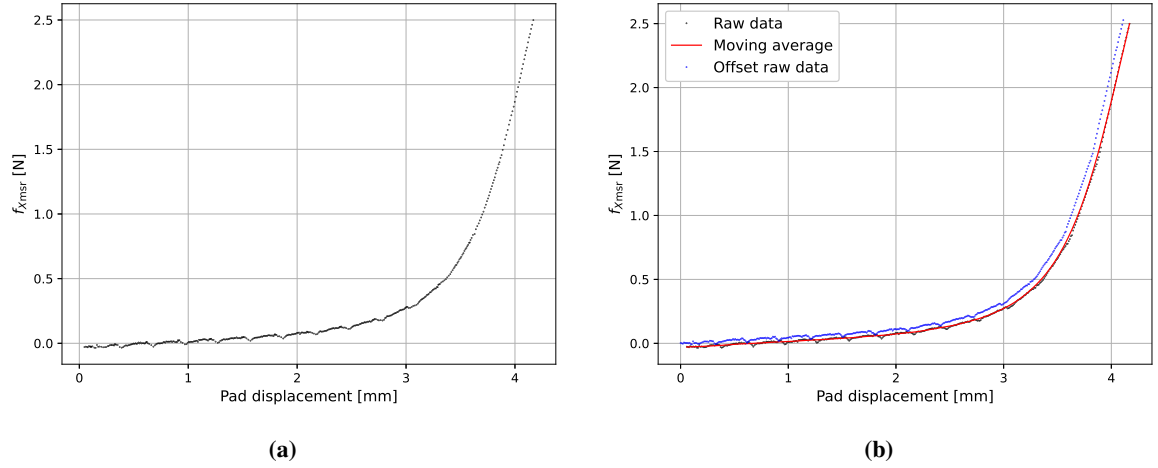
Figure 4.3: Force-displacement curve from the uni-axial test performed on a keloid scar and surrounding skin.

Lucas–Kanade method (Eq. 2.5) was applied to the frames to convert them to displacement fields.

In Figure 4.4, the moving and fixed pads are marked in cyan and red, respectively. Their known length sets up a scale to convert DIC displacements from pixel to millimeter. Marking the fixed pad help align and orient the frames through a combination of functions implemented in `OpenCV` Python library. An interactive program has been created to assist the surgeon in marking the pads with 4 points selected from the screen directly. To avoid this operation that might add uncertainties to displacement fields, the patient's arm must be stabilized within a standardized protocol, inversely to the protocol exhibited in Figure 4.1d.

selected
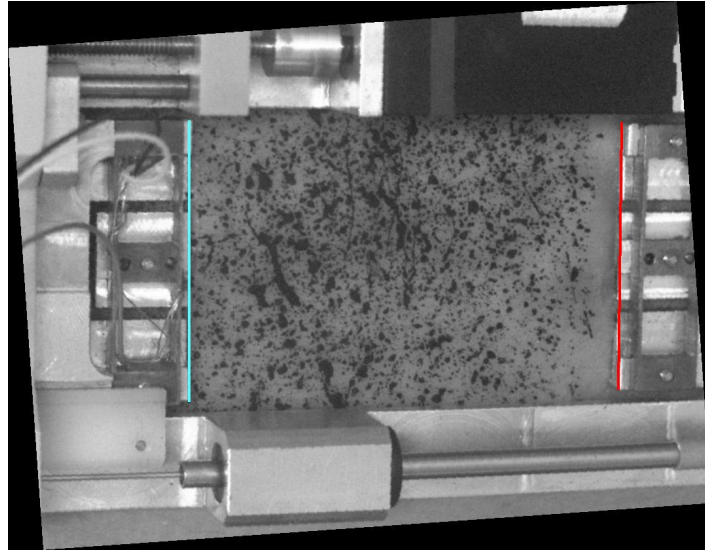
Figure 4.4: A video frame of the uni-axial extension test. The cyan and red lines indicate the boundaries of the moving and fixed pad.

On the other hand, marking the moving pad is the key to the synchronization between DIC fields and the reaction forces. For that purpose, each frame is converted into a displacement field (Fig. 2.5), hence the pad displacement is obtained in the sense of DIC, namely $\bar{u}_{X\,\text{DIC}}$. The latter's value is pointed out on the force-displacement curve *via* the controlled pad displacement $\bar{u}_X$. Therefore, each frame is assigned to the respective reaction force. At that level, the assignment errors are tightly related to DIC uncertainty.

Calibration Study

To optimize the errors resulting chiefly from the cumulative application of DIC from one frame to another, a calibration study was conducted, where the DIC parameters a_W and d_G are chosen (introduced in Section 2.1.2.2). To recall, they represent in the order the side of a square correlation window centered on every grid node and the gap between grid points. For a bunch of combinations of a_W and d_G, the relative mismatch $\varepsilon_{C-DIC} = |\bar{u}_{X\,DIC} - \bar{u}_X|/|\bar{u}_X|$ was evaluated. The displacements were taken from the end of the loading to count for the accumulation effect. Subsequently, the 3D surfaces in Figure 4.5a map ε_{C-DIC} values and shows that optimums can be chosen arbitrarily from a valley, where the errors do not exceed 2 %. Thus, we chose $a_W = 64$ px and $d_G = 10$ px that corresponds to $\varepsilon_{C-DIC} = 1.75$ %. Figure 4.5b illustrates the computation time t_{C-DIC} (in seconds) for all DIC parameter sets and reports that an increase in the DIC grid resolution highly impacts them. The calibrated DIC parameters requiring 27 seconds of computations are in line with both plots in Figure 4.5.

(a)   (b)
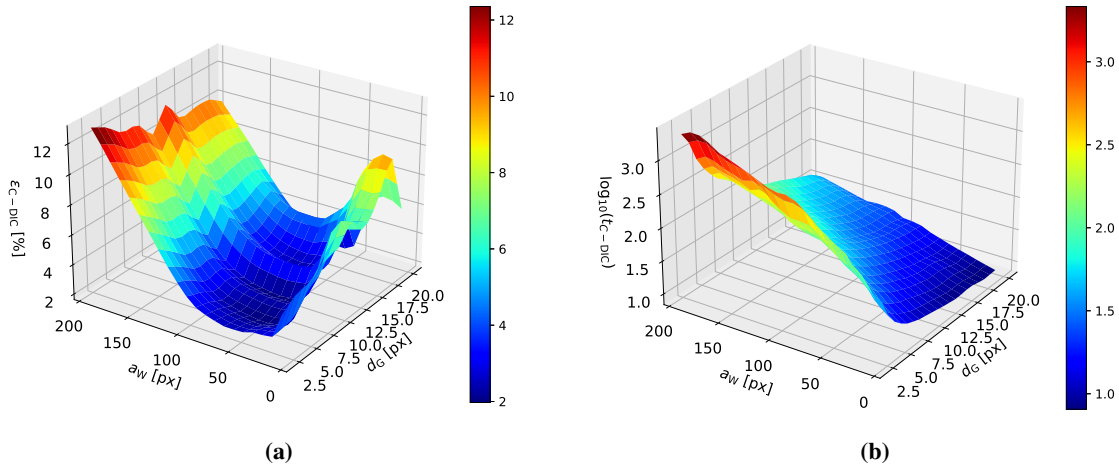
Figure 4.5: A calibration study to optimize DIC uncertainty applied to the uni-axial extension. As the Z-axis could not be converted into the logarithmic scale, the logarithmic values of T were manually computed, supposing 1 s = 1 dimensionless unity.

Application

Considering the optimal DIC parameters and the scale discussed above, the displacement fields were computed for all the 98 frames. The grid points' initial and final positions are superposed in Figure 4.6. Correspondingly, most top and bottom rows are deformed differently than the other intermediate rows, indicating an effect from the moving pad corners. Back to Figure 3.8, the simulations have also shown significant uncertainty around the pad corners. One needs to remove the displacement data from the 3 most external top and bottom rows. Hence, the width of the measurement domain in the numerical model, $\Omega^{msr} = \{\Omega_k \cup \Omega_{hs}^{msr}\}$ (Fig. 2.7), has been reduced to 20 mm.

To evaluate the uncertainty on displacements, a comparison was carried out between the controlled pad displacements, on the one hand, and the ones captured with DIC over the whole series of frames, on the other hand. Out of lack of known displacements over all the space between the pads, the uncertainty S_{DIC} corresponds to the standard deviation of the mismatch in Figure 4.7a. Thus, $S_{DIC} = 84$ μm, revealed to be smaller than the maximum admissible measurement uncertainty for the displacement, $S_{DIC}^{adm} = 120$ μm.
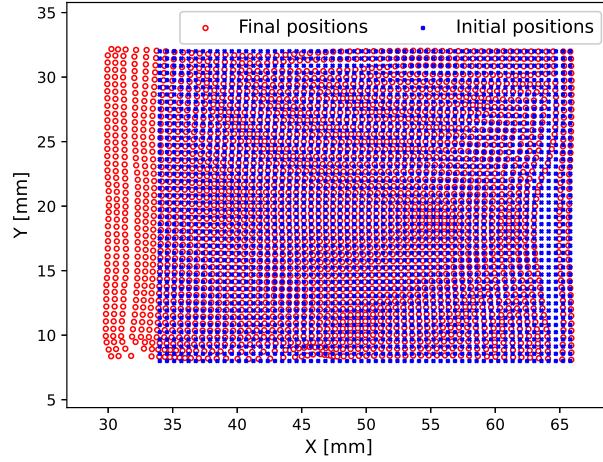
Figure 4.6: Initial and final configuration of measurement domain.

Furthermore, the uncertainty of the DIC process on the synchronization was analyzed. In fact, if considerable errors on DIC occurred, the frame would have been assigned to an invalid reaction force value. Figure 4.7b indicates the range of the force-displacement curve where both data types are available and valid. Because of a mismatch at the end of the curve in Figure 4.7a, $\bar{u}_{X\,\text{DIC}} = 4.06$ mm *versus* $\bar{u}_X = 4.17$ mm, the DIC process failed to match the totality of force data acquired with the extensometer. In this situation, the force-displacement curve will be truncated up to 2.11 N instead of 2.5 N. As for the video frames to keep since the average mismatch between the controlled and the evaluated pad displacement is 84 µm, they all are considered valid.

(a)

(b)
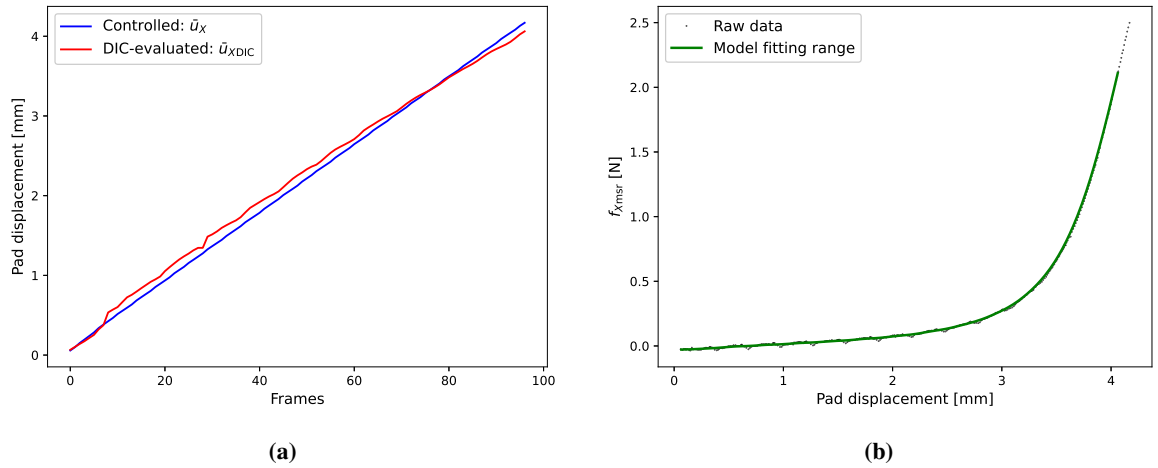
Figure 4.7: Error analysis of the DIC process and validation range of the experimental data.

4.2 Parameter Identification

The inverse problem described thoroughly in Chapter 2 was applied to the validated DIC fields and force data, based on uncertainty analyses from Chapter 3, to identify the material parameters of the keloid and surrounding skin. This section covers the adaptation of the inverse problem principally, as part of the SoFTI method, to the patient-specific problem and its applications for various cases.

4.2.1 Numerical Method

As a reminder, the FEMU-based inverse problem incorporated in SoFTI (Fig. 2.1) has two major parts, the forward and optimization solvers. The former underwent some modifications to match as close as possible with the uni-axial extension test addressed in Section 4.1. As for the optimization solver, we redefine the algorithms and equations with more suitable notation in this part.

4.2.1.1 Forward Solver

The adjustment of the forward problem (Sec. 2.1.3) concerned the total elastic energy and the mesh domain. As for the hyperelastic behavior, the isotropic Gent model (Eq. 2.8) was allocated to both materials. The boundary conditions and the plane strain conditions had not been changed. As discussed in Section 3.4.2.1, the soft tissue thickness has a crucial influence on the reaction force and should be included in the total energy function to build the weak formulation. With $\overline{th}_{hs} = 1.34$ mm and $\overline{th}_k = 2.93$ mm as constants into Equation 3.11, one could write

$$\Pi^{PS}(t_k) = \overline{th}_k \int_{\Omega_k} \psi_k(\boldsymbol{u}, t_k) \, d\Omega + \overline{th}_{hs} \int_{\Omega_{hs}^{msr} \cup \Omega_{hs}^{unmsr}} \psi_{hs}(\boldsymbol{u}, t_k) \, d\Omega \tag{4.1}$$

where PS refers to "patient-specific". As reminder, both materials were assumed isotropic (see Section 2.1.3.1).

The original mesh domain, sized as $L_\Omega = 100$ mm and $W_\Omega = 50$ mm, was subjected to expansion on the basis of uncertainty studies in Sections 3.3 and 3.4. Thus, $L_\Omega^{PS} = 150$ mm and $W_\Omega^{PS} = 150$ mm. Concerning the mesh density, for better accuracy, a 44 k element mesh was employed for parameter identification to the extent possible (Fig. 4.8). Using an adaptive mesh was possible too, but it would have increased some uncertainties.
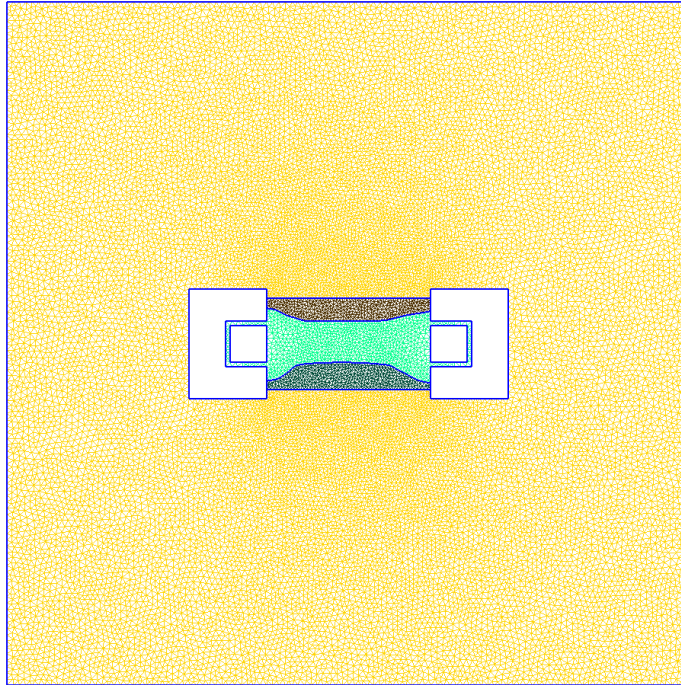
Figure 4.8: Mesh domain adapter for the patient-specific parameter identification.

We observe a lack of speckled pattern with a closer look at the area next to the fixed pad, marked with the red line in Figure 4.4. Regrettably, it could considerably disturb the DIC process, resulting in

erroneous displacement data. The miscalculation of the displacement can be visualized as a leap on the right of the field in Figure 4.6. A qualitative study on the coherence of the experimental displacement field was carried out by comparing the latter with arbitrary displacements issued from the model. The coherence can be defined, given the problem, as a regular evolution of displacement from the fixed pad side to the moving pad's one. If one uses experimental data from all over Ω^{msr}, including the leap region, the parameter will definitely be misidentified. By mapping the nodal difference between the actual experimental displacement field and any model-issued nodal displacement (assumed to be coherent) in Figure 4.9, the zone of incoherent data can be avoided. The zone delimited by black dashed lines, namely, Ω^{PS}, will be subjected to optimize the mismatch between experimental and model displacement.
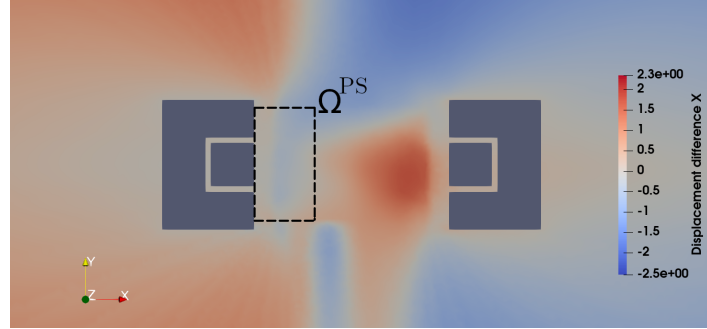
Figure 4.9: Reducing observation domain to avoid incoherence areas. The shown domain is partial and cropped off from the patient-specific mesh domain (Fig. 4.8).

4.2.1.2 Optimization Solver

The keloid and peripheral healthy skin parameters were assessed through the minimization of two objective functions introduced in Section 2.1.4.1. The first (Eq. 2.13), based on the Lagrange multiplier method, has proven to be more adapted to the bi-material characterization problem with faster convergence. Its application to patient-specific data takes the following shape.

$$
\begin{aligned}
\mathcal{J}_{\mathrm{L}}^{\mathrm{PS}}(\boldsymbol{m}, \Lambda) = {} & \frac{1}{2\alpha_u^2 N_E} \sum_{k=1}^{N_E=98} \|\boldsymbol{u}(\boldsymbol{m}, t_k) - \boldsymbol{u}_{\mathrm{msr}}(t_k)\|_{\Omega^{\mathrm{PS}}}^2 \\
& + \Lambda \frac{1}{\beta_f N_E} \sum_{k=1}^{N_E=98} \big(f_X(\boldsymbol{u}(\boldsymbol{m}, t_k)) - f_{X\,\mathrm{msr}}(t_k)\big)
\end{aligned}
\tag{4.2}
$$

The results of the second objective functions (Eq. 2.18) summarized in Figure 2.17, with a quadratic mismatch in reaction forces and without Lagrange multiplier, could be an alternative tool for this practical case. Thus, its adaptation is expressed as

$$
\begin{aligned}
\mathcal{J}_{\mathrm{q}}^{\mathrm{PS}}(\boldsymbol{m}) = {} & \frac{1}{2\alpha_u^2 N_E} \sum_{k=1}^{N_E=98} \|\boldsymbol{u}(\boldsymbol{m}, t_k) - \boldsymbol{u}_{\mathrm{msr}}(t_k)\|_{\Omega^{\mathrm{PS}}}^2 \\
& + \frac{1}{2\beta_f^2 N_E} \sum_{k=1}^{N_E=98} \big(f_X(\boldsymbol{u}(\boldsymbol{m}, t_k)) - f_{X\,\mathrm{msr}}(t_k)\big)^2
\end{aligned}
\tag{4.3}
$$

Identifying the material parameters with two different optimizers is expected to verify their deviation. One last thing to modify is the convergence criterion (step 6 in Section 2.1.4.2). With no guarantee that the experimental displacement field is close to the model's, the tolerance on the convergence might be reconsidered. Therefore, the identification is assumed to be converged if the change in the cost, instead of the change in the parameters, is less than a threshold.

4.2.2 Results and Analyses

We discuss hereby the material parameters identification results and their contribution to validate the hyperelastic model. When it comes to secure successful convergence, the modeler will face the most challenging operation in deterministic-based parameter calibration, *i.e.*, setting the initial guess. The uncertainty studies (Sec. 3.2.1.2) led to understand the link between the parameters and the data, based on dummy measurement noises. As a recall, it has been shown in Section 3.2.1.2 that identifying J_{mk} and J_{mhs} can only be achieved in the presence of displacement data. To identify μ_k, the force-displacement curve data are more than enough. While for μ_{hs}, both data sets are mandatory. Therefore, setting the initial guess would not be done randomly, but inspired from the mechanical response. The strategy followed for that purpose, is simulating the forward solver for various sets of parameters and observe the force-displacement curve to grow some intuition (informative guess). Based on that, the initial set used to guarantee the optimizer convergence was $\boldsymbol{m}_0^{PS} = \{\mu_k = 0.1 \text{ MPa}, J_{mk} = 0.05, \mu_{hs} = 0.05 \text{ MPa}, J_{mhs} = 0.5, \Lambda = 10^{-4}$.

4.2.2.1 Lagrange Multiplier Method

As suggested in Section 3.1.2, the ability of linear mesh to converge in the inverse problem and the accuracy of quadratic mesh could be jointly exploited to estimate the parameters to improve identifiability. The first optimization resulted in the converged set $\hat{\boldsymbol{m}}_l^{PS} = \{\mu_k = 0.07898 \text{ MPa}, J_{mk} = 0.01918, \mu_{hs} = 0.05629 \text{ MPa}\}$. Figure 4.10a summarizes and evolution of the parameters for each iteration until the convergence, with m_i^{PS}/m_{0i}^{PS} the relative value compared to the initial set.

This first application of patient-specific data revealed some anomalies compared to the *in silico* data (Fig. 2.17). The inverse solver failed to identify J_{mhs}, and it has not been represented in Figure 4.10a because its non-convergence was so significant that the convergence of other parameters could not be distinguished. The non-convergence of J_{mhs} was caused by a lack of displacement data from the healthy-skin area. Earlier, it was reported that the measurement domain was cropped to 30 % to avoid incoherence areas (Fig. 4.9), where the discard between the experimental data and the model is considerable. And since J_{mhs} is highly impacted by displacement data quality, its value would be volatile if Ω^{msr} does not cover enough the surrounding skin. Figures 4.10b, 4.10c, and 4.10d, express the minimized costs for each iteration and reveal that the optimizer tend to prioritize the minimization of force rather than displacement, probably because of data quantity put in play.

Afterward, by setting the converged set $\hat{\boldsymbol{m}}_l^{PS}$ as the initial guess for the optimization with quadratic elements, we obtain slightly different but more accurate parameter set $\hat{\boldsymbol{m}}_L^{PS} = \hat{\boldsymbol{m}}_q^{PS} = \{\mu_k = 0.0779 \text{ MPa}, J_{mk} = 0.0176, \mu_{hs} = 0.0569 \text{ MPa}\}$. Figure 4.11 exhibits the optimization convergence with data projected on a mesh with quadratic elements. The latter operation confirmed the usefulness of the "double-trigger" technique presented earlier in Section 3.1.2.2 but this time for real data.

By introducing $\hat{\boldsymbol{m}}_L^{PS}$ in the forward solver and running the simulation, the best-fit solution was obtained and compared to the experimental data in Figure 4.12a for forces and Figure 4.12b for displacement. The accuracy of the identification was assessed with the following relative errors

$$\varepsilon_f^{PS} = \frac{\sqrt{\sum_{k=1}^{N_E=98} \left(f_X(\boldsymbol{u}(\hat{\boldsymbol{m}}^{PS}, t_k)) - f_{X\,msr}(t_k) \right)^2}}{\sqrt{\sum_{k=1}^{N_E=98} \left(f_{X\,msr}(t_k) \right)^2}} \tag{4.4}$$

and

(a) Parameters

(b) Total mismatch

(c) Force mismatch

(d) Displacement mismatch
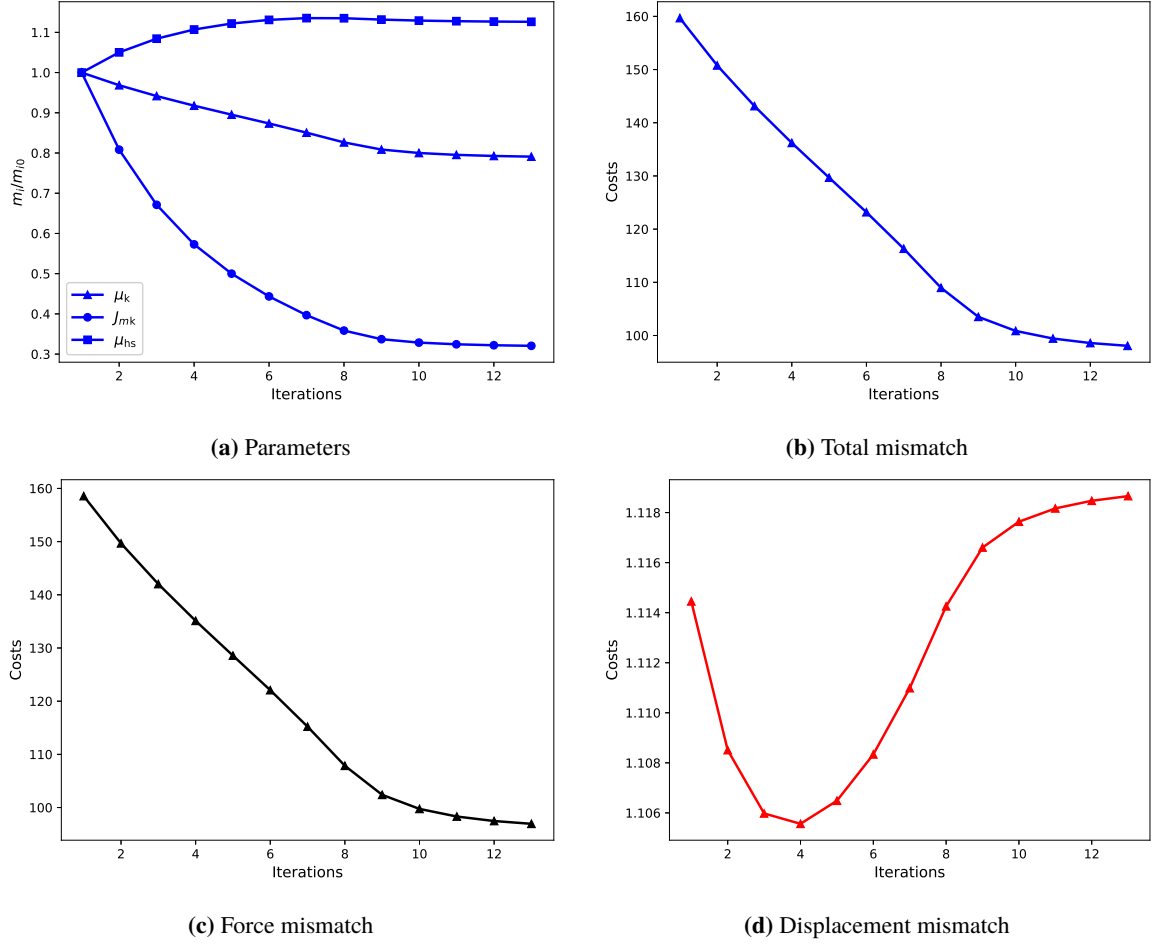
Figure 4.10: Convergence of the optimization solver for the patient-specific data projected on linear elements.

$$\varepsilon_u^{\text{PS}} = \frac{\sqrt{\sum_{k=1}^{N_E=98} \left\| \boldsymbol{u}(\hat{\boldsymbol{m}}^{\text{PS}}, t_k) - \boldsymbol{u}_{\text{msr}}(t_k) \right\|_{\Omega^{\text{PS}}}^2}}{\sqrt{\sum_{k=1}^{N_E=98} \left\| \boldsymbol{u}_{\text{msr}}(t_k) \right\|_{\Omega^{\text{PS}}}^2}} \tag{4.5}$$

Therefore, the mismatch on forces with the identified parameter set $\hat{\boldsymbol{m}}_{\text{L}}^{\text{PS}}$, based on the Lagrange multiplier method, was $\varepsilon_f^{\text{PS}} = 16.8$ %, and $\varepsilon_u^{\text{PS}} = 1.82$ % for displacement. Contrary to what could be noticed in Figure 4.12a, the mismatch errors are not small enough to validate the hyperelastic model if one refers to $\varepsilon_f^{\text{PS}}$. An alternative way to assess the model fitting error is using the square of Pearson correlation coefficient R_2. Even though it was designed for linear models, it has been employed for hyperelastic model fitting in many studies [251, 261]. Hence, for the given configuration, we get $R_2^{\text{L}} = 0.984$, which is assumed to be enough to validate the similarity of the Gent model with the experimental data regarding the correlation coefficients calculated for dozens of hyperelastic models in [251]. The mismatch errors on the displacement, on the other hand, are not significant within the measurement domain Ω^{PS}, as can be shown on the displacement difference field (on the last frame), in Figure 4.12b. A direct comparison between the latter and Figure 4.9 witnesses the successfulness of the optimization solver in minimizing the errors between the model and data collected from an *in vivo* experiment.

4.2.2.2 Unconstrained Optimization

The application of the objective function with a quadratic mismatch on force (Eq. 4.3) was carried out on the patient-specific data. We have shown through Figures 2.17 and 2.21 that the mentioned

(a) Parameters   **(b)** Total mismatch
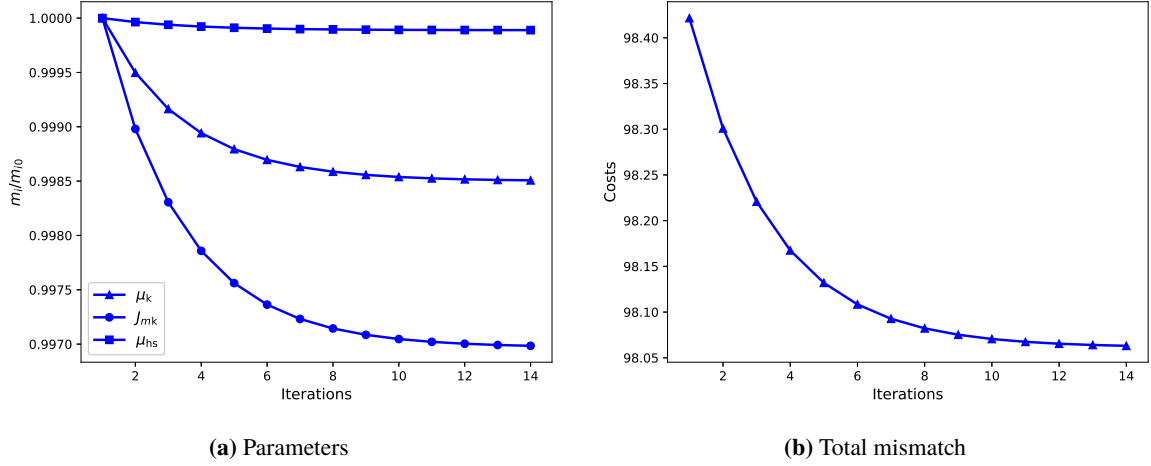
Figure 4.11: Convergence of the optimization solver for the patient-specific data projected on quadratic elements. Initial set: $\boldsymbol{m}_0^{\mathrm{PS}} = \{\mu_{\mathrm{k}} = 0.07898 \text{ MPa}, J_{m\mathrm{k}} = 0.01918, \mu_{\mathrm{hs}} = 0.05629 \text{ MPa}\}$

equation is unable to identify all bi-material parameters at once, but showed helpful in identifying a monolithic material's parameters. In our case, Equation 4.3 will be utilized in two steps. In the first position, μ_{hs} and $J_{m\mathrm{hs}}$ are calibrated based on a set of data collected from a uni-axial extension test performed on the upper right arm, where the skin is entirely healthy [106]. This operation is known as the contra-lateral test (supplementary results are exposed in Appendix B). Subsequently, once μ_{hs} and $J_{m\mathrm{hs}}$ are determined, they will be fixed in the bi-material problem, and hence the optimizer will seek μ_{k} and $J_{m\mathrm{k}}$ values.

Using the contra-lateral experiment data, which covers only the healthy-skin material, and projected on the quadratic mesh, led to the determination of $\hat{\boldsymbol{m}}_{\mathrm{hs}}^{\mathrm{PS}} = \{\mu_{\mathrm{hs}} = 0.03692 \text{ MPa}, J_{m\mathrm{hs}} = 0.103\}$, with the respective errors $R_2^{\mathrm{hs}} = 0.974$ and $\varepsilon_u^{\mathrm{PS}} = 0.4$ % (Fig. 4.13a). Later, by fixing the latter in the bi-material model, the identification resulted in $\hat{\boldsymbol{m}}_{\mathrm{k}}^{\mathrm{PS}} = \{\mu_{\mathrm{k}} = 0.0491 \text{ MPa}, J_{m\mathrm{k}} = 0.0175\}$, with the respective errors $R_2^{\mathrm{k}} = 0.969$ and $\varepsilon_u^{\mathrm{PS}} = 1.33$ % (Fig. 4.13b).

4.2.2.3 Definitive Parameter Set

At first sight, both objective functions, $\mathcal{J}_{\mathrm{L}}^{\mathrm{PS}}$ and $\mathcal{J}_{\mathrm{q}}^{\mathrm{PS}}$, succeeded in identifying at least 3 material parameters out of 4. With additional datasets of force-displacement curves and displacement field from a contra-lateral test, the identification of $J_{m\mathrm{hs}}$ was fruitful. However, as mentioned in Chambert *et al.*' study [106], there was no guarantee that the mechanical response of the right arm (contra-lateral) would be the same as the left one, where the keloid took place. On the grounds that the quality of displacement data within the domain Ω^{PS} was not consistent enough to identify $J_{m\mathrm{hs}}$, and that the effectiveness of $\mathcal{J}_{\mathrm{q}}^{\mathrm{PS}}$ was acted on the availability of a second dataset covering only the healthy-skin, the contra-lateral experiment data had to be exploited. With saying that, considering that the identified value of $J_{m\mathrm{hs}}$ represents the surrounding skin lies on a strong assumption.

The values of $J_{m\mathrm{k}}$ determined with both cost functions are similar, $J_{m\mathrm{k}} = 0.0175$ through the Lagrange multiplier method, and $J_{m\mathrm{k}} = 0.0176$ through the unconstrained optimization. Since $J_{m\mathrm{k}}$ is not correlated with forces, but with displacement, its optimal value was expected to be the same knowing that the two cost functions have the same mismatch function on the displacements. As for μ_{k} and μ_{hs}, the ratio $\mu_{\mathrm{hs}}/\mu_{\mathrm{k}}$ was 0.75 and 0.73 for $\mathcal{J}_{\mathrm{L}}^{\mathrm{PS}}$ and $\mathcal{J}_{\mathrm{q}}^{\mathrm{PS}}$, respectively. Those results are in line with the ratio 0.8 adopted by Akaishi *et al.* in their numerical study for relationship between keloid growth pattern and stretching tension [111]. However, their respective values are separately different, which can be visualized by comparing the force-displacement curves between the two optimization functions. A

(a) Force-displacement curve

(b) Displacement field
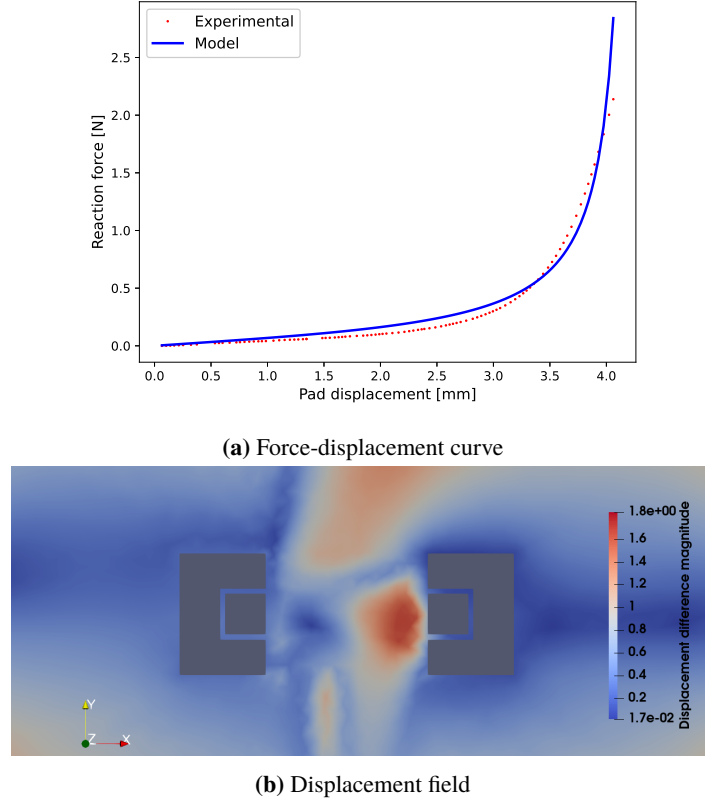
Figure 4.12: Comparison of the experimental data and inverse solution for the identified set $\hat{\boldsymbol{m}}_{\mathrm{L}}^{\mathrm{PS}}$. The shown domain is partial and cropped off from the patient-specific mesh domain (Fig. 4.8)

significant distinction was perceived in a matter of model fitting approach. Figure 4.12a shows that $\mathcal{J}_{\mathrm{L}}^{\mathrm{PS}}$ seems to give importance equally to the entire observation pseudo-times counter to $\mathcal{J}_{\mathrm{q}}^{\mathrm{PS}}$ that tends to emphasize the influence of the initial slope. Figures 4.13a and 4.13b exhibit a strong model fitting on the linear part but show a weaker correlation for the rest of the curve. Another criterion that was taken into account to decide about the definitive material parameters set is fitting the initial slope. The endmost objective of the SoFTI methodology is determining the preferential direction of keloid growth from the standing natural skin tension field. Therefore, model fit quality should be the best at that quasi-undeformed keloid/healthy-skin medium. We should then rely on the results that fit better with the initial curve slopes, *i.e.*, μ_{k} and μ_{hs} values, based on $\mathcal{J}_{\mathrm{q}}^{\mathrm{PS}}$ objective function. This manner of choice would not impact the final value of $J_{m\mathrm{k}}$, and by analogy $J_{m\mathrm{hs}}$, considering that both optimization functions converge to the same values.

Finally, the definitive parameter set of keloid and surrounding healthy skin is $\hat{\boldsymbol{m}}^{\mathrm{PS}} = \{\mu_{\mathrm{k}} = 0.0491 \text{ MPa}, J_{m\mathrm{k}} = 0.0175, \mu_{\mathrm{hs}} = 0.03692 \text{ MPa}, J_{m\mathrm{hs}} = 0.103\}$.

Needless to say, the application of SoFTI on real data did not occur as straightforwardly compared to synthetic data in Chapter 3. The experiment outputs have not been gathered in the best conditions. The captured displacement field (Fig. 4.9) was not consistent all over the measurement area because of the discontinuity of a speckle pattern. Therefore, the identification zone area had to be restricted to ensure model fit, but to the detriment of some parameters, $J_{m\mathrm{hs}}$, for instance. To overcome the disadvantage, the SoFTI framework was adapted without difficulty to identify the parameters based on two data sets, the main and contra-lateral experiments. The second consisted of a uni-axial extension on undamaged skin in the symmetrical site with no guarantee that the body symmetry conserves the mechanical response. A better way to compensate for the lack of data quality in the main experiment was to perform the uni-axial test on the same side but a bit closer to the studied site. In our case, the second uni-axial extension should be carried out on the forearm instead of the upper right arm. The

119

(a) Healthy-skin mono-material

(b) Keloid/healthy-skin bi-material
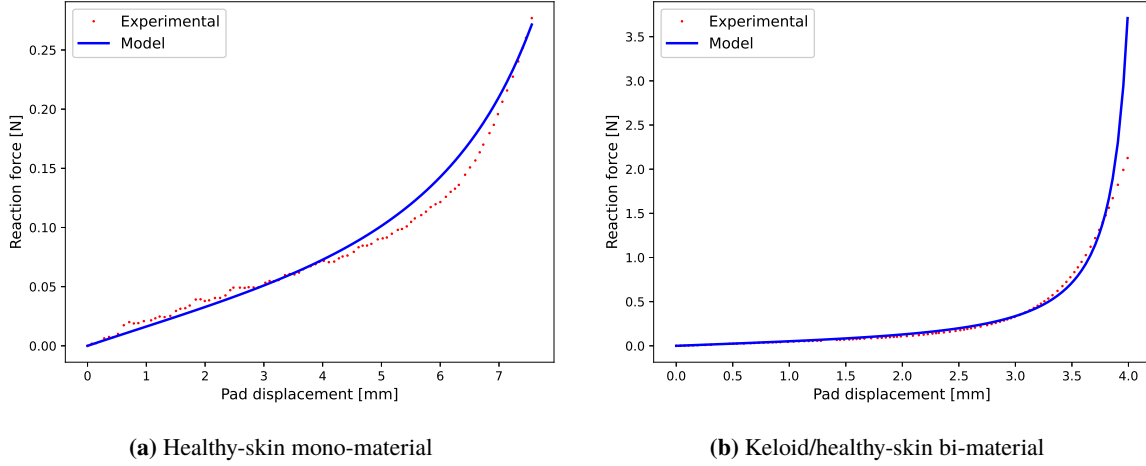
Figure 4.13: Model fitting based on combining the bi-material and mono-material contra-lateral experiments.

present experience taught us that in a biomechanical protocol, we would need to gather as much data as possible that can help face imperfection cases.

4.3 Post Treatment

Understanding the internal forces contributing to keloid propagation starts with mapping the prestress distribution all over the medium, considered the last step of its characterization. Provided with the identified material parameter set $\hat{\boldsymbol{m}}^{\mathrm{PS}}$, a nonlinear FEM model was constructed to simulate the mechanical response under natural tension along two perpendicular directions. As outputs, the model provides two fields of the normal stress along the principal tension direction and the shear stress on the studied plan. By accounting for the isotropy hypothesis, the privileged direction of keloid growth can be obtained from the eigenvectors of the stress tensor. In addition, a qualitative and quantitative parametric study will be conducted to analyze the sensitivity of the favored directions.

4.3.1 Stress Fields

Section 2.1.5 addressed the methods and the materials leading to compute the stress fields. We will discuss in this part the adaptation of the FEM solver to the patient-specific case and report the results for fixed values of natural pre-stretch.

4.3.1.1 Preliminary

The changes that took place in the FEM nonlinear solver (Sec. 2.1.5.1) are principally setting the mixed boundary conditions. For Neumann-type conditions, the values of the applied tractions, representing the natural skin tension, $\boldsymbol{t}_1$, and $\boldsymbol{t}_2$, were chosen based on the literature. On the other hand, the Dirichlet-type conditions remained unchanged because they ensured the solution unicity by eliminating the floating structure configuration.

For all the references read out during the thesis, the prestress values may not have been explicitly assessed on the living skin. To set $\boldsymbol{t}_1$ and $\boldsymbol{t}_2$, we may refer to Reihsner *et al.*'s work [18]. Using the *in vivo* geometry as a reference, a set of incremental strains was applied to specimens excised from several sites. After stress relaxation of the sample, assumed to be orthotropic, was accomplished, the final values of stresses were captured along two perpendicular axes, namely, $\sigma_{\max}$ and $\sigma_{\min}$. Suppose that the model is oriented such that $\boldsymbol{t}_1$ is aligned with $\sigma_{\max}$, one could write

$$t_1 = \{\sigma_{\max}, 0\}^T \quad , \quad t_2 = \{0, \sigma_{\min}\}^T \tag{4.6}$$

For the outer side of the upper arm, the study issued the values $\sigma_{\max} = 0.9\,\mathrm{Nm/g}$ and $\sigma_{\min} = 0.6\,\mathrm{Nm/g}$. The unity "Nm/g" is used to quantify the stiffness of sheets. Being incapable of converting the latter into the international system, we propose to set arbitrary values while conserving the ratio $\sigma_{\max}/\sigma_{\min} = 1.5$. The influence of changes in prestress for a fixed ratio on the privileged keloid's growth direction will be studied later.

Furthermore, the model domain, opposingly to the inverse problem, was not expanded because applying the surface forces causes constant normal stresses across the healthy-skin area. Thus, expanding the domain would be pointless. The domain size was set to $W_\Omega = 50\,\mathrm{mm}$ and $L_\Omega = 100\,\mathrm{mm}$. Besides, similarly to Equation 4.1, the average thicknesses of keloid and healthy-skin were introduced in the total energy function. To finish, pseudo-times t_l (Eq. 2.19), referring to the load increments, will not be described, and they are chosen, so that solution to the nonlinear problem converges. The stress field is to be quantified on the last configuration.

4.3.1.2 Application

For the sake of demonstration, the natural bi-axial stretch was simulated for the case $\sigma_{\min} = 1\,\mathrm{kPa}$. With the ratio retrieved from the literature [18], the longitudinal stress is set to $\sigma_{\max} = 1.5\,\mathrm{kPa}$. As a result, the Cauchy stress field was mapped *via* `Paraview` in Figure 4.14 for the relevant components: the normal stress σ_{XX} and σ_{YY}, and the shear stress σ_{XY}. By exploring stress distribution and different secondary fields (principal stress and principal directions), we will set an approach to efficiently exploit the SoFTI outputs with the aim of stopping the keloid tumor propagation.

As a response to the normal prestresses in the X-direction (Fig. 4.14a), constantly applied with $\sigma_X^{\mathrm{prestress}} = \sigma_{\max} = 1.5\,\mathrm{kPa}$, a concentration of mechanical loads might have occurred on the central zone of the butterfly-shaped scar between the two lobes. The concentration is an interpretation of the increase in longitudinal stress up to 2.3 kPa, *i.e.*, 53 %. One may explain this concentration by a change in the keloid's cross-section along its axis. The loads perceived on the outer side of the lobes could be mostly transferred to the narrow part of the stiffest material (keloidic tissue). On the contrary, with the σ_{YY} field, the internal area seems to incur the same efforts as the outer zone, as if the healthy-skin and keloid behave identically. Figure 4.14b reveals the existence of effort concentration on the outer side of the lobes, where the average stress increased of 25 % compared to the applied transversal prestress $\sigma_Y^{\mathrm{prestress}} = \sigma_{\min} = 1\,\mathrm{kPa}$. Furthermore, like in Tsai and Ogawa' study [400], the finite-element analysis showed that there is high tension at the keloid edges and lower tension at the centre. It seems as if the current topology dictates the pattern and degree of keloid's growth.

The rise compared to the applied load for both longitudinal and transversal normal stress can be related to the current tumor shape. Higher stress, if not countered, would progressively drive the keloid toward the X- and Y- arbitrary directions. However, another behavior should be countered separately, linked to the resulting shear stress σ_{XY}. Figure 4.14c indicates that keloid's corners are subjected to relatively intense shear, which may cause a twist inward. If no solution were applied to annihilate σ_{XY} on those areas, it would be prognosticated that lobes would become more rounded.

4.3.1.3 Complementary Operations

The first utilization of the original fields of σ_{XX} and σ_{YY} is removing the prestress from the Cauchy stress tensor components to visualize only the critical areas. In Figures 4.15a and 4.15b, the color map was rescaled such that the minimum value was zero (to count only for the stretches in the keloid) and discretized into 20 levels. This manipulation confirms the observations made for the original

(a) σ_{XX}

(b) σ_{YY}

(c) σ_{XY}
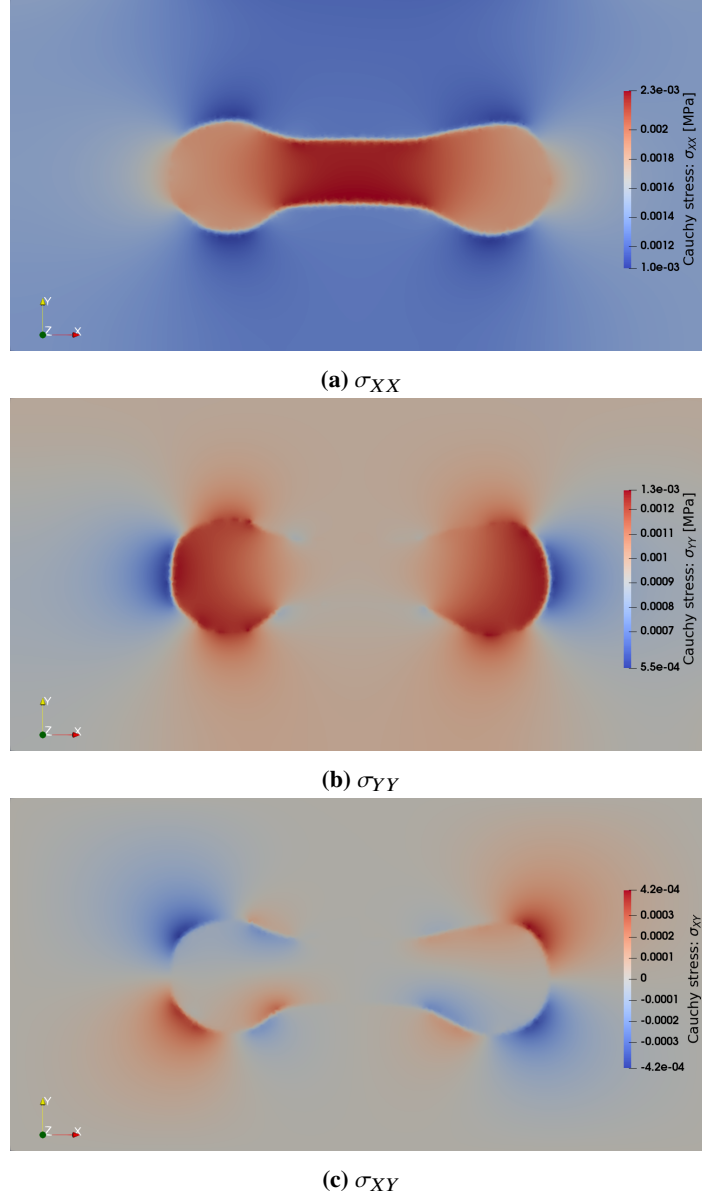
Figure 4.14: Cauchy stress field of the patient-specific sample under bi-axial prestress for $\sigma_{\mathrm{max}} = 1.5$ and $\sigma_{\mathrm{min}} = 1$ kPa.

SoFTI outputs in Figure 4.14: the critical areas for σ_{XX}, respectively σ_{YY}, are the inner zone between the lobes, respectively the lobes' outer curved sides.

The surgeon would use medical solutions with a uni-directional effect along the targeted component when it comes to countering the normal stress in the keloid and around it. On its side, the solution to annihilate the shear stress is not trivial. An alternative way is countering only the normal components of the diagonalized Cauchy stress tensor $\bar{\sigma}$. Thus, the stresses are expressed on a new basis with a null shear stress component.

$$\bar{\sigma} = \begin{bmatrix} \bar{\sigma}_{\mathrm{max}} & 0 \\ 0 & \bar{\sigma}_{\mathrm{min}} \end{bmatrix} \tag{4.7}$$

The diagonal element, namely, the principal stresses, are obtained by solving a 2-D eigenvalue problem $\det(\boldsymbol{\sigma} - \bar{\sigma}_i \boldsymbol{I}) = 0$ (i refers to the subscripts max and min). One could write

(a) $\sigma_{XX} - \sigma_X^{\text{prestress}}$
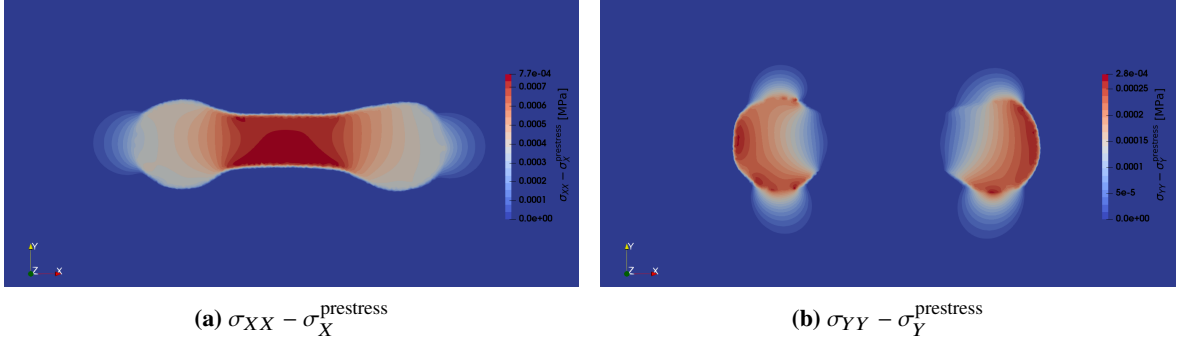
(b) $\sigma_{YY} - \sigma_Y^{\text{prestress}}$

Figure 4.15: Subtraction of the prestress from the Cauchy stress field.

$$\bar{\sigma}_i = \frac{1}{2}\left(\sigma_{XX} + \sigma_{YY} \pm \sqrt{(\sigma_{XX} + \sigma_{YY})^2 - 4(\sigma_{XX}\sigma_{YY} - \sigma_{XY}^2)}\right) \quad (4.8)$$

In solid mechanics, the eigenvalues of $\boldsymbol{\sigma}$ are generally distinct, guaranteeing its denationalization and a new basis with orthogonal directions labeled eigenvectors. They are calculated for each eigenvalue by solving the system

$$\begin{bmatrix} \sigma_{XX} - \bar{\sigma}_i & \sigma_{XY} \\ \sigma_{XY} & \sigma_{YY} - \bar{\sigma}_i \end{bmatrix} \begin{bmatrix} \bar{n}_X^i \\ \bar{n}_Y^i \end{bmatrix} = \begin{bmatrix} 0 \\ 0 \end{bmatrix} \quad (4.9)$$

with $\bar{n}_X^i$ and $\bar{n}_Y^i$ the components of one principal vector for the respective eigenvalue. With respect to the cartesian basis, the new basis is oriented with an angle $\bar{\psi}_i$.

$$\bar{\psi}_i = \tan^{-1}\left(\frac{\bar{n}_Y^i}{\bar{n}_X^i}\right) \quad (4.10)$$

The equations above were implemented in SoFTI and applied to the patient-specific outputs. The reader can refer to Appendix C.1 for the detailed code. Since the principal stresses witnessed similar values as the nominal stress, $\bar{\sigma}_{\max} \equiv \sigma_{XX}$, and $\bar{\sigma}_{\min} \equiv \sigma_{YY}$, it is preferable to address the eigenvector for the case of maximum principal stress. Since the objective of the method is to prevent the keloid growth, evaluating locally (on every element) $\bar{\psi}_{\max}$ would guide the surgeon to counter the internal load in such a way the shear stress is null.

Figure 4.16 shows the local assessment of $\bar{\psi}$ for the maximum eigenvalue all over the domain. The black arrows, mapped over the principal stress magnitude ($\bar{\sigma}_{\text{magnitude}} = \sqrt{\bar{\sigma}:\bar{\sigma}}$), would indicate the privileged direction of the materials under the permanent bi-axial prestress. With both information, magnitude, and direction, the keloid propagation would be stopped providing that the counter-stress should be higher than the residual one and applied in the opposite direction to the eigenvector.

Implementing the two visualization methods, the primary Cauchy stress field and its relative eigenvector field, illustrated in Figures 4.14 and 4.16, provides the surgeon with more than a strategy. A qualitative confrontation for the present patient-specific case reveals that the solutions could be too different. Either removing the nominal stress globally based on Figures 4.14a and 4.14b (or Figures 4.15a and 4.15b) and the shear stress according to Figure 4.14c or proceed locally based on Figure 4.16 without paying attention to the shear stress. In our specific case, the second option appears to be challenging with an inconsistent distribution of eigenvectors. As for the first option, considered as naive method, the difficulty lies in compensation for the twists caused by σ_{XY}.
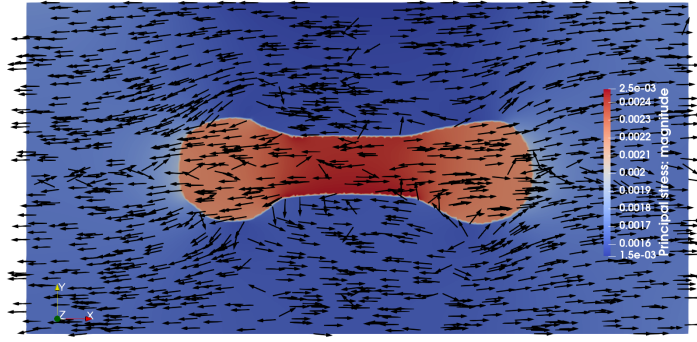
Figure 4.16: Eigenvectors distribution for the maximum principal stress.

4.3.1.4 Parametric Study

The analysis performed with recent results would be available under the assumption of a known prestress field. In reality, measuring the prestress could be beyond our possibilities to date. Therefore, shedding light on the prestress' influence on the keloid can help set rules about its adjustment. We propose then to simulate the bi-axial stretch problem for different cases where the Neumann boundary conditions are varied. For each case, the maximum values of σ_{XX}, σ_{YY}, and σ_{XY}, are retrieved. Besides, stress fields were mapped in Figure 4.17 for some cases.

Table 4.1 summarizes the resulting maximum stresses for the cases combining 2 values of $\sigma_{\max}/\sigma_{\min}$ and 3 values of $\sigma_{\min}$. By augmenting the bi-axial prestress ratio, all the components of σ rise, even the YY-component, which would be expected to be compensated by the compression caused by Poisson's effect. Augmenting the magnitude of the prestress resulted, trivially, in an increase of σ elements.

If the change in prestress ratio and magnitude had a clear impact on the stress in keloid, the distribution of the latter remained similar as the studied case in Section 4.3.1.2, where $\sigma_{\max}/\sigma_{\min}$ = 1.5 and $\sigma_{\min}$ = 1 kPa. Indeed, for the same stress component, σ_{XX} for example, the comparison of Figures 4.14a, 4.17a, and 4.17b, indicates that most critical zone is the inner area between the lobes, and more precisely on edge. By analogy, the critical zone positions for σ_{YY} and σ_{XY} were more likely sensitive to the prestress variation. Those observations can be exploited to our advantage as follows. For any random prestress field, the zones with the highest stress prevail the same. And, even though the prestress magnitude is indeterminable, the surgeon would apply very high compression to ensure that the tensions are countered. At the same time, the compression should be comfortable for the patient and not lead to side effects.

Table 4.1: Maximum values of the components of Cauchy stress tensor for several prestress conditions.

	max$_\Omega$ σ_{XX} [kPa]			max$_\Omega$ σ_{YY} [kPa]			max$_\Omega$ σ_{XY} [kPa]		
$\sigma_{\min}$	1 kPa	5 kPa	10 kPa	1 kPa	5 kPa	10 kPa	1 kPa	5 kPa	10 kPa
$\sigma_{\max}/\sigma_{\min}$ = 1.5	2.3	38	180	1.3	11	41	0.43	13	72
$\sigma_{\max}/\sigma_{\min}$ = 2	3.1	70	300	1.4	15	62	0.58	24	120

4.3.2 Clinical Solution

The user of SoFTI, at the end of the pipeline, will need to implement the findings in order to come up with a clinical solution to contain the patient-specific scar. With a lack of mechanical experience, the surgeon would have, in the first position, to explicit the technical requirements, precautions, and safety measures, within specifications. The specifications will be recast into realistic equipment as part of the bio-engineering activities.

(a) $\sigma_{max}/\sigma_{min} = 1.5$, $\sigma_{min} = 5$ kPa

(b) $\sigma_{max}/\sigma_{min} = 2$, $\sigma_{min} = 5$ kPa

(c) $\sigma_{max}/\sigma_{min} = 1.5$, $\sigma_{min} = 5$ kPa

(d) $\sigma_{max}/\sigma_{min} = 2$, $\sigma_{min} = 5$ kPa

(e) $\sigma_{max}/\sigma_{min} = 1.5$, $\sigma_{min} = 5$ kPa

(f) $\sigma_{max}/\sigma_{min} = 2$, $\sigma_{min} = 5$ kPa
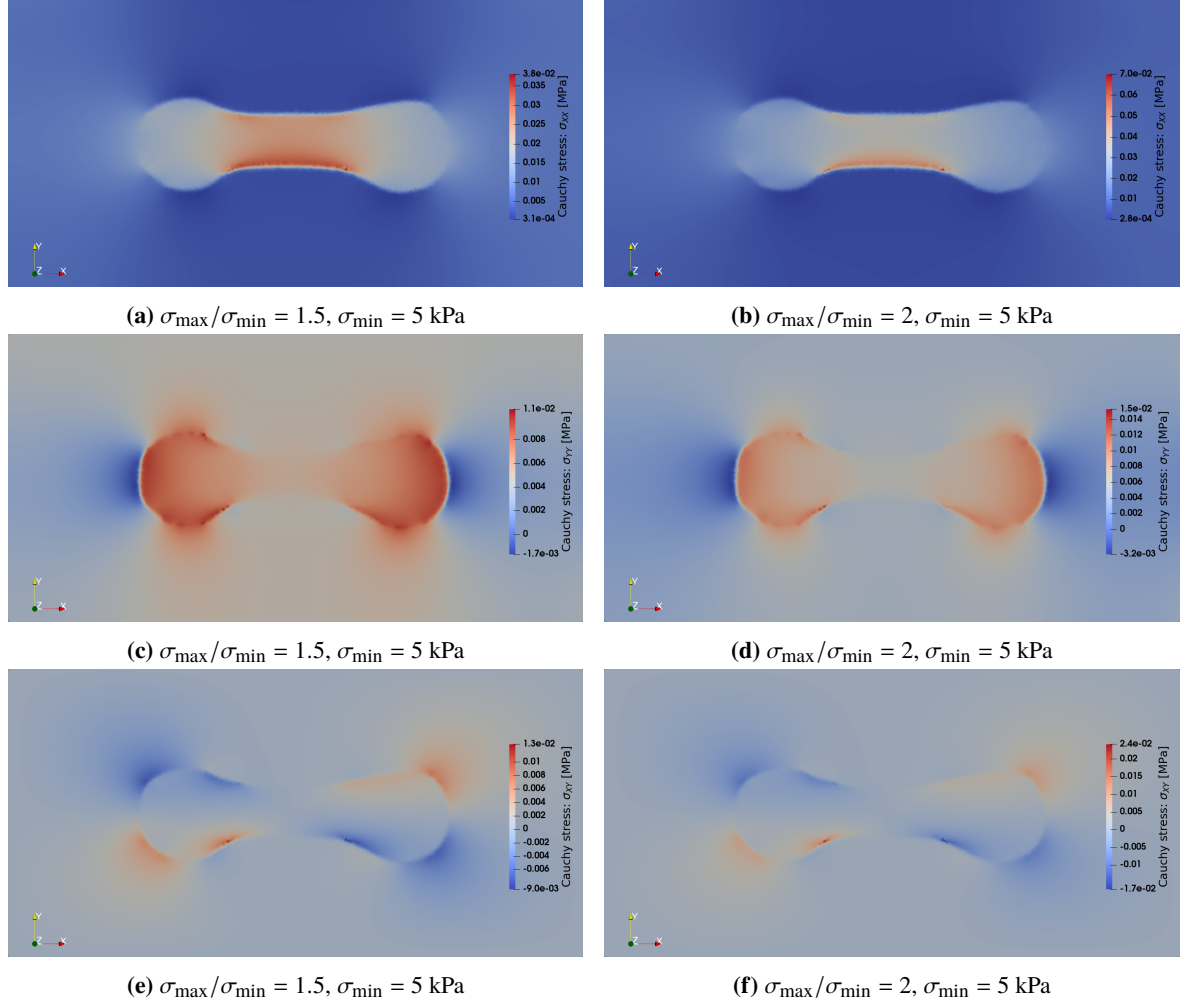
Figure 4.17: Parametric study of prestress's influence on keloid. (a) and (b): Cauchy stress σ_{XX}. (c) and (d): Cauchy stress σ_{YY}. (e) and (f): Cauchy stress σ_{XY}.

4.3.2.1 Specifications

In a recent article by Limmer and Glass [401], different types of keloid treatment methods were listed: chemical, electromagnetic, *etc*. The wound healing may be improved via the manipulation of its mechanical environment. Given our requirements, the specifications established for the present specific-patient share some common features with the mechanical-based solution, principally regarding health safety. Table 4.2, inspired from a random World Health Organization specification, reports the first version of the main characteristics of the targeted solution. The specifications will be updated according to the feedback from the engineers and the patients.

4.3.2.2 Exemplar

We discuss in this part a probable technical solution that satisfies the requirements in Table 4.2. One should focus on the device's utility to prevent keloid enlargement if the patient refuses a surgical excision. As for the safety side, it will be considered in the improvement phase. In Section 1.1.3.2, it was mentioned that an innovative technique, known as pressotherapy, was processed after keloid surgery and consisted in pressing the earlobe from both sides to minimize the stretching tensions [116]. We can imagine a technique motivated by the latter approach.

The primary function of the proposed solution is uniaxial compression, which involves a system

Table 4.2: Specifications of a clinical solution to prevent keloid growth adapted to patient-specific.

MEDICAL DEVICE SPECIFICATION		
i	Version No.	1.0
ii	Date of initial version	02/02/2023
iii	Date of last modification	02/02/2023
iv	Completed / submitted by	Aflah Elouneg
v	Generic name	Keloid Container
PURPOSE OF USE		
1	Clinical purpose	Total stoppage of the keloidic scar's propagation after or without excision.
2	Level of use	University Hospital Center / Dermatology Service
3	Overview of functional requirements	- Has the ability to counter the predominant natural tensions, normal and shear stresses, in the keloidic scar and on its interface with the surrounding undamaged skin - Is exclusively designed for the current scar shape of the patient-specific - It can be applied comfortably on the patient's skin for as long as possible to reach the scar remodeling phase - Ensures biocompatibility with the skin to avoid any kind of allergic reaction - Grants autonomy for the patient to remove it and set it up
TECHNICAL CHARACTERISTICS		
4	Detailed requirements	- Access to all keloid's plane surfaces and curved edges - Contact or contactless elimination of stress - Local adjustment of the applied counter-stress - Resistance to the relative humidity up to 100 % - Working temperature between -50 to $50\,°C$ - Waterproof and washability - Resistance to sterilization under high temperature - Design color mostly similar to the skin - Protection alarm for high compression risks - Anti-accumulation of moisture - Portability and stability for high-tense physical activities
5	Displayed parameters	- Counter-stress magnitude for each Cauchy stress component - Date of first use
PHYSICAL/CHEMICAL CHARACTERISTICS		
6	Components	- Compatible with the skin with no allergic reaction
7	Raw materials	- Environmentally friendly

of micro belts positioned on the critical zone and aligned with the dominant tension component as demonstrated in Figure 4.14 or 4.15. Each belt is composed of two small pads attached to the skin (with biological adhesives) and connected by a solid strip, which can be adjusted to stretch inward and provide compression. These belts, illustrated by a line and double arrows in Figure 4.18, can be positioned to eliminate normal stress and, in turn, eliminate shear stress, according to the proposed theory.
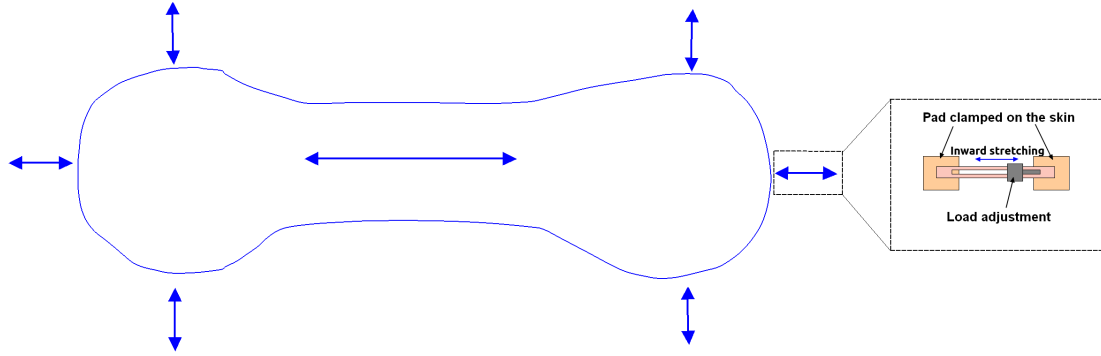
Figure 4.18: Proposal of a medical device to contain the keloid according to the specifications.

Conclusions

The present Chapter treated the application of SoFTI to a patient-specific case, where the material parameters of the keloid scar and the surrounding healthy-skin were calibrated *via* the Gent model. The model calibration was based on a dataset that combined measurement of displacement and reaction force captured during a uni-axial extension experiment. The recommendations formulated in Chapter 2 regarding the uncertainty analysis on the measurement and discretization errors, and also the data quantity, were fulfilled to ensure accurate parameter identification. However, a substantial inconsistency (associated with a lack of the DIC speckle pattern) was noticed on the displacement fields. Thus the observation area had to be restricted. With fewer displacement data, especially for the healthy-skin medium, the optimization of the Lagrange-Multiplier-based objective function failed to identify $J_{m\text{hs}}$, unlike with synthetic data in Chapter 2. To overcome the issue, a set of data gathered from a contra-lateral test was employed to back up the identification. As a result, the definitive material parameter set for the patient-specific was $\hat{\boldsymbol{m}}^{\text{PS}} = \{\mu_{\text{k}} = 0.0491 \text{ MPa}, J_{m\text{k}} = 0.0175, \mu_{\text{hs}} = 0.03692 \text{ MPa}, J_{m\text{hs}} = 0.103\}$, revealing that the keloid is 33 % stiffer than undamaged skin. The application of the pipeline to real data witnessed its ability to assess the material parameters and its adaptability to the low data quantity case. In addition to the uni-axial extension test performed on the scar, performing a second one at a closer undamaged site is recommended as a backup. Besides, the results led to the validation of the Gent model, which has been chosen for its extensibility-limited characteristic. Model calibration with other hyperelastic constitutive laws may be fruitful for the study and can be proposed as a perspective.

In the post-treatment phase, the Cauchy stress field was mapped for normal and tangential components by utilizing the output $\hat{\boldsymbol{m}}^{\text{PS}}$. For that, an arbitrary bi-axial prestress, representing the natural tension in the skin, was put in place. The primary results showed stability of stress concentration zones for different values of prestress ratio and magnitude. Annihilating the stresses on those zones would help stop the propagation of keloid growth. Furthermore, an alternative way to contain the keloidic scar was addressed. The stress data were expressed on a new basis such that the shears are null by

solving the eigenvalues problem. Therefore, stopping the scar's propagation would be equivalent to eliminating the maximum principal stress along the principal vectors determined locally. At that level, the surgeon has two techniques to identify the critical zones, either with the Cauchy stress tensor or its diagonalized form. At the end of the pipeline, specifications of a clinical solution adapted to the patient-specific set were suggested, which led to the proposal of a medical device.

Two weaknesses of the SoFTI framework in its actual version must be pointed out. First, the user without experience in mechanical modeling would need technical assistance to convert recorded tests into DIC fields, mesh the domain and the observation zone, and configure the optimizer to ensure convergence in the parameter identification. Consequently, one should consider developing a user interface for the sake of ergonomy in the future. Second, even though the change in the prestresses doesn't affect the position of the critical zone, the magnitude of the stress to eliminate is highly impacted. In other words, measuring accurately the prestress *a priori* would help adjust the medical device to counter the exact stress.

Chapter 5

Characterization of the Anisotropy of the Human Skin: Preliminary Study

The second major topic of the thesis, originally independent from Chapters 2, 3, and 4, covers the study of the anisotropy aspect in living skin. The approach of dividing the problem into segments involved modeling healthy skin as an isotropic material in the anterior sections. Nevertheless, previous research has shown that undamaged skin exhibits an anisotropic behavior when subjected to mechanical loads, contrary to the assumption of isotropy. The anisotropy can be related to the alignment of collagen fibers in the mechanically dominant layer, the dermis. It is indicated by a greater stiffness of the undamaged skin in a particular direction, namely, Langer's line. The method and results reported in this chapter, published recently [402], aim to explore the usability and the limits of a system experiment/framework in identifying the anisotropic material parameters of the skin. The study includes the application of the methodology to a series of multi-axial stretch tests conducted on one patient. The day-to-day comparison of the mechanical response would indicate the system's reliability and the skin behavior's variability. The latter was labeled *intra*-subject variation.

The importance of identifying the anisotropy axis orientation resides in assisting the surgeons in performing incisions without causing undesirable scars. This perspective could be accounted for as a parallel approach to prevent the apparition of keloids if one establishes a link with the previous chapters. To recall, in Section 1.1.3.1, it has been shown that keloids on a patient's back seemed to follow the direction of Langer's line. Another lead that can be investigated regarding Langer's line's effect on keloid prorogation is modeling the healthy-skin with an anisotropic hyperelastic law. The chapter is structured as follows: (i) describing the *in vivo* apparatus and the experimental protocol allowing the measurement of the displacement under multi-axial stretch, (ii) analyzing the numerical methodology leading to identify the anisotropic parameters based on data, (iii) providing results of *intra*-subject variation application.

5.1 Experiments

Characterizing the anisotropic behavior of soft tissue could be done by studying the mechanical response under a multi-axial loading (Sec. 1.2.1.2). The test can be in the form of multiple uni-axial stretches carried out combinedly in many directions, either *in vivo* [18] or *ex vivo* [146]. If the test allows us to identify the direction of the highest stiffness correlated with the abundance of collagen fibers, it would have one major drawback. Gathering the uni-axial response in each direction is time-consuming and would necessitate meticulous protocol. At the same time, reducing the resolution by conducting fewer numbers of them will affect the identification accuracy. In this Section, we describe a novel technique to overcome the reported issue and the numerical tool implemented to treat data. The anisotropy could be quantified also with elastic waves [403, 404] and optical method [202].

5.1.1 Materials and Methods

The experimental apparatus in the present study includes two essential parts: a commercial device to apply an annular-suction-based test and record the deformation and an open-source software to convert the test records into displacement field data.

5.1.1.1 Multi-Axial Annular Suction Test

In this experimental method, the multi-axial stretch on a plane circular membrane is caused by an out-plane suction around it, hence the designation "annular suction" or "ring suction." The equipment was built around a commercial apparatus CutiScan® CS 100 (referenced with CutiScan® for easiness throughout the manuscript), developed by Courage + Khazaka electronic [149] (same company as Reviscometer® used for characterizing anisotropy with elastic waves) (Fig. 5.1a). It includes a central device and a probe, the main parts of CutiScan®, and a support to hold the specimen and the probe, manufactured and designed in the Department Applied Mechanics in FEMTO-ST.

The central device, where the vacuum pump is situated, supplies negative pressure to the probe to vacuum the biological tissue. As seen in the sectional view of Figure 5.1a, the annular suction fits the opening between the blue plastic and the yellow conic reflector made of aluminum. The inner and outer diameters of the ring-shaped opening are 5 mm and 14 mm, respectively. The purple rectangles surrounding a camera in the center emit ultra-violet light. The camera, visible in Figure 5.1b, is a black-and-white charge-coupled device that records soft tissue deformation. The pink medium represents the soft tissue, and black arrows display the direction of the observable area extension. When applying a constant suction pressure uniformly, denoted p, for a predefined phase t_{creep}, the central zone is subjected to a radial extension (Fig. 5.1b). Afterward, the pressure is instantaneously released for another phase with duration t_{relax}. For the total creep-relaxation cycle, the deformation of the studied sample within the observation zone of 5 mm diameter is recorded with a µEye® camera. In addition, a double-sided adhesive was placed to prevent slippage between the probe and the sample's surface beyond the outer diameter.

Despite the way of analyzing data, the experiment technique of the proposed method could be identical to Laiacona et al.'s [148], but it has the potential for superior performance. One key advantage is that the CutiScan® device has a smaller application area (ring diameter: 5-14 mm) versus (ring diameter: 30-49 mm), allowing for more precise and localized measurements on various parts of the body. Additionally, CutiScan® allows for easy and direct pressure control, while the Laiacona et al.'s device relies on a valve to control pressure.

A closed-source framework is provided with the commercial device for setpoint adjustment and configuration and for treating the raw data. For all tests performed for the presented anisotropy studies in the thesis, it had been set t_{creep} = 1 s and t_{relax} = 1 s in the pre-cycle, then $t_{standby}$ = 10 s. The latter is the waiting time between a pre-cycle and the principal recorded cycle. For the principal cycle (or measurement cycle), t_{creep} = 3 s, and t_{relax} = 3 s (Fig. 5.2). Due to viscous effects, the pre-cycle could be skipped as soft materials may take longer to recover their initial configuration. However, it is recommended to maintain the pre-cycle to regulate brightness inside the probe. A brightness perturbation may cause artifacts in a DIC-based treatment.

5.1.1.2 Digital Image Correlation

The other function in the CutiScan® software is converting the videos into temporal displacement through an optical flow algorithm, namely, Horn–Schunck, which assumes smoothness in the flow over the whole image. Therefore, the outputs are creep-relaxation curves and maximum extension ($V1$) along every angle, as illustrated in Figure 5.3. However, the exact position of the point where the
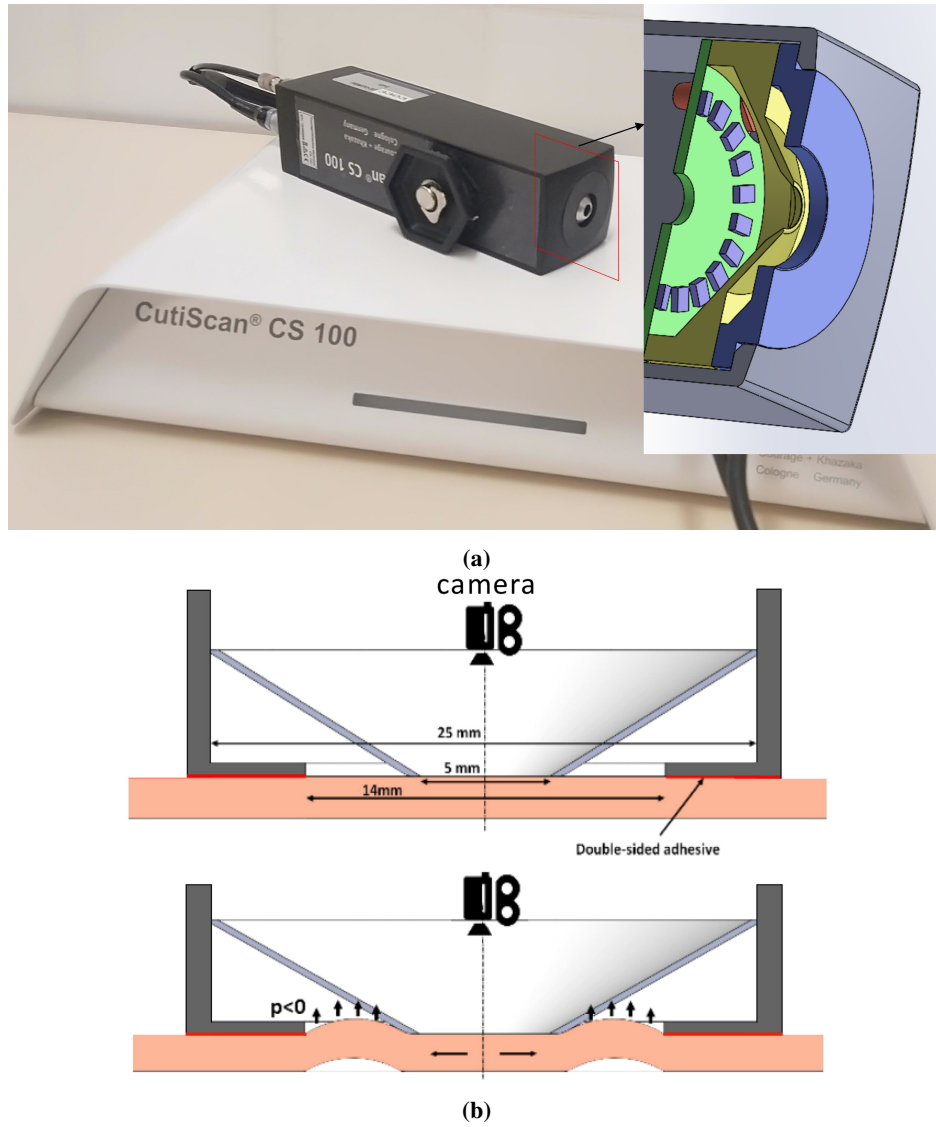
Figure 5.1: Multi-axial annular suction test apparatus. (a) CutiScan® CS 100 equipment with a CAD model showing the internal elements in the probe (permission granted from Courage + Khazaka GmbH). Adapted from [402]. (b) A cross-section view of the probe before and during the suction (published in [124]).

curves are built is unknown, and the user cannot access the full-field data. Moreover, the last subfigure on the right in Figure 5.3 does not indicate the presence of a symmetry axis that can be considered as Langer's line.

To overcome the limitation, Quentin Lucot, a former intern in the Biomechanics team – Department Applied Mechanics/FEMTO-ST, constructed during his Master internship a Python program based on the PyDIC tool [406]. Its main function is splitting the videos recorded with CutiScan®into frames and computing the displacement vectors at uniformly-mapped nodes. To track motions, the program uses the Lucas-Kanade method (Sec. 2.1.2.2). For better adaptability, the program has been modified and shared publicly on `https://github.com/aflahelouneg/MARSAC/blob/main/pydic.py`. The nodes can be either mapped following the Cartesian or the polar coordinates (Fig. 5.4)

Considering the characteristics of radial stretch, it would be more appropriate to opt for a polar mapping. However, since the subset correlation windows are square-shaped, arranging them radially could potentially cause conflicts with the adjacent windows. Consequently, the Cartesian mappings
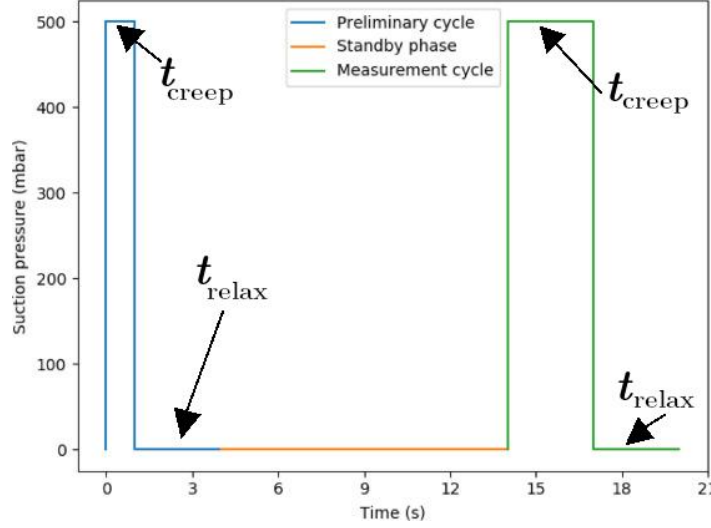
Figure 5.2: Pressures setpoints for the two loading cycles. Modified from [405].
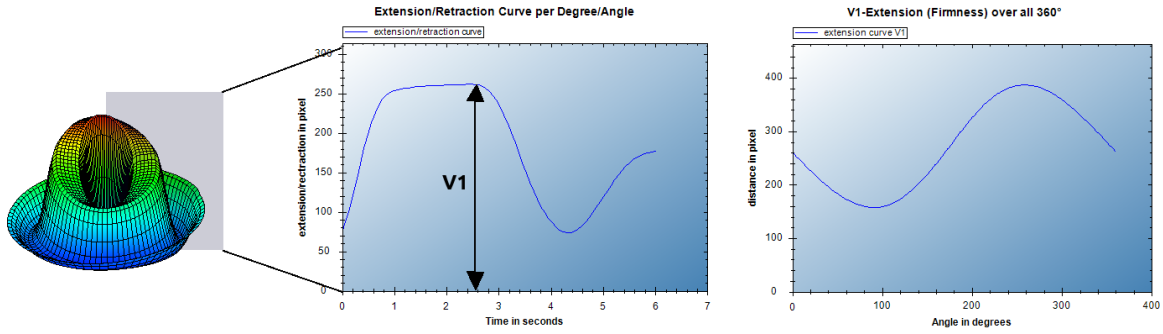
Figure 5.3: Outputs of the software provided with the commercial device CutiScan®.

were used to generate displacement data for all video frames. On the basis of an auxiliary calibration study (similar to Sec. 4.1.2.2), the correlation parameters, grid resolution, and correlation window size were fixed to be $d_G = 20$ px and $a_W = 40$ px, respectively. The coordinate grid is mapped with 49×49 nodes (Fig. 5.4a).

5.1.1.3 Displacement Data

With the alternative developed tool, it is henceforth possible to get information all over the field. If the targeted point is situated between grid nodes, a linear interpolation of the quantity of interest is operated. With the cubic interpolation, the relative change in displacement was 0.4%. The DIC process supplies the new positions of the grid nodes from one video frame to another. The program computes the displacements in pixels and millimeters a second time if a scale is provided. The displacement can be expressed both with Cartesian and polar components. In the actual study, the experimental data were expressed in a coordinate system $\{e'_1, e'_2\}$, corresponding to the probe-camera referential, with e'_1 oriented along the angle $0°$ (Fig. 5.5).

5.1.2 *In vivo* Tests on Human Skin

A series of multi-axial stretch tests were carried out on a volunteer to study the reproducibility and robustness of the experimental design. This part will address the experimental protocol and the relevant mechanical responses in the form of displacement. The entire dataset was shared for free and dully described in a data paper [405].

(a) Cartesian   **(b)** Polar
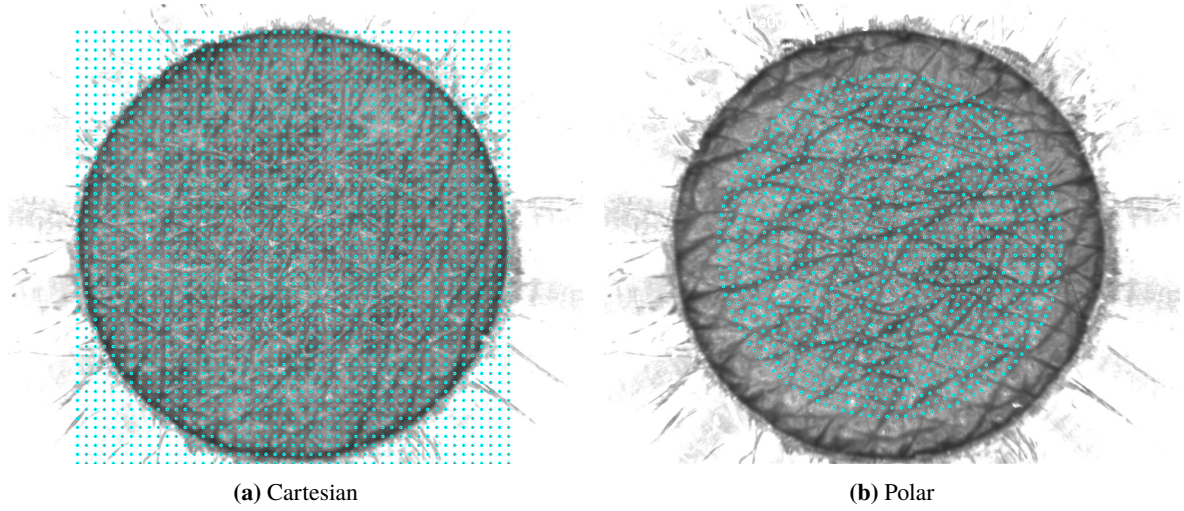
Figure 5.4: DIC coordinate grid in the initial configuration.

5.1.2.1 Protocol

The volar left forearm of a 28-year-old Caucasian male was tested 30 times, as often as possible, at the same time slot. The anatomical site, located at a distance of 15 cm from the wrist, was chosen for its flatness and exposedness. The CutiScan®probe-camera was positioned perpendicular to the site, whose position is controlled with a sliding column designed by myself and fabricated in the laboratory for that purpose. A level tool was used to ensure the horizontality of the site. The orientation of the probe with respect to the arm axis is indicated in Figure 5.5.
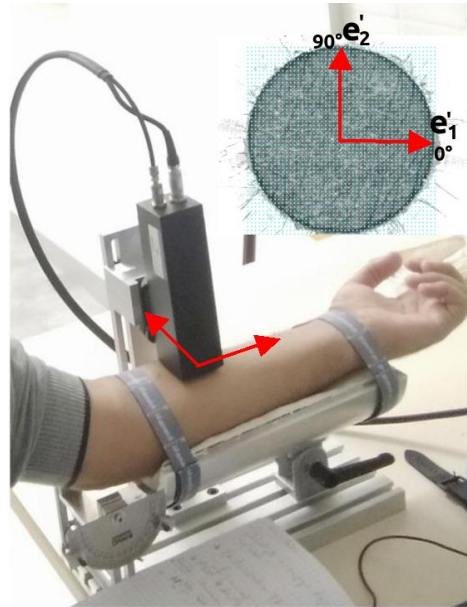
Figure 5.5: Orientation of the probe and observation zone. Adapted from [405].

One annular suction test series consists of 21 creep-relaxation cycles (Figure 7a in [405]) with pressure setpoints varying from 100 to 500 mbar with an increment of 20 mbar. Between every two cycles, a delay of 2 minutes inactivity was arbitrarily set, considering that a weak load has a non-significant impact on skin conditioning. In Takema *et al.*'s study [407], the relaxation period was 2 seconds for 3 pressure levels, 200, 300, and 400 mbar, with a Cutometer device. In addition, CutiScan®applies a pre-load cycle of 10 s before each recordable process, making the influence of the delay period less

significant.

5.1.2.2 *Intra*-Subject Tests

The video files (primary data) recorded with CutiScan®probe-camera were collected in a public repository `http://dx.doi.org/doi:10.25666/DATAOSU-2021-08-25` and were converted into displacement fields (secondary data) using the DIC-based program. As the present study focuses on the anisotropy characterization in healthy skin independently of viscoelastic effects, only the video frame at the end of the creep phase (around 3 s) was employed. Also, among the pressure setpoints, the median level $p = 300$ mbar was exploited. According to our observations, the experimental data could be more reproducible around that pressure level.

As a demonstration, the average of displacement curves over all tests (for better visualization) is plotted in Figure 5.6. In Figure 5.6b, the radial component of displacement vector, $u_r(\theta_r)$, is interpolated along every circle with radius in $\{0.5, 1.0, 1.5, 2.0, 2.5\}$ mm, such that θ is the angle with respect to the axis e'_1. As a result, the angular distribution of the radial displacement exhibits an anisotropic aspect with 2 dips and 2 peaks (except for the radius 2.5 mm) that could match, respectively, Langer's line (minimum displacement) and its transverse (maximum displacement). The latter are called principal directions in our context. The plots shows that u_r grows gradually for circles with radii 0.5, 1.0, then 1.5 mm then drops for 2.0, then 2.5. It is possible that the drop may be caused by several phenomena, including the edge effect on the DIC process and friction. Additionally, Figure 5.6c, demonstrating u_r interpolated along 4 distinctive directions, reveals that displacement could be considered linear within the radius 1 mm. Subsequently, one should restrict the zone of interest (ZOI) used for the analysis with a maximum radius of 1.0 instead of 2.5 mm.

Instead of analyzing the anisotropy based on the displacement curves, it may be interesting to process with the deformed configuration, as illustrated in Figure 5.7 (with a scale of a factor of 5). The initial circle became elliptic in the deformed state, whose semi-axes designate the principal directions. Langer's line angle is visually around $45°$. As will be described later, making use of the deformed state's ellipses was a suitable approach to calibrate the material parameters, one of which is Langer's line angle.

5.2 Modeling

Analyzing the experimental data to characterize the anisotropic behavior of biological tissue, for instance, human skin, can be achieved through modeling. This Section describes building an analytical mechanical model to fit the observations and identify the material parameters based on the misfit optimization. An open-source pipeline baptized MARSAC (Multi-Axial Ring Suction for Anisotropy Characterization), available on `https://github.com/aflahelouneg/MARSAC`, has been established to calibrate the model parameters starting from the experiment record video file. Additionally, the application of the Bayesian inference, not implemented into MARSAC yet, will be explored in this part. The latter could be helpful in simultaneously assessing the material parameters and their uncertainties.

5.2.1 Orthotropic Linear Elasticity

It was noticed earlier that the elastic deformation seemed to exhibit two principal orthogonal directions, roughly along $45°$ and $135°$ according to the basis $\{e'_1, e'_2\}$. Through an intuitive argument, one could assume that the constitutive law is transverse isotropic like once adopted by Reihsner *et al.* [18]. Besides, the measured displacements for one sample representing the mean values exhibit strains under 3%, regarding the ZOI, as plotted in Figure 5.6. For such a small strain, we assume that

(a) Displacement field

(b) Angular distribution

(c) Radial distribution
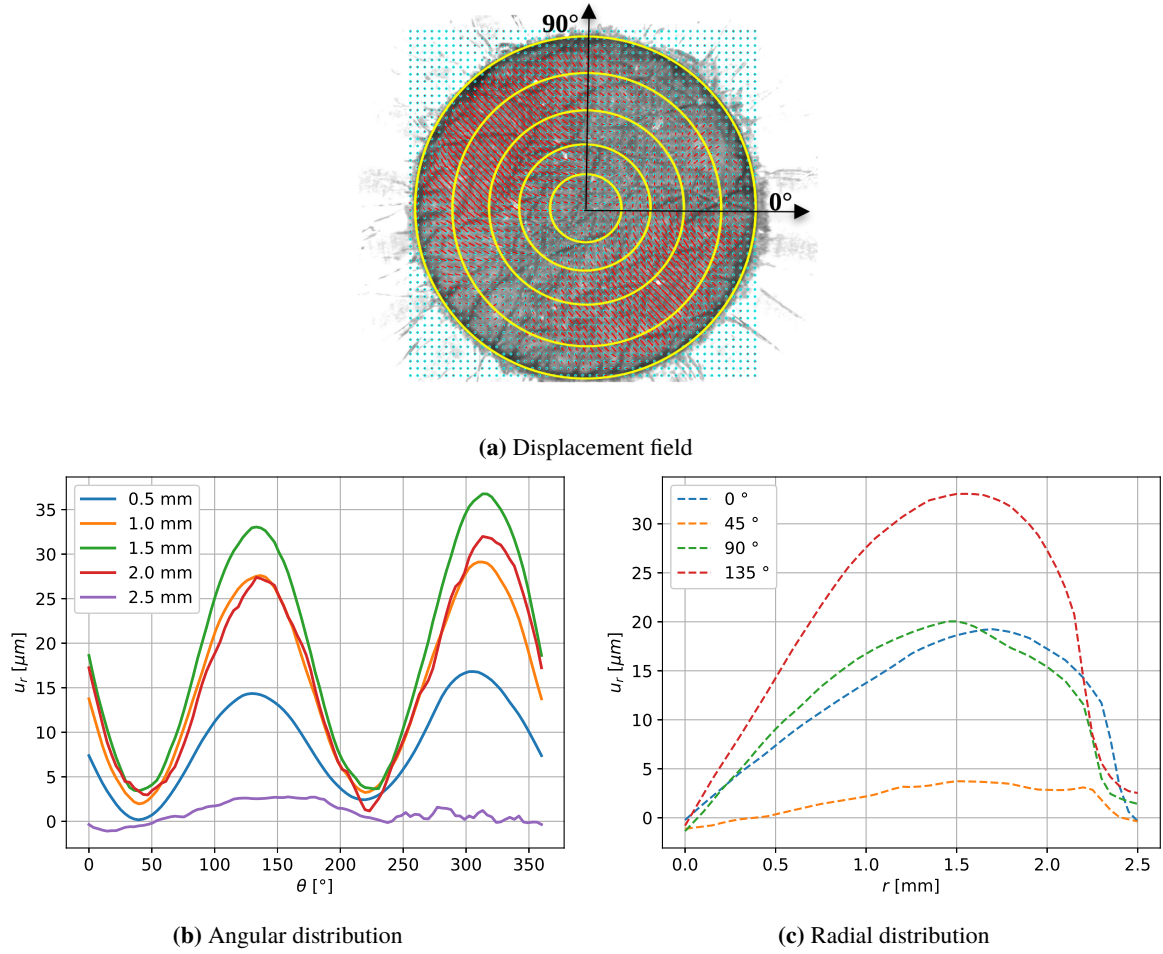
Figure 5.6: Demonstration of displacement data projected on distinctive circles and lines.

the mechanical behavior of the skin is within the toe region, as stated in the literature 1.3.1.2. Jacquet *et al.* carried out *in vivo* extension measurements on the forearm along several directions [143], and all stress-strain curves proved linear for strains up to 3%. To incrementally increase the complexity of the model, this study initially focuses on exploring the linear relationship between applied load and deformations. This involves approximating the resulting coefficients, which are the elastic moduli. In Section 5.4.1, the study will then address the nonlinearity aspect at small strains.

5.2.1.1 Continuum Mechanics

Modeling the annular suction test was achieved with a 2D problem governed by plane stress conditions in the (X_1, X_2) plane (as coordinates of the basis $\{e_1, e_2\}$)[1]. The angle $(\phi = e'_1, e_1)$, with e'_1 oriented parallel to the left volar forearm toward the hand, represents the orientation of the Langer's line (Fig. 5.8). The boundary conditions are characterized by (i) the radial traction force t applied to the edge, (ii) the locking conditions with null displacements at the center of the domain to avoid rigid body displacements (Fig. 5.9a). Other facts about the current approach are summarized as follows. The friction effects between the skin and the CutiScan®probe are not considered. Besides, A uniform in-plane radial stress σ_r taking place over all the observable zone is assumed to be linearly correlated with the supplied vacuum pressure.

---

[1]The Cartesian basis $\{e_1, e_2\}$ on which the model is expressed is not to be confused with the basis $\{e'_1, e'_2\}$ used for the experimental displacement fields
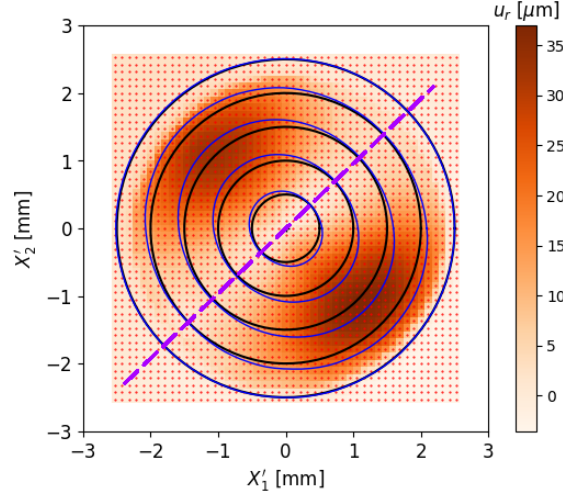
Figure 5.7: Orientation of the probe and observation zone. X_1' and X_2' are the coordinates in the basis $\{e_1', e_2'\}$. Langer's line is succinctly drawn in a magenta dashed line.
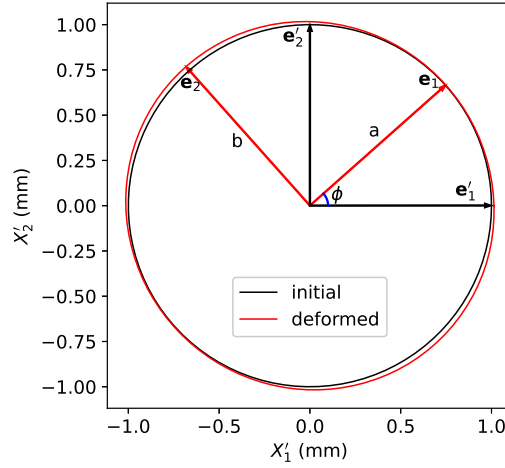
Figure 5.8: Langer's line orientation with respect to the probe referential.

In the coordinate system $\{e_1, e_2\}$, $(X_1 = 0)$ and $(X_2 = 0)$ are symmetry axes. From geometrical and material points of view, only a quarter of the problem can be taken into account (Fig. 5.9b). Subsequently, the edge $\partial\Omega$ of the domain Ω can be split into a Dirichlet part $\partial\Omega_\mathrm{D}$ and a Neumann part $\partial\Omega_\mathrm{N}$ such as $\partial\Omega = \partial\Omega_\mathrm{D} \cup \partial\Omega_\mathrm{N}$.

The local formulation of the static problem consists in finding the displacement vector $\boldsymbol{u} = \{u_1, u_2\}$, strain vector $\boldsymbol{\varepsilon} = \frac{1}{2}\left(\boldsymbol{\nabla}\boldsymbol{u} + (\boldsymbol{\nabla}\boldsymbol{u})^T\right)$, and second-order stress tensor $\boldsymbol{\sigma}$, that satisfy in the absence of body forces the following equations :

$$\begin{aligned}
\boldsymbol{\nabla} \cdot \boldsymbol{\sigma} &= \boldsymbol{0} \quad \text{in } \Omega \\
\boldsymbol{\sigma} \cdot \boldsymbol{n} &= \sigma_r\, \boldsymbol{n} \quad \text{on } \partial\Omega_\mathrm{N} \\
u_1(0, X_2) &= 0 \quad \text{and} \quad u_2(X_1, 0) = 0 \quad \text{on } \partial\Omega_\mathrm{D} \\
\boldsymbol{\sigma} &= \boldsymbol{C}_\mathrm{e} : \boldsymbol{\varepsilon}
\end{aligned} \tag{5.1}$$

Eq. (5.1a) represents the equilibrium equations within the deformable domain. Eq. (5.1b) stands for

(a) Global problem   **(b)** Reduced problem
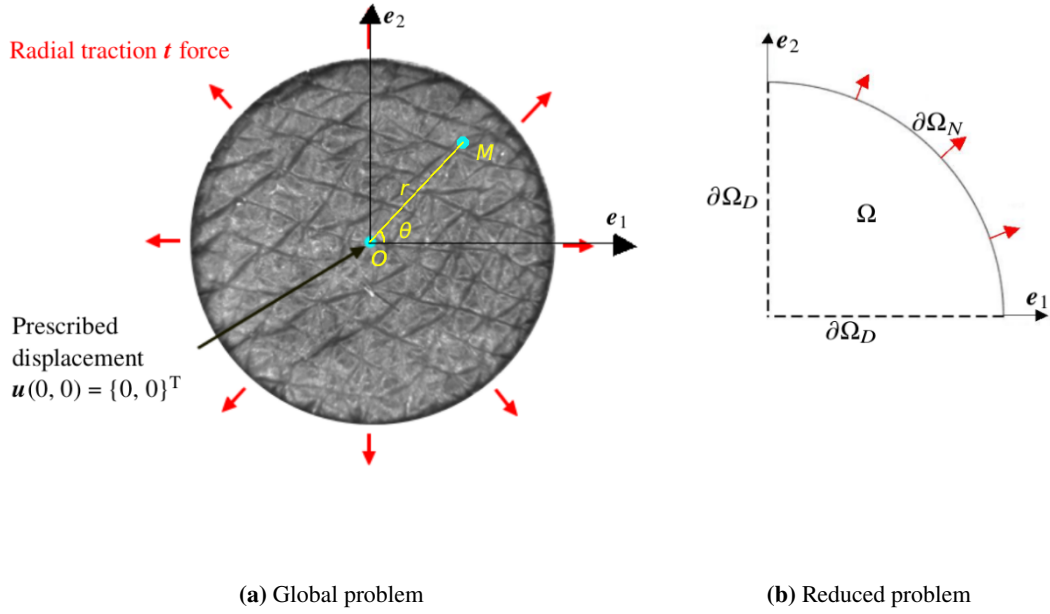
Figure 5.9: Boundary conditions of the annular suction test model. Published in [402].

the Neumann boundary conditions such that n is the normal vector to the edge and σ_r is the radial stress, resulted from the applied t. Eq. (5.1c) is for the Dirichlet boundary conditions. Eq. (5.1d) constitutes the stress-strain equations with C_e a the fourth-order tensor representing the transverse isotropic linear stiffness. It is given under plane-stress conditions by [408]:

$$
\begin{Bmatrix} \sigma_{11} \\ \sigma_{22} \\ \sigma_{12} \end{Bmatrix} = \frac{1}{1 - \nu_{12}\nu_{21}} \begin{bmatrix} E_1 & \nu_{21}E_1 & 0 \\ \nu_{12}E_2 & E_2 & 0 \\ 0 & 0 & (1 - \nu_{12}\nu_{21})G_{12} \end{bmatrix} \begin{Bmatrix} \varepsilon_{11} \\ \varepsilon_{22} \\ 2\varepsilon_{12} \end{Bmatrix} \tag{5.2}
$$

σ_{11}, σ_{22} and σ_{12} (respectively, ε_{11}, ε_{22} and ε_{12}) are the components of the stress tensor σ (respectively, the strain tensor ε). E_1 and E_2 are the elastic moduli along the axes e_1 and e_2. This study could interpret them as stiffness along and across Langer's line, respectively. ν_{12} and ν_{21} are the Poisson's ratios along and across Langer's line. G_{12} is the shear modulus. Since the in-plane radial stress σ_r presupposed to be uniform all over the domain, we set $\sigma_{11} = \sigma_{22} = \sigma_r$.

For symmetry conditions on the compliance and stiffness matrices, one reads:

$$
\frac{\nu_{12}}{E_1} = \frac{\nu_{21}}{E_2} \tag{5.3}
$$

Consequently, 4 material parameters out of 5 are independent: E_1, E_2, ν_{12}, and G_{12}. For pure radial stretch, there might be no way to identify the shear modulus. The annular suction test allows then identifying potentially three parameters.

5.2.1.2   Analytical Solution

According to the deformed elliptical shape observed in Figure 5.8, with the semi-axes a and b, the analytical displacement components in the model referential take the form:

$$
\begin{cases} u_1(r, \theta) = A_1 r \cos\theta \\ u_2(r, \theta) = A_2 r \sin\theta \end{cases} \quad ; \quad r \in [0, R] \quad ; \quad \theta \in [0, 360°] \,, \tag{5.4}
$$

with r and θ are the cylindrical coordinates defined by $r = \|\overrightarrow{OM}\|$ and $\theta = (e_1, \overrightarrow{OM})$, in which $\overrightarrow{OM}$ is the position vector of a material point in the Cartesian system $\{O; e_1, e_2\}$ (Fig. 5.9a). The radius R corresponds to the frontier of the observable zone. A_1 and A_2 are constants calculated from Neumann boundary conditions (5.1b). The infinitesimal strain-displacement relations, $u = \{u_1, u_2\}$, combined to the constitutive equations in Equation 5.2 lead to uniform strain for any point in Ω. After computations, we express A_1 and A_2 as:

$$\begin{cases} A_1 = \dfrac{\sigma_r(1 - \nu_{12})}{E_1} \\ A_2 = \dfrac{\sigma_r(1 - \nu_{21})}{E_2} \end{cases} \tag{5.5}$$

Finally, the analytical solution for the displacement field in terms of Cartesian material coordinates X_1, and X_2 is given by:

$$\begin{cases} u_1(X_1, X_2) = \dfrac{\sigma_r(1 - \nu_{12})}{E_1} X_1 \\ u_2(X_1, X_2) = \dfrac{\sigma_r(1 - \nu_{21})}{E_2} X_2 \end{cases} \tag{5.6}$$

As far as I know, the proposed solutions to the radial stretch problem for transverse isotropic elasticity could not be found in the literature. Thus, it may be considered a scientific contribution. In a non-classical approach, the finite element method was employed as a reference to validate the solution (Eq. 5.6) and check its unicity.

5.2.1.3   FEM Solution

The same 2D problem (Fig. 5.9) can be written in a weak formulation for the domain Ω and its boundary boundary $\partial\Omega$ in the absence of body force as

$$\text{Find } u \in \mathcal{U} \text{ such that } \forall v \in \mathcal{V}_0, \int_{\Omega} \sigma(u) : \nabla^{\text{sym}} v \, d\Omega = \int_{\partial\Omega} (\sigma_r n) \cdot v \, d\Gamma \tag{5.7}$$

$\mathcal{U}$ denotes a space of sufficiently smooth functions that verifies Dirichlet conditions and $\mathcal{V}_0$ its counterpart satisfying homogeneous boundary condition on the Dirichlet boundary $\partial\Omega_{\text{D}}$.

The FE-model was solved for various parameter sets with the FEniCS framework, where Ω, taking the shape of a quarter of a disk, was meshed into quadratic triangular finite elements (55 k cells and $N_n = 110$ k nodes). The FE solver was executed and its solutions u_{FE} were confronted with the analytical ones u for different orders of E_1-magnitude ($E_1 = \{0.01, 0.1, 1, 10\}$ MPa) and ratio $E_1/E_2 = \{1, 2, \ldots, 19, 20\}$, combined with the values $\nu_{12} = \{0, 0.05, \ldots, 0.90, 0.95\}$ and $G_{12} = 1$ MPa. E_1 and E_2 value ranges were set from the literature [106, 128, 131–135, 141, 357]. For each set, the maximum absolute errors between the numerical and analytical displacement solution was evaluated for all nodes (Eq. 5.8). See Figure D.1 in Appendix D for all results. The maximum and minimum absolute errors between the numerical and analytical displacement solution evaluated on nodes are $2.81e - 6$ mm and $3.0e - 15$ mm, respectively. Given a parameter set for the maximum error, $E_1 = 0.01$ MPa, $E_1/E_2 = 20$ kPa, $\nu_{12} = 0.5$, $G_{12} = 1$ MPa, the displacement vectors for both analytical and FE models were compared each other along the usual circles with radii $\{0.5, 1.0, 1.5, 2.0, 2.5\}$ mm in Figure 5.10.

$$\varepsilon_{\max} = \max_{i=1,\ldots,N_n} \sqrt{\|u_{\text{FE}}{}^{(i)} - u^{(i)}\|^2} \tag{5.8}$$

The last result confirmed that the analytical solutions fit perfectly the FE data. One of the relevant benefits of its application is the ease of calculating the Gradient and Hessian matrix for parameter optimization. As its computation cost is too low, it can be used for stochastic optimization requiring thousands of calculations, such as the Bayesian calibration.

(a) u_1 (X_1-component)

(b) u_2 (X_2-component)

(c) u_r (radial component)

(d) u_θ (ortho-radial component)
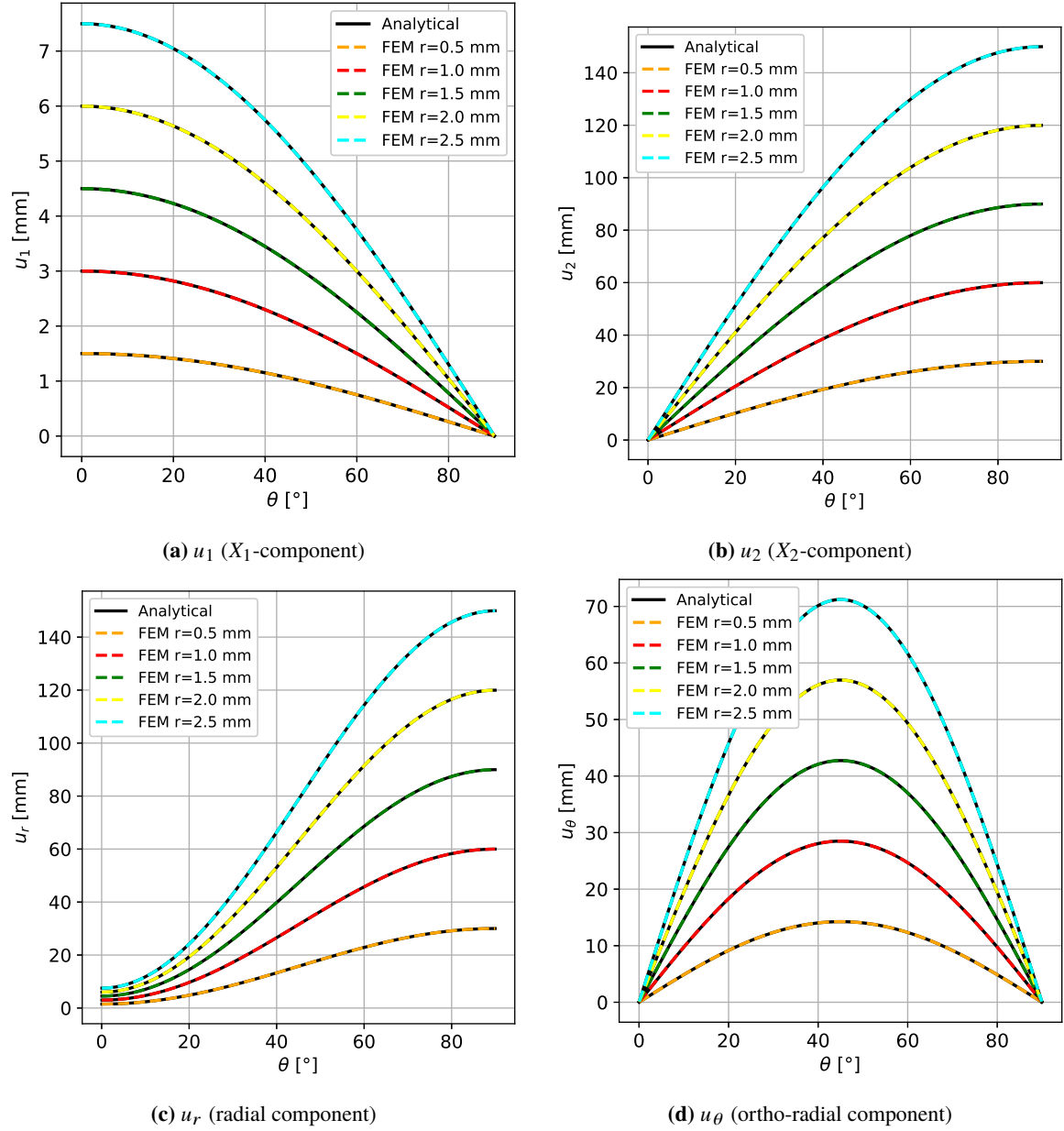
Figure 5.10: Validation of the analytical solution based on FE simulation.

5.2.2 Parameter Identification

The strategy established to identify the targeted material parameters $\{\phi, E_1, E_2\}$ follows two steps. First, the geometrical parameters $\boldsymbol{m}_g = \{a, b, \phi\}$, the semi-axes of the deformed ellipse and Langer's line, are calibrated from the elliptic deformation. After that, the remaining material parameters are deducted from the constitutive law linking observed displacement to the applied stress. Although ϕ is a material characteristic, it is identified in the first phase, outside a mechanical model, because of its geometric feature (orientation with respect to the arm axis).

5.2.2.1 Geometrical Parameters

For the study of the presented methodology, the data used for model fitting are gathered from a circle of radius r_{fit}. The minimization of the objective function can be processed within a non-linear least-squares problem solved with Newton's algorithm. With the results witnessing the linearity of the mechanical response within the circular zone $r < 1$ mm in Figure 5.6), we opt for fitting model

to data from one circle instead of full-field measurement. For a defined circle, its deformed ellipse spatial coordinates read:

$$
\begin{cases}
x_1(r_{\text{fit}}, \theta) = a(r_{\text{fit}}) \cos \theta \\
x_2(r_{\text{fit}}, \theta) = b(r_{\text{fit}}) \sin \theta
\end{cases}
\quad ; \quad \theta \in [0, 360°]
\tag{5.9}
$$

Similarly, as in [167], the objective function $\mathcal{J}_{\text{aniso}}$ evaluates for each angle θ_k the difference of euclidean distances between an observed deformation point and the referential origin, for the model and experimental data. The model includes geometrical transformations of its respective ellipse points to fit a fixed experimental one in the deformation state. Thereby, the basis $\{e_1, e_2\}$ is oriented with ϕ and shifted with $\{x_{10}, x_{20}\}^T$ vector to match the basis $\{e'_1, e'_2\}$. Therefore, the targeted geometrical parameters set is extended to $\tilde{m}_g = m_g \cup \{x_{10}, x_{20}\}$.

$$
\mathcal{J}_{\text{aniso}\,k}(\tilde{m}_g, r_{\text{fit}}, \theta_k) = \frac{1}{2} \left(d^{\text{model}}(\tilde{m}_g, r_{\text{fit}}, \theta_k) - d^{\text{exp}}(r_{\text{fit}}, \theta_k) \right)^2
\tag{5.10}
$$

For the experimental data the euclidean distance reads:

$$
d^{\text{exp}}(r_{\text{fit}}, \theta_k) = \sqrt{x'_{1_k}{}^2 + x'_{2_k}{}^2} \quad ; \quad \theta_k = \arctan\left(x'_{2_k} / x'_{1_k}\right)
\tag{5.11}
$$

Let us express the rotated spatial coordinates related to the model. They are introduced by

$$
\begin{cases}
x_1^{\text{R}}(r_{\text{fit}}, \theta, a, b, \phi) = a(r_{\text{fit}}) \cos(\theta - \phi) \cos \phi - b(r_{\text{fit}}) \sin(\theta - \phi) \sin \phi \\
x_2^{\text{R}}(r_{\text{fit}}, \theta, a, b, \phi) = a(r_{\text{fit}}) \cos(\theta - \phi) \sin \phi + b(r_{\text{fit}}) \sin(\theta - \phi) \cos \phi
\end{cases}
\tag{5.12}
$$

As a result, the euclidean distance for model data is defined as

$$
d^{\text{model}}(\tilde{m}_g, r_{\text{fit}}, \theta_k) = \sqrt{\left(x_1^{\text{R}}(r_{\text{fit}}, \theta_k, a, b, \phi) - x_{10}\right)^2 + \left(x_2^{\text{R}}(r_{\text{fit}}, \theta_k, a, b, \phi) - x_{20}\right)^2}
\tag{5.13}
$$

Since the displacement vectors are independent of each other, the total mismatch is quantified for all N_E points as

$$
\mathcal{J}_{\text{aniso}}(r_{\text{fit}}, \tilde{m}_g) = \frac{1}{N_E} \sum_{k=1}^{N_E} \mathcal{J}_{\text{aniso}\,k}(\tilde{m}_g, r_{\text{fit}}, \theta_k)
\tag{5.14}
$$

Starting from an initial guess $\tilde{m}_g^{(0)}$, the change in the parameters $\delta \tilde{m}_g$ is iteratively computed by way of the Newton-Raphson method (Eq. 5.15)) until reaching the absolute convergence criteria of 10^{-9} for every model parameter.

$$
\tilde{m}_g^{(n+1)} = \tilde{m}_g^{(n)} - \left[\frac{\partial^2 \mathcal{J}_{\text{aniso}}}{\partial \tilde{m}_g^2}\right]^{-1} \cdot \left[\frac{\partial \mathcal{J}_{\text{aniso}}}{\partial \tilde{m}_g}\right]
\tag{5.15}
$$

The detailed expressions of the Gradient vector $\partial \mathcal{J}_{\text{aniso}}/\partial \tilde{m}_g$ and Hessian matrix $\partial^2 \mathcal{J}_{\text{aniso}}/\partial \tilde{m}_g^2$ were shared publicly on `https://github.com/aflahelouneg/MARSAC/blob/main/newton.py`.

5.2.2.2 Material Parameters

Once the optimal set of $\tilde{m}_g$ is identified, and among them the anisotropy axis, the remaining material parameters in m_{m} can derive from the principal minor and major semi-axes of the ellipse, *via* the model (Eq. 5.6) as

$$
\begin{cases}
a(r_{\text{fit}}) = r_{\text{fit}} + u_1(r_{\text{fit}}) = r_{\text{fit}}\left(1 + \dfrac{\sigma_r(1 - \nu_{12})}{E_1}\right) \\[4mm]
b(r_{\text{fit}}) = r_{\text{fit}} + u_2(r_{\text{fit}}) = r_{\text{fit}}\left(1 + \dfrac{\sigma_r(1 - \nu_{12}E_2/E_1)}{E_2}\right)
\end{cases}
\tag{5.16}
$$

In consequence,

$$\begin{cases} E_1(r_{\text{fit}}) = \dfrac{\sigma_r(1 - \nu_{12})r_{\text{fit}}}{a - r_{\text{fit}}} \\[3mm] E_2(r_{\text{fit}}) = \dfrac{\sigma_r(1 - \nu_{12})r_{\text{fit}}}{b(1 - \nu_{12}) + \nu_{12}a - r_{\text{fit}}} \end{cases} \tag{5.17}$$

One should point out that the multi-axial stretch does not lead to identifying the Poisson's ratios, ν_{12}. Ting and Chen [409] showed that Poisson's ratio for anisotropic materials could have no theoretical bounds. Though, it was fixed arbitrarily for human skin between 0.3 and 0.5 because of its rubber-like mechanical properties [30, 134, 410, 411]. Destrade *et al.* [412] reported that the usual practice of arbitrarily choosing a value of Poisson's ratio almost certainly, led to a significant difference between the simulated and actual normal stresses in a sheared block. Moreover, the collagen fiber orientation affects Poisson's ratio variation [413]. Given the latter remarks, the modeler would need a strong hypothesis to associate the classical Poisson's ratio (determined by a uni-axial test) with the parameter ν_{12}. Hence, based on an multi-axial study conducted by Reihsner *et al.* [18], we define: $\nu_{12} = C_{e12}/C_{e22}$ with $C_{e12} = \nu_{12}E_2/(1 - \nu_{12}\nu_{21})$ and $C_{e22} = E_2/(1 - \nu_{12}\nu_{21})$ are elastic coefficient (Eq. 5.2).

5.2.3 Calibration Study

A calibration study was carried out on a soft material whose mechanical properties are known to analyze the method's efficacy in identifying the material parameters. By combining numerical simulation and experimental characterization, an adjustment of ratio p/σ_r took place in the model for posterior applications.

5.2.3.1 Reference Material

The multi-axial annular suction test was performed 3 times at constant pressure $p = 300$ mbar on a thin homogeneous and isotropic layer of rubber latex of 220 μm thickness. As the radial in-plane stress σ_r is uniform, the anisotropy is due only to the directional variation of the stiffness. Thus, using an isotropic latex material for validation of an transverse isotropic model (Eq. 5.6) is plausible for the condition $E_1 = E_2$ (and $\nu_{12} = \nu_{21} = 0.5$).

In the central observable zone (1) in Figure (5.11), the UV camera captures the displacement of the stretched layer subjected to suction applied to the annular zone (2). A double-sided annular sticker was settled on the annular zone (3). From the recorded video, the displacement field, expected to be purely radial, was computed with the DIC process. In a second experiment, the uni-axial tensile test was applied to 3 rectangular samples from the same tissue, cut out along the directions $0°$, $45°$, and $90°$. From the initial tangent of the stress-stretch curves, one may obtain the elastic modulus $E_{\text{latex}} = 2.7 \pm 0.42$ MPa. The results of the multi- and uni-axial experiments were used afterward for the model adjustment.

One must check that the captured deformation of the reference material is radially regular. Through the linear interpolation all over the grid (provided by `SciPy` library), the value of the radial component of the displacements, u_r, was computed and displayed in Figure 5.12 as a form of contour lines, as well as along the radial lines with the respective orientations $\{0°; 45°; 90°; 135°\}$. The index "CL" in Figure 5.12b stand for the usual circle cutlines for different radii.

Figures 5.12a and 5.12b demonstrate isotropic and spatially linear behaviors in the material within a limited area. Indeed, the displacement data captured between the circles of $r = 1.3$ mm and $r = 2$ mm (zone Z_a) are highly perturbed. While between $r = 2$ mm and $r = 2.5$ mm (zone Z_b), the displacements decrease drastically until they reach 0 mm. This edge effect occurs because the material slips under the observable limit during the ring suction process. The disappearing zone is then interpreted as zero displacements with the DIC reader. This abnormality spreads toward the center and impacts

141

(a) Initial configuration   (b) Deformed configuration   (c) Observable zone
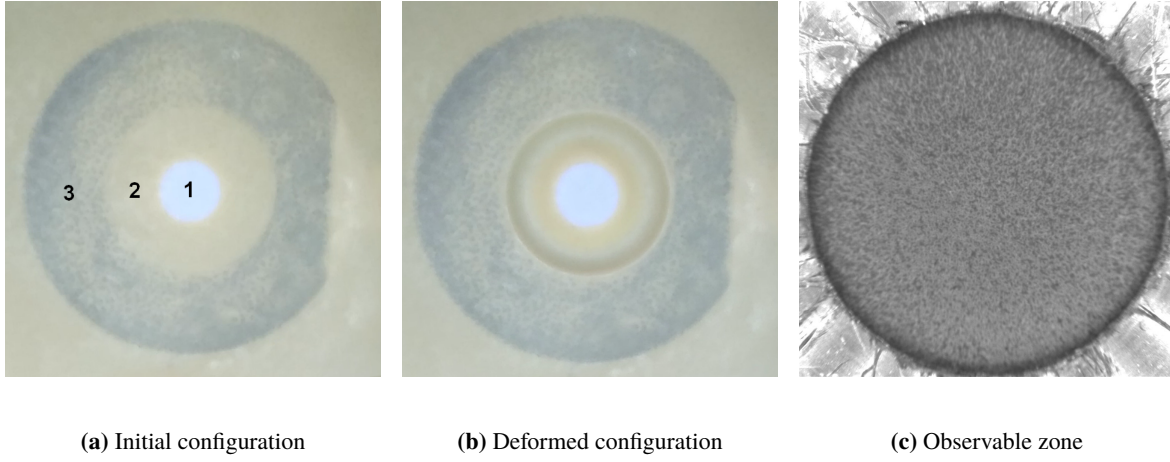
Figure 5.11: Multi-axial annular suction experiment on a latex tissue. Published in [402]. **(a), (b)** Bottom view before and after loading. **(c)** Top view of the observable zone obtained by the camera.

(a) Contour lines of u_r-component   (b) Radial cutlines
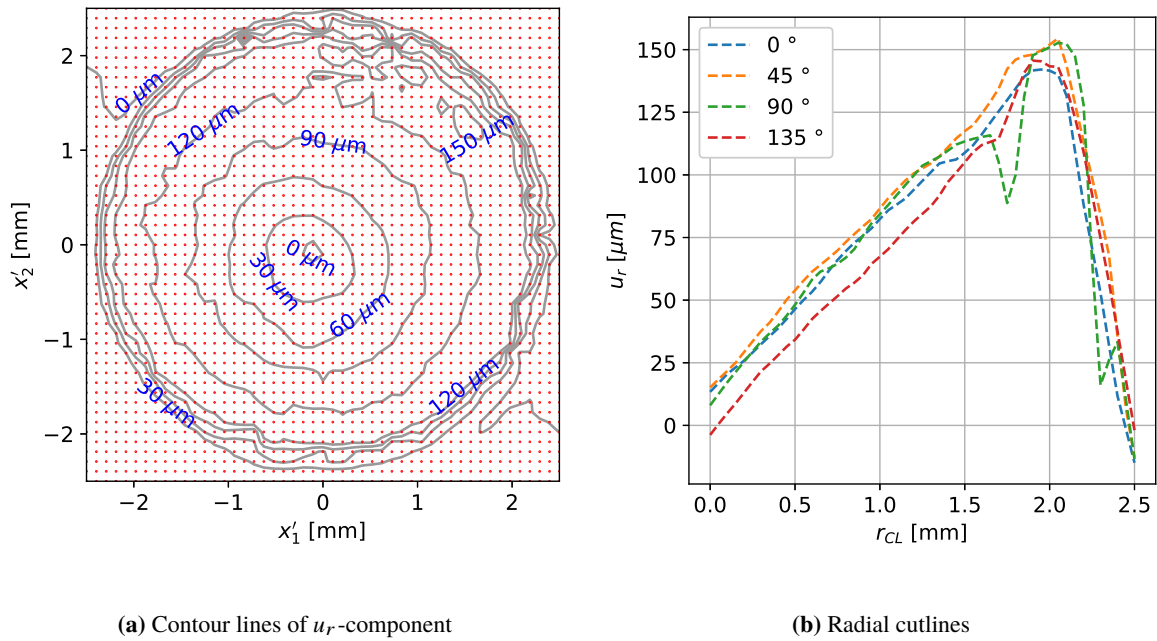
Figure 5.12: Radial displacement component of the latex material under multi-axial ring suction load for $p = 300$ mbar. Published in [402].

the data in zones Z_a and Z_b.

Starting from an initial guess corresponding to an anisotropic situation $\tilde{\boldsymbol{m}}_g^{(0)} = \{a = 1.0 \text{ mm}; b = 1.1 \text{ mm}; \phi = 0°; x_{10} = 0 \text{ mm}; x_{20} = 0 \text{ mm}\}$ and by choosing $N_E = 100$, the inverse identification performed on each test data over the circle ($r_{\text{fit}} = 1$ mm) led to converging set I, II, and III, stand for 3 tests, respectively) $\tilde{\boldsymbol{m}}_g^I = \{a = 1.0708 \text{ mm}; b = 1.071 \text{ mm}; \phi = -0.67°; x_{10} = 11.2 \, \mu\text{m}; x_{20} = 9.8 \, \mu\text{m}\}$ with coefficient of correlation $R_{\text{cor}} = 0.973$. Results from 2 similar test conducted in the same conditions are $\tilde{\boldsymbol{m}}_g^{II} = \{a = 1.0707 \text{ mm}; b = 1.0721 \text{ mm}; \phi = -17.97°; x_{10} = 11.7 \, \mu\text{m}; x_{20} = 12.1 \, \mu\text{m}\}$ ($R_{\text{cor}} = 0.9813$) and $\tilde{\boldsymbol{m}}_g^{III} = \{a = 1.0718 \text{ mm}; b = 1.0727 \text{ mm}; \phi = -34.53°; x_{10} = 10.8 \, \mu\text{m}; x_{20} = 11.0 \, \mu\text{m}\}$ ($R_{\text{cor}} = 0.9753$). Thus, the ratio u_1/u_2 used to quantify the isotropicity of the latex material over the 3 tests is 0.9875 ± 0.0097. The optimization algorithm did not calibrate a specific value of ϕ in $\tilde{\boldsymbol{m}}_g^I$, $\tilde{\boldsymbol{m}}_g^{II}$, and $\tilde{\boldsymbol{m}}_g^{III}$, which may be explained by an absence of anisotropy effect characterized a substantial discrepancy between u_1 and u_2. The converged values were the same on fixing the parameter $\phi = 0°$ in the inverse solver arbitrarily. To illustrate the isotropic behavior of the latex material, the model fitting for the first test is represented in Figure 5.13 before and after the recentring. For that, the distance d^{exp} (or r_{deformed}) as $r_{\text{fit}} + u_r$ are recalculated to the new center position marked with the green dot (the black dot refers to the zero position). In Figure 5.13b, experiment and model data after the recentering could exhibit alignment,$i.e.$isotropicity. For the same curve, the fluctuation of the experimental points near the model curve was exploited to quantify the measurement uncertainty Δ_u. It denotes the average distance between the two data sets, hence $\Delta_u = 2.7 \, \mu\text{m}$.

(a)

(b)
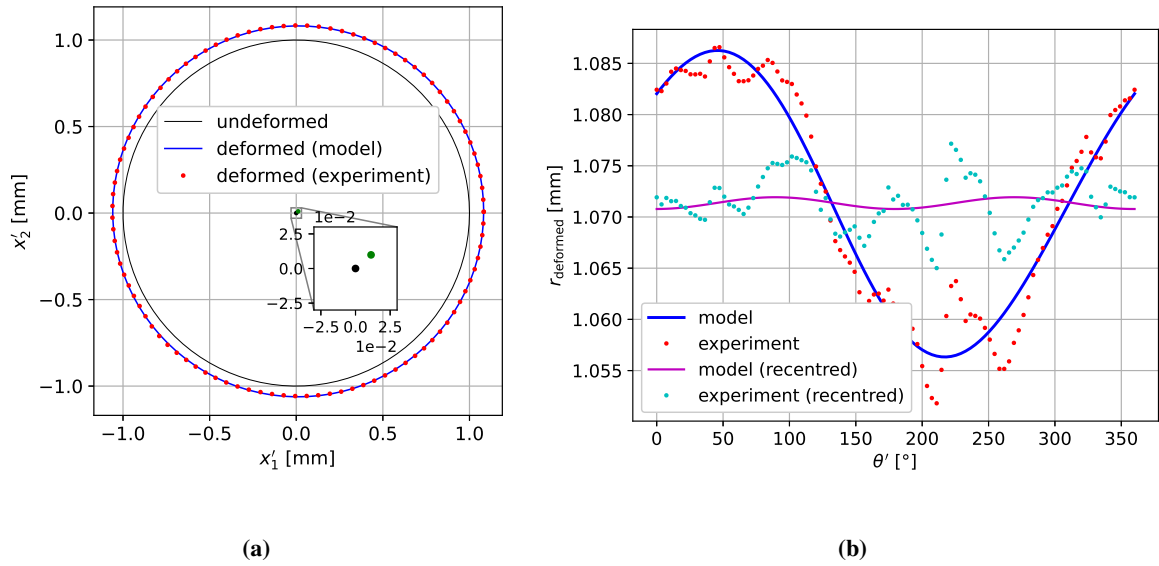
Figure 5.13: Model fitting with the identified parameters of the latex material $\boldsymbol{m}_g^I$. Published in [402].

5.2.3.2 Model Adjustments

The radial stress in the mechanical model (Eq. 5.6) is unknown and results from the suction with pressure p. From an established correlation with he latter one can predict the value of radial stress to complete inverse problem and evaluate the material parameters. Some adjustments could be brought to the model to ensure their exactness.

This part emphasizes the study of the relation between the applied pressure, p, on the annular section and the unknown radial stress, σ_r. From an established correlation one can predict the radial stress to evaluate the material parameters. Some adjustments could be brought to the model to ensure their exactness.

A frictionless-contact-based 2D axisymmetric FE model was constructed with the ability to assess σ_r in the observable zone (Fig. 5.14). The details about the mesh and the boundary conditions are described in Figure 5.15. A thickness of 0.22 mm and elastic modulus $E = 2.7$ MPa were assigned to the incompressible latex rubber domain. To simulate incompressibility, the Poisson's ratio was set to $\nu_{\text{latex}} = 0.495$. $\tilde{\sigma}_r$ represents the radial stress in the 2D axisymmetric FE model, while σ_r is associated with the analytical plane model (Eq. 5.6). An adjustment coefficient η was introduced through $\sigma_r = \eta\tilde{\sigma}_r$, such that the elastic moduli in both models are equivalent, to compensate for the discrepancy resulting from model simplification. It could be associated with the transition from a thick to plane geometry.
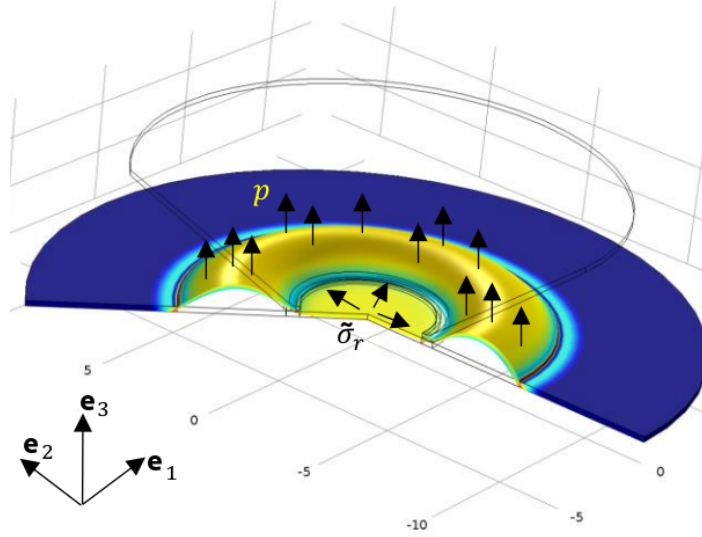
Figure 5.14: Deformed configuration of a 2D axisymmetric model subjected to a multi-axial annular suction test. The FE model was built in COMSOL Multiphysics® software. Published in [402].
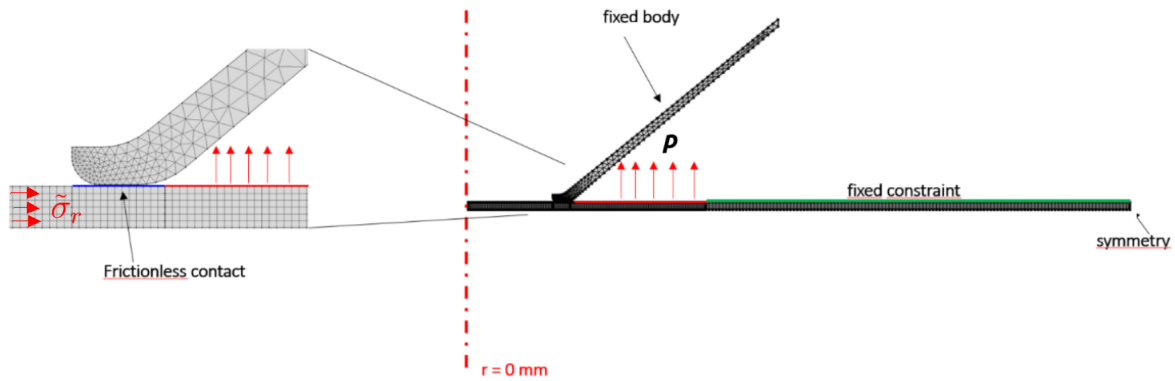
Figure 5.15: 2D axisymmetric FE model boundary conditions. Published in [402].

Before exploiting the FE model, it had to be validated with the first multi-axial test dataset. Once the rigid body motion was removed (recentring), the displacement of the latex was confronted against the simulation, performed at $p = 300$ mbar, in Figure 5.16 and confirmed that FE modeling was accurately formulated. Given the stress value $\tilde{\sigma}_r = 0.47$ MPa and the measured displacements, evaluated in post-treatment along one principal axis $u_1(r_{\text{fit}} = 1 \text{ mm}) = a - r_{\text{fit}} = 71 \text{ μm}$, and $E_{\text{latex}} = 2.7$ MPa, one can obtain $\eta = 0.81$ based on Equation 5.17 and the relation $\sigma_r = \eta\tilde{\sigma}_r$.

The validated simulation was run for different pressure $p \in \{50, 100, 150, 200, 250, 300\}$ mbar and $\tilde{\sigma}_r$
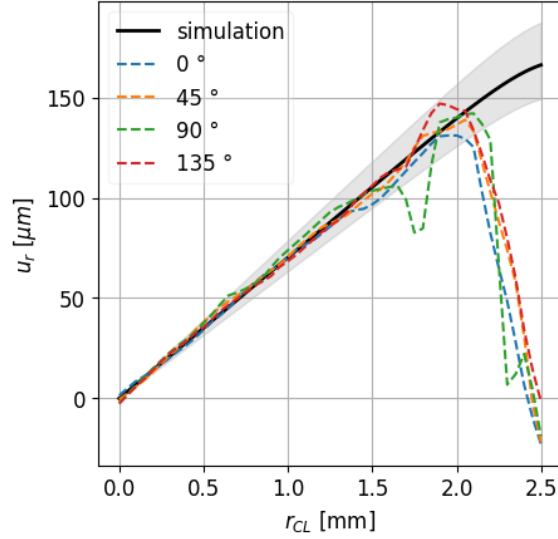
Figure 5.16: Comparison of radial displacements obtained for the latex layer with the FE model and the CutiScan® for the deformation of the latex layer. The gray area represents the 95% confidence interval of radial displacement obtained using a range of $E_{\text{latex}} = 2.7 \pm 0.42$ MPa. Published in [402].

was evaluated on for each step. The FE model struggled to converge for pressures equal to or bigger than 350 mbar. As exhibited in Figure 5.17, p seems to be linearly correlated to $\tilde{\sigma}_r$ with a slope of $\xi = 633$ (correlation coefficient $R_{\text{cor}} = 0.995$). As such, we may establish a function to assess the radial stress for any applied pressure, between 0 and 300 mbar at least, as following

$$\sigma_r(p) = \frac{\eta p}{\xi} \tag{5.18}$$
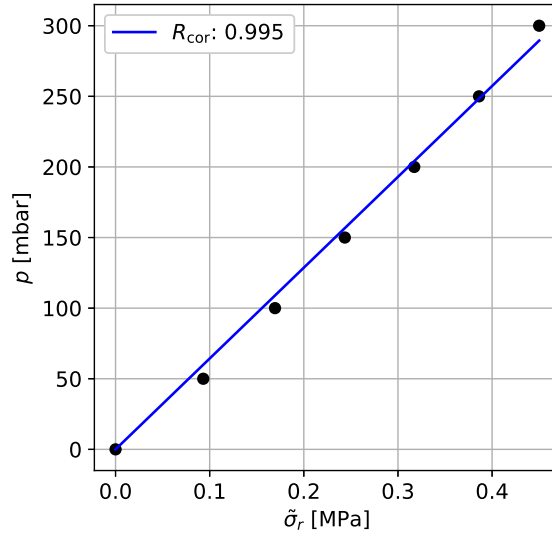
Figure 5.17: Correlation between the suction pressure p and the radial stress σ_r, with the slope $\xi = 633$. Published in [402].

Such a result would help simplify the full 2D axisymmetric into a radial stretch since the stress can be deduced directly from the applied pressure (Fig. 2.6). A further analysis revealed that ξ was different in 5 times thicker geometry, but was insensitive to the change in stiffness. Simply put, to model a soft material with different E but as thick as the studied latex sample, it would be possible to set $\xi = 633$ and $\eta = 0.81$. However, for another material with different thickness, ξ and η should be calibrated

145

based on FE simulations.

5.3 Application

The method was applied to one volunteer's skin for 30 data series introduced in Section 5.1.2.2. For each one of them, the material parameters were estimated. The results will tackle the robustness of the experiment/analysis system in characterizing the anisotropy of variability of the mechanical response *intra*-subject. They are structured into the subsections hereinafter: introducing the parameter estimation process on the human skin case and analyzing the day-to-day variability of the determined parameters quantitatively and qualitatively. The value of ν_{12}, defined as $\nu_{12} = C_{e12}/C_{e22}$, as a reminder, was calculated from the study in [18]. $C_{e12} = 4.0 \pm 0.6$ Nm/g and $C_{e22} = 9.4 \pm 1.4$ Nm/g were experimentally determined on 16 sites of a 30-years-old subject skin. Thus, $\nu_{12} = 0.43 \pm 0.09$.

5.3.1 Parameters Identification

The parameter identification was performed on the fitting circle with the radius 1 mm to avoid edge effects. In the meantime, it is not recommended to select data near the center $r_{\text{fit}} < 0.5$, where displacements are not predominant against Δ_u. For that living material, an ultrasound echography (see Sec. 6.1.1.1) was processed to quantify the epidermis-dermis layer's thickness: $th_{\text{h}} = 1.47$ mm. The latter was assigned to a similar calibration study as in Section 5.2.3.2 to determine the adjustments coefficients, $\xi_{\text{h}} = 24300$ and $\eta_{\text{h}} = 1.033$ (Tab. 5.1).

Table 5.1: ξ and η calibration for different stiffness variation with $th_{\text{h}} = 1.47$ mm. ξ is obtained from linear regression as in Figure 5.17, and the corrective coefficient η is set such that $E = E^{\text{FE}}$. E^{FE} and u^{FE} are elastic modulus and radial displacement at $r = 1$ mm in the simulation model. The choice of ξ and η was based on the value of $u^{\text{FE}} = 25.5$ μm in line with the captured displacement across Langer's line, u_2. u_2 was prioritized compared to u_1 for its reproducibility.

E [MPa]	0.25	0.5	1.0	2.0	3.0	4.0	5.0
ξ	2.43	2.25	2.2	2.18	2.17	2.16	2.16
u^{FE} [μm]	25.5	13.7	7.2	3.6	2.4	1.8	1.46
E^{FE} [MPa]	0.242	0.487	0.947	1.91	2.88	3.86	4.76
η	1.033	1.028	1.056	1.046	1.042	1.037	1.051

5.3.1.1 Results Sample

As an example, the model fitting for the first data set is plotted in Figure 5.18. for a converging parameter, set $\tilde{\boldsymbol{m}}_g^{(1)} = \{a = 1.0029 \text{ mm}; b = 1.0632 \text{ mm}; \phi = 60.24°; x_{10} = -17.8 \text{ μm}; x_{20} = 14.9 \text{ μm}\}$ with $R_{\text{cor}} = 0.9849$. Afterward, based on Equation 5.17 (where $\sigma_r = 0.0123$ MPa), elastic moduli along and across Langer's line are $E_1^{(1)} = 2.42 \pm 0.38$ MPa and $E_2^{(1)} = 0.188 \pm 0.002$ MPa, respectively.

Figure 5.18b shows the offset rigid body motion parameters, $\{x_{10}, x_{20}\}$ is of major concern. The model and experimental data expressed to the new origin are seemingly symmetrical. The center shift distance was of the order of magnitude of the displacements. Differently said, it must not be neglected. Three technical reasons may describe the necessity of recentering. First, the real center of the deformed skin is unknown. In fact, the origin of the DIC grid was arranged in a such way that the width matches the diameter of the observable zone of the CutiScan®probe (Fig. 5.4a). Second, even though the pressure is uniformly applied around the observable zone, some factors may lead to imperfect load distribution. Among them is the non-perpendicularity of the probe (the device is not perfectly tangent to the skin surface). Third, the friction between them could affect the contact skin/probe and result in a non-uniform load radial distribution. A thorough tribology investigation is suggested to study the friction's effect on the center shifting.
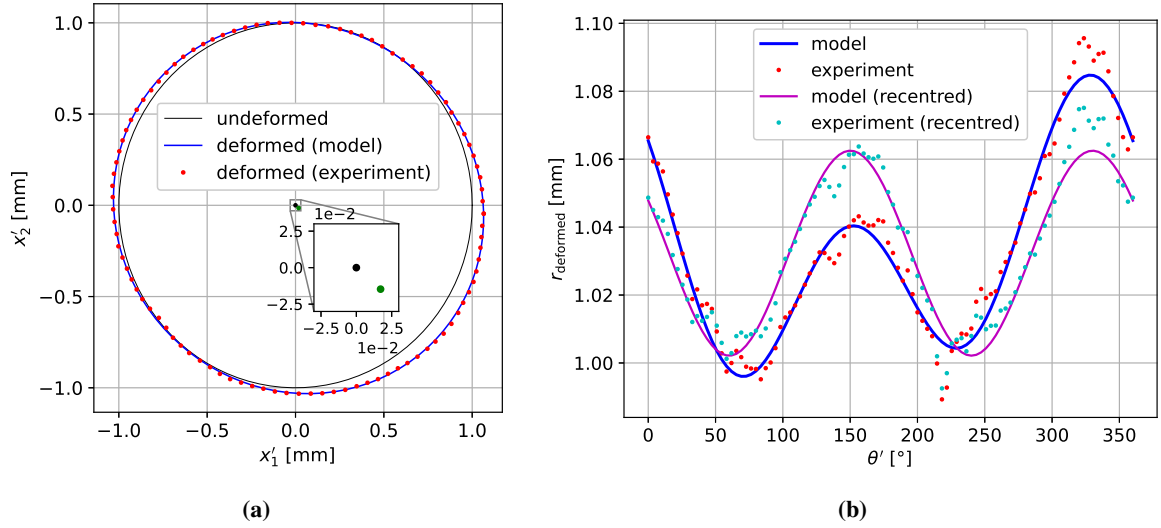
Figure 5.18: Model fitting with the identified parameters of the volunteer's skin on the day 1. Published in [402].

5.3.2 Quantitative Analysis

The geometrical parameters $\tilde{\boldsymbol{m}}_g$ were assessed with MARSAC for all 30 tests (available in Appendix D, Table E.1 and Figure E.1). The initial parameter values were fixed to be $\{\phi = 45°; x_{10} = 0 \text{ mm}; x_{20} = 0 \text{ mm}\}$, whereas a and b are chosen according to the circle used for identification such that $a < b$. In our case, for $r = 1$ mm, we choose $a = 1$ mm and $b = 1.01$ mm At first glance, the values of the correlation coefficient witness an accurate model fit for 28 tests ($R_{\text{cor}} > 0.95$). Again through Equation 5.17, we deduce the material parameters for every test.

5.3.2.1 Overview

Based on the interquartile range (IQR) method, outliers were removed from calculating the day-to-day mean and standard deviation. IQR is the interval [median - 1.5×IQ, median + 1.5×IQ], such that IQ is the difference between the 3$^{\text{rd}}$ and the 1$^{\text{st}}$ quartiles. The median was computed regarding all tests, while the mean was computed after discarding the outliers. Therefore, as can be seen in Figure 5.19, 12 values were removed for E_1, 4 for E_2, and 3 for ϕ.

5.3.2.2 Frequentist Statistics

$\hat{E}_1$, $\hat{E}_2$, and $\hat{\phi}$, describe the average over the tests of E_1, E_2, and ϕ, respectively. The global uncertainty of $\hat{E}_j$ ($j = \{1, 2\}$) takes into account the day-to-day variation of the mechanical response and the uncertainty in ν_{12} ($\Delta_{\nu_{12}}$). The values were computed according to the weighted standard deviation method,

$$
\bar{E}_j = \frac{\sum_i^{n_j} w_i E_j^{(i)}}{\sum_i^{n_j} w_i}
$$

$$
\bar{\Delta}_{E_j} = \sqrt{\frac{\sum_i^{n_j} w_i (E_j^{(i)} - \bar{E}_j)^2}{(n_j - 1) \frac{\sum_i^{n_j} w_i}{n_j}}}
$$

(5.19)

with n_j the number of admissible values within the interquartile range, and the weights $w_i = \Delta_{E_j}^{(i)^{-2}}$, such that $\Delta_{E_j}^{(i)}$ is the uncertainty of $E_j^{(i)}$ for each test i. In practice, $\hat{E}_j = \bar{E}_j \pm \bar{\Delta}_{E_j}$.
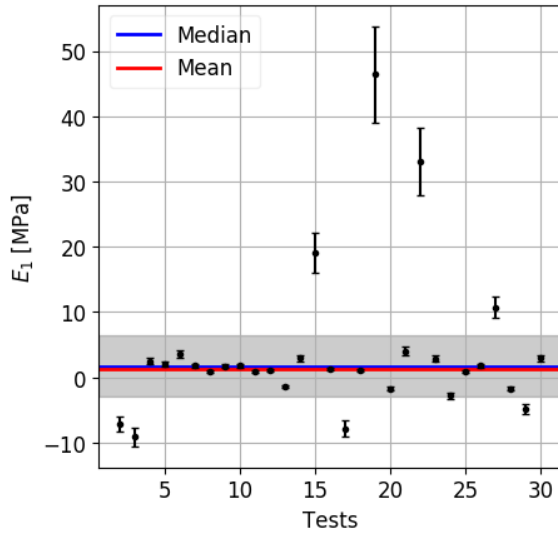
(a) Stiffness along Langer's line
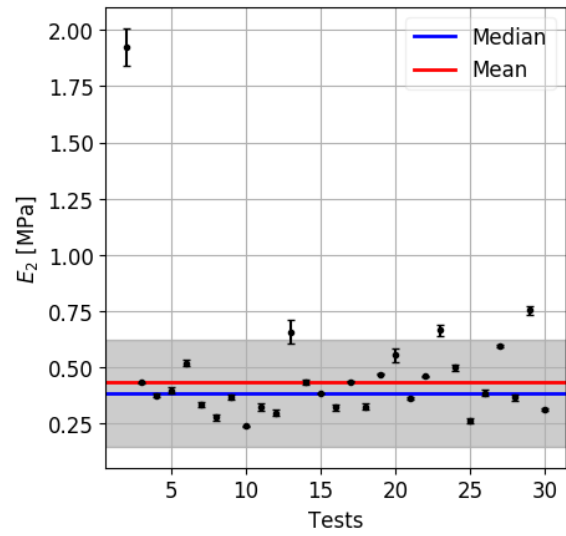
(b) Stiffness across Langer's line
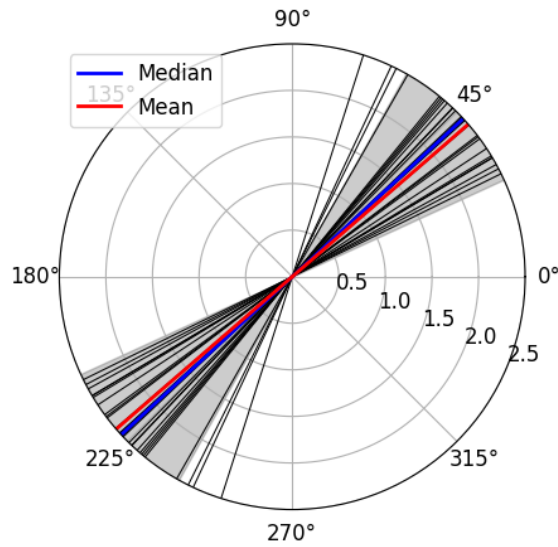
(c) Anisotropy angle ϕ

Figure 5.19: Skin material parameters E_1, E_2, and ϕ for every test. The grey bands in all subfigures represent the interquartile range. The thin black lines in (c) represent the identified anisotropy axes oriented with ϕ to the axis $0°$. Published in [402].

Subsequently, one can get $\hat{\phi} = 40.9 \pm 8.2\,°$, $\hat{E}_1 = 1.35 \pm 0.65$ MPa, and $\hat{E}_2 = 0.43 \pm 0.07$ MPa. The plots in Figure 5.19 demonstrate the weak deviations on $\hat{\phi}$, $\hat{\Delta}_\phi = 8.2\,°$, and on $\hat{E}_2$, $\hat{\Delta}_{E_2} = 0.07$ MPa, whose removing outliers were no more than 4, unlike $\hat{E}_1$ ($\hat{\Delta}_{E_1} = 0.65$ MPa), whose 12 outliers were discarded, as occurring in one of the two following situations: (i) E_1 takes a negative value, (ii) u_1 is almost zero along Langer's line, and thus E_1 reaches higher stiffness. In the former scenario, negative E_1 indicates that the skin is compressed along Langer's line instead of being stretched. A dome inside the observable zone takes shape by pressing the probe strongly against the skin. A high sensitivity of E_1 assessment could be related to the fact that u_1 values are within the measurement uncertainty evaluated earlier, $\Delta_u = 2.7\,\mu$m. On the other hand, the displacement u_2 is substantial compared to Δ_u, which may justify the reliability of its assessment. As for ϕ, completely independent to E_1 and E_2, regarding the deviation $\hat{\Delta}_\phi = 8.2\,°$, the process of its identification can be considered robust.

The Langer's line on the studied subject is oriented obliquely at a mean angle $\hat{\phi} = 40.9$ relative to the forearm axis. This result is in accordance with the literature [47, 141, 414, 415] but sensibly different from Khatyr *et al.* [134] (0–10°). If the symmetry is admitted in a contralateral study on the right forearm, ϕ would be similar to the one reported by Lakhani *et al.* [416] and Kirby *et al.* [201]. Nevertheless, most recent studies described efficient tools and methodology to determine the Langer's line orientation, which was historically defined to be parallel to the forearm's long axis [74, 76, 417].

The ratio $\hat{E}_1/\hat{E}_2 = 3.14 \pm 1.60$ could be in line with the results in [128, 132, 134, 139, 141, 417]. $\hat{E}_1 = 1.35 \pm 0.65$ MPa and $\hat{E}_2 = 0.43 \pm 0.07$ MPa are in line with the Elastic modulus in some of the earlier papers [128, 134] but stiffer compared to [139, 141]. Higher stiffness may occur if the effect of the epidermis, known to be stiffer than the dermis [30, 36, 63], is not neglected. This assumption is adequate with the nature of the CutiScan®device's function, which applies out-plane suction to cause an in-plane stretch in the superficial layers. Even though the epidermis under superficial stretch tends to dominate the skin stiffness, the dermis has an important effect on the homogenized mechanical response since the collagen and elastin fibers are present in the dermis, not in the epidermis.

5.3.3 Qualitative Analysis

To elucidate the variability of the material parameters from one day to another, we display in Figure 5.20 a series of skin pictures recorded at the first 6 tests. A change in the texture of the skin surface was noticed. If one observes the frames from tests $\{3, 4, 5, 6\}$, the furrows are mostly oriented along the same Langer's line identified with the respective angles 30.77°, 27.61°, 31.25°, and 50.26°, but not on test 1 with $\phi = 60.24°$ (Table E.1). This result may support the observations made in [414, 418]. However, this equivalence could not be observed for the test 2, where the skin lines are almost absent, and the relative ϕ is the most extreme with respect to the median. The skin microrelief change may depend on hydration conditions: the wrinkles are more pronounced in a dry stratum corneum [419].

The experimental protocol should consider particular attention to skin hydration to reduce the fluctuations of the material parameters, for instance, avoiding exposing the studied site to any liquid. Despite that, the day-to-day variation of skin wrinkles observed in Figure 5.20 could be associated with the change in the anisotropy axis. Considering that the uppermost layer's deformation is directly correlated to the radial stretch, any change in its texture would have an impact on the radial displacement distribution and thus on ϕ.

5.4 Extended Study: Bayesian Inference

To recap, the primary functions of the MARSAC pipeline involve converting mechanical test video into displacement data, calibrating geometrical parameters through a deterministic nonlinear least-squares algorithm, and deriving material parameters using an transverse isotropic linear elastic model. While

(a) Test 1   **(b)** Test 2   **(c)** Test 3

(d) Test 4   **(e)** Test 5   **(f)** Test 6
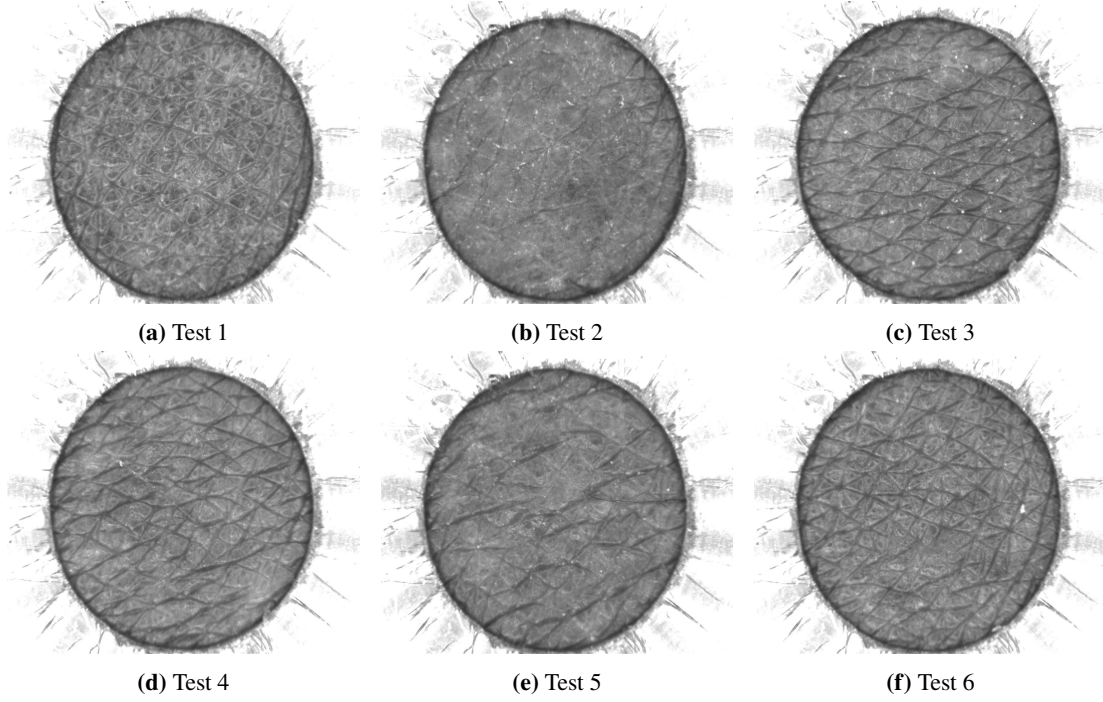
Figure 5.20: Snapshots of skin texture taken by the probe-camera for the 6 first tests. Published in [402].

the pipeline is considered operational for large-scale studies, there are two areas that could benefit from improvement. These areas stem from two assumptions made in the methodology. Firstly, the stiffness is assumed to be constant over the subdomain between the circles of $r = 0.5$ mm and $r = 1$ mm; as a result, fitting the model with data over the r_{fit} circle is sufficient. Secondly, the stress-strain relation is assumed to be linear based on the small strain hypothesis.

Hence, to expand the potential applications of MARSAC, additional inquiries were pursued. Firstly, the transverse isotropic elastic material was evaluated with regards to its non-linear properties. In a concurrent investigation, the Bayesian method was utilized in place of the deterministic optimization algorithm to evaluate both the uncertainty surrounding the identified material parameters, as well as the parameters themselves. It was posited that utilizing all available displacement data in the observable valid zone could greatly augment understanding of the parameters. Due to time constraints, however, the proposed extensions were not implemented for supplementary data.

5.4.1 Nonlinear Anisotropic Hyperelasticity

The stress-strain curves plotted along different directions could exhibit a nonlinear behavior even for small deformations. Fitting them with a nonlinear hyperelastic constitutive law might lead to identifying more accurate material parameters.

5.4.1.1 Inverse Problem

Similarly to the forward solver in Section 2.1.3.2, the displacements are solved under applied loads and boundary conditions through a weak formulation as in Equation 2.9, for the assigned material parameters. Inversely, the material parameters can be calculated for the known displacement field. Hence, the inverse problem consists in updating the forward solution by changing the parameters until the mismatch minimum with the measured displacement is reached.

The mesh used for this FE-based forward solver was subdivided into 3 parts (Fig. 5.21). A central zone with the radius $0 < r < 0.5$ mm, an annular zone $\Omega_{\text{msr}}^{\text{MARS}}$ subjected to the fitting area with the

radius $0.5 < r < 1$ mm, and the external zone. MARS stands for Multi-Axial Ring Suction. The objective function assembles the mismatch $\|u - u^{\text{MARS}}\|_2$ for all points in $\Omega_{\text{msr}}^{\text{MARS}}$ and for all the 21 pressures from 100 mbar to 500 mbar.
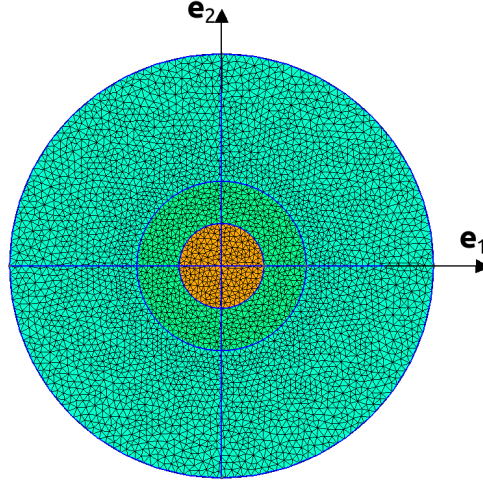
Figure 5.21: Domain meshing for the muti-axial radial stretch problem. The mesh contains 8 k quadratic elements.

For nonlinear FE solvers, the behavior law takes the shape of a strain energy density function. For anisotropic materials, this function is a sum of an isotropic and anisotropic expression (Eq. 1.38). Built around the invariants I_1 and I_4, I propose an energy function as a combination of the isotropic Gent model (incompressible) and the fiber-part function in [167], such that:

$$\psi(I_1, I_4, \boldsymbol{m}) = -\frac{\mu J_m}{2} \ln\left(1 - \frac{J^{-2/3} I_1 - 3}{J_m}\right) + \frac{\mu_{\text{fib}}}{4}(I_4 - 1)^2 \tag{5.20}$$

I_4 corresponds to the stretch along the privileged direction, like the main collagen fibers direction. As introduced in Equation 1.39, I_4 is based on the identified fiber direction vector $\boldsymbol{N}_{\text{f}} = \{\cos\phi, \sin\phi, 0\}^T$. The targeted material parameters vector $\boldsymbol{m}$ in the presented problem is $\boldsymbol{m}_{\text{nonlin}} = \{\mu, J_m, \mu_{\text{fib}}, \phi\}$. The algorithm's functions used for that purpose were adapted from the SoFTI framework, such as the inverse solver. The equation above suggests that the isotropic part will stiffen more than the anisotropic part when the stretch gets close to the asymptote due to $J^{-2/3} I_1 - 3 \approx J_m$. One should verify that it is not the case for the given parameters.

5.4.1.2 Application

The abovementioned method was applied to the first among the 30 test data to investigate its potential. For numerical reasons, the parameter ϕ was not calibrated with the others. In the first step, it was calculated with MARSAC and used to rotate the experimental displacement vectors with respect to the mesh referential with ϕ. As such, the vector $\boldsymbol{N}_{\text{f}}$ is always $\{1, 0, 0\}^T$.

Starting from an initial set $\boldsymbol{m}^0 = \{\mu = 1.0 \text{ MPa}, J_m = 0.1, \mu_{\text{fib}} = 5 \text{ MPa}\}$, and knowing that $\xi_{\text{h}} = 24300$, and $\eta_{\text{h}} = 1.033$ (Eq. 5.18), the identified optimal set was $\hat{\boldsymbol{m}} = \{\mu = 0.1494 \text{ MPa}, J_m = 0.0016, \mu_{\text{fib}} = 3.27 \text{ MPa}\}$.

As a result, the experimental and optimized stress-strain curves were superposed in Figure 5.22. The curve of direction $90°$, representing the direction across the Langer's line, was so far the best fit, and

to a lesser extent, the direction along the Langer's line ($0°$ direction). For the latter, the fitting was more accurate for pressure higher than 300 mbar. The curves along the diagonal direction, $45°$ and $135°$, supposed to be aligned, matched the model poorly. Nevertheless, the proposed method could identify the material parameters through a full data series.
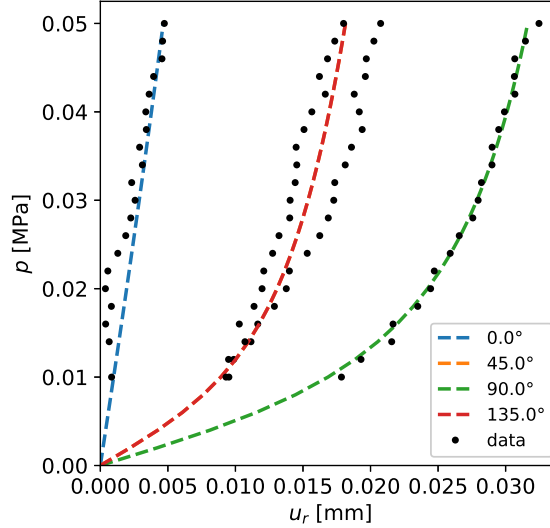
Figure 5.22: Model fitting for the nonlinear anisotropic case with data from the test 1.

MARSAC could improve SoFTI's accuracy once the healthy skin is modeled with an anisotropic behavior law in the latter. Closely to the approach around Equation 5.20, the collagen's main direction N_f can be determined with MARSAC, but not with the uni-axial test. We could imagine an advanced version of SoFTI, where the bi-material soft tissue is composed of isotropic and anisotropic materials, where MARSAC has a crucial role in identifying the anisotropy axis orientation.

5.4.2 Bayesian Inference

As an alternative to the classical least-squares optimization, the Bayesian method has been employed for the inverse problem with the aim of assessing the uncertainty while identifying the material parameters [420]. The principle of the method lies in the uncertainty reduction of prior knowledge with every additional measurement data. The Bayesian theory output, the *a posteriori* knowledge, will contain two valuable pieces of information: the average value of estimated parameters and their respective uncertainties. Therefore, the application of the Bayesian inference to the Multi-Axial stretch study examines the accuracy of identifying the parameters $m = \{\phi, E_1, E_2, \nu_{12}\}^T$. Some Bayesian studies state that using a huge amount of data will improve the method's efficiency and that the influence of the prior knowledge (generally misunderstood) on the posterior results decreases [292, 397, 421]. Hence the interest is to use measurement data of a whole zone for model fitting instead of a circle.

5.4.2.1 Methods

The Bayesian inference is a stochastic approach to replace the deterministic one in optimizing the mismatch $\|u - u^{\mathrm{MARS}}\|_2$ over $\Omega_{\mathrm{msr}}^{\mathrm{MARS}}$. Its methodology may be introduced as follows. Starting from an *a priori* assumption on the parameter values, and based on observation data, we look for their posterior distribution (or the posterior), according to Bayes' theorem hereafter.

$$P(m|y) \propto P(m)P(y|m) \tag{5.21}$$

$y \in \mathbb{R}^{N_d}$ contains N_d measurement values evaluated on nodes in $\Omega_{\mathrm{msr}}^{\mathrm{MARS}}$. The prior $P(\boldsymbol{m})$ is the probability of a certain parameter material set to exist. $P(\boldsymbol{y}|\boldsymbol{m})$, namely, the likelihood, is the probability of the observation to happen regarding an arbitrary parameter set. The posterior $P(\boldsymbol{m}|\boldsymbol{y})$ is the probability that material has $\boldsymbol{m}$ if the observations $\boldsymbol{y}$ occur certainly. Once the posterior expressions are established, three statistical quantities are evaluated: the mean $\boldsymbol{m}_{\mathrm{post}}$, the covariance matrix $\boldsymbol{\Gamma}_{\mathrm{post}}$, and the 'maximum-a-posteriori-probability' point (MAP), at which the posterior is maximum. The reader can look through Appendix F for the details.

5.4.2.2 Application

The investigation of the Bayesian inference in identifying $\boldsymbol{m}$ concerned all the 30 tests carried out at $p = 300$ mbar. All the priors was set with Gaussian distribution:

- $\phi_{\mathrm{prior}} \sim \mathcal{N}(45, 10^2)\,^{\circ}$

- $E_{1\mathrm{prior}} \sim \mathcal{N}(5, 5^2)$ MPa

- $E_{2\mathrm{prior}} \sim \mathcal{N}(5, 5^2)$ MPa

- $\nu_{12\mathrm{prior}} \sim \mathcal{N}(0.25, 0.25^2)$

The number of valid samples was set to $N_s = 4 \times 10^4$, with 4000 (10 %) first samples discarded after convergence. Accordingly,

$$\boldsymbol{m}_{\mathrm{post}} = \begin{bmatrix} \phi = 41.059\,^{\circ} \\ E_1 = 4.059 \text{ MPa} \\ E_2 = 0.428 \text{ MPa} \\ \nu_{12} = 0.264 \end{bmatrix} \quad ; \quad \boldsymbol{\Gamma}_{\mathrm{post}} = \begin{bmatrix} 0.5287 & 0.04909 & 0.0006 & -0.0039 \\ 0.04909 & 2.5517 & 0.0141 & -0.1350 \\ 0.0006 & 0.0141 & 0.0002 & -0.0019 \\ -0.0039 & -0.1350 & -0.0019 & 0.0241 \end{bmatrix}$$

The diagonal elements of $\boldsymbol{\Gamma}_{\mathrm{post}}$ introduce the variance for each parameter, whose square root is the standard deviation or the uncertainty in our context. The extra-diagonal values indicate how every two parameters are mutually correlated. Thus, the binaries with strong correlation are ϕ/E_1 (as E_1 is the stiffness along ϕ), and E_1/ν_{12}. E_2 is apparently weakly uncorrelated with all parameters.

The identified material parameters are then given in terms of normal distribution in Table 5.2, along with the MAP values, and the results for the same parameters assessed earlier with MARSAC in Section 5.3.2.2 (frequentist statistics). The posterior values above align with the MAP point approving that the sampling, performed with the Hasting-Metropolis scheme, could converge toward the optimal region while narrowing the standard deviations. The evolution of the samples can be plotted in two forms: iteratively with a continuous curve (Fig. F.2) and with histogram to highlight the distribution (Fig. F.3).

Table 5.2: Comparison of the identified anisotropic material parameters for the Bayesian and MARSAC approaches.

$\boldsymbol{m}$	Bayesian Inference		MAP	MARSAC	
	Mean	Standard deviation		Mean	Standard deviation
ϕ [°]	41.059	0.727	40.491	40.9	8.2
E_1 [MPa]	4.059	1.597	3.635	1.35	0.65
E_2 [MPa]	0.428	0.016	0.442	0.43	0.07
ν_{12}	0.264	1.552	0.228	from literature	

Afterward, comparing the optimal parameter sets and their related uncertainty showed an equivalence of ϕ and E_2 between the Bayesian inference and MARSAC. One could affirm CutiScan®'s ability

to assess ϕ and E_2 accurately and its incapacity to identify E_1 (because of quasi-null displacement along Langer's line) and ν_{12} (because of the radial nature of the mechanical load). The comparison shows that the Bayesian method led to lower uncertainties for ϕ and E_2 as the objective function was extended to more informative data. In Appendix F, Figure F.4 illustrates the Bayesian inference's role in improving prior parameter knowledge. By considering more valuable data, our uncertainty about the mechanical properties decreases.

Furthermore, despite the Bayesian inference not improving the uncertainty about ν_{12}, the modeler did not need to look for their values in the literature, unlike for MARSAC. With a considerable data quantity, some necessary knowledge can be bypassed without altering the final results. However, the Bayesian approach, which needs a massive amount of random samples, may struggle with non-analytical forward solvers, which are computationally costly.

Conclusions

Skin anisotropy is defined by two principal directions, which correspond to the maximum and minimum stiffness, respectively. The direction with the highest stiffness is introduced as Langer's line, whose identification aroused the interest of many studies. This first chapter of the second thesis's branch addressed the analysis of a pipeline combining *in vivo* experiment and modeling to evaluate Langer's line locally and rapidly and side material parameters. In a nutshell, the pipeline consists of two main procedures: measuring the displacement of the sample subjected to the multi-axial stretch and identifying the parameters by optimizing the misfit between the experimental data and a model.

For the experimental procedure, support was designed to hold and stabilize a commercial device probe, CutiScan® CS 100, responsible for the multi-axial extension resulting from annular suction. The software accompanying the apparatus provided incomplete data, so an `OpenCV`-based framework has been adapted to extract the displacement full-field from the recorded videos during the tests, based on the DIC technique. The correlation parameters, the window correlation size, and the grid nodes step were calibrated to meet the lowest errors.

The parameter identification procedure includes modeling the anisotropic behavior and optimizing the error between the latter and the experimental data. Once observing that the principal directions are orthogonal, transverse isotropic linear elasticity was assumed within the continuum mechanics theory to capture the skin deformation. The solution of the displacement-based problem exhibits an elliptical shape, which matches the deformed configuration of circles defined on the undeformed field. Thus, the identification scheme was split into two steps: evaluating the center shift, the rotation, and the semi-axes of the deformed ellipses, and later deducing the material parameters *via* the physical model. With this strategy, one can propose a mechanical model and identify its parameters without affecting the geometrical values assessed in the first step. A calibration study was conducted on a latex material formerly characterized to adjust the mechanical model to ensure that the calibrated elastic moduli, along and across Langer's line, represent accurate stiffnesses.

The analyzed methodology, labeled MARSAC, was applied to a 30 tests series carried out on a volunteer's forearm. For each, the parameters set were identified. The day-to-day variation of parameters gave insight into the reproducibility of the whole system experiment/analysis. The results revealed that with the actual equipment, it would be possible to assess Langer's line and the stiffness across it with high confidence. The development of a DIC tool as a replacement for commercial software, and the addition of a center shift to the deformed ellipse, have shown how CutiScan®can be useful. Previous experimental studies in the literature have disclosed a lack of its robustness. It is important to emphasize another scientific contribution. Based on the results of model fitting, it seems that the skin may be more likely to exhibit a transverse isotropic behavior under multi-axial extension, as had

been previously suggested by Reihsner *et al.* [18].

Apart from this, secondary paths were investigated with the view to improving the efficiency of the method. To begin with, a FE simulation model with a non-linear anisotropic hyperelastic behavior law was implemented to fit the stress-strain curve along different directions, considering all the pressure levels. Therefore, the optimal solution displayed an acceptable fit. However, the identified parameters that were supposed to represent skin stiffness significantly differed from the values evaluated with SoFTI in Section 4.2.2.3. Even so, this experience showed that SoFTI could be improved by adding an anisotropy feature to the peripheral medium hyperelastic model in the bi-material (Sec. 2.2). In this situation, the anisotropy axis direction will be quantified *a priori* with MARSAC.

The second investigation addressed the application of Bayesian inference to estimate the anisotropy parameters and their uncertainty simultaneously. The theory stipulates that adding informative data, even with moderate measurement error, will help narrow prior knowledge about the parameters. Consequently, the posterior distribution of the parameters confirmed that CutiScan®'s efficiency comprises an accurate assessment of Langer's line and the stiffness across it. Thanks to the mechanical model's analytical aspect, using the Bayesian method would be plausible for further studies with massive data quantity in a reasonable time.

With a free-ready-to-use framework, available on `https://github.com/aflahelouneg/MARSAC`, the surgeon can rapidly determine Langer's line on the patient before operating the incision. The next chapter will examine the use of MARSAC in a clinical trial and study the variability subjet-to-subject of skin anisotropy.

Chapter 6

Characterization of the Anisotropy of the Human Skin: Subject-to-Subject Variability

The mechanical behavior of living organs is known to vary between individuals, even with common characteristics, such as age, sex, ethnicity, *etc.* This variability, a natural part of human performance, could be significant or not for several anatomical factors. Identifying them and studying their role in the non-reproducibility of measurements by considering individual specificities is a step forward in understanding skin biomechanics. One way to accomplish it is by conducting a clinical trial and analyzing the data with appropriate statistical methods. Given the thesis's context, a clinical investigation was realized for 30 volunteers to analyze the *inter*-subject variability of the anisotropic material parameters belonging to the model developed and reviewed in the previous chapter.

This last chapter is presented with two main topics. Foremost, the experimental part of the clinical trial is fully described with an accent on the protocol adaptation, which accounted for one of the thesis's contributions. The latter includes the volunteers' inclusion, the measurement of their skin thickness, and the characterization of their anisotropic material parameters based on the CutiScan®device. Ulteriorly, the results in raw and treated measurement data, based on MARSAC framework, are discussed and used to statistically analyze the subject-to-subject variability's significance to age and sex. This significance was evaluated with the well-known P-value [422]. Carrying out the actual clinical trial aimed to contribute to assessing Langer's line's variability and exploring the performance of the method depending on the CutiScan®. The latter showed substantial sensitivity for clinical trials in its original configuration [151, 154].

6.1 Clinical Trial

In collaboration with the University Hospital of Besançon, a clinical study under the name SKUM (SKin Uncertainties Modeling) was initiated with the help of Dr. Thomas Lihoreau and Dr. Gwenaël Rolin, as the project chiefs, and Dr. Brice Chatelain, as the principal investigator. The project was first submitted to the CPP (Committee of Person Protection) and then approved under the study registration number: 2020-A01863-36. The campaign aimed to collect data on anisotropic viscoelastic properties of the forearm skin among healthy volunteers using the CutiScan®. 30 volunteers participated in the trial according to two clusters. One involved all of them for the *inter*-subject variability analysis, with 3 mechanical measurement sessions for each. The other one involved only 5 subjects for an *intra*-subject variability with 30 mechanical measurement sessions for each. Because of time limitations and the considerable amount of data, the second case has not been analyzed yet. For the same reason, viscoelasticity has not been studied. Table 6.1 summarizes preliminary information about the clinical

156

trial.

Table 6.1: SKUM clinical trial description sheet.

Study title	Construction of a human skin mechanics database for mathematical modeling of uncertainties in cutaneous tissue
Identification number	2020-A01863-36
Objective	Providing a database of transient displacement fields of the forearm skin undergoing multi-axial extension.
Duration	55 days
Type	Interventional
Emplacement	Department of Dermatology, Centre Hospitalier Universitaire de Besançon (France)
Principal investigator	Dr. Brice Chatelain
Project chiefs	Dr. Thomas Lihoreau, Dr. Gwenaël Rolin
Number of subjects and tests	*inter*-subject study: 30 subjects (3 tests each) *intra*-subject study: 5 subjects (30 tests each)
Inclusion criteria	- Healthy volunteer - Age between 18 and 50-year-old - Non-opposition to participating in the SKUM study - Affiliation to the French social security
Operators	Operator 1: Mr. Aflah Elouneg: 29 subjects Operator 2: Mrs. Intissar Ben Moussa

6.1.1 Measurements

Every volunteer from the subject-to-subject study that meets the inclusion criteria participated in 3 tests, mostly scheduled in the same time slot over three days. The test, consisting of mechanical measurement, lasted 1 hour, except for the first one, which lasted 1 hour and 15 minutes, as an additional measurement of the skin thickness was processed. Both measurements introduced hereinafter.

6.1.1.1 Skin Thickness Measurement

By means of an ultrasound echography system, DUB SkinScanner75 [423], the epidermis and dermis thickness were measured on a site located in the left forearm at 15 cm from the wrist, where the multi-axial extension with the CutiScan®was performed. The system is equipped with a probe to emit a wave of frequency of 22 MHz through the rectangular slot in contact with the skin (Fig. 6.1a). The skin surface was soaked with pure water to favor the impedance gradient for clear visibility of the skin layer. Once the echography was obtained, correctness was applied to the skin surface and the color with the associated tools to emphasize the skin layers boundaries, which could be determined visually (Fig. 6.1b). For the set frequency, 22 MHz, the penetration, and resolution were 10 mm and 72 μm. The thicknesses of the epidermis and dermis are represented with th_{ed} and th_d.

6.1.1.2 Mechanical Measurement

The term "mechanical measurement," as mentioned in the official document of the clinical trial authorization, refers to the multi-axial extension to characterize the transient anisotropy behavior of the skin. The mechanical measurement arose from the protocol in Section 5.1.2.1 and was slightly modified in such a way the CutiScan®probe support is identical for all volunteers. The most significant difference between the two protocols lies in ensuring the reproducibility technique of the horizontal equilibrium of the studied site. Carving arm support made of plaster helped fix the arm's perpendicularity to the probe-camera over 30 days with the 28-year-old volunteer in the preliminary study (Fig. 5.5).

(a) Measurement probe   **(b)** Skin echography
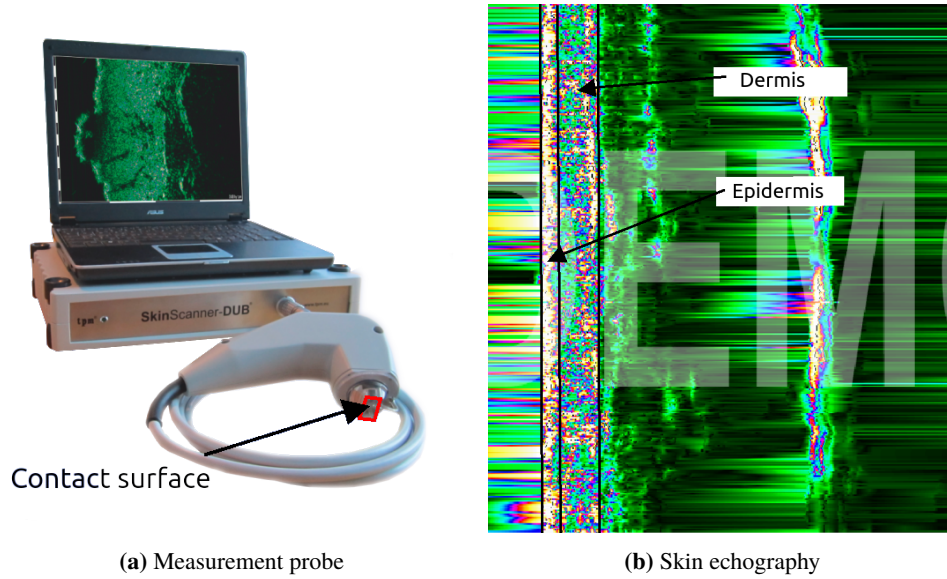
Figure 6.1: Skin thickness measurement with DUB SkinScanner75 system.

However, in a clinical trial, the fixing process should be standardized. Also, modeling a handler conforms to the arm shape requires artistic skills and is time-consuming. The fixation method was replaced by two elements: an NBR-made (Nitrile Butadiene Rubber) layer to reduce the gap between the arm and the U-shaped support and a mini lifting table adjusted according to the subject's arm morphology. Figure 6.2 exhibits a rear view of the standardized equipment used in the clinical trial to characterize the anisotropy for 30 subjects.

The mechanical measurement's duration was 60 minutes, divided into two phases: pre-test (20 minutes) and loading series (40 minutes). During the pre-test, acclimation occurred, and adjustments were processed for the sake of reproducibility. The length L_h is fixed to 200 mm. The heights H_s and L_v were noted for each test. Also, the temperature and the relative humidity were recorded. As for the loading series, as described in Section 5.1.2.1, it consisted of 21 creep-relaxation loads with pressures sweeping uniformly from 100 to 500 mbar.

After including a subject from the intra-individual case, 3 mechanical measurements were performed on the volunteer's left forearm at mainly the same time slot. The loading series, which lasts exactly 40 minutes, was carried out after 20 minutes of acclimatization, namely, pre-test, to the ambient conditions. The protocol operations for the two phases are detailed below.

Pre-Test (20 minutes):

1. Adjust the chair to a height such that the subject places its arm on the support ergonomically for one hour.

2. Disinfect the NBR layer placed on the inner surface of the U-shaped holder with a wipe (Fig.6.2).

3. Place the subject's arm with the wrist coinciding with the edge of the U-shaped holder. The arm is oriented as shown in Figure 5.5. If the arm is not large enough, another NBR layer can be added to compensate for the gap.

4. Loosen the clamping lever and turn the endless screw of the mini-lifting table until the probe is perfectly parallel to the studied site on the forearm, located at 15 cm from the wrist. Use a needle or digital level to adjust the parallelism since the probe and the skin surface must be both horizontal. Measure and note the height H_s with a caliper (0.01 mm accuracy).
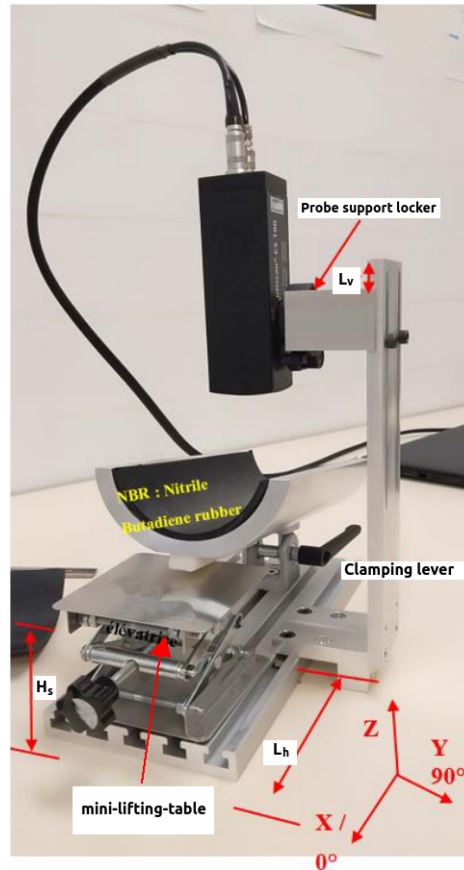
Figure 6.2: Standardized annular suction equipment for the subject-to-subject variability study.

5. Attach the forearm without pressure at two ends of the support, meeting the elbow and wrist, with the velcro tapes.

6. Stick one of the annular adhesive sides to the bottom side of the probe with its rod pointed in the $0°$ direction.

7. Lower the probe to a position about 1 mm above the skin surface. Technically it is done by loosening and then tightening the screws on the vertical column.

8. Run the CS100 software to monitor the measurement zone captured by the camera inside the probe. If the area is not hairless, move the arm barely back or forth until securing a clear zone.

9. Higher the probe up to 2 cm to have enough space to remove the cover from the stick on the bottom. The second face is now ready to adhere to the skin surface.

10. Lower the probe one last time very slowly until ensuring tangent contact without pressure, then tighten the screws immediately. This operation is decisive. The first contact could have a significant influence on the amplitude of the displacement. Measure the value L_v with a caliper and report it.

Loading Series (40 minutes):

1. In case of a new inclusion, create in the database a folder with the name `volunteer_XXX` (`XXX` stands for the subject's code number in 3 digits).

2. Create a folder with the current date `YYYY_MM_DD_XXX` inside the folder `volunteer_XXX`.

3. For set pressures from 220 to 500 mbar, skip this step. Otherwise, increase the pressure setpoint by 20 mbar and prepare to start suction but do not execute it. Redefine the setpoint to the targeted pressure, then start the creep-relaxation cycle. By way of explanation, to perform loading at $p = 120$ mm, we need to set the micro-compressor setpoint at $p = 140$ mm, then program the set point for $p = 120$. This maneuver is used to overcome a CutiScan®bug that constantly occurs for low pressures, between 100 and 200 mbar. Forcing the compressor to release pressure instead of accumulating avoids the software crash.

4. Save the video recorded by the probe-camera at the end of the second creep-relaxation phase in the directory `volunteer_XXX\YYYY_MM_JJ_XXX\p_pressure` under the name `pressure.avi`. For a pressure 240 mbar, *e.g.*, the complete directory is `volunteer_001\2021_11_15_001\` `p_240\240.avi`. It is important to mention the code number in different folders to avoid inadvertence mistakes while chaining tests with a gap of 2 minutes.

5. Process the image correlation with the commercial software even though it will not be analyzed since the outputs are incomplete. Save the files with the extensions `.ctm` and `.xml` in the same directory alongside the video file under the respective pressure, for example, `240.ctm` and `240.xml`.

6. Repeat steps 3, 4, and 5 for all 21 pressure steps within precisely 2 minutes.

7. Disinfect the tools used and the entire device except for the observable zone of the probe, which must remain intact from any physical or chemical change.

6.1.2   Data Management

Considering only the *inter*-subject study, 1890 original video files were collected across the tests. Those raw data appertain jointly to the Hospital of Besançon and FEMTO-ST institute. Sharing the raw data or any derivative data must be concluded upon agreement with the instances. Hence, the clinical trial outputs are not public for the time being.

6.1.2.1   Raw Data

A test video lasts 6 s and can be fragmented with an average frequency of 14 frames/s. Subsequently, around 86 frames are extracted for each test among the 21 pressure series. The fastest way to exploit the data (for mechanical characterization, for instance) one can use the 360 viscoelastic curves obtained by the commercial software (Fig. 5.3). They were stored in the database. Despite that, as explained in Section 5.1.1.2, the positions on which the curves were calculated are unknown. The user also has no access to full-field data from the observable zone.

6.1.2.2   Secondary Data

With the help of the DIC framework shared in MARSAC (see the example on `https://github.com/aflahelouneg/MARSAC/blob/main/sample/pydic.py`), the frames from the 1890 video files were fully converted into 2D displacement fields (analogically to Fig. 5.7) using the correlation parameters $d_G = 20$ px and $a_W = 40$ px. Bearing in mind that the anisotropy characterization treated the quasi-static state, only the 41st displacement field was retained for the analysis.

6.2   Variability Study

Analyzing the variability significance of the physical properties is conditional on the existence of clusters sharing similar features. If the quantification of how the difference is relevant between the groups to a defined factor is based on a P-value, the population is subdivided into two groups. The

subject was asked to provide data susceptible to being correlated with variability, especially age, sex, preferred hand, and profession. The two latter were excluded since all the subjects are related to the research domain, and only 3 are left-handed, *i.e.*, the clustering would be unbalanced. Therefore, the groups are formed according to two features, age and sex.

Figure 6.3 concisely informs the two studied factors for all volunteers. To begin with the biological factor, two groups were composed automatically of 7 males and 23 females. As for age, one could organize almost equal groups [151] separated by the black line: Generation I, under 28 years old, rallying 16 subjects, and Generation II, with the remaining 14 subjects. Additional information can be directly observed on the diagram if the subjects are sorted by age. Consequently, new indexes were assigned to the volunteers and are valid only for the present study.
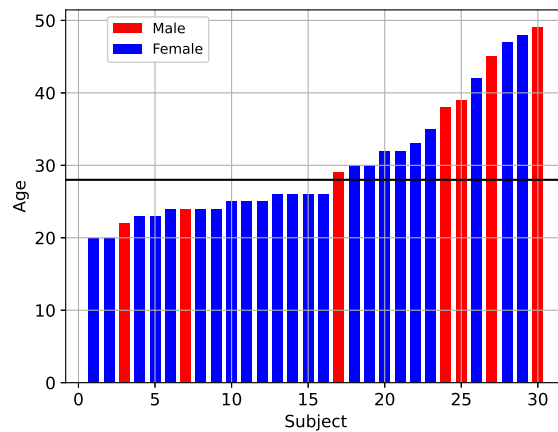
Figure 6.3: Age and sex data of the subjects.

P-value Calculation

Statistically, significance indicates that the result was not produced by chance and must have a reason. One needs to state the Null Hypothesis, which assumes the observation is not statistically significant. The Two-Tailed Test (or T-test) checks the Null Hypothesis following a normal distribution. A T-value is calculated and associated with a P-value. The T-value is a way to quantify the difference between means belonging to different populations. If the Null Hypothesis is true, the P-value is the probability of obtaining the T-value.

An example is proposed to clarify the point. To determine the significance of the elastic modulus variability between two groups of young and old volunteers, the Null Hypothesis is stated:

"there is no significant difference in skin stiffness between young and old subjects."

The T-value corresponds to the discard between the mean elastic moduli in the two populations, named $\Delta \bar{E}$. *P*-value (designed with P_v in the next sections), evaluates the probability of $\Delta \bar{E}$ to occur. The Null Hypothesis is rejected if the P-value is close to 0. In other words, if we assume that the two populations have equal skin stiffnesses and that there is most likely no chance that this "small" difference exists, then the situation is paradoxical. Therefore, the difference must be significant. The module `scipy.stats` was implemented to easily compute the T-values and their respective P-values.

6.2.1 Skin Thickness

Skin thickness is a physical characteristic that may affect the stiffness variation. If the results conform with similar studies in the literature, it will enhance the reliability of the material used to measure the

thickness. The analysis treats the data related to the epidermis and dermis thicknesses independently and conjointly.

Table 6.2 recaps the thickness data by means and standard deviation for the groups organized based on sex and age. Relating to the P-values, a tendency of the thickness of the dermis regarding sex was noticed. The dermis' thickness would be more pronounced for Males with $P_v < 0.0001$. Similar observations were made for the composition of epidermis-dermis considering that the dermis is most abundant. On the contrary, the epidermis between Females and Males did not differ considerably. As for age, it seemed that the population under 50 exhibited equivalent dermis and epidermis skin thickness. Those remarks can be recognized in Figure 6.4. Another way to emphasize the significance of a quantity between groups is through Whisker boxes. Figure 6.5 condenses much information in a rectangle centered on the sample mean, whose orange line indicates the median, and the box's length the interquartile range. The extreme bars imply the minimum and maximum permissible values. The outliers are shown with isolated circles.

Table 6.2: The study of age and sex factors in the skin thickness variability. N_v denotes the number of volunteers for a category.

Analysis	Groups	Epidermis	Dermis	Total
Thickness *vs.* sex	Female ($N_v = 23$)	197 ± 47 μm	919 ± 96 μm	1117 ± 86 μm
	Male ($N_v = 7$)	192 ± 18 μm	1158 ± 67 μm	1351 ± 65 μm
		$P_v = 0.78$	$P_v = 2.5\text{e}{-6}$	$P_v = 5.9\text{e}{-7}$
Thickness *vs.* age	Generation I ($N_v = 16$)	192 ± 51 μm	962 ± 107 μm	1155 ± 102 μm
	Generation II ($N_v = 14$)	199 ± 27 μm	989 ± 161 μm	1190 ± 151 μm
		$P_v = 0.66$	$P_v = 0.59$	$P_v = 0.47$
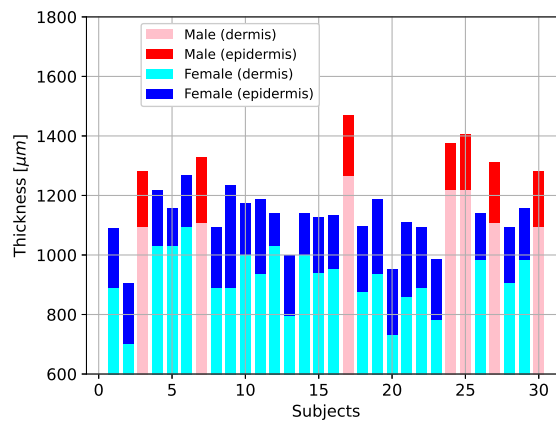
Figure 6.4: Skin layer thicknesses variability.

The dermis thickness may correlate with the quantity of collagen in the medium affected by hormones. Males have more hormone testosterone in their bodies, making their skin thicker than Females [424]. The results above agree with Rahrovan *et al.*'s study [425]. The latter also reported no sex or skin type-related differences in epidermal thickness. As for the aging effect, according to Leveque *et al.* [426], the skin thickness decreases starting from 45 years for both Males and Females, unlike for Shuster *et al.* [48], who demonstrated that skin thickness in Males decreased linearly with age, starting at age 20 but remained constant in women until approximately 50 years. In our case, with $P_v = 0.66$, and maximum age of 49, one cannot conclude the aging effect on skin thickness. Further, linear regression was applied to skin thickness data *versus* the age for all volunteers (Fig. 6.6). The results show no correlation between age and thickness change for people under 50 in the studied population.
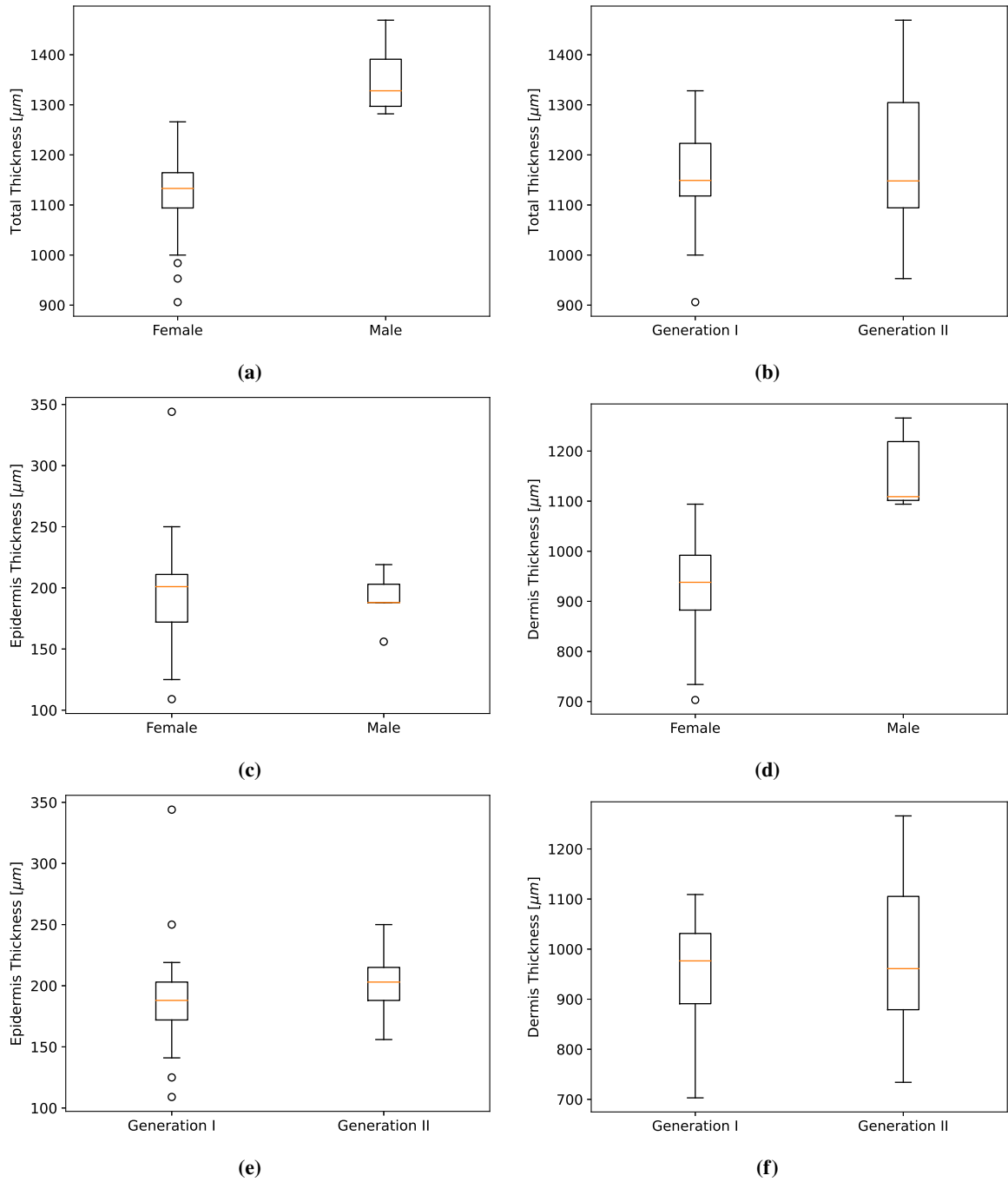
Figure 6.5: Comparison of the epidermis-dermis thickness regarding subjects' sex and age.
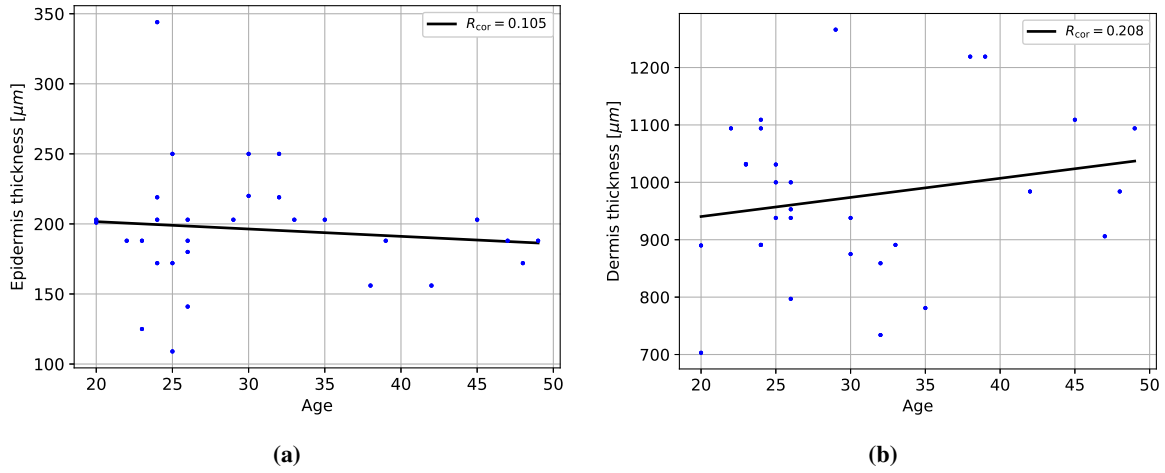
Figure 6.6: Study of the aging effect on epidermal and dermal thicknesses.

6.2.2 Material Parameters

By following the same logic in Section 5.2.2, the material parameters $\boldsymbol{m}_m = \{\phi, E_1, E_2\}$ were identified with data from the circle $r_{fit} = 1$ mm for each subject and each test after initial calibration of $\boldsymbol{m}_g$ elements. Subsequently, for every subject, one can define the median for each m_i in $\boldsymbol{m}_m$ among the three tests. The complete sets of optimal parameters are summarized in Table G.1. For illustrative purposes, model fitting results of plenty of tests are exposed in Figure 6.7. They are composed of: (i) radial displacement heatmap to visualize roughly the symmetry axis that represents Langer's line, (ii) superposition of the deformed experimental- and model-issued ellipses, and (iii) model fitting.

Afterward, the subject-to-subject variability over 30 subjects is assessed by averaging the medians array to obtain $\hat{m}_i = \mu_{m_i} \pm \Delta_{m_i}$. μ_{m_i} and Δ_{m_i} are the global mean and standard deviation given a population or group with the size N_s ($N_s = 30$ for all subjects, or $N_s = 23$ for Females, *etc.*). One must point out that 5 subjects participated in more than 3 tests because they volunteered for the intra-individual study, with 30 tests carried out. Their code numbers after the sorting are $\{12, 16, 17, 27, 30\}$. Selecting tests among 30 would be taking trivially the three first ones. However, as the calibrated geometrical parameter a can sometimes be negative (occurring when the probe is not correctly positioned perpendicular to the skin), the selection involved the 3 first tests with a valid a value.

6.2.2.1 Langer's Line

The averaging of identification results of ϕ between subjects led to a global value of $\tilde{\phi}^{all} = 21.6 \pm 8.3\,^\circ$. The periodic nature of the quantity does not aid in qualifying the variability by looking only at the standard deviation. Normalizing $\Delta_\phi^{all} = 8.3\,^\circ$ to $\mu_\phi^{all} = 21.6\,^\circ$ is counter intuitive. Supposing that $8.3\,^\circ$ is not considerable compared to $90\,^\circ$, referring to the orthogonality of the coordinate system, one would suggest that the Langer's line has a predefined direction in the forearm, for all human bodies.

A qualitative and quantitative study of the variability was conducted individually within the population. Figure 6.8a displays the identified values $\tilde{\phi}$ and their respective deviation over 3 tests. At first sight, $\Delta_\phi^{(j)}$ (j referring a subject) does not exceed $10\,^\circ$ for 24/30 cases, with 6 cases less than $3\,^\circ$. As the soft tissue measurement demonstrates minor reproducibility, one can put forward the success of the clinical trial. The collected data could be of good use to the scientific community. An explanation of the individual variation of ϕ will eventually be proposed according to the raw video frame.

The last-mentioned figure implies that the Langer's line could deviate more from the arm's axis ($0\,^\circ$) for Males than Females. Looking through this hypothesis requires quantifying how much the dif-

(a) Subject 6, test 3

(b) Subject 2, test 1

(c) Subject 9, test 3

(d) Subject 10, test 3
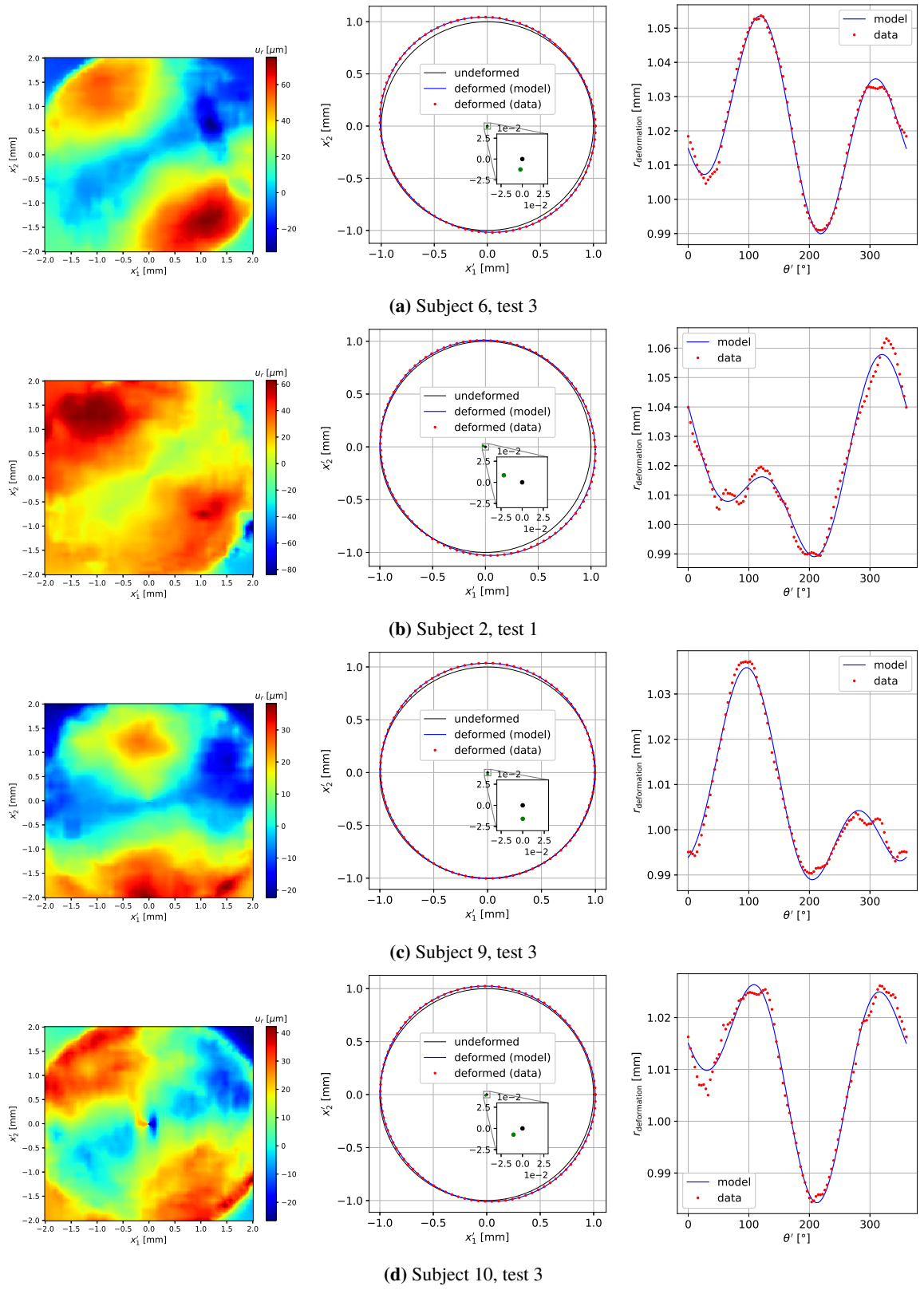
Figure 6.7: Inverse solution for the four highest fitting score cases. The values are reported in Table G.1.

ference is statistically significant. For this reason, the results were averaged the two groups; hence, $\tilde{\phi}^{\text{Female}} = 20.6 \pm 7.9\,°$ and $\tilde{\phi}^{\text{Male}} = 31.4 \pm 7.5\,°$ (Fig. 6.8b). With $P_v = 0.0038$, the assumption could be considered correct regarding the validation criteria of the P-value. The analysis theorizes that Langer's line is sex-related. The latter result is one of the main contributions of the clinical trial.

In relation to age, Figure 6.8c might reveal no significant difference in terms of Langer's line direction between the two generations. The statistical analysis resulted in $\tilde{\phi}^{\text{G.I}} = 18.4 \pm 6.3\,°$ and $\tilde{\phi}^{\text{G.II}} = 24.3 \pm 9.1\,°$ (G. designates Generation), confirms through $P_v = 0.69$ that ϕ parameter is not correlated to age under 50.
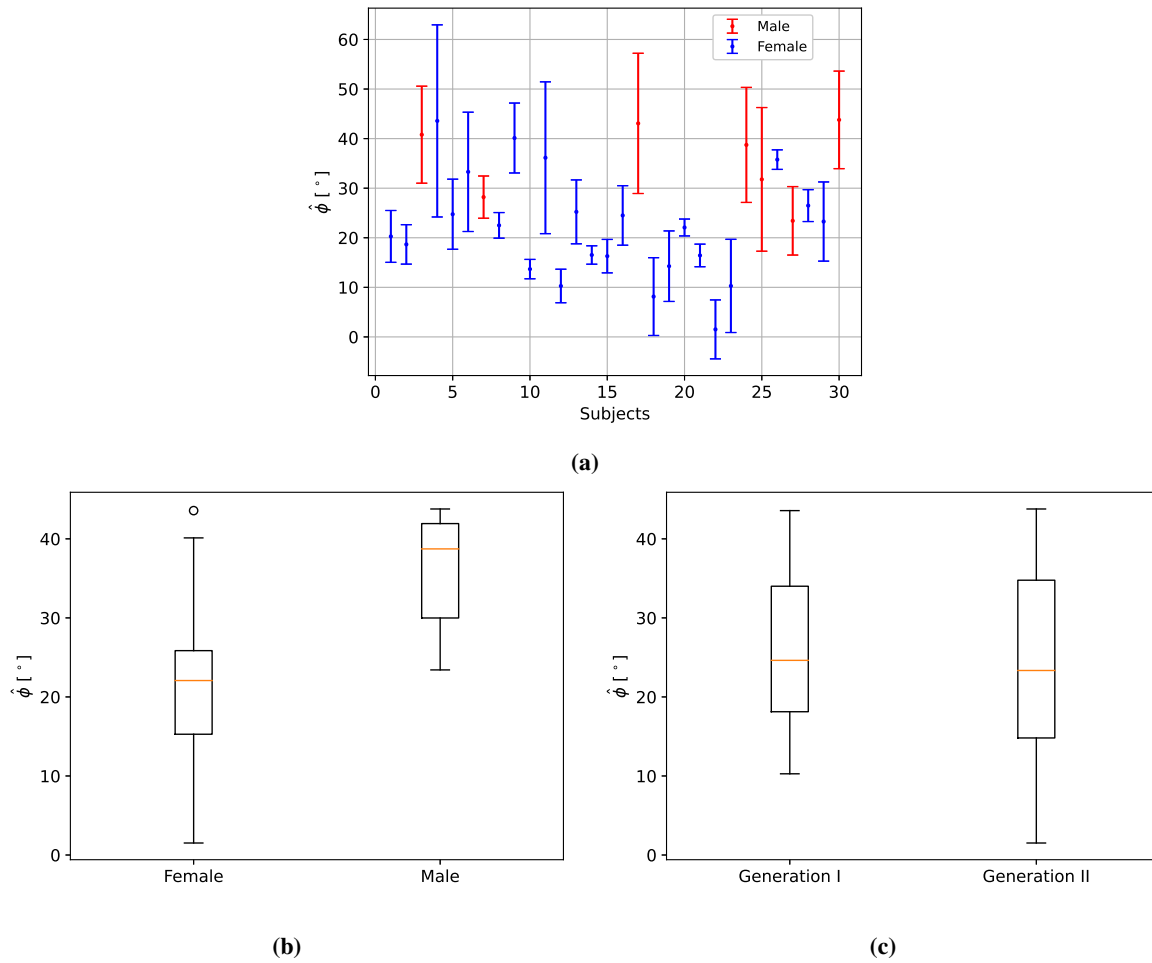
Figure 6.8: Variability of Langer's line per subject and for all tests.

The interpretation of Langer's line difference between Females and Males may be related to purely anatomical factors. Further studies should be followed up at micro and macro scales. One could imagine that hormones impact the collagen network nesting with maximum abundance along Langer's line. Or else the arm morphology would drive and drag the collagen bundles. In the future, the protocol should include the measurement of the arm's circumference at different locations (wrist, forearm, elbow) [427, 428].

Let us have a closer look at the extreme cases for each sex and compare the most and the least reproducible data in Table 6.3. The comparison involving volunteers, 20 and 4 for Females, and 7 and 25 for Males, included the standard deviations and measurable variables, the preferred hand, the experiment quality, the temperature, and the relative humidity. Experiment quality is an arbitrary evaluation of mechanical response reproducibility based on primary data provided by the CutiScan®software.

Globally, the juxtaposition of the ϕ variation from one side and the variables on the other did not reveal any correlation between them.

Table 6.3: Comparison of Langer's line and experiment variables for the most and the least reproducibility.

Variables	Females		Males	
Volunteers	20	4	7	25
Age	32	23	24	39
Preferred hand	Right	Right	Right	Right
	22.1°	53.2°	24.4°	56.8°
Langer's line	25.7°	43.6°	28.2°	22.5°
	22.0°	8.1°	34.7°	31.8°
Langer's line (average)	23.3 ± 1.7°	35.0 ± 19.4°	29.1 ± 4.3°	37.1 ± 14.5°
	4/5	4.5/5	4.5/5	2/5
Experiment quality	3/5	5/5	4/5	4/5
	4/5	5/5	4.5/5	3/5
	22.8	22.4	24.2	25.3
Temperature °C	22.0	22.3	34.2	27.9
	25.0	20.0	37.1	25.5
	31.2	27.6	24.2	25.3
Relative humidity [%]	30.8	23.5	34.2	27.9
	27.2	28.1	37.1	25.5

Similarly to the qualitative study in the preliminary research (Sec. 5.3.3), the captured skin surfaces of the studied four subjects are displayed to investigate their link with the minimum and maximum deviations of the respective Langer's line identified values. For the volunteer 4, corresponding to the most substantial variation of ϕ among Females (and all subjects), we observe an apparent change in the skin texture at the third test (Fig. 6.9). A similar observation arose in Table 6.3 for the third value of ϕ (8.1°), showing a significant shift with respect to the mean value (35.0°). Superficially, the furrows' direction seems to have changed, conversely to volunteer 20 whose skin's texture was nearly the same, which is compatible with the weak variation of her Langer's line (Fig. 6.10).

Test 1: $\phi = 53.2°$ Test 2: $\phi = 43.6°$ Test 3: $\phi = 8.1°$
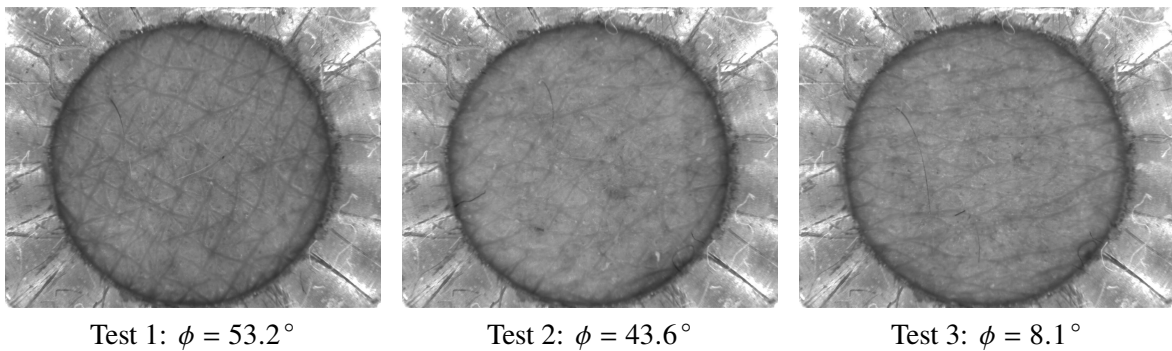
Figure 6.9: Test frame of the quasi-static state with pressure 300 mbar for the volunteer 4. Model fitting results are plotted in Figure G.1a and detailed in Table G.1.

As for Males, subjects 7 and 25, the skin texture frames were exhibited in Figures 6.11 and 6.13, respectively. The hairs present in subject 7's skin might perturb the DIC process quality. Figure 6.12 supplied model fitting curves for the three tests to check a possible artifact effect. Therefore, the plots exhibit unsatisfactory fitting goodness, leading to inaccurate identification of a and b parameters. However, the position of the peaks and dips seems to be not perturbed by the hair's presence. The estimation of ϕ in such conditions was somehow reproducible (29.1 ± 4.3°). As an outcome, one

Test 1: $\phi = 22.1°$ Test 2: $\phi = 25.7°$ Test 3: $\phi = 22.0°$
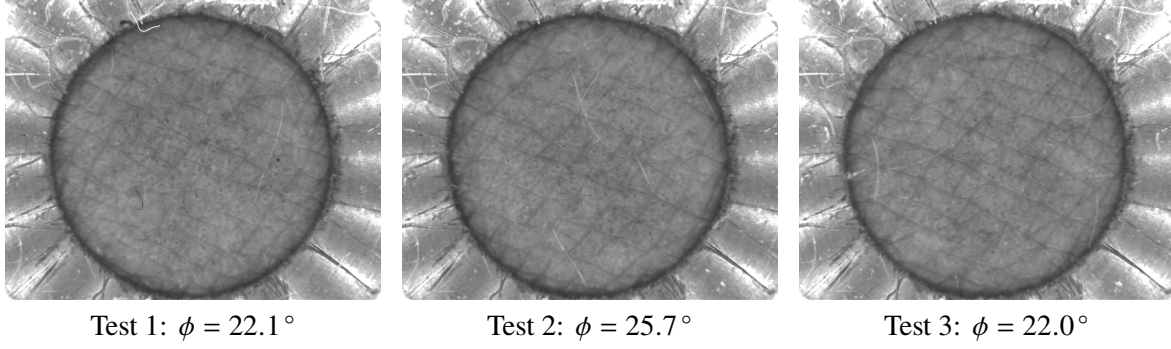
Figure 6.10: Test frame of the quasi-static state with pressure 300 mbar for the volunteer 20. Model fitting results are plotted in Figure G.1b and detailed in Table G.1.

could emphasize the ability of the DIC algorithm used in MARSAC to identify the skin anisotropy axis in the presence of potential artifacts. For the second case, subject 25, the confrontation of Langer's line variation with the skin texture change could not provide a factual finding. Establishing a clear correlation between skin texture change and ϕ variation ought to conduct quantitative analysis about furrows distribution at the micro-scale, which demands advanced scan techniques and post-treatment algorithm [418].

Test 1: $\phi = 24.4°$ Test 2: $\phi = 28.2°$ Test 3: $\phi = 34.7°$
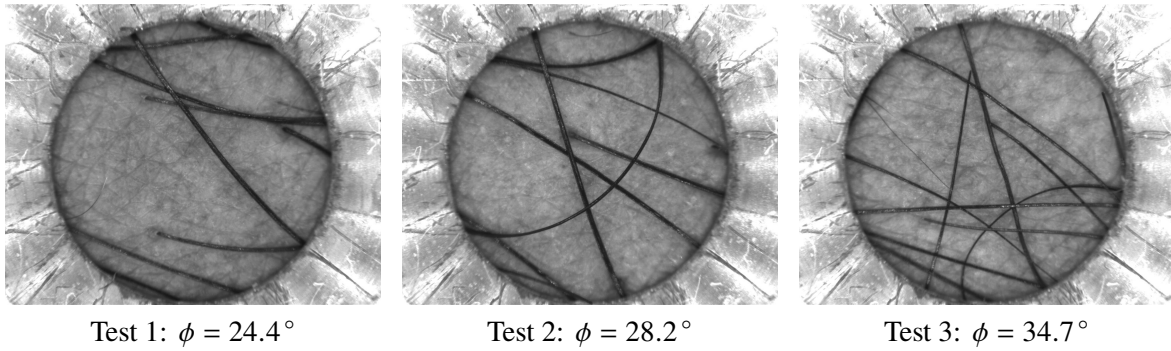
Figure 6.11: Test frame of the quasi-static state with pressure 300 mbar for the volunteer 7. Model fitting results are plotted in Figure 6.12 and detailed in Table G.1.

Test 1: $\phi = 24.4°$ Test 2: $\phi = 28.2°$ Test 3: $\phi = 34.7°$
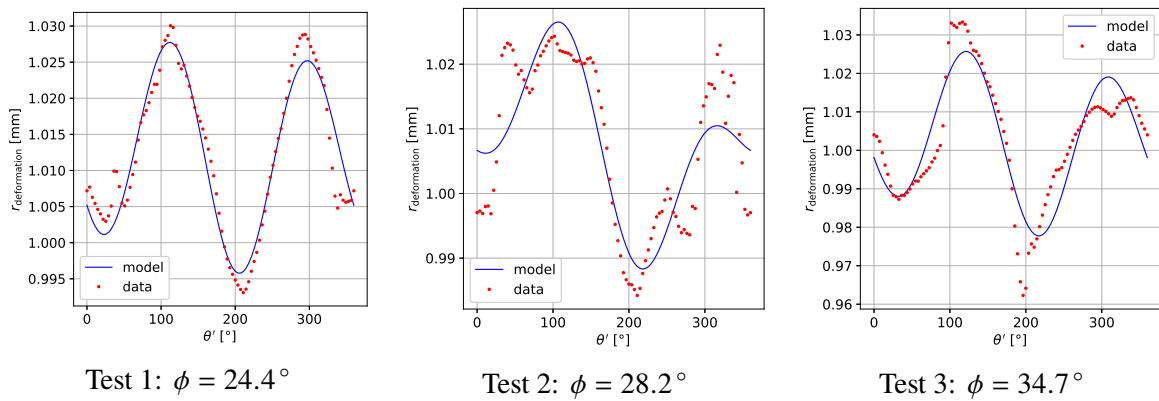
Figure 6.12: Model fit on the circle $r_{\text{fit}} = 1$ mm for the volunteer 7.

6.2.2.2 Skin Stiffness

Similarly to ϕ, the elastic modulus along and across Langer's line were identified for an applied pressure $p = 300$ mbar, which causes a radial stress of $\sigma_r = 0.0123$ (see Sec. 5.3.1.1). The Poisson's

Test 1: $\phi = 56.8°$ Test 2: $\phi = 22.5°$ Test 3: $\phi = 31.8°$
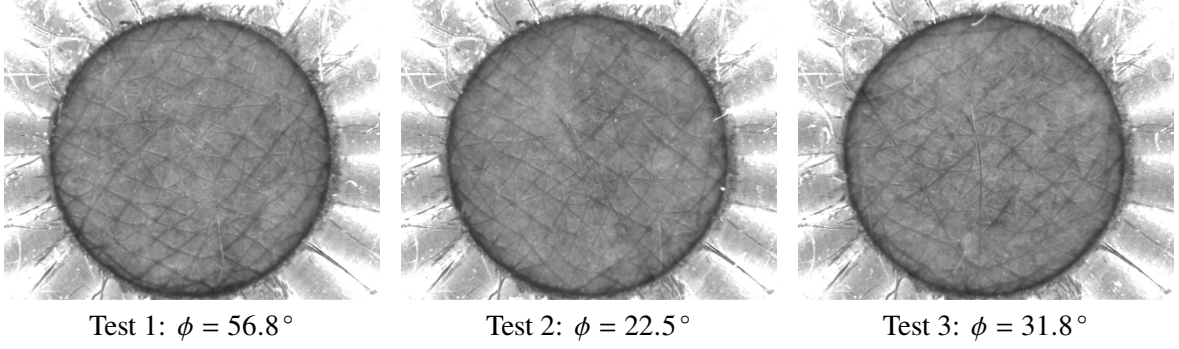
Figure 6.13: Test frame of the quasi-static state with pressure 300 mbar for the volunteer 25. Model fitting results are plotted in Figure G.1c and detailed in Table G.1.

ratio ν_{12} was set to 0.43 according to the literature as described in Section 5.3. Figure 6.14 shows E_1 and E_2 error bars and scatters. For 9 subjects, only one valid value was accounted for because E_1 was negative for the two other tests. As E_2 is linked to E_1, such that $E_2 = \nu_{21}E_1/\nu_{12}$, it was not counted for the same 9 subjects. Subjects 7 and 24 were discarded entirely from this analysis since all three tests provided $E_1 < 0$. Because of hair presence (Fig. 6.15), the DIC technique failed to capture accurate semi-axis a displacement. To overcome the issue, the subject should be kindly asked to shave the studied site at home off the protocol for later clinical trials. Regardless, the DIC quality did not severely impact the ϕ parameter for both subjects, thanks to the data quantity. Back to Figure 6.8a, Langer's line over 3 tests showed moderate variation.
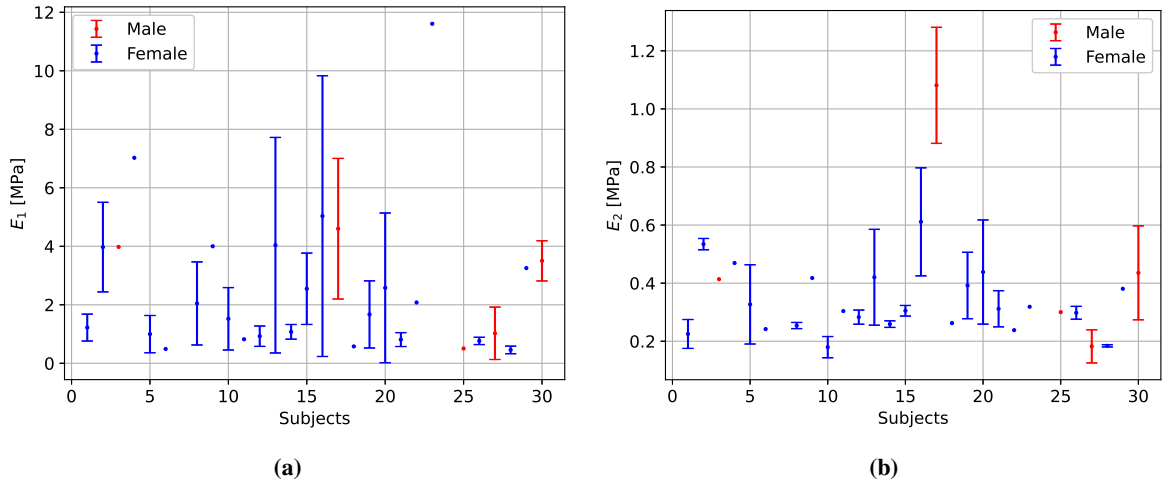
Figure 6.14: Variability of the skin stiffness per subject and for all tests.

With a global weighted mean $\hat{E}_1^{\text{all}} = 2.70 \pm 1.76$ MPa, assessing the elastic modulus along Langer's line is hugely fluctuating, even if a bunch of subjects witnesses reproducibility of E_1 (standard deviation < 1 MPa), for volunteer 6, 9, 13, 16, 18, and 28. As expected, according to the pre-clinical study (Sec. 5.3.2.2), the identification of E_1, interpreted as the collagen stiffness, was highly fluctuating. The displacements along the semi-axis with minimum deformation are almost null, so its associated elastic moduli sensitivity would be high. Besides, E_2 revealed a global mean of $\hat{E}_2^{\text{all}} = 0.35 \pm 0.18$ MPa. Since the displacement is higher across Langer's line direction, their fluctuation is relatively low. Therefore, E_2 exhibited less sensitivity compared to E_1. Although several E_2 values were discarded, the majority of them are within the interval 0.35 ± 0.18 and could be considered valid. In reality, in Table G.1, only 4/90 were negative. It could be possible to account for positive E_2 values associated with negative E_1 for the mean calculation, but the whole couple was eliminated for ease. Above all, the clinical trial results witnessed, at some level, a consistency of identified skin stiffness across Langer's

(a) Subject 7, $R_{\text{cor}} = 0.7561$

(b) Subject 24, $R_{\text{cor}} = 0.8836$
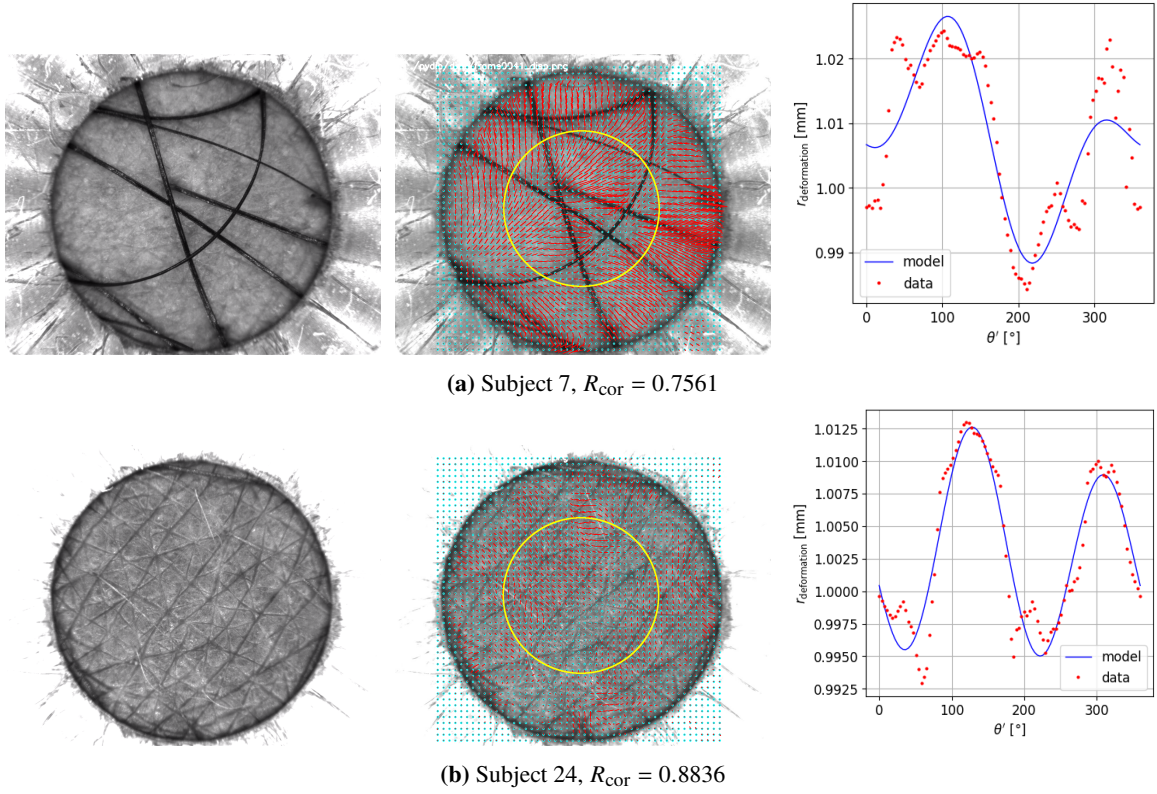
Figure 6.15: model fitting results of the discarded subjects. The frames were taken from the quasi-static state from the second test.

Table 6.4: Study of skin stiffness variability between groups constituted according to sex and age.

	Females ($N_{\text{s}} = 23$) *vs.* Males ($N_{\text{s}} = 5$)	Generation I ($N_{\text{s}} = 15$) *vs.* Generation II ($N_{\text{s}} = 13$)
E_1	$E_1^{\text{Females}} = 2.29 \pm 2.58$ MPa	$E_1^{\text{G.I}} = 2.38 \pm 1.80$ MPa
	$E_1^{\text{Males}} = 2.70 \pm 1.76$ MPa	$E_1^{\text{G.II}} = 2.42 \pm 2.97$ MPa
	$P_{\text{v}} = 0.92$	$P_{\text{v}} = 0.94$
E_2	$E_2^{\text{Females}} = 0.32 \pm 0.10$ MPa	$E_2^{\text{G.I}} = 0.35 \pm 0.11$ MPa
	$E_2^{\text{Males}} = 0.45 \pm 0.32$ MPa	$E_2^{\text{G.II}} = 0.35 \pm 0.22$ MPa
	$P_{\text{v}} = 0.09$	$P_{\text{v}} = 0.76$

line.

Furthermore, the quantification of the variability significance concerning sex and age was addressed as well. The results for all situations are organized in Table 6.4. Following *P*-values, no substantial difference was sensed between Females and Males, as noticed in [429, 430], and between the two Generations. The results were not in line with Vexler *et al.*'s findings [431]. The authors found a strong statistical significance of skin elasticity difference between the two sexes, *i.e.*, Females' skin softer than Male's. Besides, one remark could intrigue the reader concerning the variability according to age. Through the age column, the standard deviation for younger subjects is smaller for both cases, E_1 and E_2. The interpretation forwarded here is that aging induces higher fluctuation of the mechanical response. Figure 6.14b shows higher sensitivity for the second half of the subjects (ascendingly sorted by age). This comparison would not be credible if two sample sizes were not close, like for Females *vs.* Males case.

6.2.3 Sensitivity Analysis

We discuss in this last part the sensitivity of the mechanical response to a change in intrinsic and extrinsic factors. The formers include the skin layer thicknesses. The latters consist of the ambient temperature, ambient relative humidity, and the adjustment variables. The study aims to spot the sources of data variability within and between subjects.

6.2.3.1 Skin Layer Thicknesses

The continuum mechanics theory stipulates that applying annular suction on a thicker layer would cause less deformation in the central surface zone. Still, it would not be the case if the radial stress was uniform in depth. In this situation, the change in skin thickness will not affect the displacement measurement on the surface. Assuming the thickness is directional invariable, its influence on Langer's line orientation is not considered. The linear regression between the thickness and skin stiffness does indicate a negligible linear correlation in Figure 6.16. Nothing suggests that the volume of collagen, which may define the dermis thickness, nor the epidermis thickness, has no contribution to the homogenized elastic moduli. The thickness values were likely too close to let appear the predicted correlation. Quentin Lucot, an intern who collaborated in the analysis of CutiScan®'s performance, has performed 3D simulations to study the effect of skin layer thicknesses sensitivity combined with a change in the stiffness on the mechanical response. It would be interesting to extend his work considering the last findings.
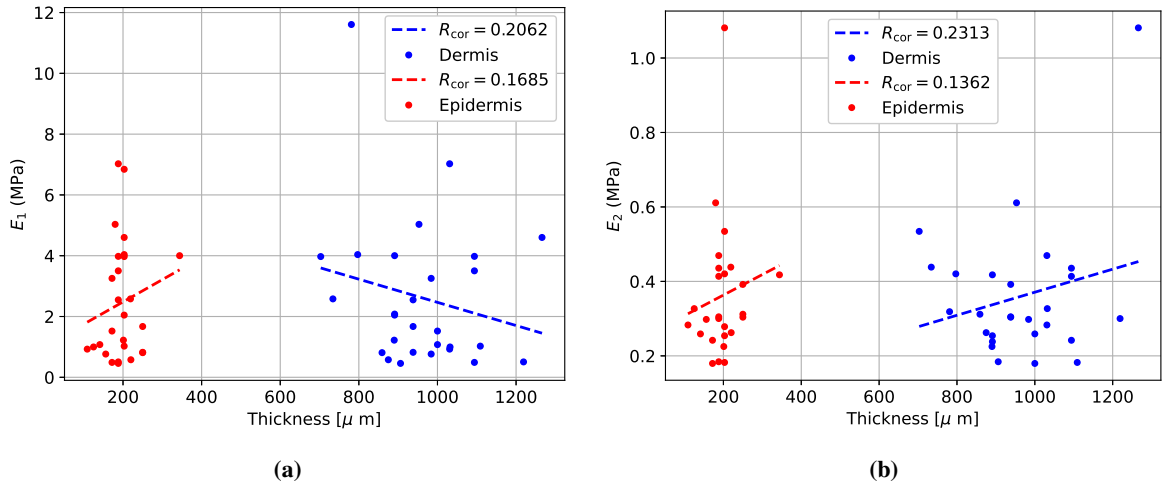
Figure 6.16: ϕ assessment sensitivity regarding the change in the thickness.

6.2.3.2 Environmental Conditions

In a clinical trial, an air conditioning system generally controls the ambient temperature and humidity. It sometimes happens that the environmental conditions need to be better regulated, and hence they vary considerably. With the intention of studying the consequences of their variations on the skin's mechanical response, a linear regression was performed on six scatter plots, three for temperature Te and three for the relative humidity RH. For each case, the points link the variation of the ambient conditions, Δ_{Te} and Δ_{RH}, with the variation of a material parameter in $\boldsymbol{m}_m$, for every subject over the 3 tests.

As reported in Figure 6.17, the Langer's line direction fluctuation does not appear to be linearly correlated with Δ_{Te}, and neither with Δ_{RH}. Subsequently, one could be confident about the insensitivity of skin's behavior measurement to the technical irregularity of the air conditioner. Under the hypothesis that temperature change could have an effect on the orientation of collagen fibers, one way to accomplish it is through thermal expansion. The latter, yet to be characterized according to the literature,

would have a non-negligible contribution in the case of high-temperature gradients. Whereas for the relative air humidity, it was speculated that it affects the skin water content. It seems that a deviation of 5% of RH was not significant enough to alter the collagen network formation. By analogous analysis, referring to scatter plots in Figures 6.18 and 6.19, the skin stiffness along and across Langer's line exhibited insensitivity to the variation of Te and RH, with standard deviations up to 2 °C and 5.5%, respectively.
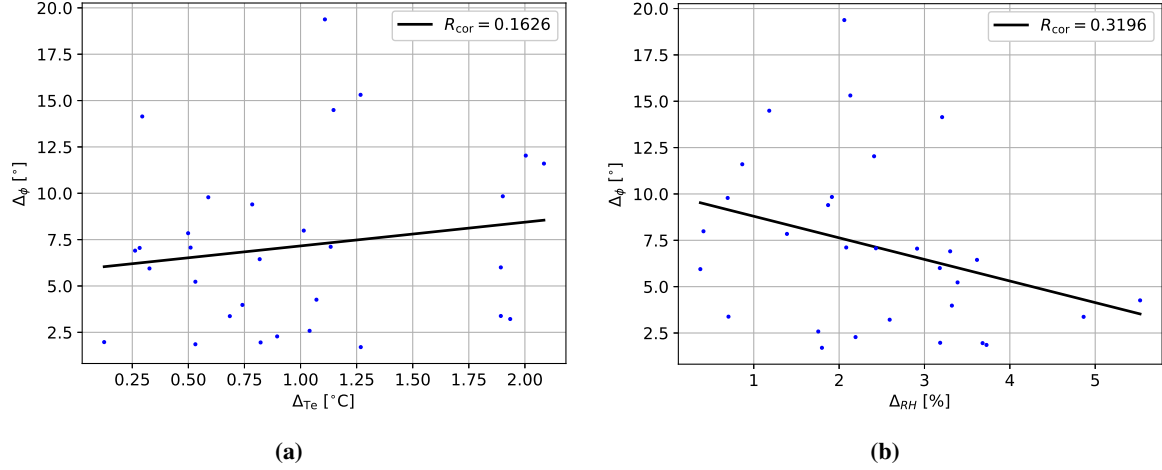
Figure 6.17: ϕ assessment sensitivity regarding the change in the environmental conditions.
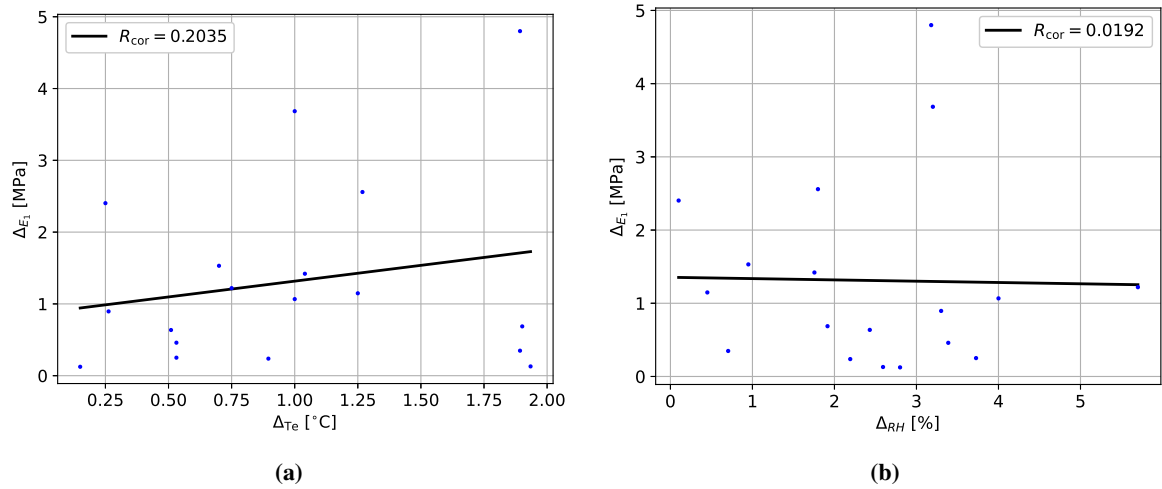
Figure 6.18: E_1 assessment sensitivity regarding the change in the environmental conditions.

6.2.3.3 Operator Influence

It has been reported in Table 6.1 that two operators carried out the mechanical experiment. Except for subject 17's forearm, on which the operator 2 performed the tests, all the other 29 inclusions were assisted by the operator 1. To investigate the operator factor on the variability of skin stiffness measurement, one must compare the identification results from tests performed on the same subject. Hopefully, subject 17 had participated in the pre-clinical study in Section 5.1.2.2. Hence, the optimal parameters from both datasets are confronted with each other in Table 6.5 under the assumption that the experimental protocols (slightly different) produce the same outputs.

The results above revealed that the characterization of $\tilde{E}_1$ and $\tilde{E}_2$ significantly differed from operator to operator. It means that the accuracy of elastic moduli assessment is crucially impacted by the
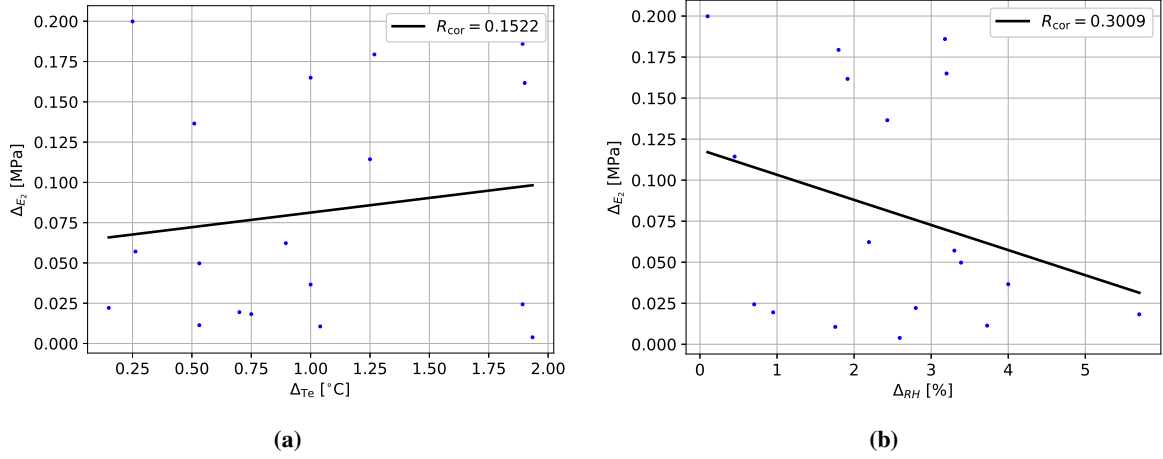
Figure 6.19: E_2 assessment sensitivity regarding the change in the environmental conditions.

Table 6.5: Comparison of the anisotropic material parameters characterization conducted by two operators on subject 17.

	Operator 1	Operator 2
$\tilde{\phi}$	$40.9 \pm 8.2\,°$	$43.07 \pm 14.14\,°$
$\tilde{E}_1$	1.35 ± 0.65 [MPa]	4.60 ± 2.40 [MPa]
$\tilde{E}_2$	0.43 ± 0.07 [MPa]	1.08 ± 0.20 [MPa]

operator's interaction with the equipment. Suppose one examines in detail the human actions in the experimental protocol (Sec. 6.1.1.2). In that case, some tasks will be recognized as a potential reason for the mechanical response variability between operators, for instance, in step 10. In this task, the operator needs to lower the probe progressively until making very light contact with the skin. The latter is executed while guided by personal perception, unlike other tasks, where measurement tools are used, hence less variability. As a matter of fact, laying the probe on the skin surface with some indentation would increase the friction on the interface. Consequently, the deformation may encounter energy loss. The captured displacement would then be smaller, and the stiffness would increase. For identification accuracy, step 10 in the protocol must be assisted with a standardized measurement tool.

Nevertheless, one encouraging result to deduce from this study is that the assessment of Langer's line faced negligible operator effect. The values of $\tilde{\phi}$ were in accordance with both operators. Therefore, one could state that the MARSAC-CutiScan®system is robust in identifying the anisotropy axis on the skin.

Conclusions

After describing in the previous chapter the methodology developed around the CutiScan®for anisotropy characterization, the actual chapter addresses its application to a clinical trial dataset. The study aimed first place to analyze the *intra*-subject variability of the anisotropic material parameters, for instance, the Langer's line and the elastic moduli along and across it. Therefore, 30 subjects (7 Males and 23 Females), aged between 18 and 50, took part in the campaign at the University Hospital of Besançon. Every subject participated in a mechanical measurement on the interior left forearm for 1 hour, conducted three times, and preceded by a measure of skin thickness. The mechanical measurement consisted of a multi-axial annular suction at 21 pressure levels, from 100 to 500 mbar. By means of the DIC technique, whose algorithm is embedded in MARSAC, the video frames that cover the full creep-relaxation periods during the skin deformation were converted into 360-degree transient displacement fields. By the end of the trial, $30 \times 3 \times 21$ sets were collected and ready to use for

studying the viscoelasticity and anisotropy behaviors. The database is itself an achievement, which can be helpful for the biomechanics community in the context of open science if the owners, University of Franche-Comté and the hospital of Besançon, accept to share it publicly.

With a focus on the anisotropy aspect, the data analysis was conducted exclusively to the quasi-static state, at pressure 300 mbar, *i.e.*, the viscoelasticity has not been addressed. Frequentist statistics methods were used to quantify: (i) the variability of mechanical properties between all subjects and (ii) the significance of discards regarding a quantity between two groups. The groups were formed accordingly to sex, Females and Males, and age, Generation I (16 subjects under 29) and Generation II (14 subjects above 29). For the *inter*-subject variability, the averages values were $\tilde{\phi}^{\mathrm{all}} = 21.6 \pm 8.3\,°$, $\tilde{E}_1^{\mathrm{all}} = 2.70 \pm 1.76$ MPa, and $\tilde{E}_2^{\mathrm{all}} = 0.35 \pm 0.18$ MPa. One could conclude from the deviation in $\tilde{\phi}^{\mathrm{all}} = 21.6 \pm 8.3\,°$ that Langer's line orientation on a human's forearm is in 95% of the cases between 13 and 30°. The relative variability between individuals of E_1 and E_2, no less than 50 %, combined with high discard of elastic moduli in the literature, does not lead to stipulating the existence of universal skin stiffness. On that account, on the issue of modeling the peripheral healthy skin to the keloid scar, one needs to identify specifically the patient's material parameters interpreted as the skin stiffness. As for the anisotropy, the modeler could rely on the presented clinical trial results to fix the parameter representing the main collagen fiber direction, with an uncertainty of 8.3°.

The quantification of variability significance was run between partial groups for different quantities: skin thickness and material parameters. As such, the Males' dermis is mostly thicker than the Females' with a $P_{\mathrm{v}} < 0.0001$, but not the epidermis. The aging did not affect the skin thickness variation (at least for subjects under 50) since the difference was insignificant for the dermis and epidermis. Besides, the analysis of the material parameters revealed that Langer's line is sex-related according to the result $P_{\mathrm{v}} < 0.005$. Actually, the anisotropy axis for both sexes was $\tilde{\phi}^{\mathrm{Female}} = 20.6 \pm 7.9\,°$ and $\tilde{\phi}^{\mathrm{Male}} = 31.4 \pm 7.5\,°$. As far as I know, this finding has not been reported in the literature and might be one of the relevant contributions of the thesis. In addition, the investigation of the operator's influence led to pertinent results about the accuracy of the methodology. Precisely, two operators characterized the anisotropy of the same subject' skin. The identification outcomes displayed large discards for the elastic moduli but negligible for Langer's line. Accordingly, the MARSAC-CutiScan®pipeline is a serious candidate for identifying the anisotropy axis in human skin with encouraging accuracy.

Conclusions

Contributions

No matter how many studies are carried out to characterize the mechanical properties of the skin and relative scars, they remain ill-defined and uncertain. Like dozens of recent studies, this dissertation participated in answering questions arising from the observations with model-based approaches. By the end of the journey, we need to highlight the contributions for better novelty emphasizing. They are inventoried hereafter within two interconnected topics. The first topic focuses on the mechanical characterization of a bi-material composed of keloid scar and healthy skin, which undergoes large deformation. Both materials were initially assumed to be isotropic to increase the complexity gradually. Later, the undamaged skin's anisotropy was addressed in the second topic to improve the bi-material modeling. Another link to be hinted between the two topics is that assessing precisely Langer's line could spare the incised skin (in surgery, for instance) from developing abnormal wounds that would become keloids later.

Bi-material Mechanical Characterization

This project sought to forward a medical solution to contain a patient-specific keloid scar and prevent its growth. For that purpose, an open-source numerical pipeline, namely, SoFTI, has been built in FEniCS based on continuum mechanics, scientific computing, and *in vivo* experiments. Given the similarities inter living tissues, from a mechanical point of view, SoFTIwas conceived to include all soft tissues.

Chapter 2 described the structure and methods of SoFTI as follows. Experimental data, such as force-displacement curves and displacement 2D fields captured from a uni-axial extension, are input for primary treatment and formatting. A part of them is used to set boundary conditions of a forward FE solver that simulates the keloid/healthy-skin deformation. The geometry of tested heterogeneous bi-material needs to be provided. As for the behavior law, it can be implemented effortlessly with a strain energy density function. Next, an optimization algorithm iteratively updates the forward solver (for each new parameter set) until reaching a small discrepancy between the simulation and experimental data. In the outputs, the stress field of the whole domain is obtained for the optimal parameters. With further processes, the forthcoming shape of the keloid could be predicted. Therefore, a medical solution would be advised. Besides, the validation of the forward and optimization solvers showed two promising results: the simulation with Gent model using FEniCS framework, and inverse identification of bi-material parameters through a constrained optimization.

In Chapter 3, the accuracy of the identified model parameters was quantified for different uncertainty sources, mesh discretization, measurement noise, data quantity, boundary conditions, and the 3D dimension. The latter could significantly affect the estimation. Hence, defining low uncertainty ranges and criteria was aimed in that study. To achieve this objective, synthetic data used as reference were generated on an extremely fine mesh using an arbitrary parameter set, taken as reference. Quantifying the influence of mesh discretization on the parameter identification led to generating an optimal mesh

that could produce approximately the same solutions as the reference but with a lower computation cost. The discretization study revealed that linear elements increase the possibility of converging toward the optimal set and that quadratic elements improve accuracy. Accordingly, a strategy assembling the two types of elements was made up to ensure convergence starting from a far initial guess. Furthermore, with the measurement deviation analysis, it was possible to set a threshold for data noise to secure accuracy in parameter estimation. Additionally, testing several subsets with different steps from the entire dataset could shed light on the data quantity needed to reduce uncertainty. As for the boundary conditions, a parametric study with varying proportions of topology was conducted. As a result, a mesh domain whose boundaries have negligible influence on the mechanical response was determined. Last but not least, exploring the forward solver in 3D dimensions could confirm the necessity of considering the thickness in the model.

Considering the accuracy limits set in the previous study, Chapter 4 presents the application of the method on a dataset acquired from an actual experiment performed on the upper arm of a 22-year-old Caucasian female subject. By combining the force-displacement curve and DIC-issued displacement fields, the material parameters of the keloid and the surrounding skin were assessed, with and without an additional contra-lateral test. Because of imperfections in the extension test, the observation zone for the DIC field had been restricted. Thus, identifying the bi-material parameters at once could not succeed. Conversely, with additional data from a similar experiment on the other upper arm, the inverse solver could determine the parameters. The results might witness the advantage of employing the Gent energy function to fit the experimental data for keloid scar and healthy skin undergoing large deformation. After all, the Gent model was selected for its similarity with skin in terms of limited extensibility when approaching singularity. Later, by imposing a pre-stress field, the Cauchy stress tensor was solved on every element and interpolated all over the domain. Consequently, maps of the normal and shear components have exposed the stress concentration areas that could be responsible for keloid propagation. Containing the tumor would start by countering the effort in those critical zones. A medical device specification, as well as technical suggestion, were proposed for this patient-specific case.

Characterization of the Anisotropy of the Human Skin
The second project addresses the anisotropy aspect of undamaged skin. With the aim to identify Langer's line, another open-source numerical framework, MARSAC, has been developed and described in Chapters 5 et 6. It consists of two principal procedures: (i) deformation measurement with a multi-axial annular section test and (ii) anisotropic material parameters identification by fitting an analytical model.

Chapter 5 describes the experimental, analytical, and numerical methods linked to MARSAC. In the first step, by applying negative pressure over an annular section on the skin surface, the tissue is sucked perpendicularly, causing a stretch in the central area in all directions. This procedure is performed with a commercial device probe, CutiScan® CS 100. Two technical weaknesses had to be overcome for better use of the equipment. For reproducibility, a support was designed and fabricated to hold the probe firmly and guarantee reasonable control of its motion. Since the original software provides incomplete data, a DIC-based framework has been adapted to extract the full displacement data from the recorded videos during the tests. The second step consists of establishing an analytical solution deriving from the orthotropic linear elasticity to capture observed deformation, which is more likely ellipse-shaped. The presence of principal orthogonal directions characterizes the model. The last step is the identification of the material parameters, which is accomplished in two levels. Geometrical ellipse-curve parameters are assessed with an inverse problem, then used to retrieve the mechanical parameters. The latter are Langer's line and skin stiffness along and across it. Thanks to the center shift parameters added to the optimization problem, the model fitting was highly accurate, which may

help secure the reproducibility of the test. To test its robustness, MARSAC methdology was applied to a 30-test series, where the mechanical parameters were identified for each. The day-to-day variability study revealed that the equipment allows determining Langer's line and the stiffness across it with high confidence. With a free-ready-to-use framework, the surgeon could rapidly determine Langer's line on the patient before operating an incision. In a further study, two contributions were proposed. First, an orthotropic extension of the hyperelastic Gent model was implemented within FENICS. Second, an application of the Bayesian inference in the optimization to estimate the mechanical parameters along with uncertainty directly. These results showed that adding more informative data, even with moderate measurement error, will help decrease the uncertainty.

The last Chapter reports the results of a clinical trial at the University Hospital of Besançon, involving 30 volunteers to analyze the subject-to-subject variability of anisotropic material parameters. By the campaign's end, the database contained 1890 multi-axial stretch test records. Every record can be divided into multiple frames processed with DIC to generate 360-degree creep-relaxation displacement fields. In the context of open science, the database could be helpful for the biomechanics community if the owners, FEMTO-ST institute and University Hospital of Besançon, agree to share it publicly. By ignoring the viscoelasticity effects, the study focused on quantifying the variability of mechanical properties at the quasi-static state between all subjects and the significance of differences regarding a factor between two given groups. The groups were formed accordingly to sex, Females and Males, and age, Generation I and Generation II (with almost the same number of subjects each). Global mean and standard deviation over all the subjects showed that Langer's line could have a universal orientation on the forearm, unlike skin stiffness in both orthogonal directions. Therefore, when modeling the peripheral healthy skin to the keloid scar, one would fix the parameter representing the main collagen fiber direction in the hyperelastic energy function. Moreover, The quantification of variability significance was conducted between partial groups for skin thickness and material parameters. Consequently, the Males' dermis was found to be mostly thicker than the Females'. Also, the analysis revealed that Langer's line is sex-related. This finding could not have been reported in the literature and might be one of the relevant contributions of the clinical trial. In addition, the investigation addressed the operator's influence on reproducibility. Therefore, the Langer's line values obtained by two different operators displayed negligible discards, which encourages confidently applying the MARSAC-CutiScan pipeline in the future.

Limitations

If not for several limitations listed below, the results would have been more conclusive.

- **Computation capacity**. Analytical solutions are known to be a time and memory saver. However, advanced problems in physics are commonly approximated with numerical solutions. The duration and the memory size required for the computational process represent a considerable impediment for numerical models like the FEMU-based inverse problem, given the hardware supplied to conduct the thesis, . Concerning the memory size, the forward solver ought to fail if the linear system is on the order of millions of degrees of freedom. In other words, simulating the 3D model with finer elements (to reach convergence) is difficult. On top of that, for the optimization process, the FE solver must run for many iterations, and thus the computation time will increase drastically. Although parallel programming could be considered to reduce the cost, it is still demanding in terms of memory in our situation. Improving the computer performance would secure fast and recursive simulations, such as applying Bayesian inference to full 3D FE models.

- **Patient-specific data**. The SoFTI method was applied to the dataset available in Biomecat's repository. With lots and various cases of keloidic scars, we could have analyzed the method's robustness and had first-hand experience to improve the efficiency. One of the proposals

to overcome this constraint is initiating collaborations with hospitals in countries with high abundance rates of keloid and conducting the experiments. Or, one could create an open international database to receive data compatible with SoFTI's input format: force-displacement curve and deformation video records. The collaborators would have to follow a standardized protocol for better DIC accuracy, for instance, camera position and ambient brightness.

- **CutiScan reproducibility**. The *intra-* and *inter-*subject variability study of anisotropic properties exhibited weak reproducibility of skin stiffness along Langer's line. According to the adopted model, higher stiffness is inversely proportional to strain. The latter was mostly insignificant. Therefore, its sensitivity had a major impact on the variability of skin stiffness along Langer's line. It has been reported that the perpendicularity of the probe with the skin surface was manually controlled, which may contribute to the fluctuation of the small strains. As such, adding a function to the device to achieve perfect perpendicularity and quasi-null contact with the tested sample automatically.

- **Sexual parity** In the clinical trial, there were three times more Females than Males. The statistical methods used in data analysis accounted for the sample size, such as *P*-value. However, the difference in sample sizes between the two groups could not impact some results if the variability is too significant, like for the dermis thickness. Nevertheless, ensuring parity between volunteers would eliminate doubts.

Perspectives

With a multifaceted problem and due to technical limitations and time constraints, some specific questions were left unanswered and can be addressed later as partial or complete research projects. The following items detail proposals for future research:

- **Upgrade the SoFTI method to full 3D geometry**. The actual 2D geometry of SoFTI incorporates the average thickness of the keloid body and neglects its out-plane height variation. The next step will be considering the real shape of keloids and the site's curvature, which would allow characterizing non-flat anatomical sites too.

- **Develop a user-friendly version of the SoFTI framework for surgeons with no prior experience in mechanical modeling**. SoFTI has no graphical interface and some principal operations, for instance, data treatment and parameter identification, are performed by hand. As a considerable amount of patient-specific cases is required to improve the results, the process should be executed autonomously in the easiest possible way.

- **Apply the DWR method to automatically generate adaptive meshes**. The adaptive mesh studied and applied in Chapters 2, 3, and 4, was generated with manually-mapped nodes over the discretization error zones. Generating automatic adaptive mesh could optimize error minimization for optimal computation cost.

- **Test several hyperelastic models for the keloid/healthy-skin bi-material and investigate their dependency on the Cauchy stress field**. The Gent model was implemented to fit experimental data and identify the material parameters, which led to the mechanical stress quantification in and around the keloid. It would be more convincing to compare those stresses against other hyperelastic models fitting the data.

- **Master the contact of the CutiScan® probe with the skin surface**. The experimental device showed low reproducibility of the displacement measurement along Langer's line. It was linked to the contact probe/skin operated by hand. For such low deformation correlated with stiffer direction, it would be necessary to design a technical solution to ensure a uniform and consistent contact.

- **Construct an *in vivo* Langer's lines map**. The MARSAC method could be applied to different areas of the human body to establish a global new Langer's lines map. The actual one referenced in the literature was retrieved from corpses one century and a half ago. The quick process of MARSAC and the small size of its relative device are assets for carrying out such an ambitious work.

- **Extend the analysis of data from the clinical trial**. Besides the identification of Langer's line on every volunteer, the clinical trial data could be utilized to (i) analyze the effects of viscoelasticity (using the whole creep-relaxation cycle), (ii) fit nonlinear hyperelastic models (for all suction pressures), (iii) employ the Bayesian inference (to study subject-to-subject uncertainty), (iv) train artificial neural networks, *etc*.

Bibliography

[1] D. Sutula, A. Elouneg, M. Sensale, F. Chouly, J. Chambert, A. Lejeune, D. Baroli, P. Hauseux, S. Bordas, and E. Jacquet, "An open source pipeline for design of experiments for hyperelastic models of the skin with applications to keloids," *Journal of the Mechanical Behavior of Biomedical Materials*, vol. 112, p. 103999, 2020. 4, 20, 29, 36, 65, 73, 80, 97, 99

[2] J. Brandner and J. Jensen, "The skin: an indispensable barrier," *Exp Dermatol*, vol. 17, pp. 1063–72, 2008. 8, 9

[3] P. Oltulu, B. Ince, N. Kokbudak, S. Findik, F. Kilinc, *et al.*, "Measurement of epidermis, dermis, and total skin thicknesses from six different body regions with a new ethical histometric technique," *Turkish Journal of Plastic Surgery*, vol. 26, no. 2, p. 56, 2018. 8

[4] G. Limbert, ed., *Skin Biophysics*. Springer International Publishing, 2019. 8, 23

[5] "Integumentary system." https://uta.pressbooks.pub/histology/chapter/integumentary-system/. Accessed: 2022-07-21. 8

[6] G. F. Odland and I. Goldsmith, "Physiology, biochemistry and molecular biology of the skin," *Oxford: Oxford University Press, 1991, Vol. I, p. 3*, 1991. 8

[7] W. G. Nelson and T.-T. Sun, "The 50-and 58-kdalton keratin classes as molecular markers for stratified squamous epithelia: Cell culture studies," *The Journal of Cell Biology*, vol. 97, no. 1, pp. 244–251, 1983. 9

[8] J. McGrath, R. Eady, F. Pope, *et al.*, "Rook's textbook of dermatology," *Burns T, Breathnach SM, Cox NH, Griffiths C, editors*, vol. 8, 2004. 9

[9] H. Shimizu, *Shimizu's textbook of dermatology*. JA KUBU, 2007. 9

[10] C. Czekalla, K. H. Schönborn, J. Lademann, and M. C. Meinke, "Noninvasive determination of epidermal and stratum corneum thickness in vivo using two-photon microscopy and optical coherence tomography: impact of body area, age, and gender," *Skin Pharmacology and Physiology*, vol. 32, no. 3, pp. 142–150, 2019. 9

[11] J. Lademann, N. Otberg, H. Richter, L. Meyer, H. Audring, A. Teichmann, S. Thomas, A. Knüttel, and W. Sterry, "Application of optical non-invasive methods in skin physiology: a comparison of laser scanning microscopy and optical coherent tomography with histological analysis," *Skin Research and Technology*, vol. 13, no. 2, pp. 119–132, 2007. 9

[12] R. E. Burgeson and A. M. Christiano, "The dermal—epidermal junction," *Current Opinion in Cell Biology*, vol. 9, no. 5, pp. 651–658, 1997. 9

[13] X. Xiong, T. Wu, and S. He, "Physical forces make rete ridges in oral mucosa," *Medical Hypotheses*, vol. 81, no. 5, pp. 883–886, 2013. 9

[14] I. R. Williams, "Fibroblasts," in *Encyclopedia of Immunology (Second Edition)* (P. J. Delves, ed.), pp. 905–909, Oxford: Elsevier, second edition ed., 1998. 9

[15] Q. Zeng, L. Macri, A. Prasad, R. Clark, D. Zeugolis, C. Hanley, Y. Garcia, and A. Pandit, "Skin tissue engineering," in *Comprehensive Biomaterials* (P. Ducheyne, ed.), pp. 467–499, Oxford: Elsevier, 2011. 9

[16] A. Birbrair, T. Zhang, D. C. Files, S. Mannava, T. Smith, Z.-M. Wang, M. L. Messi, A. Mintz, and O. Delbono, "Type-1 pericytes accumulate after tissue injury and produce collagen in an organ-dependent manner," *Stem Cell Research & Therapy*, vol. 5, no. 6, pp. 1–18, 2014. 10

[17] G. A. Di Lullo, S. M. Sweeney, J. Körkkö, L. Ala-Kokko, and J. D. San Antonio, "Mapping the ligand-binding sites and disease-associated mutations on the most abundant protein in the human, type i collagen," *Journal of Biological Chemistry*, vol. 277, no. 6, pp. 4223–4231, 2002. 10

[18] R. Reihsner, B. Balogh, and E. Menzel, "Two-dimensional elastic properties of human skin in terms of an incremental model at the in vivo configuration," *Medical Engineering & Physics*, vol. 17, no. 4, pp. 304–313, 1995. 10, 12, 21, 52, 120, 121, 129, 134, 141, 146, 155

[19] K. E. Kadler, C. Baldock, J. Bella, and R. P. Boot-Handford, "Collagens at a glance," *Journal of Cell Science*, vol. 120, pp. 1955–1958, 06 2007. 10

[20] T. Ushiki, "Collagen fibers, reticular fibers and elastic fibers. a comprehensive understanding from a morphological viewpoint," *Archives of Histology and Cytology*, vol. 65, no. 2, pp. 109–126, 2002. 10

[21] K. Lin, D. Zhang, M. Macedo, W. Cui, B. Sarmento, and G. Shen, "Advanced collagen-based biomaterials for regenerative biomedicine," *Advanced Functional Materials*, vol. 29, 01 2019. 10

[22] L. T. Smith, K. A. Holbrook, and J. A. Madri, "Collagen types i, iii, and v in human embryonic and fetal skin," *American Journal of Anatomy*, vol. 175, no. 4, pp. 507–521, 1986. 10

[23] R. Fleischmajer, E. D. MacDonald, J. S. Perlish, R. E. Burgeson, and L. W. Fisher, "Dermal collagen fibrils are hybrids of type i and type iii collagen molecules," *Journal of Structural Biology*, vol. 105, no. 1-3, pp. 162–169, 1990. 10

[24] K. Gelse, E. Pöschl, and T. Aigner, "Collagens—structure, function, and biosynthesis," *Advanced Drug Delivery Reviews*, vol. 55, no. 12, pp. 1531–1546, 2003. 10

[25] C. Kielty, "Sherratt mj, shuttleworth ca," *Elastic fibres. J Cell Sci*, vol. 115, pp. 2817–2828, 2002. 10

[26] H. Oxlund, J. Manschot, and A. Viidik, "The role of elastin in the mechanical properties of skin," *Journal of Biomechanics*, vol. 21, no. 3, pp. 213–218, 1988. 10, 27

[27] J. Gosline, M. Lillie, E. Carrington, P. Guerette, C. Ortlepp, and K. Savage, "Elastic proteins: biological roles and mechanical properties," *Philosophical Transactions of the Royal Society of London. Series B: Biological Sciences*, vol. 357, no. 1418, pp. 121–132, 2002. 10

[28] E. M. Green, J. C. Mansfield, J. S. Bell, and C. P. Winlove, "The structure and micromechanics of elastic tissue," *Interface Focus*, vol. 4, no. 2, p. 20130058, 2014. 10

[29] W. F. Daamen, S. T. Nillesen, R. G. Wismans, D. P. Reinhardt, T. Hafmans, J. H. Veerkamp, and T. H. Van Kuppevelt, "A biomaterial composed of collagen and solubilized elastin enhances angiogenesis and elastic fiber formation without calcification," *Tissue Engineering Part A*, vol. 14, no. 3, pp. 349–360, 2008. 10

[30] P. Agache and P. Humbert, *Measuring the Skin*. Springer Science & Business Media, 2004. 11, 50, 141, 149

[31] R. Tregear, "The mechanical properties of skin," *Journal of the Society of Cosmetic Chemists*, vol. 20, pp. 467–477, 1969. 11

[32] H. Oxlund and T. Andreassen, "The roles of hyaluronic acid, collagen and elastin in the mechanical properties of connective tissues.," *Journal of Anatomy*, vol. 131, no. Pt 4, p. 611, 1980. 11

[33] C. Oomens, D. Van Campen, and H. Grootenboer, "In vitro compression of a soft tissue layer on a rigid foundation," *Journal of Biomechanics*, vol. 20, no. 10, pp. 923–935, 1987. 11

[34] C. Stecco, W. Hammer, A. Vleeming, and R. De Caro, "Subcutaneous tissue and superficial fascia," *Functional Atlas of the Human Fascial System*, pp. 21–49, 2015. 11

[35] J. Burton and W. Cunliffe, *Subcutaneous Fat: text book of dermatology*. Blackwell Scientific Publications, New York, 1992. 11

[36] X. Feng, G.-Y. Li, A. Ramier, A. M. Eltony, and S.-H. Yun, "In vivo stiffness measurement of epidermis, dermis, and hypodermis using broadband rayleigh-wave optical coherence elastography," *Acta Biomaterialia*, 2022. 11, 12, 149

[37] "Human skin: Basic anatomy and functions." `https://www.acne.org/human-skin-basic-anatomy-and-functions.html`. Accessed: 2022-07-22. 11

[38] E. Dalimier and D. Salomon, "Full-field optical coherence tomography: a new technology for 3d high-resolution skin imaging," *Dermatology*, vol. 224, no. 1, pp. 84–92, 2012. 11

[39] M. Crisan, D. Crisan, G. Sannino, M. Lupsor, R. Badea, and F. Amzica, "Ultrasonographic staging of cutaneous malignant tumors: an ultrasonographic depth index," *Archives of Dermatological Research*, vol. 305, no. 4, pp. 305–313, 2013. 11

[40] A. Mamalis, D. Ho, and J. Jagdeo, "Optical coherence tomography imaging of normal, chronologically aged, photoaged and photodamaged skin: a systematic review," *Dermatologic Surgery*, vol. 41, no. 9, p. 993, 2015. 12

[41] H. Alexander and T. Cook, "Accounting for natural tension in the mechanical testing of human skin," *Journal of Investigative Dermatology*, vol. 69, no. 3, pp. 310–314, 1977. 12, 23

[42] C. Y. Tan, B. Statham, R. Marks, and P. A. Payne, "Skin thickness measurement by pulsed ultrasound; its reproducibility, validation and variability," *British Journal of Dermatology*, vol. 106, no. 6, pp. 657–667, 1982. 12

[43] C. Lasagni and S. Seidenari, "Echographic assessment of age-dependent variations of skin thickness," *Skin Research and Technology*, vol. 1, no. 2, pp. 81–85, 1995. 12

[44] Y. Lee and K. Hwang, "Skin thickness of korean adults," *Surgical and Radiologic Anatomy*, vol. 24, no. 3, pp. 183–189, 2002. 12

[45] A. Sutradhar and M. J. Miller, "In vivo measurement of breast skin elasticity and breast skin thickness," *Skin Research and Technology*, vol. 19, no. 1, pp. e191–e199, 2013. 12

[46] T. Van Mulder, M. de Koeijer, H. Theeten, D. Willems, P. Van Damme, M. Demolder, G. De Meyer, K. Beyers, and V. Vankerckhoven, "High frequency ultrasound to assess skin thickness in healthy adults," *Vaccine*, vol. 35, no. 14, pp. 1810–1815, 2017. 12

[47] J. Cha, J. Kim, and S. Kim, "Noninvasive determination of fiber orientation and tracking 2-dimensional deformation of human skin utilizing spatially resolved reflectance of infrared light measurement in vivo," *Measurement*, vol. 142, pp. 170–180, 2019. 12, 149

[48] S. Shuster, M. M. BLACK, and E. McVitie, "The influence of age and sex on skin thickness, skin collagen and density," *British Journal of Dermatology*, vol. 93, no. 6, pp. 639–643, 1975. 12, 162

[49] C. Escoffier, J. De Rigal, A. Rochefort, R. Vasselet, J.-L. Lévêque, and P. G. Agache, "Age-related mechanical properties of human skin: an in vivo study," *Journal of Investigative Dermatology*, vol. 93, no. 3, pp. 353–357, 1989. 12, 24, 52

[50] S. Diridollou, V. Vabre, M. Berson, L. Vaillant, D. Black, J. Lagarde, J. Grégoire, Y. Gall, and F. Patat, "Skin ageing: changes of physical properties of human skin in vivo," *International Journal of Cosmetic Science*, vol. 23, no. 6, pp. 353–362, 2001. 12

[51] C. H. Daly and G. F. Odland, "Age-related changes in the mechanical properties of human skin," *Journal of Investigative Dermatology*, vol. 73, no. 1, pp. 84–87, 1979. 12

[52] M. G. Shah and H. I. Maibach, "Estrogen and skin," *American Journal of Clinical Dermatology*, vol. 2, no. 3, pp. 143–150, 2001. 12

[53] R. Y. Ha, K. Nojima, W. P. Adams Jr, and S. A. Brown, "Analysis of facial skin thickness: defining the relative thickness index," *Plastic and Reconstructive Surgery*, vol. 115, no. 6, pp. 1769–1773, 2005. 12

[54] I. Yannas, "Principles of skin regeneration," in *Biomaterials for Treating Skin Loss* (D. Orgill and C. Blanco, eds.), Woodhead Publishing Series in Biomaterials, pp. 212–230, Woodhead Publishing, 2009. 13, 14

[55] I. V. Yannas, *Tissue and Organ Regeneration in Adults: Extension of the Paradigm to Several Organs.* Springer New York, 2015. 13, 14

[56] R. Ogawa, "Keloid and hypertrophic scarring may result from a mechanoreceptor or mechanosensitive nociceptor disorder," *Medical Hypotheses*, vol. 71, pp. 493–500, 08 2008. 13, 17

[57] R. Ogawa and D. P. Orgill, "Mechanobiology of cutaneous wound healing and scarring," in *Bioengineering Research of Chronic Wounds: A Multidisciplinary Study Approach* (A. Gefen, ed.), pp. 31–42, Berlin, Heidelberg: Springer Berlin Heidelberg, 2009. 13

[58] S. H. Kwon, J. Padmanabhan, and G. C. Gurtner, "Mechanobiology of skin diseases and wound healing," in *Mechanobiology in Health and Disease*, pp. 415–448, Elsevier, 2018. 13

[59] D. Son and A. Harijan, "Overview of surgical scar prevention and management," *Journal of Korean Medical Science*, vol. 29, no. 6, pp. 751–757, 2014. 13, 15

[60] "How wounds heal: The 4 main phases of wound healing." `http://www.shieldhealthcare.com/community/popular/2015/12/18/how-wounds-heal-the-4-main-phases-of-wound-healing/`. Accessed: 2022-07-26. 13

[61] A. J. Singer and R. A. Clark, "Cutaneous wound healing," *New England Journal of Medicine*, vol. 341, no. 10, pp. 738–746, 1999. 13, 14

[62] R. F. Diegelmann, M. C. Evans, *et al.*, "Wound healing: an overview of acute, fibrotic and delayed healing," *Front Biosci*, vol. 9, no. 1, pp. 283–289, 2004. 13, 14

[63] A. G. Ferdman and I. V. Yannas, "Scattering of light from histologic sections: a new method for the analysis of connective tissue," *Journal of Investigative Dermatology*, vol. 100, no. 5, pp. 710–716, 1993. 14, 149

[64] P. P. Van Zuijlen, J. J. Ruurda, H. A. Van Veen, J. Van Marle, A. J. Van Trier, F. Groenevelt, R. W. Kreis, and E. Middelkoop, "Collagen morphology in human skin and scar tissue: no adaptations in response to mechanical loading at joints," *Burns*, vol. 29, no. 5, pp. 423–431, 2003. 14

[65] C. A. Harrison, F. Gossiel, C. M. Layton, A. J. Bullock, T. Johnson, A. Blumsohn, and S. MacNeil, "Use of an in vitro model of tissue-engineered skin to investigate the mechanism of skin graft contraction," *Tissue Engineering*, vol. 12, no. 11, pp. 3119–3133, 2006. 14

[66] D. Orgill and C. Blanco, *Biomaterials for treating skin loss*. 01 2009. 14, 15

[67] R. Ogawa, "Mechanobiology of scarring," *Wound Repair and Regeneration*, vol. 19, pp. s2–s9, 2011. 14, 15, 16, 17, 18

[68] P. Melis, C. J. van Noorden, and C. M. van der Horst, "Long-term results of wounds closed under a significant amount of tension," *Plastic and Reconstructive Surgery*, vol. 117, no. 1, pp. 259–265, 2006. 14

[69] J. B. Lansman, "Going with the flow," *Nature*, vol. 331, no. 6156, pp. 481–482, 1988. 14

[70] T. Ohura, M. Takahashi, and N. Ohura Jr, "Influence of external forces (pressure and shear force) on superficial layer and subcutis of porcine skin and effects of dressing materials: are dressing materials beneficial for reducing pressure and shear force in tissues?," *Wound Repair and Regeneration*, vol. 16, no. 1, pp. 102–107, 2008. 14

[71] G. Gabbiani, G. Ryan, and G. Majno, "Presence of modified fibroblasts in granulation tissue and their possible role in wound contraction," *Experientia*, vol. 27, no. 5, pp. 549–550, 1971. 14

[72] L. Cuttle, M. Kempf, G. E. Phillips, J. Mill, M. T. Hayes, J. F. Fraser, X.-Q. Wang, and R. M. Kimble, "A porcine deep dermal partial thickness burn model with hypertrophic scarring," *Burns*, vol. 32, no. 7, pp. 806–820, 2006. 14

[73] G. C. Gurtner, S. Werner, Y. Barrandon, and M. T. Longaker, "Wound repair and regeneration," *Nature*, vol. 453, no. 7193, pp. 314–321, 2008. 14

[74] K. Langer, "Zue anatomie und physiologie de haut. ueber der spaltbarkeit der cutis," *Sitzungsberich der Academie der Wissenschaften in Wien*, vol. 44, no. 19, p. 1861, 1861. 15, 149

[75] B. J. Wilhelmi, S. J. Blackwell, and L. G. Phillips, "Langer's lines: to use or not to use.," *Plastic and Reconstructive Surgery*, vol. 104, no. 1, pp. 208–214, 1999. 15

[76] K. Langer, "On the anatomy and physiology of the skin: I. the cleavability of the cutis," *British Journal of Plastic Surgery*, vol. 31, no. 1, pp. 3–8, 1978. 15, 18, 149

[77] M. Ridge and V. Wright, "The directional effects of skin: A bio-engineering study of skin with particular reference to Langer's lines," *Journal of Investigative Dermatology*, vol. 46, no. 4, pp. 341–346, 1966. 15

[78] T. Gibson, H. Stark, and J. Evans, "Directional variation in extensibility of human skin in vivo," *Journal of Biomechanics*, vol. 2, no. 2, pp. 201–204, 1969. 15, 20

[79] J. B. Finlay, *Biodynamic studies of human skin: torsional characteristics in relation to structure*. PhD thesis, University of Strathclyde, 1970. 15

[80] X. Markenscoff and I. Yannas, "On the stress-strain relation for skin," *Journal of Biomechanics*, vol. 12, no. 2, pp. 127–129, 1979. 15

[81] A. N. Annaidh, K. Bruyère, M. Destrade, M. D. Gilchrist, and M. Otténio, "Characterization of the anisotropic mechanical properties of excised human skin," *Journal of the Mechanical Behavior of Biomedical Materials*, vol. 5, no. 1, pp. 139–148, 2012. 15, 51

[82] A. Ní Annaidh, K. Bruyère, M. Destrade, M. D. Gilchrist, C. Maurini, M. Otténio, and G. Saccomandi, "Automated estimation of collagen fibre dispersion in the dermis and its contribution to the anisotropic behaviour of skin," *Annals of Biomedical Engineering*, vol. 40, no. 8, pp. 1666–1678, 2012. 15

[83] S. Aarabi, K. A. Bhatt, Y. Shi, J. Paterno, E. I. Chang, S. A. Loh, J. W. Holmes, M. T. Longaker, H. Yee, and G. C. Gurtner, "Mechanical load initiates hypertrophic scar formation through decreased cellular apoptosis," *The FASEB Journal*, vol. 21, no. 12, pp. 3250–3261, 2007. 15

[84] A. F. Borges, "Relaxed skin tension lines (rstl) versus other skin lines.," *Plastic and Reconstructive Surgery*, vol. 73, no. 1, pp. 144–150, 1984. 15

[85] J. V. M. Méndez, *Mechanical properties of single keloid and normal skin fibroblast measured using an atomic force microscope*. PhD thesis, School of Mechanical, Aerospace and Civil Engineering, Manchester, 2010. 15

[86] T.-L. Tuan and L. S. Nichter, "The molecular basis of keloid and hypertrophic scarformation.," *Molecular Medicine Today*, vol. 4 1, pp. 19–24, 1998. 15, 16

[87] A. Bayat, D. McGrouther, and M. Ferguson, "Skin scarring," *BMJ*, vol. 326, no. 7380, pp. 88–92, 2003. 15, 16

[88] B. Berman and F. Flores, "The treatment of hypertrophic scars and keloids," *European Journal of Dermatology*, vol. 8, no. 8, pp. 591–6, 1999. 15

[89] A. N. Neely, C. E. Clendening, J. Gardner, D. G. Greenhalgh, and G. D. Warden, "Gelatinase activity in keloids and hypertrophic scars," *Wound Repair and Regeneration*, vol. 7, no. 3, pp. 166–171, 1999. 15

[90] T. S. Alster and E. L. Tanzi, "Hypertrophic scars and keloids," *American Journal of Clinical Dermatology*, vol. 4, no. 4, pp. 235–243, 2003. 15

[91] R. Ogawa and M. S. Chin, "Animal models of keloids and hypertrophic scars," *Journal of Burn Care & Research*, vol. 29, no. 6, pp. 1016–1017, 2008. 16

[92] G. Limandjaja, J. Belien, R. Scheper, F. Niessen, and S. Gibbs, "A study looking at the differences between hypertrophic scars and keloid scars," *British Journal of Dermatology*, vol. 182, no. 4, pp. e140–e140, 2020. 16

[93] "Keloid vs hypertrophic scar." https://www.plarecon.com/keloid-vs-hypertrophic-scar/. Accessed: 2022-07-27. 16

[94] J. C. Murray, S. V. Pollack, and S. R. Pinnell, "Keloids: a review," *Journal of the American Academy of Dermatology*, vol. 4, no. 4, pp. 461–470, 1981. 16

[95] J. Breasted, *The Edwin Smith surgical papyrus.*, pp. 403–406. Chiacago: University of Chicago Press., 1930. 16

[96] W. B. Rockwell, I. K. Cohen, and H. P. Ehrlich, "Keloids and hypertrophic scars: A comprehensive review," *Plastic and Reconstructive Surgery*, vol. 84, no. 2, pp. 827–837, 1989. 16, 17

[97] A. E. Slemp and R. E. Kirschner, "Keloids and scars: a review of keloids and scars, their pathogenesis, risk factors, and management," *Current Opinion in Pediatrics*, vol. 18, p. 396–402, 2006. 16

[98] C. J. Chike-Obi, P. D. Cole, and A. E. Brissett, "Keloids: pathogenesis, clinical features, and management," in *Seminars in plastic surgery*, vol. 23, pp. 178–184, © Thieme Medical Publishers, 2009. 16

[99] F. B. Niessen, P. H. Spauwen, J. Schalkwijk, and M. Kon, "On the nature of hypertrophic scars and keloids: a review," *Plastic and Reconstructive Surgery*, vol. 104, no. 5, pp. 1435–1458, 1999. 16

[100] M. Hillmer and S. MacLeod, "Experimental keloid scar models: a review of methodological issues," *Journal of Cutaneous Medicine and Surgery: Incorporating Medical and Surgical Dermatology*, vol. 6, no. 4, pp. 354–359, 2002. 16

[101] Z. Wang, Z. Gao, Y. Shi, Y. Sun, Z. Lin, H. Jiang, T. Hou, Q. Wang, X. Yuan, X. Zhu, *et al.*, "Inhibition of smad3 expression decreases collagen synthesis in keloid disease fibroblasts," *Journal of Plastic, Reconstructive & Aesthetic Surgery*, vol. 60, no. 11, pp. 1193–1199, 2007. 16

[102] S. Davidson, N. Aziz, R. M. Rashid, and A. Khachemoune, "A primary care perspective on keloids," *The Medscape Journal of Medicine*, vol. 11, no. 1, p. 18, 2009. 17

[103] A. Gefen, *Bioengineering research of chronic wounds: a multidisciplinary study approach*, vol. 1. Springer Science & Business Media, 2009. 17

[104] J. Chambert, L. Zhao, D. Remache, and E. Jacquet, "Numerical analysis of keloid scar in the presternal area," *Computer Methods in Biomechanics and Biomedical Engineering*, vol. 15, no. sup1, pp. 23–24, 2012. 17, 19

[105] H. Jiao, T. Zhang, J. Fan, and R. Xiao, "The superficial dermis may initiate keloid formation: histological analysis of the keloid dermis at different depths," *Frontiers in Physiology*, vol. 8, p. 885, 2017. 17

[106] J. Chambert, T. Lihoreau, S. Joly, B. Chatelain, P. Sandoz, P. Humbert, E. Jacquet, and G. Rolin, "Multimodal investigation of a keloid scar by combining mechanical tests in vivo with diverse imaging techniques," *Journal of the Mechanical Behavior of Biomedical Materials*, vol. 99, pp. 206–215, 07 2019. 17, 20, 38, 51, 55, 61, 102, 108, 109, 110, 118, 138

[107] R. Ogawa, K. Okai, F. Tokumura, K. Mori, Y. Ohmori, C. Huang, H. Hyakusoku, and S. Akaishi, "The relationship between skin stretching/contraction and pathologic scarring: the important role of mechanical forces in keloid generation," *Wound Repair and Regeneration*, vol. 20, no. 2, pp. 149–157, 2012. 17, 18

[108] A. Abdel-Fattah, "The evolution of pre-sternal keloids," *British Journal of Plastic Surgery*, vol. 29, no. 1, pp. 56–58, 1976. 17, 19

[109] A. Bayat, G. Arscott, W. Ollier, M. Ferguson, and D. Mc Grouther, "Description of site-specific morphology of keloid phenotypes in an afrocaribbean population," *British Journal of Plastic Surgery*, vol. 57, no. 2, pp. 122–133, 2004. 18

[110] E. S. Pozos, *The effect of skin tension on the formation of keloid scars*. PhD thesis, School of Meterials, The University of Manchester, Manchester, UK, 2014. 18

[111] S. Akaishi, M. Akimoto, R. Ogawa, and H. Hyakusoku, "The relationship between keloid growth pattern and stretching tension: Visual analysis using the finite element method," *Annals of Plastic Surgery*, vol. 60, 2008. 18, 19, 118

[112] T. Nagasao, N. Aramaki-Hattori, Y. Shimizu, S. Yoshitatsu, N. Takano, and K. Kishi, "Transformation of keloids is determined by stress occurrence patterns on peri-keloid regions in response to body movement," *Medical Hypotheses*, vol. 81, no. 1, pp. 136–141, 2013. 18

[113] A. Al-Attar, S. Mess, J. M. Thomassen, C. L. Kauffman, and S. P. Davison, "Keloid pathogenesis and treatment," *Plastic and Reconstructive Surgery*, vol. 117, no. 1, 2006. 18

[114] M. H. Gold, T. D. Foster, M. A. Adair, K. Burlison, and T. Lewis, "Prevention of hypertrophic scars and keloids by the prophylactic use of topical silicone gel sheets following a surgical procedure in an office setting," *Dermatologic Surgery*, vol. 27, no. 7, pp. 641–644, 2001. 18

[115] J.-A. M. Atkinson, K. T. McKenna, A. G. Barnett, D. J. McGrath, and M. Rudd, "A randomized, controlled trial to determine the efficacy of paper tape in preventing hypertrophic scar formation in surgical incisions that traverse langer's skin tension lines," *Plastic and Reconstructive Surgery*, vol. 116, no. 6, pp. 1648–1656, 2005. 18

[116] T. Lihoreau, B. Chatelain, G. Rolin, C. Vidal, N. Butterlin, E. Jacquet, A. Elouneg, J. Chambert, X. Bertrand, C. Meyer, *et al.*, "End-user need based creation of a medical device: an experience of co-design to struggle pathological scars," in *International Joint Conference on Biomedical Engineering Systems and Technologies*, 2020. 18, 125

[117] T. S. Ellenbecker, M. De Carlo, and C. DeRosa, *Effective functional progressions in sport rehabilitation*. Human Kinetics, 2009. 18

[118] K. Morooka, S. Sonoki, R. Kurazume, and T. Hasegawa, "A method for estimating patient specific parameters for simulation of tissue deformation by finite element analysis," in *International Work-Conference on the Interplay Between Natural and Artificial Computation*, pp. 113–120, Springer, 2013. 19

[119] J. W. Jor, M. D. Parker, A. J. Taberner, M. P. Nash, and P. M. Nielsen, "Computational and experimental characterization of skin mechanics: identifying current challenges and future directions," *Wiley Interdisciplinary Reviews: Systems Biology and Medicine*, vol. 5, no. 5, pp. 539–556, 2013. 19

[120] S. Avril and S. Evans, eds., *Material Parameter Identification and Inverse Problems in Soft Tissue Biomechanics*. Springer International Publishing, 2017. 19, 33

[121] T. Krusche and W.-I. Worret, "Mechanical properties of keloids in vivo during treatment with intralesional triamcinolone acetonide," *Archives of Dermatological Research*, vol. 287, no. 3, pp. 289–293, 1995. 20

[122] D. T. Corr, C. L. Gallant-Behm, N. G. Shrive, and D. A. Hart, "Biomechanical behavior of scar tissue and uninjured skin in a porcine model," *Wound Repair and Regeneration*, vol. 17, no. 2, pp. 250–259, 2009. 20

[123] J. Chambert, T. Lihoreau, S. Joly, B. Chatelain, E. Jacquet, and G. Rolin, "Experimental analysis of a keloid on upper arm by using biomechanical devices," in *International Keloid Symposium*, (Rome, Italy), June 2018. 20

[124] A. Elouneg, Q. Lucot, E. Veyrat-Durebex, A. Lejeune, J. Chambert, T. Lihoreau, B. Chatelain, G. Rolin, and E. Jacquet, "Biomechanical characterization of earlobe keloid by ring suction test," *Computer Methods in Biomechanics and Biomedical Engineering*, vol. 23, no. sup1, pp. S99–S100, 2020. 20, 22, 131

[125] B. Mueller, J. Elrod, O. Distler, C. Schiestl, and E. Mazza, "On the reliability of suction measurements for skin characterization," *Journal of Biomechanical Engineering*, vol. 143, no. 2, 2021. 20, 23

[126] A. Pissarenko and M. A. Meyers, "The materials science of skin: Analysis, characterization, and modeling," *Progress in Materials Science*, vol. 110, p. 100634, 2020. 20

[127] W. A. Sodeman and G. E. Burch, "A direct method for the estimation of skin distensibility with its application to the study of vascular states," *The Journal of Clinical Investigation*, vol. 17, no. 6, pp. 785–793, 1938. 20

[128] P. Wijn, A. Brakkee, G. Stienen, and A. Vendrik, "Mechanical properties of the human skin in vivo for small deformations; a comparison of uniaxial strain and torsion measurements," in *Bed sore biomechanics*, pp. 103–108, Springer, 1976. 20, 24, 52, 138, 149

[129] T. Burlin, W. Hutton, and H. Ranu, "A method of in vivo measurement of the elastic properties of skin in radiotherapy patients," *Journal of Investigative Dermatology*, vol. 69, no. 3, 1977. 20, 51

[130] H. Stark, "Directional variations in the extensibility of human skin," *British Journal of Plastic Surgery*, vol. 30, no. 2, pp. 105–114, 1977. 20, 21

[131] J. F. M. Manschot and A. Brakkee, "The measurement and modelling of the mechanical properties of human skin in vivo—i. the measurement," *Journal of Biomechanics*, vol. 19, no. 7, pp. 511–515, 1986. 20, 21, 51, 138

[132] J. Manschot and A. Brakkee, "The measurement and modelling of the mechanical properties of human skin in vivo—ii. the model," *Journal of Biomechanics*, vol. 19, no. 7, pp. 517–521, 1986. 20, 138, 149

[133] R. Meijer, L. F. A. Douven, and C. W. J. Oomens, "Characterisation of anisotropic and non-linear behaviour of human skin in vivo," *Computer Methods in Biomechanics and Biomedical Engineering*, vol. 2, no. 1, pp. 13–27, 1999. 20, 21, 26, 54, 138

[134] F. Khatyr, C. Imberdis, P. Vescovo, D. Varchon, and J.-M. Lagarde, "Model of the viscoelastic behaviour of skin in vivo and study of anisotropy," *Skin Research and Technology*, vol. 10, no. 2, pp. 96–103, 2004. 20, 21, 138, 141, 149

[135] E. Jacquet, G. Josse, F. Khatyr, and C. Garcin, "A new experimental method for measuring skin's natural tension," *Skin Research and Technology*, vol. 14, no. 1, pp. 1–7, 2008. 20, 51, 138

[136] S. L. Evans and C. A. Holt, "Measuring the mechanical properties of human skin in vivo using digital image correlation and finite element modelling," *The Journal of Strain Analysis for Engineering Design*, vol. 44, no. 5, pp. 337–345, 2009. 20, 37, 46, 54

[137] J. Mahmud, C. A. Holt, and S. L. Evans, "An innovative application of a small-scale motion analysis technique to quantify human skin deformation in vivo," *Journal of Biomechanics*, vol. 43, no. 5, pp. 1002–1006, 2010. 20

[138] G. Boyer, *Modelisation du comportement mecanique de la peau humaine in vivo : application au vieillissement et aux gestes du clinicien*. Theses, Ecole Nationale Supérieure des Mines de Saint-Etienne, July 2010. 20

[139] C. Flynn, A. Taberner, and P. Nielsen, "Mechanical characterisation of in vivo human skin using a 3d force-sensitive micro-robot and finite element analysis," *Biomechanics and Modeling in Mechanobiology*, vol. 10, no. 1, pp. 27–38, 2011. 20, 37, 54, 110, 149

[140] L. Coutts, J. Bamber, and N. Miller, "Multi-directional in vivo tensile skin stiffness measurement for the design of a reproducible tensile strain elastography protocol," *Skin Research and Technology*, vol. 19, no. 1, pp. e37–e44. 20, 21

[141] G. Boyer, J. Molimard, M. B. Tkaya, H. Zahouani, M. Pericoi, and S. Avril, "Assessment of the in-plane biomechanical properties of human skin using a finite element model updating approach combined with an optical full-field measurement on a new tensile device," *Journal of the Mechanical Behavior of Biomedical Materials*, vol. 27, pp. 273–282, 2013. 20, 24, 46, 54, 138, 149

[142] E. Jacquet, S. Joly, J. Chambert, K. Rekik, and P. Sandoz, "Ultra-light extensometer for the assessment of the mechanical properties of the human skin in vivo," *Skin Research and Technology*, vol. 23, no. 4, pp. 531–538, 2017. 20, 21, 58, 59

[143] E. Jacquet, J. Chambert, J. Pauchot, and P. Sandoz, "Intra-and inter-individual variability in the mechanical properties of the human skin from in vivo measurements on 20 volunteers," *Skin Research and Technology*, vol. 23, no. 4, pp. 491–499, 2017. 20, 135

185

[144] K. Lim, C. Chew, P. Chen, S. Jeyapalina, H. Ho, J. Rappel, and B. Lim, "New extensometer to measure in vivo uniaxial mechanical properties of human skin," *Journal of Biomechanics*, vol. 41, no. 5, pp. 931–936, 2008. 21

[145] R. Reihsner and E. Menzel, "On the orthogonal anisotropy of human skin as a function of anatomical region," *Connective Tissue Research*, vol. 34, no. 2, pp. 145–160, 1996. 21

[146] Y. A. Kvistedal and P. M. F. Nielsen, "Estimating material parameters of human skin in vivo," *Biomechanics and Modeling in Mechanobiology*, vol. 8, pp. 1–8, Nov. 2007. 21, 46, 54, 129

[147] J. Serup, G. B. Jemec, and G. L. Grove, *Handbook of Non-Invasive Methods and the Skin*. CRC press, 2006. 21, 22

[148] D. Laiacona, J. Cohen, K. Coulon, Z. Lipsky, C. Maiorana, R. Boltyanskiy, E. Dufresne, and G. German, "Non-invasive in vivo quantification of human skin tension lines," *Acta Biomaterialia*, vol. 88, pp. 141–148, 2019. 22, 130

[149] "CutiScan." https://www.courage-khazaka.de/en/16-wissenschaftliche-produkte/alle-produkte/179-cutiscan-e. Accessed: 2023-02-13. 22, 130

[150] C. Rosado, F. Antunes, R. Barbosa, R. Fernando, and L. M. Rodrigues, "Cutiscan®-a new system of biomechanical evaluation of the skin in vivo-comparative study of use depending on the anatomical site," *Biomedical and Biopharmaceutical Research*, vol. 12, no. 1, pp. 49–57, 2015. 22

[151] C. Rosado, F. Antunes, R. Barbosa, R. Fernando, M. Estudante, H. N. Silva, and L. M. Rodrigues, "About the in vivo quantitation of skin anisotropy," *Skin Research and Technology*, vol. 23, no. 3, pp. 429–436, 2017. 22, 156, 161

[152] H. Silva, R. Francisco, and L. Rodrigues, "Texture analysis is a useful tool to characterize the cutaneous biomechanical profile: A análise de textura é uma ferramenta útil para caracterizar o perfil biomecânico cutâneo," *Journal Biomedical and Biopharmaceutical Research*, vol. 16, pp. 188–194, 12 2019. 22

[153] M. A. Kim, Y. C. Jung, and E. J. Kim, "Evaluation of anisotropic properties of striae distensae with regard to skin surface texture and viscoelasticity," *Skin Research and Technology*, vol. 26, no. 2, pp. 220–225, 2020. 22

[154] M. Anthonissen, E. Van den Kerckhove, P. Moortgat, I. Geraerts, N. Devoogdt, T. De Vrieze, and A. De Groef, "Can the CutiScan CS 100® measure anisotropy and viscoelasticity in scar tissue after mastectomy? a reliability and validity study," *Skin Research and Technology*, vol. 28, no. 2, pp. 246–253, 2022. 22, 156

[155] H. Schade, "Untersuchungen zur organfunction des bindegewebes," *Zeitschrift für Experimentelle Pathologie und Therapie*, vol. 11, no. 3, pp. 369–399, 1912. 22

[156] J. Kirk and M. Chieffi, "Variation with age in elasticity of skin and subcutaneous tissue in human individuals," *Journal of Gerontology*, vol. 17, no. 4, pp. 373–380, 1962. 22

[157] S. Dikstein and A. Hartzshtark, "In vivo measurement of some elastic properties of human skin," in *Bioengineering and the Skin*, pp. 45–53, Springer, 1981. 22

[158] D. Bader and P. Bowker, "Mechanical characteristics of skin and underlying tissues in vivo," *Biomaterials*, vol. 4, no. 4, pp. 305–308, 1983. 22

[159] Y. Lanir, V. Manny, A. Zlotogorski, A. Shafran, and S. Dikstein, "Influence of ageing on the in vivo mechanics of the skin," *Skin Pharmacology and Physiology*, vol. 6, no. 3, pp. 223–230, 1993. 22

[160] Y. Zheng and A. F. Mak, "Effective elastic properties for lower limb soft tissues from manual indentation experiment," *IEEE Transactions on Rehabilitation Engineering*, vol. 7, no. 3, pp. 257–267, 1999. 22

[161] J. Jachowicz, R. McMullen, and D. Prettypaul, "Indentometric analysis of in vivo skin and comparison with artificial skin models," *Skin Research and Technology*, vol. 13, no. 3, pp. 299–309, 2007. 22

[162] A. Delalleau, G. Josse, J.-M. Lagarde, H. Zahouani, and J.-M. Bergheau, "A nonlinear elastic behavior to identify the mechanical parameters of human skin in vivo," *Skin Research and Technology*, vol. 14, no. 2, pp. 152–164, 2008. 22, 23, 50, 51

[163] K. Khaothong, "In vivo measurements of the mechanical properties of human skin and muscle by inverse finite element method combined with the indentation test," in *6th World Congress of Biomechanics (WCB 2010). August 1-6, 2010 Singapore*, pp. 1467–1470, Springer, 2010. 22, 46, 54

[164] J. T. Iivarinen, R. K. Korhonen, P. Julkunen, and J. S. Jurvelin, "Experimental and computational analysis of soft tissue stiffness in forearm using a manual indentation device," *Medical Engineering & Physics*, vol. 33, no. 10, pp. 1245–1253, 2011. 22, 36, 46, 54

[165] H. Zahouani, G. Boyer, C. Pailler-Mattei, M. B. Tkaya, and R. Vargiolu, "Effect of human ageing on skin rheology and tribology," *Wear*, vol. 271, no. 9-10, pp. 2364–2369, 2011. 22

[166] C. Pailler-Mattei, R. Debret, R. Vargiolu, P. Sommer, and H. Zahouani, "In vivo skin biophysical behaviour and surface topography as a function of ageing," *Journal of the Mechanical Behavior of Biomedical Materials*, vol. 28, pp. 474–483, 2013. 22

[167] L. Zhou, S. Wang, J. Zhang, J. Wang, and C. Li, "In vivo measurement of the anisotropic mechanical properties of human skin by indentation test," *Mechanics of Materials*, vol. 158, p. 103851, 2021. 22, 23, 52, 140, 151

[168] G. Boyer, C. P. Mattei, J. Molimard, M. Pericoi, S. Laquieze, and H. Zahouani, "Non contact method for in vivo assessment of skin mechanical properties for assessing effect of ageing," *Medical Engineering & Physics*, vol. 34, no. 2, pp. 172–178, 2012. 22

[169] C. Thieulin, C. Pailler-Mattei, A. Abdouni, M. Djaghloul, and H. Zahouani, "Mechanical and topographical anisotropy for human skin: Ageing effect," *Journal of the Mechanical Behavior of Biomedical Materials*, vol. 103, p. 103551, 2020. 22

[170] C. Pailler-Mattei and H. Zahouani, "Study of adhesion forces and mechanical properties of human skin in vivo," *Journal of Adhesion Science and Technology*, vol. 18, no. 15-16, pp. 1739–1758, 2004. 22

[171] Y.-P. Zheng and A. F. Mak, "An ultrasound indentation system for biomechanical properties assessment of soft tissues in-vivo," *IEEE Transactions on Biomedical Engineering*, vol. 43, no. 9, pp. 912–918, 1996. 22, 52

[172] H.-V. Tran, *Caractérisation des propriétés mécaniques de la peau humaine in vivo via l'IRM*. PhD thesis, Université de Technologie de Compiègne, 2007. 22

[173] A. Pissarenko, *The Materials Science of Skin: Experimental Characterization, Constitutive Modeling, and Tear Resistance*. PhD thesis, UC San Diego, 2019. 23

[174] R. Grahame and P. Holt, "The influence of ageing on the in vivo elasticity of human skin," *Gerontology*, vol. 15, no. 2-3, pp. 121–139, 1969. 23

[175] T. Cook, H. Alexander, and M. Cohen, "Experimental method for determining the 2-dimensional mechanical properties of living human skin," *Medical and Biological Engineering and Computing*, vol. 15, no. 4, pp. 381–390, 1977. 23

[176] P. Elsner, A. Barel, E. Berardesca, B. Gabard, and J. Serup, "Mechanical function of the skin: state of the art," *Skin Bioengineering: Techniques and Applications in Dermatology and Cosmetology*, vol. 26, pp. 69–83, 1998. 23, 51

[177] S. Diridollou, F. Patat, F. Gens, L. Vaillant, D. Black, J. M. Lagarde, Y. Gall, and M. Berson, "In vivo model of the mechanical properties of the human skin under suction," *Skin Research and Technology*, vol. 6, no. 4, pp. 214–221, 2000. 23, 52

[178] F. Hendriks, D. v. Brokken, J. Van Eemeren, C. Oomens, F. Baaijens, and J. Horsten, "A numerical-experimental method to characterize the non-linear mechanical behaviour of human skin," *Skin Research and Technology*, vol. 9, no. 3, pp. 274–283, 2003. 23, 54

[179] L. Pedersen, B. Hansen, and G. Jemec, "Mechanical properties of the skin: a comparison between two suction cup methods," *Skin Research and Technology*, vol. 9, no. 2, pp. 111–115, 2003. 23

[180] F. Hendriks, D. Brokken, C. Oomens, and F. Baaijens, "Influence of hydration and experimental length scale on the mechanical response of human skin in vivo, using optical coherence tomography," *Skin Research and Technology*, vol. 10, no. 4, pp. 231–241, 2004. 23

[181] F. Hendriks, D. Brokken, C. Oomens, D. Bader, and F. Baaijens, "The relative contributions of different skin layers to the mechanical behavior of human skin in vivo using suction experiments," *Medical Engineering & Physics*, vol. 28, no. 3, pp. 259–266, 2006. 23

[182] A. O. Barel, W. Courage, and P. Clarys, "Suction chamber method for measurement of skin mechanics: The new digital version of the cutometer," in *Handbook of Non-Invasive Methods and the Skin*, pp. 583–591, CRC press, 2006. 23

[183] A. Sutradhar and M. J. Miller, "In vivo measurement of breast skin elasticity and breast skin thickness," *Skin Research and Technology*, vol. 19, no. 1, pp. e191–e199, 2013. 23

[184] S. Badir, M. Bajka, and E. Mazza, "A novel procedure for the mechanical characterization of the uterine cervix during pregnancy," *Journal of the Mechanical Behavior of Biomedical Materials*, vol. 27, pp. 143–153, 2013. 23

[185] J. Weickenmeier, M. Jabareen, and E. Mazza, "Suction based mechanical characterization of superficial facial soft tissues," *Journal of Biomechanics*, vol. 48, no. 16, pp. 4279–4286, 2015. 23, 46, 54

[186] B. Müller, J. Elrod, M. Pensalfini, R. Hopf, O. Distler, C. Schiestl, and E. Mazza, "A novel ultra-light suction device for mechanical characterization of skin," *PLOS One*, vol. 13, pp. 1–22, 08 2018. 23

[187] B. Müller, L. Ruby, S. Jordan, M. B. Rominger, E. Mazza, and O. Distler, "Validation of the suction device nimble for the assessment of skin fibrosis in systemic sclerosis," *Arthritis Research & Therapy*, vol. 22, no. 1, pp. 1–10, 2020. 23

[188] N. Briot, G. Chagnon, N. Connesson, and Y. Payan, "In vivo measurement of breast tissues stiffness using a light aspiration device," *Clinical Biomechanics*, p. 105743, 2022. 23

[189] S. A. Elahi, *In-vivo and In-situ mechanical characterisation of soft living tissues*. PhD thesis, Université Grenoble Alpes, 2018. 23

[190] "Cutometer." https://www.courage-khazaka.de/en/scientific-products/all-products/16-wissenschaftliche-produkte/alle-produkte/266-cutometer-new-e. Accessed: 2022-07-21. 23, 24

[191] S. Diridollou, M. Berson, V. Vabre, D. Black, B. Karlsson, F. Auriol, J. Gregoire, C. Yvon, L. Vaillant, Y. Gall, and F. Patat, "An in vivo method for measuring the mechanical properties of the skin using ultrasound," *Ultrasound in Medicine & Biology*, vol. 24, no. 2, pp. 215–224, 1998. 23

[192] P. Neto, M. Ferreira, F. Bahia, and P. Costa, "Improvement of the methods for skin mechanical properties evaluation through correlation between different techniques and factor analysis," *Skin Research and Technology*, vol. 19, no. 4, pp. 405–416, 2013. 23

[193] T. K. Tonge, L. S. Atlan, L. M. Voo, and T. D. Nguyen, "Full-field bulge test for planar anisotropic tissues: Part i – experimental methods applied to human skin tissue," *Acta Biomaterialia*, vol. 9, no. 4, pp. 5913–5925, 2013. 23, 51

[194] P. G. Agache, "Twistometry measurement of skin elasticity," pp. 601–610, CRC press, 2nd edition, 2006. 24

[195] R. Sanders, "Torsional elasticity of human skin in vivo," *Pflügers Archiv*, vol. 342, no. 3, pp. 255–260, 1973. 24, 52

[196] P. G. Agache, C. Monneur, J. L. Lévêque, and J. De Rigal, "Mechanical properties and young's modulus of human skin in vivo," *Archives of Dermatological Research*, vol. 269, no. 3, pp. 221–232, 1980. 24, 52

[197] S. Catheline, J.-L. Gennisson, G. Delon, M. Fink, R. Sinkus, S. Abouelkaram, and J. Culioli, "Measurement of viscoelastic properties of homogeneous soft solid using transient elastography: An inverse problem approach," *The Journal of the Acoustical Society of America*, vol. 116, no. 6, pp. 3734–3741, 2004. 24

[198] A. Sarvazyan, T. J Hall, M. W Urban, M. Fatemi, S. R Aglyamov, and B. S Garra, "An overview of elastography-an emerging branch of medical imaging," *Current Medical Imaging*, vol. 7, no. 4, pp. 255–282, 2011. 24

[199] L. Drehfal, "170 - elasticity imaging in obstetrics," in *Obstetric Imaging: Fetal Diagnosis and Care (Second Edition)* (J. A. Copel, M. E. D'Alton, H. Feltovich, E. Gratacós, D. Krakow, A. O. Odibo, L. D. Platt, and B. Tutschek, eds.), pp. 696–700.e1, Elsevier, second edition ed., 2018. 24

[200] S. Gahagnon, Y. Mofid, G. Josse, and F. Ossant, "Skin anisotropy in vivo and initial natural stress effect: A quantitative study using high-frequency static elastography," *Journal of Biomechanics*, vol. 45, no. 16, pp. 2860–2865, 2012. 24

[201] M. A. Kirby, P. Tang, H.-C. Liou, M. Kuriakose, J. J. Pitre, T. N. Pham, R. E. Ettinger, R. K. Wang, M. O'Donnell, and I. Pelivanov, "Probing elastic anisotropy of human skin in vivo with light using non-contact acoustic micro-tapping oce and polarization sensitive oct," *Scientific Reports*, vol. 12, no. 1, pp. 1–17, 2022. 24, 149

[202] S. Nickell, M. Hermann, M. Essenpreis, T. J. Farrell, U. Krämer, and M. S. Patterson, "Anisotropy of light propagation in human skin," *Physics in Medicine and Biology*, vol. 45, pp. 2873–2886, sep 2000. 25, 129

[203] S. Sakai, M. Yamanari, Y. Lim, N. Nakagawa, and Y. Yasuno, "In vivo evaluation of human skin anisotropy by polarization-sensitive optical coherence tomography," *Biomedical Optics Express*, vol. 2, pp. 2623–2631, Sep 2011. 25

[204] D. Sergachev, D. Matthews, and E. Van Der Heide, "An empirical approach for the determination of skin elasticity: Finger pad friction against textured surfaces," *Biotribology*, vol. 18, p. 100097, 2019. 25

[205] "Bls780 - ballistometer." `http://www.dproscientific.com/dia-stron-bls780.html`. Accessed: 2022-07-27. 25

[206] A. Tosti, G. Compagno, M. L. Fazzini, and S. Villardita, "A ballistometer for the study of the plasto-elastic properties of skin.," *Journal of Investigative Dermatology*, vol. 69, no. 3, 1977. 25

[207] C. G. Fthenakis, D. H. Maes, W. P. Smith, and E. Lauder, "In vivo assessment of skin elasticity using ballistometry," *Journal of the Society of Cosmetic Chemists*, vol. 42, pp. 211–222, 1991. 25

[208] G. B. Jemec, E. Selvaag, M. Ågren, and H. C. Wulf, "Measurement of the mechanical properties of skin with ballistometer and suction cup," *Skin Research and Technology*, vol. 7, no. 2, pp. 122–126, 2001. 25

[209] C. G. Hargens, "ballistometry," pp. 627–632, CRC press, 2nd edition, 2006. 25

[210] M. Woo, K. Moon, H. Jung, S. Park, T. Moon, N. Kim, and B. Lee, "Comparison of skin elasticity test results from the ballistometer® and cutometer®," *Skin Research and Technology*, vol. 20, no. 4, pp. 422–428, 2014. 25

[211] G. B. E. Jemec, "Ballistometer," in *Non Invasive Diagnostic Techniques in Clinical Dermatology* (E. Berardesca, H. I. Maibach, and K.-P. Wilhelm, eds.), pp. 339–341, Berlin, Heidelberg: Springer Berlin Heidelberg, 2014. 25

[212] G. Pierard, "Investigating rheological properties of skin by applying a vertical pull," *Bioeng Skin Newsl*, vol. 2, p. 31, 1980. 25

[213] J. Barbenel and P. Payne, "In vivo mechanical testing of dermal properties," *Bioengineering and the Skin*, vol. 3, no. 1, pp. 8–38, 1981. 25

[214] P. A. Payne, "Measurement of properties and function of skin," *Clinical Physics and Physiological Measurement*, vol. 12, pp. 105–129, may 1991. 25, 26

[215] G. E. Box, "Science and statistics," *Journal of the American Statistical Association*, vol. 71, no. 356, pp. 791–799, 1976. 26

[216] A. Delalleau, *Analyse du comportement mécanique de la peau in vivo*. PhD thesis, Saint-Etienne, 2007. 27

[217] C. Wex, S. Arndt, A. Stoll, C. Bruns, and Y. Kupriyanova, "Isotropic incompressible hyperelastic models for modelling the mechanical behaviour of biological tissues: a review," *Biomedizinische Technik. Biomedical engineering*, vol. 60, p. 577—592, December 2015. 27

[218] G. Limbert, "Mathematical and computational modelling of skin biophysics: a review," *Proceedings of the Royal Society A: Mathematical, Physical and Engineering Sciences*, vol. 473, no. 2203, p. 20170257, 2017. 27, 35, 38

[219] G. A. Holzapfel, "Biomechanics of soft tissue," in *Handbook of Materials Behavior Models*, vol. 3, pp. 1057–1071, Academic Press San Diego, USA, 2001. 27, 28, 34

[220] Z.-W. Chen, P. Joli, and Z.-Q. Feng, "Anisotropic hyperelastic behavior of soft biological tissues," *Computer Methods in Biomechanics and Biomedical Engineering*, vol. 18, no. 13, pp. 1436–1444, 2015. 27

[221] R. Minns, P. Soden, and D. Jackson, "The role of the fibrous components and ground substance in the mechanical properties of biological tissues: a preliminary investigation," *Journal of Biomechanics*, vol. 6, no. 2, pp. 153–165, 1973. 28, 29

[222] C. S. Roy, "The elastic properties of the arterial wall," *The Journal of physiology*, vol. 3, no. 2, p. 125, 1881. 28

[223] G. A. Holzapfel, "Similarities between soft biological tissues and rubberlike materials," in *Constitutive models for rubber IV*, pp. 607–617, Routledge, 2017. 28, 36

[224] J. Diani, M. Brieu, J.-M. Vacherand, and A. Rezgui, "Directional model for isotropic and anisotropic hyperelastic rubber-like materials," *Mechanics of Materials*, vol. 36, no. 4, pp. 313–321, 2004. 29

[225] J. Bonet and R. D. Wood, "Introduction," in *Nonlinear Continuum Mechanics for Finite Element Analysis*, p. 1–21, Cambridge University Press, 2 ed., 2008. 29, 63

[226] J. Bonet and R. D. Wood, *Nonlinear continuum mechanics for finite element analysis*. Cambridge university press, 1997. 30, 31, 34, 35

[227] G. A. Holzapfel, *Nonlinear Solid Mechanics: A Continuum Approach for Engineering*. Chichester, UK: John Willey & Sons, 2000. 32, 33, 34, 35, 64

[228] O. Gonzalez and A. M. Stuart, *A first course in continuum mechanics*. Cambridge University Press, 2008. 32

[229] C. A. Miles and M. Ghelashvili, "Polymer-in-a-box mechanism for the thermal stabilization of collagen molecules in fibers," *Biophysical Journal*, vol. 76, no. 6, pp. 3243–3252, 1999. 33

[230] T. Stylianopoulos, A. Aksan, and V. H. Barocas, "A structural, kinetic model of soft tissue thermomechanics," *Biophysical Journal*, vol. 94, no. 3, pp. 717 – 725, 2008. 33

[231] G. Smith and R. S. Rivlin, "The anisotropic tensors," *Quarterly of Applied Mathematics*, vol. 15, no. 3, pp. 308–314, 1957. 34

[232] J.-P. Boehler, "A simple derivation of representations for non-polynomial constitutive equations in some cases of anisotropy," *ZAMM-Journal of Applied Mathematics and Mechanics*, vol. 59, no. 4, pp. 157–167, 1979. 34

[233] A. Spencer, "Theory of invariants, chapter continuum physics," 1971. 34

[234] G. Chagnon, J. Ohayon, J.-L. Martiel, and D. Favier, "Hyperelasticity modeling for incompressible passive biological tissues," in *Biomechanics of living organs*, pp. 3–30, Elsevier, 2017. 34, 36, 38

[235] J. Ericksen and R. Rivlin, "Large elastic deformations of homogeneous anisotropic materials," in *Collected Papers of RS Rivlin*, pp. 467–487, Springer, 1997. 34

[236] J. C. Criscione, A. S. Douglas, and W. C. Hunter, "Physically based strain invariant set for materials exhibiting transversely isotropic behavior," *Journal of the Mechanics and Physics of Solids*, vol. 49, no. 4, pp. 871–897, 2001. 34

[237] R. Ogden, G. Saccomandi, and I. Sgura, "Fitting hyperelastic models to experimental data," *Computational Mechanics*, vol. 34, 11 2004. 35

[238] G. Franceschini and S. Macchietto, "Model-based design of experiments for parameter precision: State of the art," *Chemical Engineering Science*, vol. 63, no. 19, pp. 4846–4872, 2008. 35

[239] W. Maurel, D. Thalmann, Y. Wu, and N. M. Thalmann, *Biomechanical models for soft tissue simulation*, vol. 48. Springer, 1998. 36

[240] P. A. L. S. Martins, R. M. Natal Jorge, and A. J. M. Ferreira, "A comparative study of several material models for prediction of hyperelastic properties: Application to silicone-rubber and soft tissues," *Strain*, vol. 42, no. 3, pp. 135–147, 2006. 36

[241] G. Puglisi and G. Saccomandi, "Multi-scale modelling of rubber-like materials and soft tissues: <i>an appraisal</i>," *Proceedings of the Royal Society A: Mathematical, Physical and Engineering Sciences*, vol. 472, no. 2187, p. 20160060, 2016. 36, 39, 41, 42

[242] M. Mooney, "A theory of large elastic deformation," *Journal of Applied Physics*, vol. 11, no. 9, pp. 582–592, 1940. 36

[243] R. Rivlin, "Large elastic deformations of isotropic materials iv. further developments of the general theory," *Philosophical Transactions of the Royal Society of London. Series A, Mathematical and Physical Sciences*, vol. 241, no. 835, pp. 379–397, 1948. 36

[244] A. F. Bower, *Applied mechanics of solids*. CRC press, 2009. 36

[245] Y. K. Wang, M. P. Nash, A. J. Pullan, J. A. Kieser, and O. Röhrle, "Model-based identification of motion sensor placement for tracking retraction and elongation of the tongue," *Biomechanics and Modeling in Mechanobiology*, vol. 12, no. 2, pp. 383–399, 2013. 36

[246] G. G. Barbarino, M. Jabareen, and E. Mazza, "Experimental and numerical study on the mechanical behavior of the superficial layers of the face," *Skin Research and Technology*, vol. 17, no. 4, pp. 434–444, 2011. 36

[247] D. Lemmon, T. Shiang, A. Hashmi, J. S. Ulbrecht, and P. R. Cavanagh, "The effect of insoles in therapeutic footwear—a finite element approach," *Journal of Biomechanics*, vol. 30, no. 6, pp. 615–620, 1997. 36

[248] M. Dreischarf, T. Zander, A. Shirazi-Adl, C. Puttlitz, C. Adam, C. Chen, V. Goel, A. Kiapour, Y. Kim, K. Labus, J. Little, W. Park, Y. Wang, H. Wilke, A. Rohlmann, and H. Schmidt, "Comparison of eight published static finite element models of the intact lumbar spine: Predictive power of models improves when combined together," *Journal of Biomechanics*, vol. 47, no. 8, pp. 1757–1766, 2014. 36

[249] Y. Payan and J. Ohayon, *Biomechanics of living organs: hyperelastic constitutive laws for finite element modeling*. World Bank Publications, 2017. 36, 37

[250] E. W. V. Chaves, "Hyperelasticity," in *Notes on Continuum Mechanics*, pp. 423–464, Dordrecht: Springer Netherlands, 2013. 36

[251] S. K. Melly, L. Liu, Y. Liu, and J. Leng, "A review on material models for isotropic hyperelasticity," *International Journal of Mechanical System Dynamics*, vol. 1, no. 1, pp. 71–88, 2021. 36, 37, 38, 39, 117

[252] L. Bouten, *Identification des propriétés mécaniques des tissus constitutifs du mollet pour l'étude mécanique de la contention*. Theses, Ecole Nationale Supérieure des Mines de Saint-Etienne, Mar. 2009. 181 pages. 36

[253] V. Luboz, A. Perrier, M. Bucki, B. Diot, F. Cannard, N. Vuillerme, and Y. Payan, "Influence of the calcaneus shape on the risk of posterior heel ulcer using 3d patient-specific biomechanical modeling," *Annals of Biomedical Engineering*, vol. 43, no. 2, pp. 325–335, 2015. 36

[254] L. Han, J. H. Hipwell, B. Eiben, D. Barratt, M. Modat, S. Ourselin, and D. J. Hawkes, "A nonlinear biomechanical model based registration method for aligning prone and supine mr breast images," *IEEE Transactions on Medical Imaging*, vol. 33, no. 3, p. 682 – 694, 2014. Cited by: 52. 36

[255] O. H. Yeoh, "Characterization of elastic properties of carbon-black-filled rubber vulcanizates," *Rubber Chemistry and Technology*, vol. 63, no. 5, pp. 792–805, 1990. 36

[256] J. Gerard, J. Ohayon, V. Luboz, P. Perrier, and Y. Payan, "Non-linear elastic properties of the lingual and facial tissues assessed by indentation technique: Application to the biomechanics of speech production," *Medical Engineering & Physics*, vol. 27, no. 10, pp. 884–892, 2005. Advances in the finite element modelling of soft tissue deformation. 36

[257] A. N. Gent, "A new constitutive relation for rubber," *Rubber Chemistry and Technology*, vol. 69, no. 1, pp. 59–61, 1996. 36, 38

[258] C. O. Horgan and G. Saccomandi, "A description of arterial wall mechanics using limiting chain extensibility constitutive models," *Biomechanics and Modeling in Mechanobiology*, vol. 1, pp. 251–266, Apr. 2003. 36

[259] A. E. Ehret and M. Itskov, "A polyconvex hyperelastic model for fiber-reinforced materials in application to soft tissues," *Journal of Materials Science*, vol. 42, no. 21, pp. 8853–8863, 2007. 36

[260] M. Destrade, A. Ní Annaidh, and C. D. Coman, "Bending instabilities of soft biological tissues," *International Journal of Solids and Structures*, vol. 46, no. 25, pp. 4322–4330, 2009. 36

[261] B. Rashid, M. Destrade, and M. D. Gilchrist, "Mechanical characterization of brain tissue in simple shear at dynamic strain rates," *Journal of the Mechanical Behavior of Biomedical Materials*, vol. 28, pp. 71 – 85, 2013. 36, 117

[262] B. Rashid, M. Destrade, and M. D. Gilchrist, "Mechanical characterization of brain tissue in tension at dynamic strain rates," *Journal of the Mechanical Behavior of Biomedical Materials*, vol. 33, pp. 43–54, 2014. Forensic Biomechanics. 36

[263] L. A. Mihai, L. Chin, P. A. Janmey, and A. Goriely, "A comparison of hyperelastic constitutive models applicable to brain and fat tissues," *Journal of The Royal Society Interface*, vol. 12, no. 110, p. 20150486, 2015. 36

[264] D. Garcia-Gonzalez, A. Jérusalem, S. Garzon-Hernandez, R. Zaera, and A. Arias, "A continuum mechanics constitutive framework for transverse isotropic soft tissues," *Journal of the Mechanics and Physics of Solids*, vol. 112, pp. 209–224, 2018. 36

[265] Z.-W. Chen, *Simulation numérique du comportement dynamique des organes pelviens*. PhD thesis, Evry-Val d'Essonne, 2013. 36

[266] A. Elouneg, D. Sutula, J. Chambert, A. Lejeune, S. Bordas, and E. Jacquet, "An open-source fenics-based framework for hyperelastic parameter estimation from noisy full-field data: Application to heterogeneous soft tissues," *Computers & Structures*, vol. 255, p. 106620, 2021. 36, 63, 73, 79, 84, 85, 87, 92, 93, 94, 96, 97, 98, 99

[267] R. W. Ogden and R. Hill, "Large deformation isotropic elasticity: on the correlation of theory and experiment for compressible rubberlike solids," *Proceedings of the Royal Society of London. A. Mathematical and Physical Sciences*, vol. 328, no. 1575, pp. 567–583, 1972. 37

[268] L. Treloar, "Stress-strain data for vulcanized rubber under various types of deformation," *Rubber Chemistry and Technology*, vol. 17, no. 4, pp. 813–825, 1944. 37

[269] O. Yeoh, "On the ogden strain-energy function," *Rubber Chemistry and Technology*, vol. 70, no. 2, pp. 175–182, 1997. 37

[270] K. Laksari, M. Shafieian, and K. Darvish, "Constitutive model for brain tissue under finite compression," *Journal of Biomechanics*, vol. 45, no. 4, pp. 642–646, 2012. 37

[271] T. C. Gasser, G. Görgülü, M. Folkesson, and J. Swedenborg, "Failure properties of intraluminal thrombus in abdominal aortic aneurysm under static and pulsating mechanical loads," *Journal of Vascular Surgery*, vol. 48, no. 1, pp. 179–188, 2008. 37

[272] T. Hu and J. P. Desai, "Characterization of soft-tissue material properties: large deformation analysis," in *International Symposium on Medical Simulation*, pp. 28–37, Springer, 2004. 37

[273] Y. Fung, "Elasticity of soft tissues in simple elongation," *American Journal of Physiology-Legacy Content*, vol. 213, no. 6, pp. 1532–1544, 1967. 37

[274] D. Veronda and R. Westmann, "Mechanical characterization of skin—finite deformations," *Journal of Biomechanics*, vol. 3, no. 1, pp. 111–124, 1970. 37

[275] H. Demiray, "Large Deformation Analysis of Some Soft Biological Tissues," *Journal of Biomechanical Engineering*, vol. 103, pp. 73–78, 05 1981. 37

[276] D. C. Drucker, "A definition of stable inelastic material," tech. rep., BROWN UNIV PROVIDENCE RI, 1957. 37

[277] R. Hill, "A general theory of uniqueness and stability in elastic-plastic solids," *Journal of the Mechanics and Physics of Solids*, vol. 6, no. 3, pp. 236 – 249, 1958. 37

[278] A. Johnson, C. Quigley, and J. Mead, "Large strain viscoelastic constitutive models for rubber, part i: Formulations," *Rubber chemistry and technology*, vol. 67, no. 5, pp. 904–917, 1994. 37

[279] Z. Guo and L. Sluys, "Application of a new constitutive model for the description of rubber-like materials under monotonic loading," *International Journal of Solids and Structures*, vol. 43, no. 9, pp. 2799–2819, 2006. 37

[280] J. R. Walton and J. P. Wilber, "Sufficient conditions for strong ellipticity for a class of anisotropic materials," *International journal of non-linear mechanics*, vol. 38, no. 4, pp. 441–455, 2003. 37

[281] H. Simpson and S. Spector, "On copositive matrices and strong ellipticity for isotropic elastic materials," 1982. 37

[282] L. Zee and E. Sternberg, "Ordinary and strong ellipticity in the equilibrium theory of incompressible hyperelastic solids," *Archive for Rational Mechanics and Analysis*, vol. 83, no. 1, pp. 53–90, 1983. 37

[283] G. Qiu and T. Pence, "Loss of ellipticity in plane deformation of a simple directionally reinforced incompressible nonlinearly elastic solid," *Journal of Elasticity*, vol. 49, no. 1, pp. 31–63, 1997. 37

[284] B. Wcisło, J. Pamin, K. Kowalczyk-Gajewska, and A. Menzel, "Numerical analysis of ellipticity condition for large strain plasticity," in *AIP Conference Proceedings*, vol. 1922, p. 140008, AIP Publishing LLC, 2018. 37

[285] J. Merodio and R. Ogden, "Material instabilities in fiber-reinforced nonlinearly elastic solids under plane deformation," *Archives of Mechanics*, vol. 54, no. 5-6, pp. 525–552, 2002. 37

[286] J. Merodio and R. Ogden, "Instabilities and loss of ellipticity in fiber-reinforced compressible non-linearly elastic solids under plane deformation," *International Journal of Solids and Structures*, vol. 40, no. 18, pp. 4707–4727, 2003. 37

[287] P. J. Davies, "A simple derivation of necessary and sufficient conditions for the strong ellipticity of isotropic hyperelastic materials in plane strain," *Journal of Elasticity*, vol. 26, no. 3, pp. 291–296, 1991. 38

[288] J. M. Ball, "Convexity conditions and existence theorems in nonlinear elasticity," *Archive for Rational Mechanics and Analysis*, vol. 63, no. 4, pp. 337–403, 1976. 38

[289] A. Mielke, "Necessary and sufficient conditions for polyconvexity of isotropic functions," *Journal of Convex Analysis*, vol. 12, no. 2, p. 291, 2005. 38

[290] G. Marckmann and E. Verron, "Comparison of hyperelastic models for rubber-like materials," *Rubber Chemistry and Technology*, vol. 79, no. 5, pp. 835–858, 2006. 38

[291] H. Darijani and R. Naghdabadi, "Hyperelastic materials behavior modeling using consistent strain energy density functions," *Acta Mechanica*, vol. 213, no. 3-4, pp. 235–254, 2010. 38

[292] S. Madireddy, B. Sista, and K. Vemaganti, "A bayesian approach to selecting hyperelastic constitutive models of soft tissue," *Computer Methods in Applied Mechanics and Engineering*, vol. 291, pp. 102 – 122, 2015. 38, 50, 152

[293] M. R. Forster, "Key concepts in model selection: Performance and generalizability," *Journal of Mathematical Psychology*, vol. 44, no. 1, pp. 205–231, 2000. 38

[294] E. McMullin, "What do physical models tell us?," in *Studies in Logic and the Foundations of Mathematics*, vol. 52, pp. 385–396, Elsevier, 1968. 38

[295] M. C. Boyce, "Direct Comparison of the Gent and the Arruda-Boyce Constitutive Models of Rubber Elasticity," *Rubber Chemistry and Technology*, vol. 69, pp. 781–785, 11 1996. 38, 39, 42

[296] G. Chagnon, G. Marckmann, and E. Verron, "A Comparison of the Hart-Smith Model with Arruda-Boyce and Gent Formulations for Rubber Elasticity," *Rubber Chemistry and Technology*, vol. 77, pp. 724–735, 09 2004. 38, 39

[297] C. O. Horgan and G. Saccomandi, "Simple torsion of isotropic, hyperelastic, incompressible materials with limiting chain extensibility," *Journal of Elasticity*, vol. 56, no. 2, pp. 159–170, 1999. 38

[298] C. Horgan and G. Saccomandi, "A molecular-statistical basis for the gent constitutive model of rubber elasticity," *Journal of Elasticity*, vol. 68, pp. 167–176, 07 2002. 38, 42

[299] M. F. Beatty, "An average-stretch full-network model for rubber elasticity," *Journal of Elasticity*, vol. 70, no. 1-3, pp. 65–86, 2003. 39, 40

[300] W. Kuhn and F. Grün, "Beziehungen zwischen elastischen konstanten und dehnungsdoppelbrechung hochelastischer stoffe," *Kolloid-Zeitschrift*, vol. 101, no. 3, pp. 248–271, 1942. 39, 40, 41

[301] L. R. G. Treloar, *The Physics of Rubber Elasticity*. Oxford University Press, USA, 1975. 39, 41

[302] P. Flory, *Statistical Mechanics of Chain Molecules*. New York: Hanser Publishers, 1989. 39

[303] E. M. Arruda and M. C. Boyce, "A three-dimensional constitutive model for the large stretch behavior of rubber elastic materials," *Journal of the Mechanics and Physics of Solids*, vol. 41, no. 2, pp. 389–412, 1993. 39

[304] A. V. Tobolsky, D. W. Carlson, and N. Indictor, "Rubber elasticity and chain configuration," *Journal of Polymer Science*, vol. 54, no. 159, pp. 175–192, 1961. 41

[305] A. Cohen, "A padé approximant to the inverse langevin function," *Rheologica Acta*, vol. 30, no. 3, pp. 270–273, 1991. 42

[306] P. Gilles, "Analytic stress-strain relationship for isotropic network model of rubber elasticity," *Comptes Rendus de l'Académie des Sciences-Series IIB-Mechanics-Physics-Astronomy*, vol. 328, no. 1, pp. 5–10, 2000. 42

[307] M. F. Beatty, "On constitutive models for limited elastic, molecular based materials," *Mathematics and Mechanics of Solids*, vol. 13, no. 5, pp. 375–387, 2008. 42

[308] A. G. Ramm, *Inverse problems: mathematical and analytical techniques with applications to engineering*. Springer Science & Business Media, 2006. 42

[309] S. Avril, M. Bonnet, A.-S. Bretelle, M. Grédiac, F. Hild, P. Ienny, F. Latourte, D. Lemosse, S. Pagano, E. Pagnacco, and F. Pierron, "Overview of identification methods of mechanical parameters based on full-field measurements," *Experimental Mechanics*, vol. 48, p. 381, Jul 2008. 42, 44

[310] L. Robert, V. Velay, N. Decultot, and S. Ramde, "Identification of hardening parameters using finite element models and fullfield measurements: Some case studies," *The Journal of Strain Analysis for Engineering Design*, vol. 47, pp. 3–17, 01 2012. 42

[311] D. Claire, F. Hild, and S. Roux, "A finite element formulation to identify damage fields: the equilibrium gap method," *International Journal for Numerical Methods in Engineering*, vol. 61, no. 2, pp. 189–208, 2004. 43

[312] M. Grédiac, F. Hild, and A. Pineau, eds., *Full-Field Measurements and Identification in Solid Mechanics*. John Wiley & Sons, Inc., Dec. 2012. 43, 44, 45

[313] F. Pierron, "Identification of poisson's ratios of standard and auxetic low-density polymeric foams from full-field measurements," *The Journal of Strain Analysis for Engineering Design*, vol. 45, no. 4, pp. 233–253, 2010. 43

[314] S. Avril, P. Badel, and A. Duprey, "Anisotropic and hyperelastic identification of in vitro human arteries from full-field optical measurements," *Journal of Biomechanics*, vol. 43, pp. 2978–2985, Nov. 2010. 43

[315] J.-H. Kim, S. Avril, A. Duprey, and J.-P. Favre, "Experimental characterization of rupture in human aortic aneurysms using a full-field measurement technique," *Biomechanics and Modeling in Mechanobiology*, vol. 11, no. 6, pp. 841–853, 2012. 43

[316] S. Avril, "Hyperelasticity of soft tissues and related inverse problems," in *Material Parameter Identification and Inverse Problems in Soft Tissue Biomechanics*, pp. 37–66, Springer, 2017. 43

[317] P. Ienny, A.-S. Caro-Bretelle, and E. Pagnacco, "Identification from measurements of mechanical fields by finite element model updating strategies," *European Journal of Computational Mechanics*, vol. 18, no. 3-4, pp. 353–376, 2009. 44

[318] H. Sol and C. W. Oomens, *Material Identification Using Mixed Numerical Experimental Methods: Proceedings of the EUROMECH Colloquium Held in Kerkrade, The Netherlands, 7–9 April 1997*. Springer Science & Business Media, 2012. 44

[319] K. T. Kavanagh and R. W. Clough, "Finite element applications in the characterization of elastic solids," *International Journal of Solids and Structures*, vol. 7, no. 1, pp. 11 – 23, 1971. 45, 46

[320] T. J. Keating, P. Wolf, and F. Scarpace, "An improved method of digital image correlation," *Photogrammetric Engineering and Remote Sensing*, vol. 41, no. 8, pp. 993–1002, 1975. 45

[321] F. Rouger, M. Khebibeche, and C. Le Govic, "Non determined tests as a way to identify wood elastic parameters the finite element approach," in *Mechanical Identification of Composites*, pp. 82–90, Springer, 1991. 45

[322] J. Molimard, R. L. Riche, A. Vautrin, and J. R. Lee, "Identification of the four orthotropic plate stiffnesses using a single open-hole tensile test," *Experimental Mechanics*, vol. 45, pp. 404–411, Oct. 2005. 45

[323] D. Lecompte, A. Smits, H. Sol, J. Vantomme, and D. V. Hemelrijck, "Mixed numerical–experimental technique for orthotropic parameter identification using biaxial tensile tests on cruciform specimens," *International Journal of Solids and Structures*, vol. 44, pp. 1643–1656, Mar. 2007. 45

[324] J. Henriques, J. Xavier, and A. Andrade-Campos, "Identification of orthotropic elastic properties of wood by a synthetic image approach based on digital image correlation," *Materials*, vol. 15, no. 2, p. 625, 2022. 45

[325] L. Allais, M. Bornert, T. Bretheau, and D. Caldemaison, "Experimental characterization of the local strain field in a heterogeneous elastoplastic material," *Acta Metallurgica et materialia*, vol. 42, no. 11, pp. 3865–3880, 1994. 45

[326] M. Meuwissen, *An inverse method for the mechanical characterisation of metals*. PhD thesis, Technische Universiteit Eindhoven, Eindhoven, 1998. 45

[327] M. Meuwissen, C. Oomens, F. Baaijens, R. Petterson, and J. Janssen, "Determination of the elasto-plastic properties of aluminium using a mixed numerical–experimental method," *Journal of Materials Processing Technology*, vol. 75, pp. 204–211, Mar. 1998. 45

[328] J. Kajberg and G. Lindkvist, "Characterisation of materials subjected to large strains by inverse modelling based on in-plane displacement fields," *International Journal of Solids and Structures*, vol. 41, no. 13, pp. 3439 – 3459, 2004. 45

[329] F. Mathieu, H. Leclerc, F. Hild, and S. Roux, "Estimation of elastoplastic parameters via weighted FEMU and integrated-DIC," *Experimental Mechanics*, vol. 55, pp. 105–119, May 2014. 45

[330] L. Lemagourou, F. Bos, and F. Rouger, "Identification of constitutive laws for wood-based panels by means of an inverse method," *Composites Science and Technology*, vol. 62, pp. 591–596, Mar. 2002. 45

[331] M. Barick, Y. Gaillard, A. Lejeune, F. Amiot, and F. Richard, "On the uniqueness of intrinsic viscoelastic properties of materials extracted from nanoindentation using femu," *International Journal of Solids and Structures*, vol. 202, pp. 929 – 946, 2020. 45

[332] M. Giton, A.-S. Caro-Bretelle, and P. Ienny, "Hyperelastic behaviour identification by a forward problem resolution: Application to a tear test of a silicone-rubber," *Strain*, vol. 42, pp. 291–297, Nov. 2006. 45, 46

[333] K. Genovese, L. Lamberti, and C. Pappalettere, "Mechanical characterization of hyperelastic materials with fringe projection and optimization techniques," *Optics and Lasers in Engineering*, vol. 44, no. 5, pp. 423 – 442, 2006. 45, 46

[334] J. Zhao, J. Dong, Z. Liu, and H. Xie, "Characterization method of mechanical properties of rubber materials based on in-situ stereo finite-element-model updating," *Polymer Testing*, vol. 79, p. 106015, 2019. 45

[335] M. Cavazzuti, *Optimization methods: from theory to design scientific and technological aspects in mechanics*. Springer Science & Business Media, 2012. 45, 47, 49

[336] R. Fletcher, "Practical methods of optimization john wiley & sons," *New York*, vol. 80, no. 4, 1987. 45

[337] D. P. Bertsekas, *Constrained optimization and Lagrange multiplier methods*. Academic press, 2014. 45, 64

[338] S. Wright, J. Nocedal, *et al.*, "Numerical optimization," *Springer Science*, vol. 35, no. 67-68, p. 7, 1999. 45

[339] S. Boyd, S. P. Boyd, and L. Vandenberghe, *Convex optimization*. Cambridge university press, 2004. 45

[340] J. A. Nelder and R. Mead, "A simplex method for function minimization," *The Computer Journal*, vol. 7, no. 4, pp. 308–313, 1965. 46, 54

[341] M. Avriel, *Nonlinear programming: analysis and methods*. Courier Corporation, 2003. 47

[342] M. K. Transtrum, B. B. Machta, and J. P. Sethna, "Geometry of nonlinear least squares with applications to sloppy models and optimization," *Physical Review E*, vol. 83, no. 3, p. 036701, 2011. 47

[343] W. Sun and Y.-X. Yuan, *Optimization theory and methods: nonlinear programming*, vol. 1. Springer Science & Business Media, 2006. 48

[344] J. C. Nash, *Compact Numerical Methods for Computers*. Routledge, Dec. 2018. 48

[345] D. G. Luenberger, *Optimization by vector space methods*. John Wiley & Sons, 1997. 48

[346] J. C. Spall, *Introduction to stochastic search and optimization: estimation, simulation, and control*. John Wiley & Sons, 2005. 49

[347] H.-P. Schwefel, *Numerical optimization of computer models*. John Wiley & Sons, Inc., 1981. 49

[348] H. Rappel, L. A. A. Beex, J. S. Hale, L. Noels, and S. P. A. Bordas, "A tutorial on Bayesian inference to identify material parameters in solid mechanics," *Archives of Computational Methods in Engineering*, vol. 27, no. 2, pp. 361–385, 2020. 50, 212

[349] F. Daghia, S. de Miranda, F. Ubertini, and E. Viola, "Estimation of elastic constants of thick laminated plates within a bayesian framework," *Composite Structures*, vol. 80, no. 3, pp. 461–473, 2007. 50

[350] T. Ritto and L. Nunes, "Bayesian model selection of hyperelastic models for simple and pure shear at large deformations," *Computers & Structures*, vol. 156, pp. 101 – 109, 2015. 50

[351] H. Rappel, L. A. A. Beex, and S. P. A. Bordas, "Bayesian inference to identify parameters in viscoelasticity," *Mechanics of Time-Dependent Materials*, vol. 22, no. 2, pp. 221–258, 2018. 50

[352] M. Zeraatpisheh, S. P. Bordas, and L. A. Beex, "Bayesian model uncertainty quantification for hyperelastic soft tissue models," *Data-Centric Engineering*, vol. 2, p. e9, 2021. 50

[353] T. Han, T. Lee, J. Ledwon, E. Vaca, S. Turin, A. Kearney, A. K. Gosain, and A. B. Tepole, "Bayesian calibration of a computational model of tissue expansion based on a porcine animal model," *Acta Biomaterialia*, vol. 137, pp. 136–146, 2022. 50

[354] M. Bhattacharyya and P. Feissel, "A bayesian inference of material parameters from DIC data," in *15ème colloque national en calcul des structures*, (83400 Hyères-les-Palmiers, France), Université Polytechnique Hauts-de-France [UPHF], May 2022. 50

[355] A. J. Thomas, E. Barocio, I. Bilionis, and R. B. Pipes, "Bayesian inference of fiber orientation and polymer properties in short fiber-reinforced polymer composites," *arXiv preprint arXiv:2202.12881*, 2022. 50

[356] G. Song, J. An, A. B. Tepole, and T. Lee, "Bayesian inference with gaussian process surrogates to characterize anisotropic mechanical properties of skin from suction tests," *Journal of Biomechanical Engineering*, vol. 144, no. 12, p. 121003, 2022. 50

[357] A. Kalra, A. Lowe, and A. Al-Jumaily, "Mechanical behaviour of skin: a review," *Journal of Material Science & Engineering*, vol. 5, no. 4, p. 1000254, 2016. 50, 138

[358] H. Joodaki and M. B. Panzer, "Skin mechanical properties and modeling: A review," *Proceedings of the Institution of Mechanical Engineers, Part H: Journal of Engineering in Medicine*, vol. 232, no. 4, pp. 323–343, 2018. 50

[359] M. G. Dunn and F. H. Silver, "Viscoelastic behavior of human connective tissues: relative contribution of viscous and elastic components," *Connective Tissue Research*, vol. 12, no. 1, pp. 59–70, 1983. 51

[360] M. L. Crichton, B. C. Donose, X. Chen, A. P. Raphael, H. Huang, and M. A. Kendall, "The viscoelastic, hyperelastic and scale dependent behaviour of freshly excised individual skin layers," *Biomaterials*, vol. 32, no. 20, pp. 4670–4681, 2011. 51, 52

[361] B. Jayne and M. O. Hunt, "Plane stress and plane strain in orthotropic and anisotropic media," *Wood and Fiber Science*, vol. 1, no. 3, pp. 236–247, 1969. 52

[362] E. E. Schadt, M. D. Linderman, J. Sorenson, L. Lee, and G. P. Nolan, "Computational solutions to large-scale data management and analysis," *Nature Reviews Genetics*, vol. 11, no. 9, pp. 647–657, 2010. 53

[363] P. Tong and Y.-C. Fung, "The stress-strain relationship for the skin," *Journal of Biomechanics*, vol. 9, no. 10, pp. 649–657, 1976. 54

[364] Y. Lanir, "Constitutive equations for fibrous connective tissues," *Journal of Biomechanics*, vol. 16, no. 1, pp. 1–12, 1983. 54

[365] R. Schoenberg, "Constrained maximum likelihood," *Computational Economics*, vol. 10, no. 3, pp. 251–266, 1997. 54

[366] S. J. Julier and J. K. Uhlmann, "Unscented filtering and nonlinear estimation," *Proceedings of the IEEE*, vol. 92, no. 3, pp. 401–422, 2004. 54

[367] A. Delalleau, G. Josse, J.-M. Lagarde, H. Zahouani, and J.-M. Bergheau, "Characterization of the mechanical properties of skin by inverse analysis combined with the indentation test," *Journal of Biomechanics*, vol. 39, no. 9, pp. 1603–1610, 2006. 54

[368] W. M. Vannah and D. S. Childress, "Indentor tests and finite element modeling of bulk muscular tissue in vivo," *Journal of Rehabilitation Research and Development*, vol. 33, pp. 239–252, 1996. 54

[369] M. Rubin and S. Bodner, "A three-dimensional nonlinear model for dissipative response of soft tissue," *International Journal of Solids and Structures*, vol. 39, no. 19, pp. 5081–5099, 2002. 54

[370] A. Elouneg, A. Bertin, N. Marie, Q. Lucot, D. Sutula, F. Chouly, A. Lejeune, G. Rolin, T. Lihoreau, B. Chatelain, S. Bordas, E. Jacquet, and J. Chambert, "In vivo mechanical characterization and tissue-scale modelling of keloid and surrounding healthy skin," in *26th Congress of the European Society of Biomechanics (ESB 2021)*, (Milan, Italy), pp. 506 – 506, jul 2021. 56

[371] "Infinitefocus." `https://www.alicona.com/en/products/infinitefocus/`. Accessed: 2022-10-01. 56

[372] B. O. Community, *Blender - a 3D modelling and rendering package*. Blender Foundation, Stichting Blender Foundation, Amsterdam, 2018. 57, 101

[373] L. K. Nielsen, X.-C. Tai, S. I. Aanonsen, and M. Espedal, "A binary level set model for elliptic inverse problems with discontinuous coefficients," *International Journal of Numerical Analysis and Modeling*, vol. 4, no. 1, pp. 74–99, 2007. 58

[374] S. Nanthakumar, T. Lahmer, X. Zhuang, G. Zi, and T. Rabczuk, "Detection of material interfaces using a regularized level set method in piezoelectric structures," *Inverse Problems in Science and Engineering*, vol. 24, no. 1, pp. 153–176, 2016. 58

[375] J. E. Solem, *Programming Computer Vision with Python: Tools and Algorithms for Analyzing Images*. " O'Reilly Media, Inc.", 2012. 59

[376] J. J. Gibson, *The perception of the visual world.* Houghton Mifflin, 1950. 59

[377] B. D. Lucas, T. Kanade, *et al.*, "An iterative image registration technique with an application to stereo vision," pp. 121–130, Imaging Understanding Workshop, Vancouver, British Columbia, 1981. 60

[378] B. K. Horn and B. G. Schunck, "Determining optical flow," in *Techniques and Applications of Image Understanding*, vol. 281, pp. 319–331, International Society for Optics and Photonics, 1981. 60

[379] S. S. Beauchemin and J. L. Barron, "The computation of optical flow," *ACM computing surveys (CSUR)*, vol. 27, no. 3, pp. 433–466, 1995. 60

[380] P. D. Verhaegen, P. P. Van Zuijlen, N. M. Pennings, J. Van Marle, F. B. Niessen, C. M. Van Der Horst, and E. Middelkoop, "Differences in collagen architecture between keloid, hypertrophic scar, normotrophic scar, and normal skin: an objective histopathological analysis," *Wound Repair and Regeneration*, vol. 17, no. 5, pp. 649–656, 2009. 61

[381] C. Huang, S. Akaishi, H. Hyakusoku, and R. Ogawa, "Are keloid and hypertrophic scar different forms of the same disorder? a fibroproliferative skin disorder hypothesis based on keloid findings," *International Wound Journal*, vol. 11, no. 5, pp. 517–522, 2014. 61

[382] J. P. Pascon, "Large deformation analysis of plane-stress hyperelastic problems via triangular membrane finite elements," *International Journal of Advanced Structural Engineering*, vol. 11, no. 3, pp. 331–350, 2019. 61

[383] Geuzaine, Christophe and Remacle, Jean-Francois, "Gmsh." 63, 84

[384] C. O. Horgan and G. Saccomandi, "Constitutive models for compressible nonlinearly elastic materials with limiting chain extensibility," *Journal of Elasticity*, vol. 77, pp. 123–138, 2004. 63

[385] S. Mora, C. Maurini, T. Phou, J. Fromental, B. Audoly, and Y. Pomeau, "Solid drops–supplementary material." `https://hal.archives-ouvertes.fr/hal-00842852v2/file/supp_numerics.pdf`, 2013. 63

[386] A. Mazier, A. Bilger, A. E. Forte, I. Peterlik, J. S. Hale, and S. Bordas, "Inverse deformation analysis: an experimental and numerical assessment using the fenics project," *Engineering with Computers*, pp. 1–15, 2022. 63

[387] A. Logg, K.-A. Mardal, and G. Wells, *Automated solution of differential equations by the finite element method: The FEniCS book*, vol. 84. Springer Science & Business Media, 2012. 63, 68

[388] H. P. Langtangen and A. Logg, *Solving PDEs in python: the FEniCS tutorial I.* Springer Nature, 2017. 68

[389] A. Logg and G. N. Wells, "Dolfin: Automated finite element computing," *ACM Transactions on Mathematical Software (TOMS)*, vol. 37, no. 2, pp. 1–28, 2010. 68

[390] P. E. Farrell, D. A. Ham, S. W. Funke, and M. E. Rognes, "Automated derivation of the adjoint of high-level transient finite element programs," *SIAM Journal on Scientific Computing*, vol. 35, no. 4, 2013. 68, 73

[391] P. Hauseux, J. S. Hale, S. Cotin, and S. P. Bordas, "Quantifying the uncertainty in a hyperelastic soft tissue model with stochastic parameters," *Applied Mathematical Modelling*, vol. 62, pp. 86 – 102, 2018. 68

[392] T. J. Hughes, *The finite element method: linear static and dynamic finite element analysis*. Courier Corporation, 2012. 85

[393] C. Stimpson, C. Ernst, P. Knupp, P. Pébay, and D. Thompson, "The verdict library reference manual," *Sandia National Laboratories Technical Report*, vol. 9, no. 6, 2007. 88

[394] H. P. Bui, S. Tomar, H. Courtecuisse, M. Audette, S. Cotin, and S. P. A. Bordas, "Controlling the error on target motion through real-time mesh adaptation: Applications to deep brain stimulation," *International Journal for Numerical Methods in Biomedical Engineering*, vol. 34, no. 5, p. e2958, 2018. 91

[395] M. Duprez, S. P. A. Bordas, M. Bucki, H. P. Bui, F. Chouly, V. Lleras, C. Lobos, A. Lozinski, P.-Y. Rohan, and S. Tomar, "Quantifying discretization errors for soft tissue simulation in computer assisted surgery: A preliminary study," *Applied Mathematical Modelling*, vol. 77, pp. 709–723, 2020. 91

[396] N. Marie, "Estimateurs d'erreur DWR appliqués à la biomécanique d'une peau avec chéloïde," Master's thesis, Université Bourogne Franche-Comté, 2020. 94

[397] H. Rappel, L. A. A. Beex, J. S. Hale, and S. P. A. Bordas, "Bayesian inference for the stochastic identification of elastoplastic material parameters: introduction, misconceptions and insights," *arXiv preprint arXiv:1606.02422*, 2016. 93, 152, 211, 212

[398] B. Falck, D. Falck, and B. Collette, *Freecad [How-To]*. Packt Publishing Ltd, 2012. 101

[399] W. M. Association, "World Medical Association Declaration of Helsinki: Ethical Principles for Medical Research Involving Human Subjects," *JAMA*, vol. 310, pp. 2191–2194, 11 2013. 108

[400] C.-H. Tsai and R. Ogawa, "Keloid research: current status and future directions," *Scars, Burns & Healing*, vol. 5, p. 2059513119868659, 2019. 121

[401] E. E. Limmer and D. A. Glass, "A review of current keloid management: Mainstay monotherapies and emerging approaches," *Dermatology and Therapy*, vol. 10, pp. 931–948, July 2020. 125

[402] A. Elouneg, J. Chambert, A. Lejeune, Q. Lucot, E. Jacquet, and S. Bordas, "Anisotropic mechanical characterization of human skin by in vivo multi-axial ring suction test," *Journal of the Mechanical Behavior of Biomedical Materials*, vol. 141, p. 105779, 2023. 129, 131, 137, 142, 143, 144, 145, 147, 148, 150, 209

[403] C. Deroy, M. Destrade, A. Mc Alinden, and A. Ní Annaidh, "Non-invasive evaluation of skin tension lines with elastic waves," *Skin Research and Technology*, vol. 23, no. 3, pp. 326–335, 2017. 129

[404] A. N. Annaidh and M. Destrade, "Tension lines of the skin," *Skin Biophysics: From Experimental Characterisation to Advanced Modelling*, pp. 265–280, 2019. 129

[405] A. Elouneg, A. Bertin, Q. Lucot, V. Tissot, E. Jacquet, J. Chambert, and A. Lejeune, "In vivo skin anisotropy dataset from annular suction test," *Data in Brief*, vol. 40, p. 107835, 2022. 132, 133

[406] D. André, "PyDIC, a python suite for local digital image correlation." `https://gitlab.com/damien.andre/pydic` 2019. Accessed: 15 May 2022. 131

[407] Y. Takema, Y. Yorimoto, M. Kawai, and G. Imokawa, "Age-related changes in the elastic properties and thickness of human facial skin," *British Journal of Dermatology*, vol. 131, no. 5, pp. 641–648, 1994. 133

[408] R. M. Jones, *Mechanics of composite materials*. CRC Press, Boca Raton, 2nd ed., 2018. 137

[409] T. C. T. Ting and T. Chen, "Poisson's ratio for anisotropic elastic materials can have no bounds," *The Quarterly Journal of Mechanics and Applied Mathematics*, vol. 58, pp. 73–82, 02 2005. 141

[410] C. Pailler-Mattei, S. Bec, and H. Zahouani, "In vivo measurements of the elastic mechanical properties of human skin by indentation tests," *Medical Engineering & Physics*, vol. 30, no. 5, pp. 599–606, 2008. 141

[411] A. Levy, M. B.-O. Frank, and A. Gefen, "The biomechanical efficacy of dressings in preventing heel ulcers," *Journal of Tissue Viability*, vol. 24, no. 1, pp. 1–11, 2015. 141

[412] M. Destrade, M. Gilchrist, J. Motherway, and J. Murphy, "Slight compressibility and sensitivity to changes in poisson's ratio," *International Journal for Numerical Methods in Engineering*, vol. 90, no. 4, pp. 403–411, 2012. 141

[413] K. K. Dwivedi, P. Lakhani, S. Kumar, and N. Kumar, "Effect of collagen fibre orientation on the poisson's ratio and stress relaxation of skin: an ex vivo and in vivo study," *Royal Society Open Science*, vol. 9, no. 3, p. 211301, 2022. 141

[414] H. Zahouani, M. Djaghloul, R. Vargiolu, S. Mezghani, and M. E. L. Mansori, "Contribution of human skin topography to the characterization of dynamic skin tension during senescence: morpho-mechanical approach," *Journal of Physics: Conference Series*, vol. 483, p. 012012, mar 2014. 149

[415] K. Rosicka, M. Hill, and M. Wdowski, "Skin anisotropy: Finding the optimal incision line for volar forearm in males and females," *Journal of the Mechanical Behavior of Biomedical Materials*, vol. 124, p. 104805, 2021. 149

[416] P. Lakhani, K. Dwivedi, A. Parashar, and N. Kumar, "Non-invasive in vivo quantification of directional dependent variation in mechanical properties for human skin," *Frontiers in Bioengineering and Biotechnology*, vol. 9, p. 749492, 10 2021. 149

[417] X. Liang and S. A. Boppart, "Biomechanical properties of in vivo human skin from dynamic optical coherence elastography," *IEEE Transactions on Biomedical Engineering*, vol. 57, no. 4, pp. 953–959, 2010. 149

[418] M. Ayadh, M.-A. Abellan, C. Helfenstein-Didier, A. Bigouret, and H. Zahouani, "Methods for characterizing the anisotropic behavior of the human skin's relief and its mechanical properties in vivo linked to age effects," *Surface Topography: Metrology and Properties*, vol. 8, p. 014002, mar 2020. 149, 168

[419] G. Limbert and E. Kuhl, "On skin microrelief and the emergence of expression micro-wrinkles," *Soft Matter*, vol. 14, no. 8, pp. 1292–1300, 2018. 149

[420] J. P. Kaipio and E. Somersalo, *Statistical and Computational Inverse Problems*. New York: Springer Science & Business Media, 2005. 152

[421] J. Kaipio and E. Somersalo, "Statistical inverse problems: discretization, model reduction and inverse crimes," *Journal of Computational and Applied Mathematics*, vol. 198, no. 2, pp. 493–504, 2007. 152

[422] T. Dahiru, "P-value, a true test of statistical significance? a cautionary note," *Annals of Ibadan Postgraduate Medicine*, vol. 6, no. 1, pp. 21–26, 2008. 156

[423] "Dub skinscanner75." `https://eotech-sa.com/life-science/skin-imaging/dub-skinscanner-2/`. Accessed: 2023-03-01. 157

[424] H. Dao and R. A. Kazin, "Gender differences in skin: A review of the literature," *Gender Medicine*, vol. 4, no. 4, pp. 308–328, 2007. 162

[425] S. Rahrovan, F. Fanian, P. Mehryan, P. Humbert, and A. Firooz, "Male versus female skin: what dermatologists and cosmeticians should know," *International Journal of Women's Dermatology*, vol. 4, no. 3, pp. 122–130, 2018. 162

[426] J. Leveque, P. Corcuff, J. de Rigal, and P. Agache, "In vivo studies of the evolution of physical properties of the human skin with age," *International Journal of Dermatology*, vol. 23, p. 322—329, June 1984. 162

[427] R. Anakwe, J. Huntley, and J. E. McEachan, "Grip strength and forearm circumference in a healthy population," *Journal of Hand Surgery (European Volume)*, vol. 32, no. 2, pp. 203–209, 2007. 166

[428] A. Yoldaş, M. Demir, E. Çalışgan, E. Atay, E. Geçgil, M. Çiçek, T. Ertekin, and A. Doğaner, "The comparison of measurements of the wrist, hand and finger parameters between female and male," *Kahramanmaraş Sütçü İmam Üniversitesi Tıp Fakültesi Dergisi*, pp. 6 – 10, 2020. 166

[429] T. Ishikawa, O. Ishikawa, and Y. Miyachi, "Measurement of skin elastic properties with a new suction device (i): Relationship to age, sex and the degree of obesity in normal individuals," *The Journal of Dermatology*, vol. 22, no. 10, pp. 713–717, 1995. 170

[430] A. Firooz, B. Sadr, S. Babakoohi, M. Sarraf-Yazdy, F. Fanian, A. Kazerouni-Timsar, M. Nassiri-Kashani, M. M. Naghizadeh, and Y. Dowlati, "Variation of biophysical parameters of the skin with age, gender, and body region," *The Scientific World Journal*, vol. 2012, 2012. 170

[431] A. Vexler, I. Polyansky, and R. Gorodetsky, "Evaluation of skin viscoelasticity and anisotropy by measurement of speed of shear wave propagation with viscoelasticity skin analyzer1," *Journal of Investigative Dermatology*, vol. 113, no. 5, pp. 732–739, 1999. 170

Appendix

A   Parameter Identification Uncertainty

Table A.1: Parameter estimation accuracy using noised dummy data on the reference mesh.

μ_k

S_{DIC} (μm)		1st draw				2nd draw				3rd draw		
		0	40	120	200	0	40	120	200	0	40	120	200
$S_{\text{force}} = 0$ mN	ε_{μ_k} (%)	0	0.02	0.02	0.22	0	0.04	0.07	0.18	0	0.01	0.13	0.24
	ε_{DIC} (%)	0	1.55	4.67	7.79	0	1.56	4.67	7.78	0	1.56	4.67	7.77
	$\varepsilon_{\text{force}}$ (%)	0	0	0	0	0	0	0	0	0	0	0	0
$S_{\text{force}} = 2$ mN	ε_{μ_k} (%)	0.66	0.08	0.20	0.27	0.31	0.45	0.32	0.08	0.19	0.23	0.60	0.26
	ε_{DIC} (%)	0	1.56	4.67	7.78	0	1.56	4.67	7.78	0	1.56	4.67	7.78
	$\varepsilon_{\text{force}}$ (%)	1.99	2.88	1.97	1.82	1.83	2.22	2.22	1.62	2.17	1.85	1.95	2.4
$S_{\text{force}} = 6$ mN	ε_{μ_k} (%)	0.75	0.45	0.22	0.83	2.24	1	1.26	1.16	0.11	0.43	0.93	1.33
	ε_{DIC} (%)	0	1.55	4.67	7.79	0	1.56	4.67	7.77	0	1.56	4.67	7.77
	$\varepsilon_{\text{force}}$ (%)	5.38	5.32	6.03	5.34	7.08	5.52	4.72	6.13	6.31	6.28	7.34	5.66
$S_{\text{force}} = 10$ mN	ε_{μ_k} (%)	1.20	0.58	0.17	2.11	1.32	0.89	0.52	1.62	0.04	1.14	0.71	0.41
	ε_{DIC} (%)	0	1.56	4.67	7.78	0	1.56	4.67	7.78	0	1.56	4.67	7.78
	$\varepsilon_{\text{force}}$ (%)	10.34	7.71	9.91	9.96	9.21	8.72	10.61	9.66	9.05	11.89	10.84	9.18

J_{mk}

S_{DIC} (μm)		1st draw				2nd draw				3rd draw		
		0	40	120	200	0	40	120	200	0	40	120	200
$S_{\text{force}} = 0$ mN	$\varepsilon_{J_{mk}}$ (%)	0	0.05	0.01	0.27	0	0.03	0.22	0.38	0	0.02	0.60	0.78
	ε_{DIC} (%)	0	1.55	4.67	7.79	0	1.56	4.67	7.78	0	1.56	4.67	7.77
	$\varepsilon_{\text{force}}$ (%)	0	0	0	0	0	0	0	0	0	0	0	0
$S_{\text{force}} = 2$ mN	$\varepsilon_{J_{mk}}$ (%)	0	0.12	0.24	0.18	0	0.07	0.24	0.73	0	0.02	0.35	0.17
	ε_{DIC} (%)	0	1.56	4.67	7.78	0	1.56	4.67	7.78	0	1.56	4.67	7.78
	$\varepsilon_{\text{force}}$ (%)	1.99	2.88	1.97	1.82	1.83	2.22	2.22	1.62	2.17	1.85	1.95	2.4
$S_{\text{force}} = 6$ mN	$\varepsilon_{J_{mk}}$ (%)	0	0.06	0.28	1.6	0	0.11	0.26	1.17	0	0	0.06	1.47
	ε_{DIC} (%)	0	1.55	4.67	7.79	0	1.56	4.67	7.77	0	1.56	4.67	7.77
	$\varepsilon_{\text{force}}$ (%)	5.38	5.32	6.03	5.34	7.08	5.52	4.72	6.13	6.31	6.28	7.34	5.66
$S_{\text{force}} = 10$ mN	$\varepsilon_{J_{mk}}$ (%)	0	0.14	0.08	0.52	0	0.07	0.31	0.78	0	0.01	0.68	0.39
	ε_{DIC} (%)	0	1.56	4.67	7.78	0	1.56	4.67	7.78	0	1.56	4.67	7.78
	$\varepsilon_{\text{force}}$ (%)	10.34	7.71	9.91	9.96	9.21	8.72	10.61	9.66	9.05	11.89	10.84	9.18

μ_{hs}

S_{force}	S_{DIC} (μm)	1st draw				2nd draw				3rd draw			
		0	40	120	200	0	40	120	200	0	40	120	200
$S_{force}=0$ mN	$\varepsilon\mu_{hs}$ (%)	0	0.18	0.14	1.4	0	0.40	0.41	0.94	0	0.03	0.34	1.07
	εDIC (%)	0	1.55	4.67	7.79	0	1.56	4.67	7.78	0	1.56	4.67	7.77
	εforce (%)	0	0	0	0	0	0	0	0	0	0	0	0
$S_{force}=2$ mN	$\varepsilon\mu_{hs}$ (%)	0.66	0.01	0.57	0.43	0.31	0.38	0.32	0.94	0.19	0.18	0.43	0.05
	εDIC (%)	0	1.56	4.67	7.78	0	1.56	4.67	7.78	0	1.56	4.67	7.78
	εforce (%)	1.99	2.88	1.97	1.82	1.83	2.22	2.22	1.62	2.17	1.85	1.95	2.4
$S_{force}=6$ mN	$\varepsilon\mu_{hs}$ (%)	0.75	0.39	2.18	0.68	2.24	1.0	1.69	0.64	0.11	0.63	0.04	0.61
	εDIC (%)	0	1.55	4.67	7.79	0	1.56	4.67	7.77	0	1.56	4.67	7.77
	εforce (%)	5.38	5.32	6.03	5.34	7.08	5.52	4.72	6.13	6.31	6.28	7.34	5.66
$S_{force}=10$ mN	$\varepsilon\mu_{hs}$ (%)	1.2	0.67	1.16	2.45	1.32	1.13	0.3	0.17	0.04	1.08	0.6	0.03
	εDIC (%)	0	1.56	4.67	7.78	0	1.56	4.67	7.78	0	1.56	4.67	7.78
	εforce (%)	10.34	7.71	9.91	9.96	9.21	8.72	10.61	9.66	9.05	11.89	10.84	9.18

J_{mhs}

S_{force}	S_{DIC} (μm)	1st draw				2nd draw				3rd draw			
		0	40	120	200	0	40	120	200	0	40	120	200
$S_{force}=0$ mN	εJ_{mhs} (%)	0	0.08	0.41	0.6	0	0.05	0.53	0.64	0	0.07	0.09	0.8
	εDIC (%)	0	1.55	4.67	7.79	0	1.56	4.67	7.78	0	1.56	4.67	7.77
	εforce (%)	0	0	0	0	0	0	0	0	0	0	0	0
$S_{force}=2$ mN	εJ_{mhs} (%)	0	0.06	0.82	1.06	0	0.15	0.63	0.8	0	0.32	0.45	0.68
	εDIC (%)	0	1.56	4.67	7.78	0	1.56	4.67	7.78	0	1.56	4.67	7.78
	εforce (%)	1.99	2.88	1.97	1.82	1.83	2.22	2.22	1.62	2.17	1.85	1.95	2.4
$S_{force}=6$ mN	εJ_{mhs} (%)	0	0.12	0.36	0.8	0	0.04	0.17	1.89	0	0.04	0.07	0.9
	εDIC (%)	0	1.55	4.67	7.79	0	1.56	4.67	7.77	0	1.56	4.67	7.77
	εforce (%)	5.38	5.32	6.03	5.34	7.08	5.52	4.72	6.13	6.31	6.28	7.34	5.66
$S_{force}=10$ mN	εJ_{mhs} (%)	0	0.12	0.35	0.91	0	0.01	0.51	0.39	0	0.18	0.09	0.18
	εDIC (%)	0	1.56	4.67	7.78	0	1.56	4.67	7.78	0	1.56	4.67	7.78
	εforce (%)	10.34	7.71	9.91	9.96	9.21	8.72	10.61	9.66	9.05	11.89	10.84	9.18

Table A.2: Parameter estimation accuracy using noised dummy data on the optimized mesh.

μ_k

S_{DIC} (μm)		1$^{\text{st}}$ draw				2$^{\text{nd}}$ draw				3$^{\text{rd}}$ draw			
		0	40	120	200	0	40	120	200	0	40	120	200
S_{force} = 0 mN	ε_{μ_k} (%)	0.37	0.42	0.48	0.74	0.37	0.35	0.17	0.61	0.37	0.23	0.26	0.31
	ε_{DIC} (%)	0	1.56	4.66	7.78	0	1.56	4.67	7.77	0	1.56	4.66	7.77
	$\varepsilon_{\text{force}}$ (%)	0	0	0	0	0	0	0	0	0	0	0	0
S_{force} = 2 mN	ε_{μ_k} (%)	0.46	0.17	0.2	0.74	0.54	0.77	0.17	0.61	1.26	0.07	0.72	0.31
	ε_{DIC} (%)	0	1.56	4.67	7.78	0	1.56	4.67	7.77	0	1.56	4.67	7.77
	$\varepsilon_{\text{force}}$ (%)	1.88	1.77	2.1	2.18	1.92	2.23	2.00	1.94	1.87	1.62	2.12	2.09
S_{force} = 6 mN	ε_{μ_k} (%)	0.1	0.37	1.15	1.58	0.07	0.6	0.52	1.08	0.46	0.13	0.08	0.25
	ε_{DIC} (%)	0	1.55	4.66	7.78	0	1.56	4.67	7.79	0	1.56	4.67	7.77
	$\varepsilon_{\text{force}}$ (%)	5.79	6.17	6.48	6.10	4.73	7	4.28	5.26	6.15	4.54	5.41	6.08
S_{force} = 10 mN	ε_{μ_k} (%)	0.92	1.74	0.79	0.74	1.21	1.02	3.1	0.24	0.6	1.41	0.27	3.06
	ε_{DIC} (%)	0	1.56	4.67	7.78	0	1.56	4.67	7.78	0	1.56	4.67	7.78
	$\varepsilon_{\text{force}}$ (%)	9.23	9.35	9.23	9.09	9.4	9.93	11.64	10.16	8.94	9.38	9.33	12

J_{mk}

S_{DIC} (μm)		1$^{\text{st}}$ draw				2$^{\text{nd}}$ draw				3$^{\text{rd}}$ draw			
		0	40	120	200	0	40	120	200	0	40	120	200
S_{force} = 0 mN	$\varepsilon_{J_{mk}}$ (%)	0.42	0.32	0.07	0.95	0.42	0.04	0.56	0.8	0.42	0.68	2.1	4
	ε_{DIC} (%)	0	1.56	4.66	7.78	0	1.56	4.67	7.77	0	1.56	4.66	7.77
	$\varepsilon_{\text{force}}$ (%)	0	0	0	0	0	0	0	0	0	0	0	0
S_{force} = 2 mN	$\varepsilon_{J_{mk}}$ (%)	0.42	0.12	0.6	0.3	0.42	0.05	0.77	3.3	0.42	1.49	0.43	0.36
	ε_{DIC} (%)	0	1.56	4.67	7.78	0	1.56	4.67	7.77	0	1.56	4.67	7.77
	$\varepsilon_{\text{force}}$ (%)	1.88	1.77	2.1	2.18	1.92	2.23	2.00	1.94	1.87	1.62	2.12	2.09
S_{force} = 6 mN	$\varepsilon_{J_{mk}}$ (%)	0.42	0.35	0.41	3.31	0.42	0.54	0.73	0.38	0.42	0.04	0.65	2
	ε_{DIC} (%)	0	1.55	4.66	7.78	0	1.56	4.67	7.79	0	1.56	4.67	7.77
	$\varepsilon_{\text{force}}$ (%)	5.79	6.17	6.48	6.10	4.73	7	4.28	5.26	6.15	4.54	5.41	6.08
S_{force} = 10 mN	$\varepsilon_{J_{mk}}$ (%)	0.42	0.79	1.51	0.77	0.42	0.64	0.47	0.45	0.42	0.29	0.05	0.66
	ε_{DIC} (%)	0	1.56	4.67	7.78	0	1.56	4.67	7.78	0	1.56	4.67	7.78
	$\varepsilon_{\text{force}}$ (%)	9.23	9.35	9.23	9.09	9.4	9.93	11.64	10.16	8.94	9.38	9.33	12

μ_{hs}

S_{DIC} (μm)		1st draw				2nd draw				3rd draw			
		0	40	120	200	0	40	120	200	0	40	120	200
S_{force} = 0 mN	$\varepsilon\mu_{hs}$ (%)	0.65	0.19	0.51	0.19	0.65	1.34	3.93	0.28	0.65	1.55	0.63	2.95
	ε_{DIC} (%)	0	1.56	4.66	7.78	0	1.56	4.67	7.77	0	1.56	4.66	7.77
	ε_{force} (%)	0	0	0	0	0	0	0	0	0	0	0	0
S_{force} = 2 mN	$\varepsilon\mu_{hs}$ (%)	0.75	0.66	1.24	1.98	0.83	1.71	0.45	2.66	1.55	1.38	0.37	7.44
	ε_{DIC} (%)	0	1.56	4.67	7.78	0	1.56	4.67	7.77	0	1.56	4.67	7.77
	ε_{force} (%)	1.88	1.77	2.1	2.18	1.92	2.23	2.00	1.94	1.87	1.62	2.12	2.09
S_{force} = 6 mN	$\varepsilon\mu_{hs}$ (%)	0.39	0.91	1.53	0.87	0.21	0.87	0.14	5.58	0.18	0.45	0.14	3.06
	ε_{DIC} (%)	0	1.55	4.66	7.78	0	1.56	4.67	7.79	0	1.56	4.67	7.77
	ε_{force} (%)	5.79	6.17	6.48	6.10	4.73	7	4.28	5.26	6.15	4.54	5.41	6.08
S_{force} = 10 mN	$\varepsilon\mu_{hs}$ (%)	0.64	3.91	1.66	1.86	0.93	0.79	3.16	3.6	0.89	1.97	1.56	3.96
	ε_{DIC} (%)	0	1.56	4.67	7.78	0	1.56	4.67	7.78	0	1.56	4.67	7.78
	ε_{force} (%)	9.23	9.35	9.23	9.09	9.4	9.93	11.64	10.16	8.94	9.38	9.33	12

J_{mhs}

S_{DIC} (μm)		1st draw				2nd draw				3rd draw			
		0	40	120	200	0	40	120	200	0	40	120	200
S_{force} = 0 mN	εJ_{mhs} (%)	1.54	0.75	2.3	4.27	1.54	1.24	1.83	1.75	1.54	1.44	2.05	6.63
	ε_{DIC} (%)	0	1.56	4.66	7.78	0	1.56	4.67	7.77	0	1.56	4.66	7.77
	ε_{force} (%)	0	0	0	0	0	0	0	0	0	0	0	0
S_{force} = 2 mN	εJ_{mhs} (%)	1.54	1.31	1.6	2.82	1.54	1.52	0.43	0.58	1.54	2.61	1.67	1.79
	ε_{DIC} (%)	0	1.56	4.67	7.78	0	1.56	4.67	7.77	0	1.56	4.67	7.77
	ε_{force} (%)	1.88	1.77	2.1	2.18	1.92	2.23	2.00	1.94	1.87	1.62	2.12	2.09
S_{force} = 6 mN	εJ_{mhs} (%)	1.54	1.74	2.61	5.57	1.54	1.06	0.25	2.64	1.54	1.66	0.42	0.59
	ε_{DIC} (%)	0	1.55	4.66	7.78	0	1.56	4.67	7.79	0	1.56	4.67	7.77
	ε_{force} (%)	5.79	6.17	6.48	6.10	4.73	7	4.28	5.26	6.15	4.54	5.41	6.08
S_{force} = 10 mN	εJ_{mhs} (%)	1.54	1.82	2.69	0.98	1.54	1.06	0.25	0.99	1.54	1.66	0.42	4.12
	ε_{DIC} (%)	0	1.56	4.67	7.78	0	1.56	4.67	7.78	0	1.56	4.67	7.78
	ε_{force} (%)	9.23	9.35	9.23	9.09	9.4	9.93	11.64	10.16	8.94	9.38	9.33	12

Table A.3: Parameter estimation accuracy versus number of snapshots.

Weakly nonlinear

N_S	1st draw					2nd draw					3rd draw				
N_S	100	50	20	10	5	100	50	20	10	5	100	50	20	10	5
$\varepsilon_{\mathrm{DIC}}$ (%)	6.95	7.03	7.24	7.65	8.52	6.96	7.02	7.22	7.62	8.55	6.95	7.02	7.26	7.63	8.53
$\varepsilon_{\mathrm{force}}$ (%)	19.07	18.31	21.77	20.95	20.42	15.82	17.36	18.58	20.63	10.86	16.05	15.12	19.08	16.48	15.91
ε_{μ_k} (%)	3.43	2.98	4.39	4.18	7.35	1.87	2.06	5.34	9.6	6.83	3.29	4.27	1.8	2.08	5.71
$\varepsilon_{J_{mk}}$ (%)	1.24	1.1	0.08	0.44	1.38	0.12	0.26	0.51	0.82	0.04	1.02	0.62	0.04	0.64	2.31
$\varepsilon_{\mu_{hs}}$ (%)	4.91	5.75	0.18	3.23	15.64	2.12	1.29	7.01	9.42	2.16	1.12	2.82	6.81	4.07	2.42
$\varepsilon_{J_{mhs}}$ (%)	1.73	2.21	0.32	3.04	4.7	0.12	0.8	0.8	0.26	1.1	0.83	0.06	1.62	4.02	2.52

Highly nonlinear

N_S	1st draw					2nd draw					3rd draw				
N_S	200	100	40	25	20	200	100	40	25	20	200	100	40	25	20
$\varepsilon_{\mathrm{DIC}}$ (%)	7.59	7.63	7.73	7.9	7.96	7.59	7.63	7.77	7.90	7.98	7.59	7.63	7.75	7.88	7.96
$\varepsilon_{\mathrm{force}}$ (%)	6.42	5.92	7.36	4.83	6.95	6.99	7.31	7.19	6.45	7.44	6.66	6.7	5.61	6.09	6
ε_{μ_k} (%)	0.83	0.87	0.51	5.28	0.3	4.87	2.35	14.54	7.5	11.63	0.63	1.41	5.32	2.21	3.69
$\varepsilon_{J_{mk}}$ (%)	1.93	1.56	2.96	0.72	1.5	1.43	0.4	2.46	2.77	1.56	2.3	2.62	1.41	1.19	1.33
$\varepsilon_{\mu_{hs}}$ (%)	0.09	0.61	2.28	1.7	1.56	0.14	1.26	0.65	3.68	0.31	0.61	0.92	1.43	0.84	1.02
$\varepsilon_{J_{mhs}}$ (%)	0.45	0.16	1.89	0.87	1.1	0.3	0.29	0.63	0.32	0.23	0.43	0.33	0.91	1.76	0.96
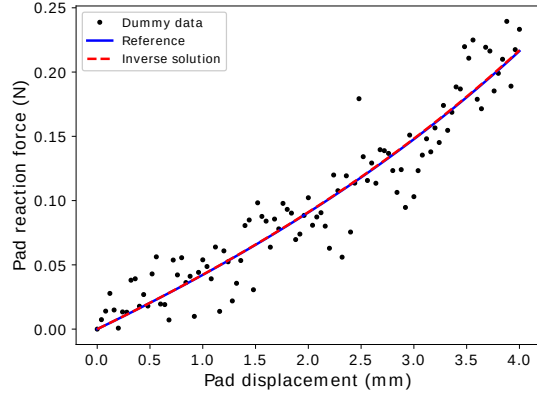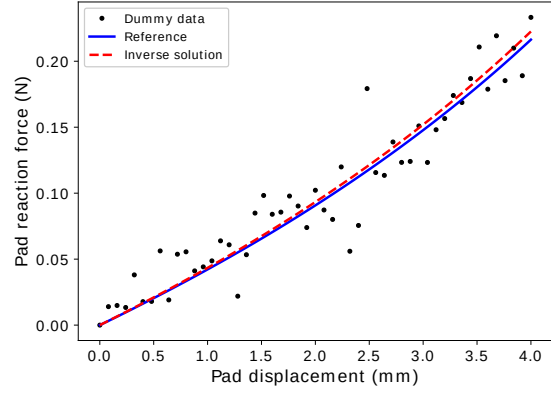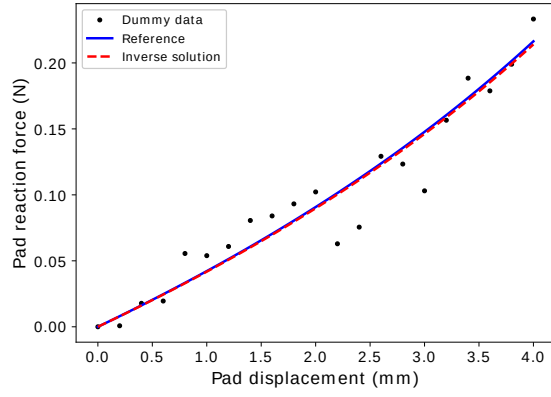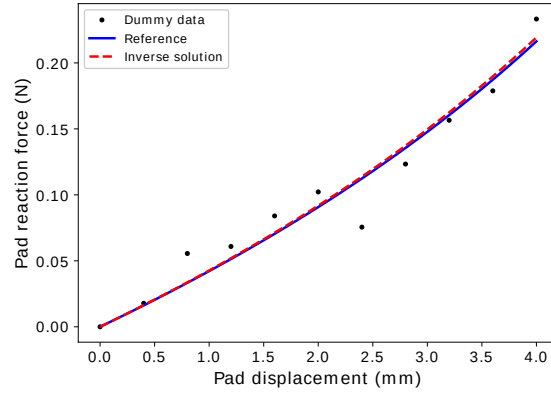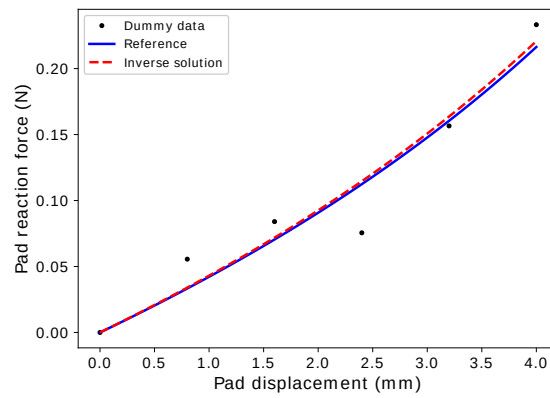
Figure A.1: Parameter identification performed on noisy dummy data for the weakly nonlinear behavior case.
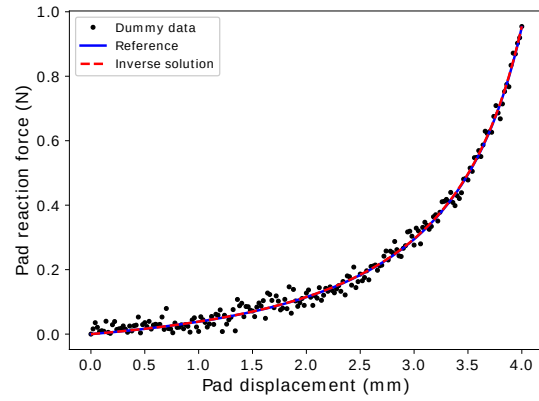
(a) $N_S = 200$
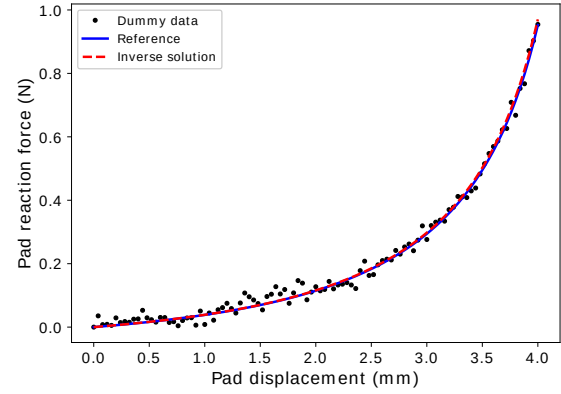
(b) $N_S = 100$
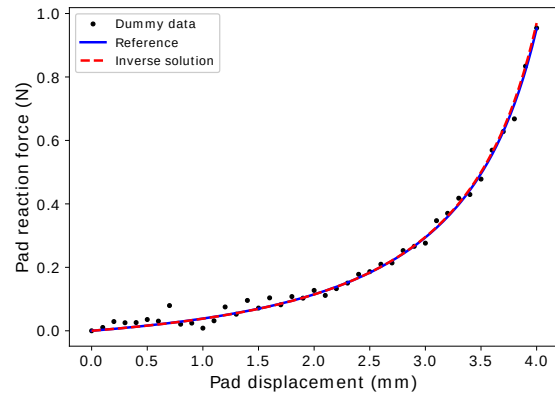
(c) $N_S = 40$
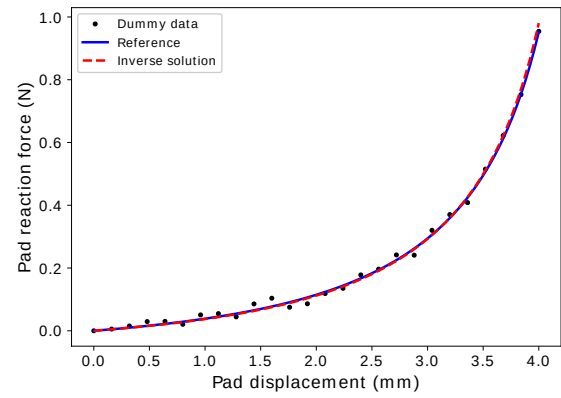
(d) $N_S = 25$
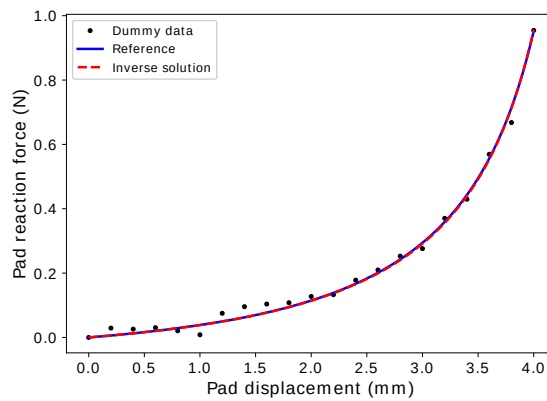
(e) $N_S = 20$

Figure A.2: Parameter identification performed on noisy dummy data for the highly nonlinear behavior case.

B Patient-Specific Data: Contra-Lateral Experiment
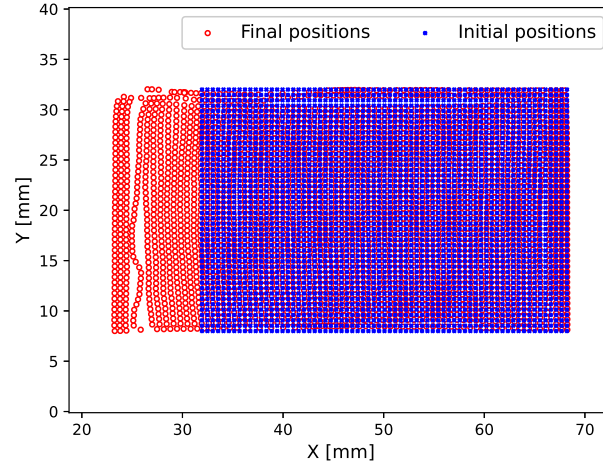
Figure B.1: Initial and final configuration of the healthy-skin measurement domain.
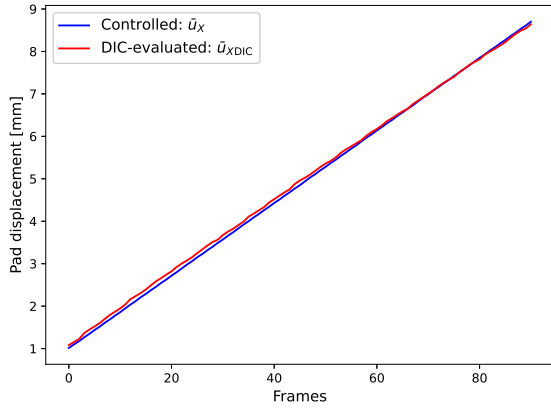
(a)
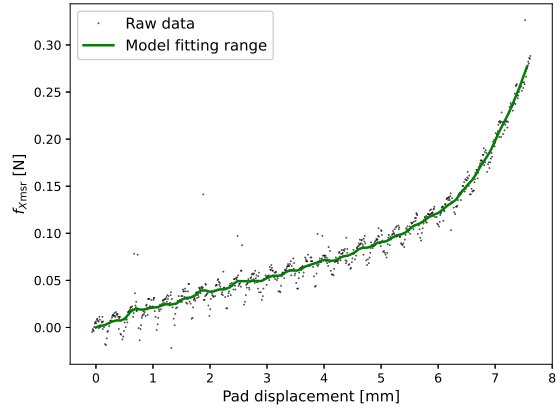
(b)

Figure B.2: Uncertainty analysis of the DIC process and validation range of the experimental data for the healthy-skin case.

C   Principal Stresses and Vectors

```python
import ufl
import dolfin

INTERPOLATION_DEGREE = 2

def stress_tensors(u, material_parameters, material_markers):
  # u: displacement field

  I = dolfin.Identity(2)
  F = dolfin.variable(I + u)
  C = F.T*F
  J = dolfin.det(F)
  I1 = dolfin.tr(C)
  mu = material_parameters[0]
  jm = material_parameters[1]
  bool_keloid  = material_markers[0]
  bool_healthy = material_markers[1]
  psi = -0.5*mu*(jm*dolfin.ln(1 - (I1 - 3)/jm) + 2*dolfin.ln(J))
  psi_all = psi*bool_keloid + psi*bool_healthy
  PK1 = dolfin.diff(psi_all, F) # Piola-Kirchoff I tensor
  Sigma = dolfin.inv(J)*PK1*F.T # Cauchy stress tensor

  return  dolfin.as_tensor([[Sigma[0, 0], Sigma[0, 1]],
          [Sigma[1, 0], Sigma[1, 1]]])

V_stress = dolfin.TensorFunctionSpace(mesh_domain, 'DG', INTERPOLATION_DEGREE)
U_stress = dolfin.FunctionSpace(mesh_domain, 'CG', INTERPOLATION_DEGREE)
stress_tensor = stress_tensor_func(u, material_parameters, material_markers)
stress_tensor = dolfin.project(stress_tensor, V_stress)

sXX = stress_tensor.sub(0)
sYY = stress_tensor.sub(3)
sXY = stress_tensor.sub(1)

eig_max = (sigma_XX + sigma_YY)/2 + dolfin.sqrt(((sigma_XX - sigma_YY)/2)**2 +
    sigma_XY**2))
eig_min = (sigma_XX + sigma_YY)/2 - dolfin.sqrt(((sigma_XX - sigma_YY)/2)**2 +
    sigma_XY**2))

nX_max = -stress_tensor[0, 1]/(stress_tensor[0, 0] - eig_max)
nY_max = 1

nX_min = -stress_tensor[0, 1]/(stress_tensor[0, 0] - eig_min)
nY_min = 1

sigma_bar = dolfin.Function(V_stress, name="Principal_Stress")
sigma_bar.assign(dolfin.project(dolfin.as_tensor(((eig_max,0.),(0.,eig_min))),
    V_stress))

psi_bar_max = ufl.atan_2(nY_max, nX_)
psi_bar_max = ufl.atan_2(nY_min, nX_min)
eig_dir_max = dolfin.project(psi_bar_max, tress)
eig_dir_min = dolfin.project(psi_bar_min, tress)


```

Algorithm C.1: Implementing the eigenvalues and eigenvectors of the Cauchy stress.

D Orthotropic Linear Model: Finite Element *versus* Analytical Solutions

(a) $E_1 = 0.01$ MPa

(b) $E_1 = 0.1$ MPa

(c) $E_1 = 1$ MPa

(d) $E_1 = 10$ MPa
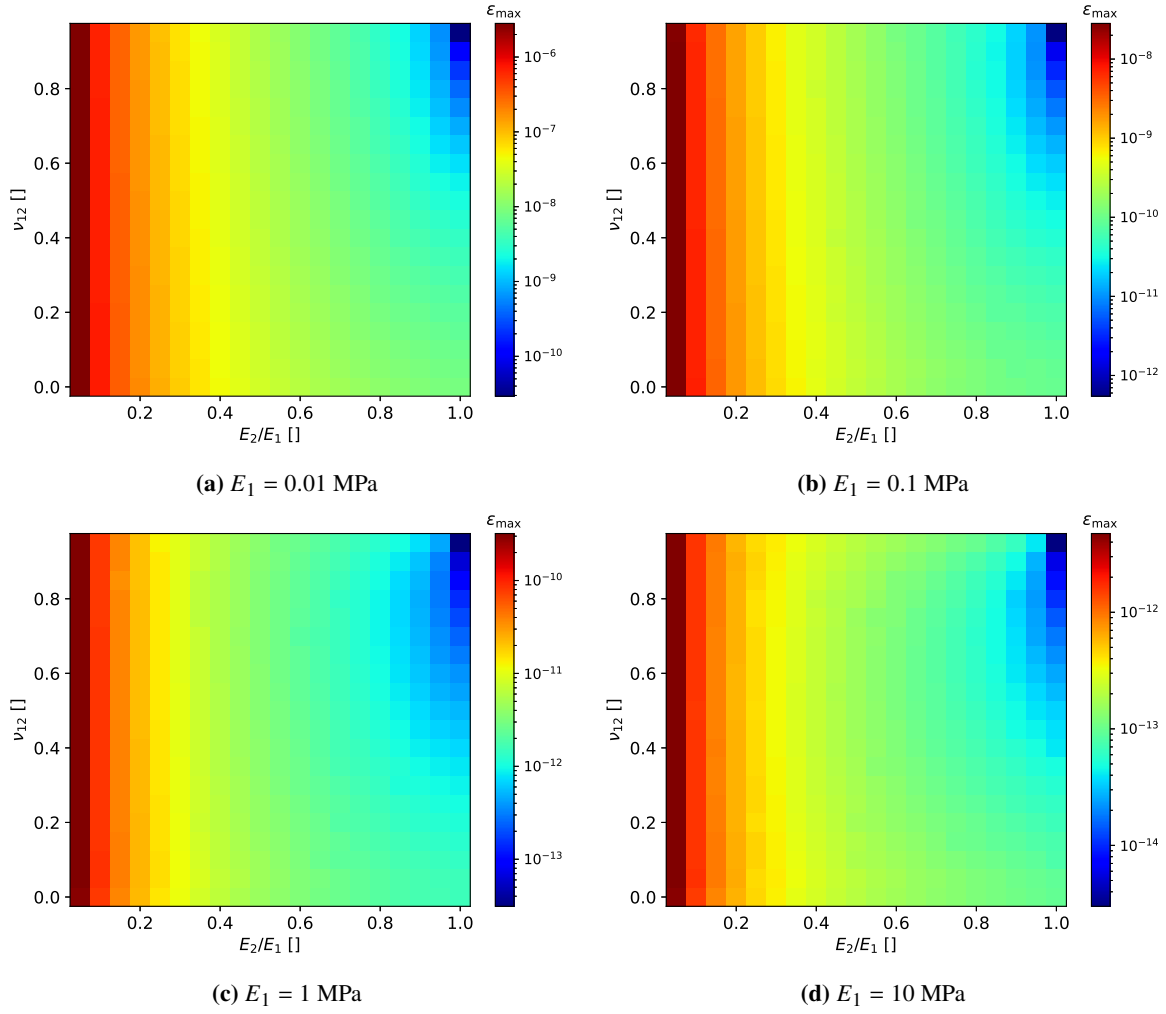
Figure D.1: Comparison of the model FEM and analytical solutions for several parameters.

E *Intra*-Subject's Skin Anisotropy Characterization

Table E.1: Numerical results of the inverse identification of $\tilde{\boldsymbol{m}}_g$ for every test. Published in [402].

Test	a [mm]	b [mm]	$\phi[°]$	$x_{10}[\mu m]$	$x_{20}[\mu m]$	R_{cor}
1	1.0029	1.0632	60.24	−17.8	14.9	0.9849
2	0.9990	1.0072	72.21	−8.3	1.7	0.9424
3	0.9992	1.0290	30.77	−4.7	−2.7	0.9687
4	1.0028	1.0306	27.61	−2.6	3.0	0.9685
5	1.0035	1.0282	31.25	−3	−8.0	0.9578
6	1.0020	1.0221	50.26	−2.7	18.9	0.9813
7	1.0039	1.0337	33.41	1.3	5.8	0.9774
8	1.0078	1.0381	43.09	−1.0	9.5	0.9868
9	1.0041	1.0301	42.35	−0.9	8.4	0.9774
10	1.0039	1.0485	36.95	−6.3	21.5	0.9889
11	1.0073	1.0321	50.80	−8.1	9.2	0.9648
12	1.0061	1.0363	46.39	2.3	13.4	0.9585
13	0.9948	1.0230	40.82	4.6	0.7	0.9826
14	1.0024	1.0265	26.25	−8.7	8.5	0.9834
15	1.0004	1.0316	37.36	−1.5	−19.5	0.9865
16	1.0058	1.0337	40.65	−6.9	6.5	0.9710
17	0.9991	1.0289	42.15	−4.0	0.3	0.9696
18	1.0063	1.0327	64.82	−9.4	−13.3	0.9866
19	1.0002	1.0260	28.81	6.0	7.0	0.9730
20	0.9960	1.0255	48.23	−1.7	17.0	0.9887
21	1.0017	1.0323	43.45	−11.7	6.7	0.9727
22	1.0002	1.0266	30.70	−1.3	12.1	0.9700
23	1.0024	1.0165	42.41	−1.9	−20.4	0.9902
24	0.9975	1.0266	49.16	3.0	3.4	0.9751
25	1.0077	1.0408	49.72	6.3	−13.0	0.9820
26	1.0039	1.0287	45.48	−2.2	−20.9	0.9786
27	1.0007	1.0201	43.09	5.4	−5.6	0.9660
28	0.9960	1.0368	46.48	12.9	−0.1	0.9861
29	0.9986	1.0175	63.46	6.7	7.5	0.9487
30	1.0024	1.0376	36.34	−0.2	8.6	0.9746

(a) Test 1   **(b)** Test 2   **(c)** Test 3

(d) Test 4   **(e)** Test 5   **(f)** Test 6

(g) Test 7   **(h)** Test 8   **(i)** Test 9

(j) Test 10   **(k)** Test 11   **(l)** Test 12

(m) Test 13   **(n)** Test 14   **(o)** Test 15
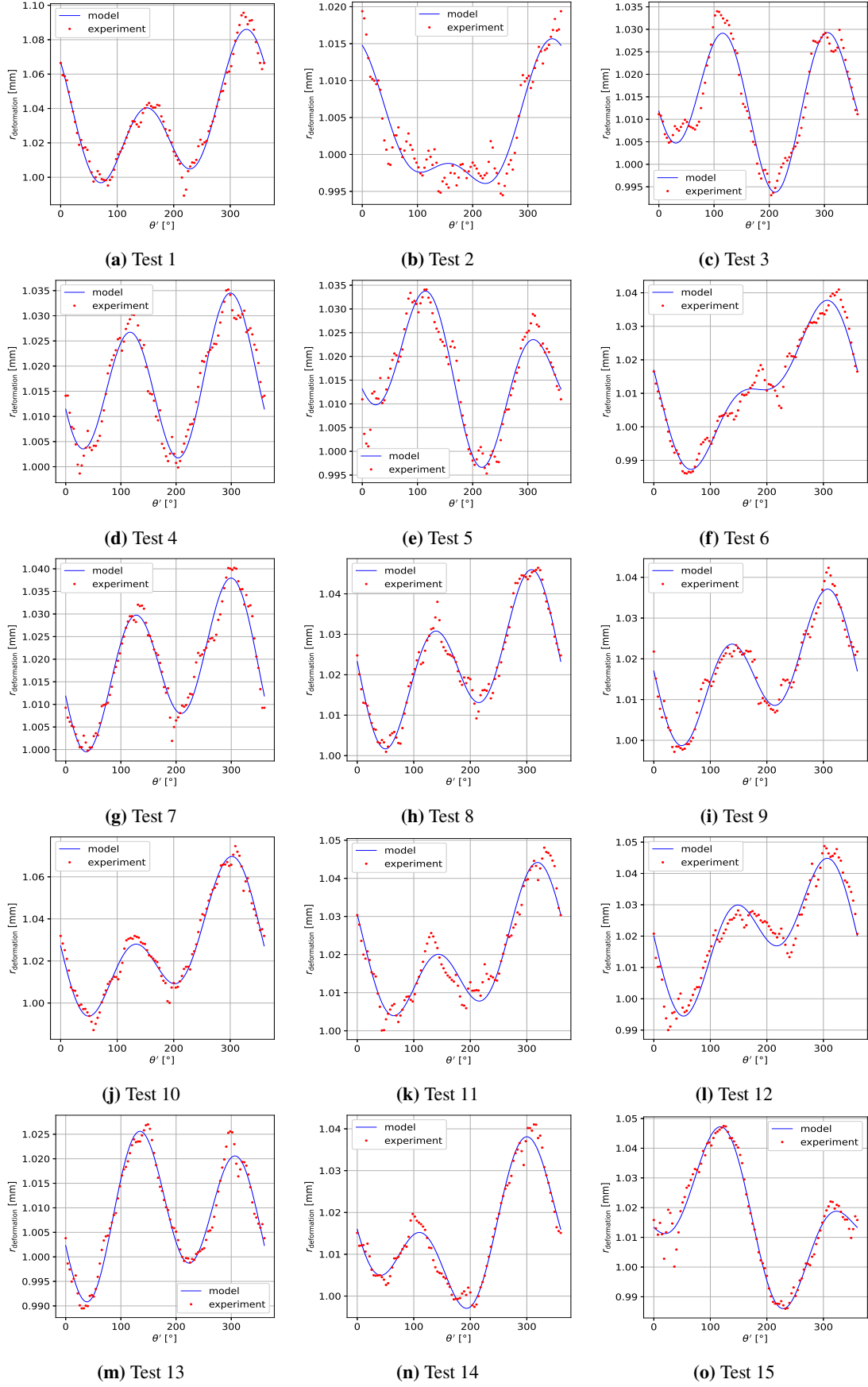
Figure E.1: Model fitting with the identified parameters of the volunteer's skin for all test.

F Bayesian Inference

The likelihood links the model to the measurement data and equals 1 when the model and observations are exactly the same. But in reality, a discard vector ϵ_{noise} between them takes place and corresponds to measurement and modeling errors. For a fixed pressure p, one could write

$$y = f(m, X) + \epsilon_{\text{noise}} \tag{6.1}$$

where $f : \mathbb{R}^{N_d} \rightarrow \mathbb{R}^{N_d}$ is the model (5.6) dependent on the set parameters and the grid nodes coordinates X. The likelihood is set as the probability of the difference ϵ_{noise} to be null with respect to a sampled parameter set. It is also interpreted as a distribution of the 'nullness' of the objective function $\mathcal{J}_{\text{B}}$ to be maximized. According to Gaussian law properties *vis-à-vis* variables independency, the posterior for measurement point i can play the role of the prior for measurement point $i + 1$. Thus, employing the likelihood expression for independent measurements $u^{\text{MARS}}(X_i)$ $(i = 1, 2, ..., N_d)$ reads

$$P(y|m) = \prod_{i=1}^{N_d} \pi^{\text{likelihood}}\left(\mathcal{J}_{\text{B}}(X_i, m, y_i)\right) \tag{6.2}$$

with the cost function

$$\mathcal{J}_{\text{B}}(X_i, m, y_i) = \|u(X, m) - u_i^{\text{MARS}}(X_i)\|_2 \tag{6.3}$$

According to Rappel *et al.*'s tutorial [397], we propose correlating likelihood distribution with available standard deviation from the experiment, s_i on every X_i node. As the number of data series is 30 for a given pressure, the noise is assumed to be normally distributed around the cost.

$$\pi^{\text{likelihood}}\left(\mathcal{J}_{\text{B}}(X_i, m, y_i)\right) = \frac{1}{\sqrt{2\pi}s_i} \exp\left(-\frac{\mathcal{J}_{\text{B}}^2(X_i, m, y_i)}{2s_i^2}\right) \tag{6.4}$$

The observation data are the interpolated displacement u^{MARS} and their respective standard deviations s_i obtained from one displacement field resulting from the averaging of the 30 fields. Figure F.1 demonstrates the displacement norm and the deviations evaluated along a circle.

The prior distribution for any m must be physically correct and consists of two quantities, m_{prior} and Γ_{prior}, respectively, the mean vector and the covariance matrix of the prior. Setting the prior is the most challenging procedure for the Bayesian inference regarding its interpretation difficulty. The user must establish it.

$$P(m) \propto \begin{cases} \exp\left(-\frac{1}{2}(m - m_{\text{prior}})^T \Gamma_{\text{prior}}^{-1}(m - m_{\text{prior}})\right), & \text{if } E_1 > 0 \quad \text{and} \quad E_2 > 0 \\ 0, & \text{otherwise} \end{cases} \tag{6.5}$$

Through Equations 5.21 and 6.5, we obtain the expression of the posterior (Eq. 6.6). The latter is used then to drive the random samples toward 'best' parameters among thousands, based on the Metropolis-Hastings algorithm, a Markov Chain Monte Carlo technique (MCMC).

$$P(m|y) \propto \exp\left(-\frac{1}{2}\left[(m - m_{\text{prior}})^T \Gamma_{\text{prior}}^{-1}(m - m_{\text{prior}}) + \sum_{i=1}^{N_d} \frac{\mathcal{J}_{\text{B}}^2(X_i, m, y_i)}{2s_i^2}\right]\right) \tag{6.6}$$

MCMC method can be divided into two sub-methods: Markov-Chain for drawing parameter samples strategy to ensure the convergence, and Monte-Carlo for approximating the quantities of interest numerically. Once the posterior is established after N_s drawn samples, let us quantify three quantities: the MAP, the mean m_{post}, and the covariance matrix Γ_{post}.

$$\text{MAP} = \underset{m_s; s=1,2,...,N_s}{\text{argmax}} P(m|y) \tag{6.7}$$

The mean of the posterior is by definition (N_p is obtained after burning a part of N_s)

$$m_{\text{post}} = \int_{\mathbb{R}^{N_P}} m\, P(m|y)\, dm \qquad (6.8)$$

However, as m is not continuous, the Monte-Carlo method is implemented to approximate the integral. For a large number of samples [397]:

$$m_{\text{post}} = \lim_{N_s \to \infty} \frac{1}{N_s} \sum_{s=1}^{N_s} m_s \qquad (6.9)$$

Moreover, the Γ_{post} matrix elements are obtained as follows [348]:

$$(\Gamma_{\text{post}})_{ij} = \frac{1}{N_s - 1} \sum_{s=1}^{N_s} \Big((m_s)_i - (\bar{m}_{\text{post}})_i \Big)\Big((m_s)_j - (m_{\text{post}})_j \Big), \ i = 1, 2, ..., N_p, \ j = 1, 2, ..., N_p \quad (6.10)$$
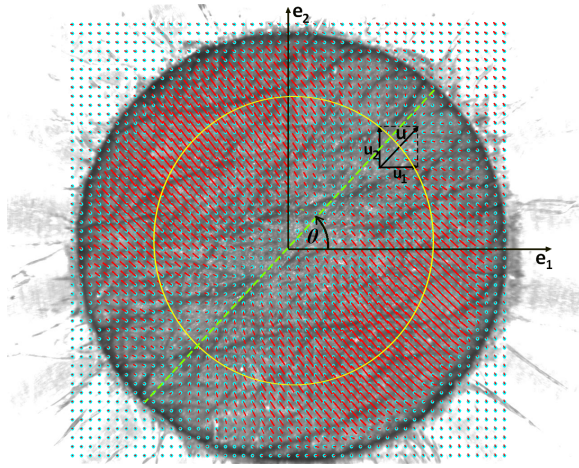
(a) 2D mean-displacement field
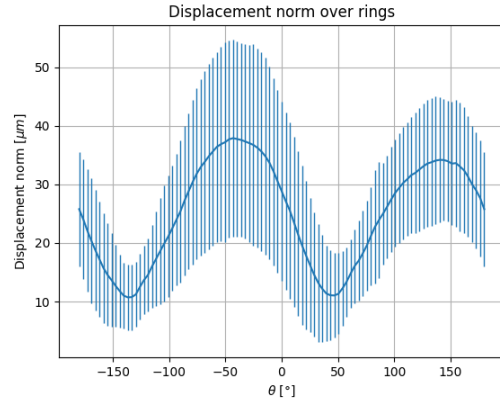
(b) Standard deviation over yellow ring, $r = 1.5$ mm

Figure F.1: Example of observation data to be used for the Bayesian inference. (a) the mean value of displacement vector on all nodes for a given pressure ($p = 300$ mbar in this case). (b) the displacement u_i^{MARS} and its relative standard deviation s_i for all angles.
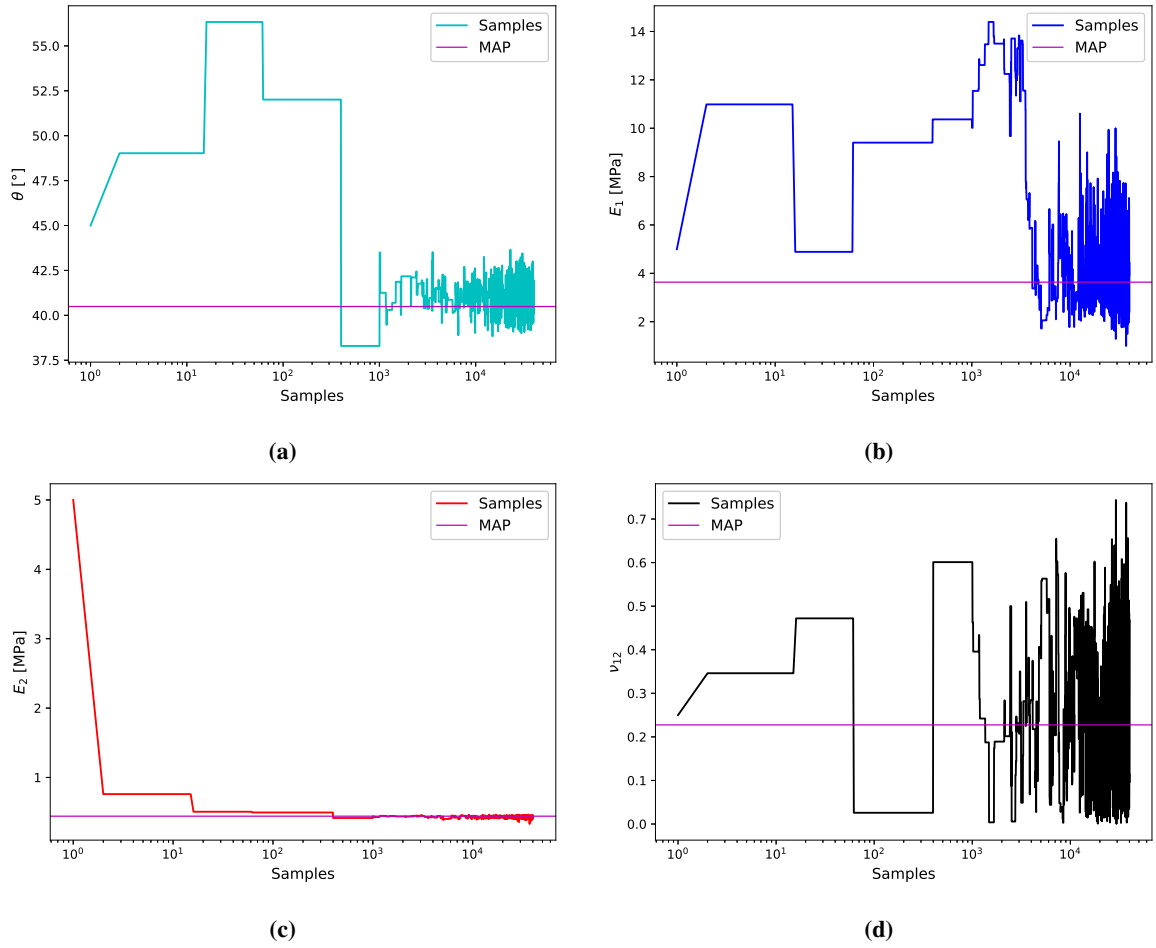
Figure F.2: Evolution of the parameter samples processed with the Metropolis-Hastings algorithm.
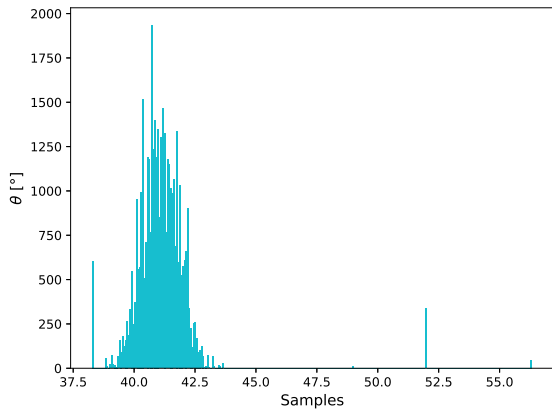
(a)
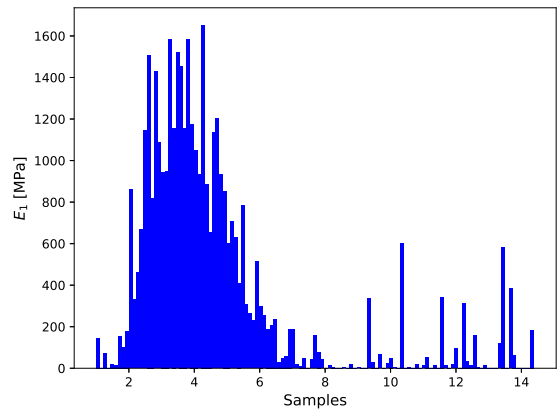
(b)

(c)

(d)

Figure F.3: Distribution of the parameter samples processed with the Metropolis-Hastings algorithm.

(a)

(b)

(c)

(d)

Figure F.4: Improving the prior knowledge the with Bayesian inference.

G   Clinical Trial

Table G.1: Complete results of the parameter identification process on the clinical trial data.

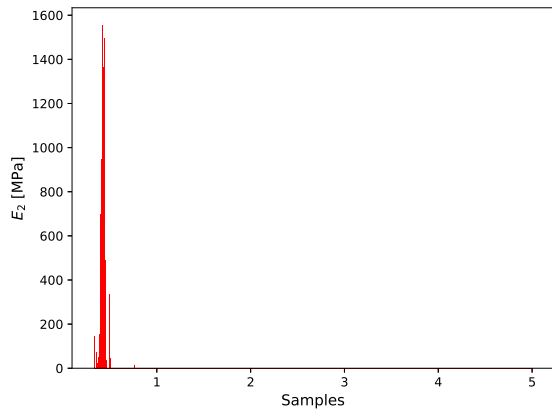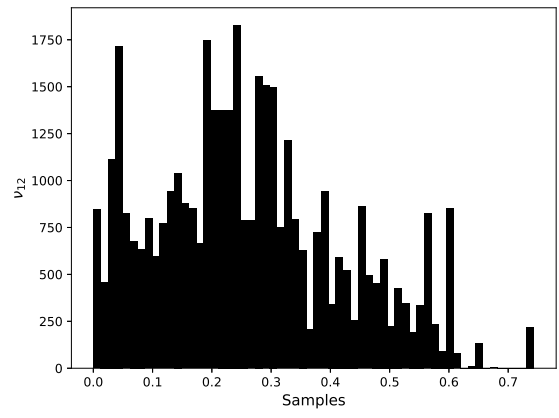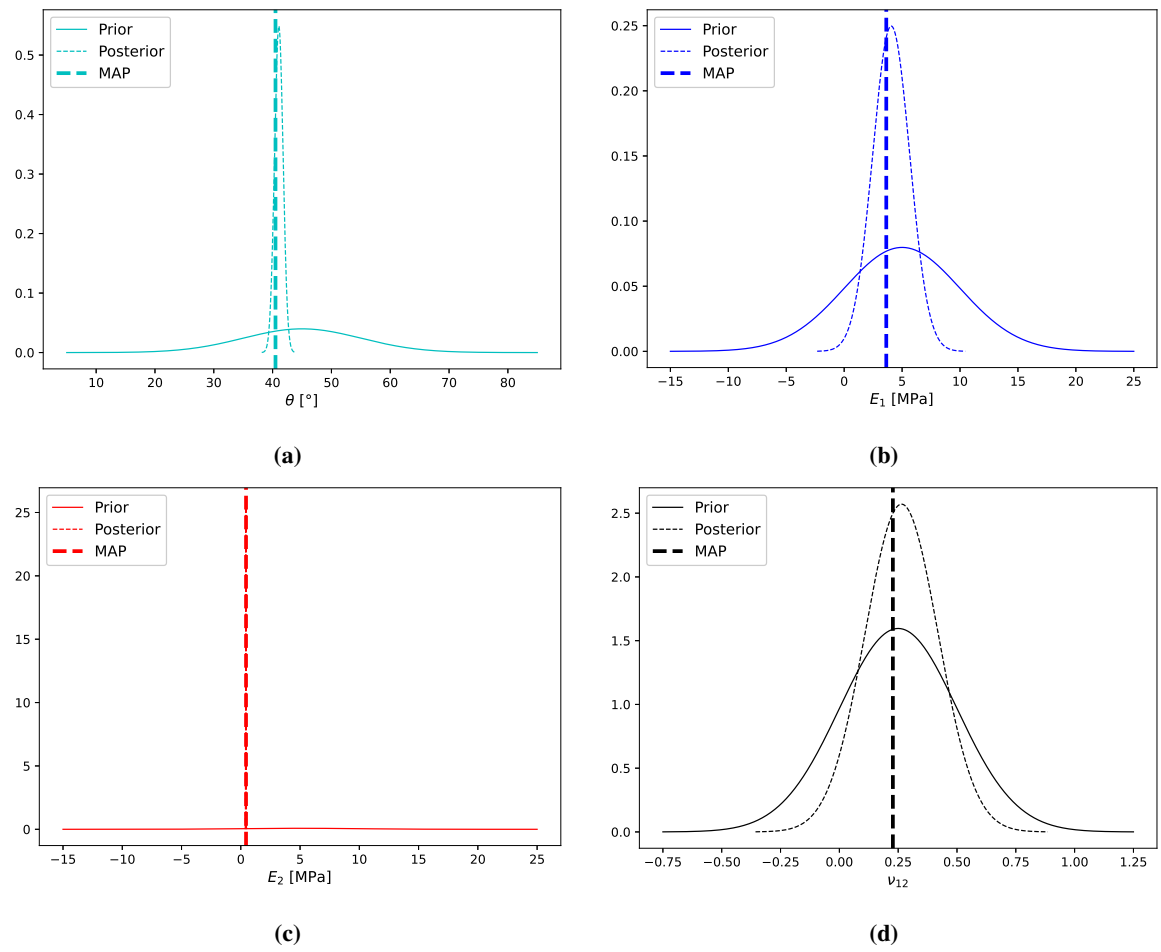| Subject	Sex	Age	ϕ [°]	a [mm]	b [mm]	x_{10} [µm]	x_{20} [µm]	R_{cor}	E_1 [MPa]	E_2 [MPa]
			20.3	1.0073	1.0401	-4.9	-9.0	0.9456	0.9612	0.2699
1	F	20	9.2	1.0084	1.0727	-2.9	10.0	0.9729	0.8358	0.1557
			20.3	1.0038	1.0465	0.1	-10.1	0.9694	1.8676	0.2495
			25.6	0.9953	1.0150	1.3	-18.2	0.9910	-1.4831	1.0789
2	F	20	16.2	1.0013	1.0212	-4.0	-15.7	0.9834	5.5031	0.5538
			18.7	1.0029	1.0217	4.9	-10.3	0.9327	2.4412	0.5149
			46.6	1.0018	1.0284	-0.5	-23.6	0.9650	3.9790	0.4136
3	M	22	40.8	0.9798	1.0027	3.9	-7.8	0.9796	-0.3476	-0.9809
			23.6	0.9936	0.9995	2.0	-1.4	0.6123	-1.0895	-2.3110
			53.2	1.0010	1.0255	5.0	-34.8	0.9905	7.0251	0.4694
4	F	23	43.6	0.9982	1.0331	-3.9	-19.2	0.9795	-3.9987	0.3876
			8.1	0.9990	1.0280	-0.4	-4.9	0.9674	-7.0110	0.4510
			12.1	1.0088	1.0401	-4.7	-2.1	0.9719	0.7972	0.2635
5	F	23	24.7	1.0207	1.0456	-3.9	-11.9	0.9001	0.3381	0.2007
			28.7	1.0038	1.0210	1.2	-16.5	0.9770	1.8577	0.5165
			38.7	1.0143	1.0401	-14.1	-12.8	0.9804	0.4899	0.2419
6	F	24	10.9	0.9854	1.0256	-6.0	-1.7	0.9259	-0.4818	0.8396
			33.3	0.9991	1.0440	-2.2	-12.5	0.9935	-7.5112	0.2844
			24.4	0.9985	1.0264	-1.9	-2.3	0.9270	-4.5320	0.4872
7	M	24	28.2	0.9982	1.0173	-4.2	-11.6	0.7561	-3.9189	0.7693
			34.7	0.9829	1.0222	-2.3	-5.7	0.8164	-0.4111	1.3137
			28.0	1.0058	1.0419	-0.9	1.1	0.9694	1.2111	0.2657
8	F	24	22.5	1.0017	1.0499	-0.4	0.6	0.9405	4.0456	0.2401
			22.5	1.0080	1.0420	-0.6	0.1	0.9319	0.8817	0.2564
			28.0	1.0018	1.0281	1.2	-10.3	0.9575	4.0017	0.4177
9	F	24	40.1	0.9958	1.0236	-7.5	-18.8	0.9875	-1.6850	0.6013
			44.7	0.9985	1.0067	-5.3	-31.3	0.9967	-4.5827	2.2051
			12.6	1.0154	1.0744	-17.2	-25.3	0.9679	0.4544	0.1430
10	F	25	17.2	0.9999	1.0473	5.1	-6.8	0.9018	-85.0850	0.2602
			13.7	1.0027	1.0548	-1.6	9.2	0.9732	2.5880	0.2162
			22.4	0.9988	1.0397	-2.5	-10.3	0.9795	-6.0628	0.3170
11	F	25	59.5	0.9978	1.0036	2.0	-8.4	0.9830	-3.2526	6.1349
			36.1	1.0085	1.0340	-10.5	-6.3	0.9157	0.8216	0.3038
			4.4	1.0052	1.0447	0.3	-0.1	0.9759	1.3522	0.2532
12	F	25	12.4	1.0141	1.0287	-11.9	-18.2	0.9905	0.4989	0.3128
			10.3	1.0075	1.0378	2.2	-7.1	0.9805	0.9297	0.2829
			33.2	0.9983	1.0293	-3.0	-0.3	0.9515	-4.2063	0.4382
13	F	26	17.4	1.0199	1.0332	-6.2	-31.0	0.9911	0.3528	0.2553
			25.2	1.0009	1.0203	0.8	-26.2	0.9903	7.7214	0.5853
			16.5	1.0090	1.0385	-6.9	-4.3	0.9167	0.7802	0.2717
14	F	26	17.5	1.0067	1.0454	4.0	-7.5	0.9443	1.0524	0.2442
			13.2	1.0050	1.0433	0.1	-1.3	0.9806	1.3938	0.2610
			15.7	1.0053	1.0389	9.2	0.5	0.9600	1.3281	0.2867
15	F	26	23.1	1.0000	1.0342	4.2	-10.0	0.9290	-195.8380	0.3601
			16.3	1.0019	1.0367	1.5	9.2	0.9684	3.7673	0.3231
			13.9	1.0006	1.0139	-1.6	-12.4	0.9480	11.7634	0.8544
16	F	26								

			24.5	1.0029	1.0192	0.0	-14.9	0.9811	2.4276	0.5761
			28.0	1.0077	1.0247	3.6	-0.8	0.9512	0.9062	0.4028
17	M	29	27.1	1.0010	1.0132	-0.1	-2.4	0.9584	7.0040	0.8812
			43.1	1.0032	1.0072	1.2	10.1	0.9843	2.1978	1.2809
			61.7	0.9883	1.0012	0.9	-15.4	0.9526	-0.5991	-1.6150
18	F	30	18.7	0.9965	1.0097	-7.2	-13.2	0.9887	-2.0174	1.7419
			-0.5	1.0121	1.0377	1.0	-6.5	0.9221	0.5771	0.2624
			8.1	0.9934	1.0200	0.1	-16.0	0.9895	-1.0555	0.8208
19	F	30	-0.6	1.0134	1.0342	-3.6	-18.4	0.9753	0.5234	0.2776
			14.3	1.0025	1.0224	-6.4	-9.5	0.9607	2.8191	0.5063
			14.6	0.9969	1.0217	-9.0	-18.8	0.9819	-2.2483	0.6363
20	F	32	22.1	1.0074	1.0297	-7.4	-4.2	0.9518	0.9431	0.3486
			25.7	1.0011	1.0170	-4.8	-10.1	0.9713	6.1926	0.6887
			22.0	1.0116	1.0355	-13.1	-2.4	0.9570	0.6031	0.2776
21	F	32	16.4	1.0061	1.0263	-5.9	-22.7	0.9861	1.1469	0.3981
			18.2	1.0108	1.0352	1.0	-13.1	0.9758	0.6515	0.2839
			12.7	1.0110	1.0402	2.1	-13.0	0.9711	0.6349	0.2534
22	F	33	12.7	0.9995	1.0493	1.2	-16.7	0.9802	-14.5035	0.2512
			-1.0	0.9761	1.0428	13.7	-4.2	0.8495	-0.2932	0.4975
			1.5	1.0034	1.0491	-8.6	-20.0	0.9680	2.0798	0.2382
23	F	35	9.1	0.9949	1.0311	-6.0	-10.8	0.9248	-1.3689	0.4511
			10.3	0.9951	1.0359	-0.5	3.3	0.9705	-1.4315	0.3814
			29.6	1.0006	1.0381	-10.6	-19.8	0.9876	11.6076	0.3187
24	M	38	43.5	0.9889	1.0187	-14.8	-4.0	0.9668	-0.6337	1.1856
			38.7	0.9953	1.0108	1.0	-1.6	0.8838	-1.4947	1.6962
			16.8	0.9915	1.0124	5.6	-2.8	0.9629	-0.8226	2.0657
25	M	39	56.8	0.9969	1.0125	-1.5	-32.5	0.9910	-2.2640	1.2099
			22.5	1.0139	1.0305	-5.5	-19.2	0.9682	0.5060	0.3002
			31.8	0.9970	1.0241	-10.5	-7.3	0.9848	-2.3570	0.5616
26	F	42	35.8	1.0079	1.0386	4.6	-1.3	0.9241	0.8890	0.2758
			39.7	1.0109	1.0302	-2.2	-4.5	0.8251	0.6403	0.3201
			35.3	0.9978	1.0349	-4.6	-8.2	0.9421	-3.2312	0.3702
27	M	45	23.4	1.0031	1.0447	-10.6	-6.1	0.9640	2.2645	0.2613
			35.3	1.0389	1.0666	3.0	4.2	0.9366	0.1803	0.1282
			19.0	1.0111	1.0697	-7.1	-3.1	0.9115	0.6309	0.1575
28	F	47	26.5	1.0110	1.0604	14.8	-18.2	0.9714	0.6369	0.1790
			24.9	1.0208	1.0507	-4.4	-6.4	0.9506	0.3377	0.1852
			32.4	1.0177	1.0520	-17.3	-30.5	0.9771	0.3971	0.1883
29	F	48	23.3	0.9912	1.0211	2.3	-7.1	0.9340	-0.7952	0.8485
			15.7	0.9905	1.0019	-1.9	-26.7	0.9794	-0.7398	-2.3606
			35.1	1.0022	1.0307	-12.9	-22.4	0.9914	3.2549	0.3806
30	M	49	43.8	1.0017	1.0363	-21.7	8.4	0.9798	4.1732	0.3278
			43.8	1.0019	1.0171	-3.1	-5.3	0.7406	3.7754	0.6641
			22.9	1.0027	1.0370	-3.8	-2.7	0.9403	2.5588	0.3147

(a) Volunteer 4

(b) Volunteer 20
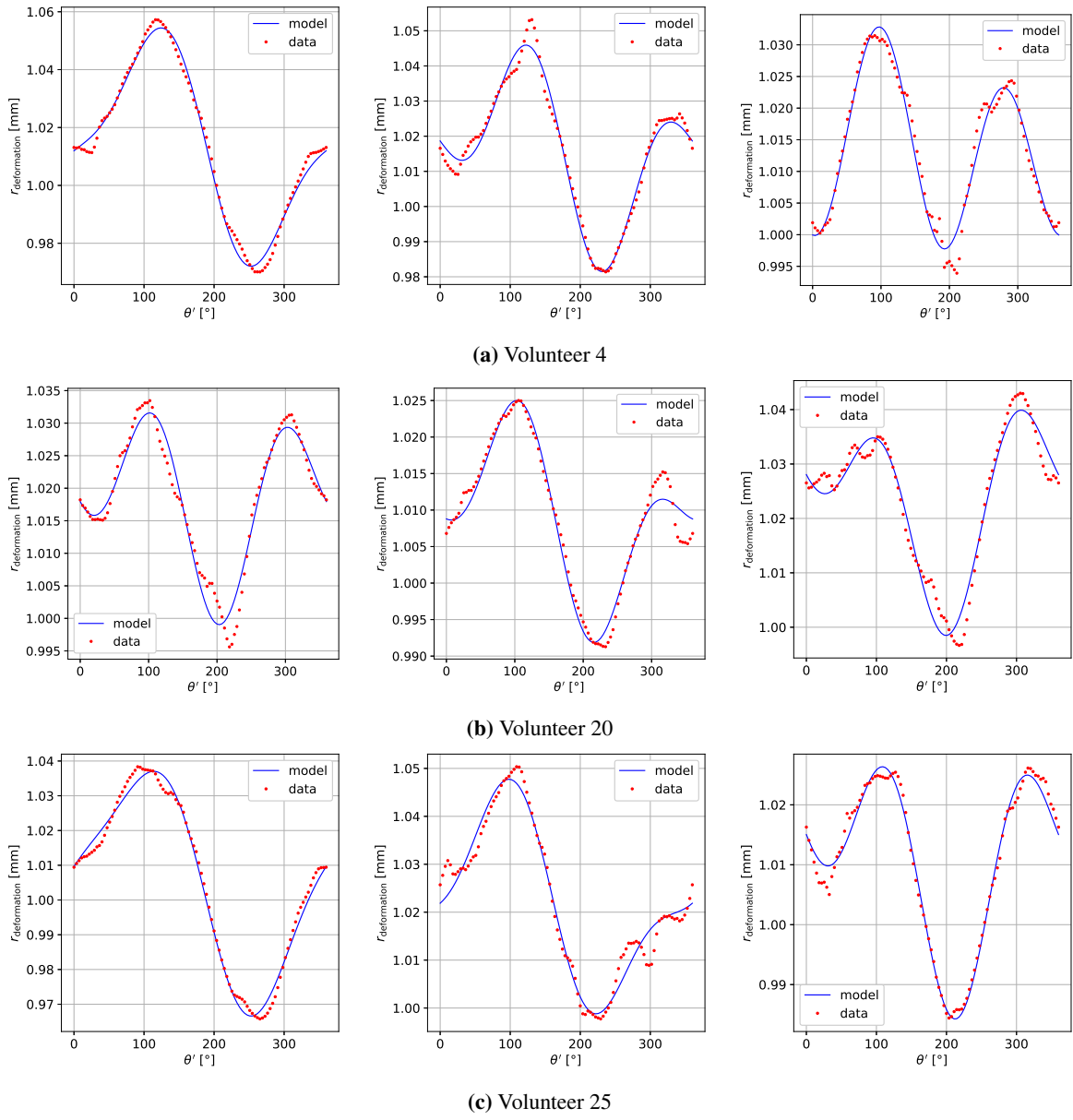
(c) Volunteer 25

Figure G.1: Model fitting with the identified parameters of the volunteer's skin for some volunteers.

UNIVERSITÉ DU LUXEMBOURG

Faculty of Science, Technology and Medicine
Doctoral School in Science and Engineering (DSSE)

Doctoral Programme in Computational Sciences

TRANSCRIPT OF THE TRAINING ACTIVITIES

This document has been generated electronically for information purposes only.

To verify the authenticity of the information in this document you are advised to refer to the official diploma supplement.

NAME, first name	ELOUNEG, Aflah
Date of Birth	10-08-1992
Place of Birth	El Guerrara, Algeria
Student ID	120002685B

Total ECTS awarded	**22.5**
Disciplinary/Interdisciplinary ECTS	17
Transferable Skills ECTS	5.5

Disciplinary / Interdisciplinary ECTS

Activity Title	Place	Date(s)/Period	ECTS
14th WCCM congress	Paris (online)	11.01.2021 to 15.01.2021	1
26th Congress of the European Society of Biomechanics	Milan, Italy (online)	11.07.2021 to 14.11.2021	1
45e Congrès de société de biomécanique	Metz, France (online)	26.10.2020 to 28.10.2020	1
Congrès Français de Mécanique	Brest, France	26.08.2019 to 30.08.2019	2
Several courses in the framework of the co-supervision at Université Bourgogne - Franche-Comté	Université Bourgogne Franche-Comté	01.10.2018 to 30.09.2021	4
Paper publication: 'An open-source FEniCS-based framework for hyperelastic parameter estimation from noisy full-field data: Application to heterogeneous soft tissues'	Elouneg et al, Computers & Structures 255	15 October 2021	2
Oral presentation at DPCS Presentation Event and General Assembly	University of Luxembourg	10.05.2022	2
Summer school - MECHANOBIOLOGY AND TRIBOLOGY OF THE SKIN - FROM EXPERIMENTAL CHARACTERISATION TO MODELLING	Centre International des Sciences Mécaniques	24.06.2019 to 28.06.2019	2
Winter School - Computer vision and machine learning for the material scientist	Online - Centre des Matériaux de Mines ParisTech	21.02.2022 to 25.02.2022	2
		Total	**17**

Transferable Skills ECTS

Activity Title	Place	Date(s)/Period	ECTS
Online Course - Research Integrity	Online	3 days	1
Courses in the framework of the co-supervision at Université Bourgogne - Franche-Comté	Université Bourgogne Franche-Comté	01.10.2018 to 30.09.2021	4
Writing Café	University of Luxembourg	02.12.2022	0.5
		Total	**5.5**

Titre : Caractérisation mécanique *in vivo* des tissus mous : application à la peau humaine et la chéloïde
Mots clés : chéloïde, expériences in vivo, identification des paramètres matériaux, méthode des éléments finis, corrélation d'images, anisotropie

Résumé :
Le développement des chéloïdes, tumeurs bénignes sur la peau humaine, n'est pas exclusivement dû à des facteurs biologiques ou génétiques. La présence de sites anatomiques favorables à l'apparition de ces tumeurs, tandis que d'autres en manquent, atteste de l'importance de l'environnement mécanique du tissu. La thèse vise à résoudre le problème de la croissance des chéloïdes en développant une méthode patient-spécifique, SoFTI, basée sur des mesures expérimentales *in vivo* et une modélisation numérique. L'objectif est de prévenir la propagation des cicatrices chéloïdiennes à l'aide d'une solution médicale de contention en identifiant les paramètres matériau optimaux pour quantifier les contraintes mécaniques et cartographier ses directions privilégiées localement. De plus, le travail de recherche présente la méthodologie MARSAC pour charactériser l'anisotropie dans la peau saine en identifiant la ligne de Langer et la raideur le long et à travers celle-ci partant d'une expérience d'aspiration annulaire multi-axiale *in vivo*. La méthode a été employée pour analyser la variabilité *intra-* et *inter*-sujets sur un essai clinique.

Title: *In vivo* mechanical characterization of soft tissues: application to human skin and keloids
Keywords: keloid, *in vivo* experiments, material parameter identification, finite element method, digital image correlation, anisotropy

Abstract:
The development of keloids, benign tumors on human skin, is not exclusively due to biological or genetic factors. The presence of anatomical sites favorable to the appearance of these tumors, while others are lacking them, attests to the importance of the mechanical environment of the tissue. The thesis aims to address the problem of keloid growth by developing a patient-specific pipeline, SoFTI, based on *in vivo* experimental measurements and numerical modeling. The objective is to prevent further propagation of keloidic scars *via* a medical containment solution by identifying optimal material parameters to quantify mechanical stress and map its privileged direction locally. Additionally, the research work introduces MARSAC methodology to characterize the anisotropy in an undamaged skin by estimating Langer's line and stiffness along and across it with an *in vivo* multi-axial annular suction experiment. The method was used to analyze *intra*-subject and subject-to-subject variability over a clinical trial.